Universitat Autònoma de Barcelona

Analysis of high-precision spectroscopic and photometric data for planet and stellar characterisation

David Baroch López

TESI DOCTORAL

Analysis of high-precision spectroscopic and photometric data for planet and stellar characterisation

---

Autor:
DAVID BAROCH LÓPEZ

Director:
JUAN CARLOS MORALES PERALTA
Tutor:
RAFEL ESCRIBANO CARRASCOSA

Tesi Doctoral presentada per a optar al grau de Doctor en Física

a la

Universitat Autònoma de Barcelona
Departament de Física, Programa de Doctorat en Física
Institut de Ciències de l'Espai (ICE, CSIC)
Institut d'Estudis Espacials de Catalunya (IEEC)

Juny 2021

Agraïments

No voldria entrar en matèria sense abans agrair totes les persones que, en un moment o altre, han contribuït a fer que aquest treball hagi pogut sortir endavant. És ben sabut que el factor més important que hi ha a l'hora de poder gaudir mentre s'és estudiant de doctorat és l'elecció d'un bon director de tesi. En el meu cas l'he encertat de ple. Gràcies, Juan Carlos, per tot el suport i guiatge durant els tres treballs que m'has supervisat, tenint en tot moment la porta del despatx oberta disposat a donar un cop de mà. Ignasi, gràcies per la confiança a l'hora de poder assumir nous projectes, i per donar-me l'oportunitat de poder formar part del grup d'exoplanetes, en el que m'he sentit com a casa durant aquests anys. Quiero agradecer también a Álvaro su invaluable ayuda en la durante uno de los proyectos más frustrantes y a la vez gratificantes de toda la tesis.

I am also grateful to all the people in CARMENES for allowing me to enjoy of such an active and collaborative project. The countless meetings and discussions made possible a much more rigorous work. En particular quiero agradecer a José su especial atención por los miembros más novatos del consorcio, haciendo que nos sintamos integrados desde el primer momento, ayudando con sus tutoriales y correcciones a iniciarse en el complicado mundo de la escritura científica.

També voldria agrair a tots aquells que m'han ajudat a desviar la mirada de l'ordinador durant tots aquests anys, ja que sense vosaltres probablement hauria perdut el seny. Gràcies Marina, Mariona, Andrea i Anna per tots els matins, dinars, postdinars, berenars, raids i qualsevol excusa per fer safareig una estona, al Pablo per les roquetes i altres fricades que m'ha ensenyat des del màster, i en general a tots els companys que han fet la meva estança a l'ICE més agradable, sé que m'emporto molts bons amics.

Gràcies a la meva família pel seu etern suport i als meus amics per ajudar-me a recuperar les forces cada cap de setmana. En especial vull agrair a la Núria el seu suport incondicional durant tots aquests anys i per creure en mi en tot moment. Finalment, el més profund agraïment als meus pares i germà, si he pogut arribar fins aquí ha sigut gràcies a vosaltres.

Resum

La detecció de la primera estrella binària més de 200 anys enrere va representar l'inici de tot un nou camp de l'astrofísica dedicat a l'estudi de l'evolució i les interaccions d'aquests sistemes, fent servir com a principal eina l'anàlisi del moviment reflex causat pel company orbitant. Va ser només qüestió de temps que els instruments de mesura assolissin un nivell de precisió prou elevat per a detectar els moviments induïts per planetes sobre les seves estrelles. El descobriment del primer exoplaneta fa quasi tres dècades va suposar la creació d'un reguitzell de projectes dedicats a la cerca de nous mons, els quals estan produint un munt de dades que també estan essent utilitzades amb la finalitat d'estudiar diferents propietats de les estrelles.

L'objectiu principal d'aquesta tesi és l'estudi i caracterització d'exoplanetes, estrelles i sistemes estel·lars mitjançant l'anàlisi de dades provinents de projectes dedicats a la cerca d'exoplanetes amb instruments d'alta precisió. Aquest és el cas dels projectes CARMENES i TESS, que tenen l'objectiu de trobar planetes fent servir el mètode de la velocitat radial i la detecció de trànsits planetaris, respectivament, posant un èmfasi especial en estrelles de tipus M.

Primerament, hem desenvolupat un nou mètode per a determinar les propietats de les taques estel·lars i dels moviments convectius en estrelles M usant la variabilitat induïda per l'activitat estel·lar. En particular, hem modelat les velocitats radials cromàtiques i la fotometria de l'estrella YZ CMi fent servir el software de modelatge d'activitat estel·lar `StarSim`. L'anàlisi ha revelat la presència d'una gran taca polar amb una temperatura $\sim 200\,\mathrm{K}$ inferior a la de l'estrella, trobant també que el moviment convectiu de l'estrella podria tenir un moviment invers a l'esperat.

A partir d'un anàlisi combinat de velocitats radials antigues i de CARMENES, en aquesta tesi presentem la detecció d'un mini Neptú i una superterra al voltant de les estrelles M LSPM J2116+0234 i GJ 686, respectivament, just fora del límit intern de les respectives zones habitables. Per tal d'evitar la determinació esbiaixada de les característiques dels planetes, hem modelat els senyals planetaris conjuntament amb els provinents de l'activitat estel·lar, els quals hem modelat amb soroll correlat. Els paràmetres orbitals resultants d'aquesta anàlisi corresponen a períodes orbitals de 14.45 d i 15.53 d, i masses mínimes de $12.8\,\mathrm{M}_{\odot}$ i $6.6\,\mathrm{M}_{\odot}$ pels planetes LSPM J2116+0234 b i GJ 686 b, respectivament.

El mètode de velocitats radials emprat per a detectar exoplanetes amb CARMENES també permet la detecció de sistemes múltiples. En aquest treball, anunciem el descobriment de 17 nous sistemes, dels quals determinem les òrbites espectrals. La mostra està formada per 15 sistemes binaris (5 amb companyes no detectades) i 3 sistemes triples. Hem determinat que les companyes no detectades de dues de les binàries tenen masses mínimes compatibles amb una nana marró, i demostrem que un sistema binari està format per una nana blanca i una estrella M. Un anàlisi conjunt de velocitats radials i astrometria ens ha permès determinar les masses d'un sistema binari, el qual esdevé un dels sistemes més joves amb masses mesurades.

Per últim, hem usat fotometria de TESS per a derivar el temps d'eclipsi de 16 binàries eclipsants excèntriques. Mitjançant l'anàlisi de l'evolució de les diferències entre el temps d'eclipsi primari i secundari amb el temps, hem determinat el moviment apsidal de 10 sistemes, 5 dels quals són mesurats per primer cop. Hem comparat les nostres mesures amb prediccions teòriques obtenint una concordança excel·lent. Hem sigut capaços de mesurar el terme relativista amb prou precisió per a testejar la relativitat general amb aquest mètode per primer cop.

Abstract

The detection of the first binary star more than 200 years ago opened the door to a whole new field of astrophysics research, devoted to the study of their evolution and mutual interactions employing the analysis of the reflex motion caused by the orbiting companion. It was therefore only a matter of time that the development of astronomical instrumentation reached a precise enough level to detect the motions induced by planetary companions over their host stars. The discovery of the first exoplanet a few decades ago prompted a rapid surge of surveys dedicated to their search, which are providing a huge amount of data that can be also used to study the properties of stars.

The main purpose of this thesis is the study and characterization of exoplanets, stars, and stellar systems by analyzing data from high-precision spectroscopic and photometric exoplanet surveys. This is for instance the case of the CARMENES and TESS projects, which aim at the discovery of such objects by means of the radial velocity imprinted on their host star or by the detection of transits, respectively, with particular emphasis on low-mass M-dwarf stars.

Firstly, we developed a novel approach to constraint the properties of starspots and convective motions on M dwarfs by using the variability induced by stellar activity. In particular, we modeled chromatic radial velocities and photometric time series of the M-dwarf star YZ CMi using the stellar activity model code `StarSim`. The results of our analysis revealed the presence of a large polar spot with a temperature $\sim$ 200 K lower than that of the surrounding photosphere, and found that the convective shift of this star may be reversed toward redshift.

Based on a combined analysis of CARMENES and archival radial velocities, we present in this thesis the detection of a mini-Neptune and a super-Earth around the M-dwarf stars LSPM J2116+0234 and GJ 686, respectively, just outside the inner edge of their habitable zones. To avoid determining biased parameters due to the contamination from stellar activity, the planetary signals were jointly modeled with a correlated noise model describing stellar variability. The derived orbital parameters resulted in orbital periods of 14.45 d and 15.53 d, and minimum masses of 12.8 $M_\odot$ and 6.6 $M_\odot$ for LSPM J2116+0234 b and GJ 686 b, respectively.

The radial velocity method used to detect exoplanets with CARMENES is also yielding multiple stellar systems as a by-product. In this work, we report on the discovery of 17 new multiple systems, for which we determined their spectroscopic orbits. The sample is composed of 15 binary systems (5 with undetected companions) and 2 triple systems. We determined that the unseen companions of two of the binaries have minimum masses compatible with a brown dwarf, and we demonstrated that one of the systems is an M-dwarf–white dwarf binary. We also found one of the youngest binary systems with measured masses by analysing both radial velocities and astrometric measurements.

Finally, we used TESS photometry to derive eclipse timings for 16 well-studied eccentric eclipsing binaries. We analyzed the change in the difference between primary and secondary eclipse timings over time to determine the apsidal motion rate of 10 of the systems in the sample, 5 of which are measured for the first time. We compared the measured values with theoretical predictions, obtaining an excellent agreement. We were able to measure the general relativistic term with sufficient precision to test general relativity for the first time using this method.

Contents

Chapter 1

Introduction

The space era in which we live marks the starting point of a second astronomical revolution. With the launch of tens of space telescopes we have been able to overcome the great disadvantage that the atmosphere have represented for past observers. Furthermore, the challenging scientific goals of these missions have encouraged the development of high-precision instruments, from which ground-based observations have also benefited. Thanks to this, in the recent years we have dramatically increased our knowledge of the universe, until the point that striking discoveries that would have made a big impact in the society a couple of generations ago have now become routine.

In a similar way, the invention of the telescope in 1608[1], and its posterior repurpose for astronomical use by the Italian astronomer Galileo Galilei, represented the beginning of the first astronomical revolution, which expanded the existing conceptual limit of the universe way beyond the Earth and culminated the transition from geocentrism to heliocentrism. The use of the telescope enabled the discovery of new celestial objects, such as for example the moons of Jupiter, nebulae, galaxies and double stars. The study of double stars was of particular interest in that epoch, and with time it has evolved in diverse astrophysical branches such as spectroscopy, astrometry, stellar dynamics, and exoplanetary science.

The term double star is generally used to describe a pair of stars with an angular separation so small that they can only be resolved with the aid of a telescope. The observed small separation can be caused either by a gravitationaly bound between the stars or by a chance line-of-sight alignment of two stars at different distances from the observer, although in 1761 John Michell used a probabilistic argument to conclude that is highly probable that double stars are physically associated. The first documented double star to be observed with a telescope was ζ UMa (Mizar) by Benedetto Castelli and Galileo in 1617 (Ondra 2004). Galileo measured an angular separation between the pairs of 15 arcsec, and he also mistakenly measured an angular diameter of the brighter component of 3 arcsec, from which he estimated that it was at a distance of only 300 au. It was also Galileo that suggested to use double stars to measure the distance to the brighter component, assuming that the dimmer companion was much more distant and therefore unaffected by parallax, overlooking the possibility that the cause of the apparent nearness of both stars was other than a chance alignment between the Earth and the two stars in nearly a straight line.

---

[1] The first record of a telescope was a patent in 1608 by Hans Lippershey.

It was not until 1779, however, that William Herschel started to search for double stars to use them to test the stellar parallax method as suggested by Galileo, also assuming that there is no physical connection between the pairs (Aitken 1918). He therefore started a detailed examination of double stars, measuring the angular separation and position angle of the systems. A review of his double star discoveries until 1797, with repeated measures during more than 25 years, revealed a remarkable change in the relative positions in a number of double stars that could not be explained by parallax. Finally in 1803, taking α Gem (Castor) as an example, Herschel demonstrated that the change in position of the components is explained by the fact that they are orbiting around each other, referring to them as binary systems.

The development of spectroscopy during the nineteenth century allowed the discovery in 1889 of a new type of binary systems, the so called spectroscopic binary systems, which are bound systems composed by a pair of stars that are so close that cannot be resolved even by the most powerful telescopes, but whose spectroscopic lines could be resolved in the spectra. The discovery of the first spectroscopic binary was made by Edward C. Pickering, who found that the spectra of the star Mizar sometimes showed double spectral lines, while other times showed just single lines. Due to the Doppler effect, these lines move redward and blueward depending on the projected velocity of each component, and therefore they merge into a single line when the velocities of both components are equal. The use of spectroscopy provides a determination of the orbital velocity projected into our line of sight which, combined with the proper motion of the systems, allowed the possibility of determining the three-dimensional motions of the stars in the space. In the case in which the spectroscopic system orbits in a plane containing our line of sight, the stars will eclipse each other, producing periodic reductions of the observed brightness. The first identification of one such system was done in 1783 by John Goodricke, who demonstrated that the brightness of the star Algol decreased every 20.9 days, although he was not sure of the cause. These systems are called eclipsing binary systems, and in combination with spectroscopic measurements, they provided the first determination of the mass and radius of a star other than the Sun.

In the years to follow several new binaries were discovered and compiled in different catalogues, such as the ninth Catalogue of Spectroscopic Binary Orbits comprising 4021 spectroscopic binaries (SB9, Pourbaix et al. 2004), or the Binary Star Database containing more than 120 000 stellar systems of various observational types (BDB, Kovaleva et al. 2015). The discovery of such an amount of systems has enabled statistical analyses of the orbital parameters and the frequency of multiple systems, which have proved to be highly valuable from a theoretical point of view (Duchêne & Kraus 2013). In general, the dependence of these parameters on primary mass should be directly related to the physical processes involved in shaping the systems throughout their lifetime, and therefore their statistical properties can be used as tests for star formation theories. Modern surveys studying the multiplicity fraction of the solar vicinity have shown that almost half of the observable stars are found in multiple systems (Raghavan et al. 2010; Chini et al. 2012; Winters et al. 2019), with a significant increase of the ratio of multiple systems with primary mass.

As already suggested by Otto Struve in the mid-twentieth century (Struve 1952), the projected radial velocity of a star can also be used to discover the exoplanets. Actually, this is how the first exoplanet around a main-sequence star, 51 Pegasi, was found in 1995 by Mayor & Queloz (1995). This discovery triggered the rapid increase of the scientific efforts and resources devoted to such matter, and as a consequence binary detection was soon relegated to a second plane in the photometric and spectroscopic surveys to follow, such as HARPS (Mayor et al.

2003), CoRoT (Auvergne et al. 2009), *Kepler* (Borucki et al. 2010), CARMENES (Quirrenbach et al. 2014), and TESS Ricker et al. (2015), to mention some of them. To date, more than 4 900[2] exoplanets have been discovered, presenting an enormous variety of masses, radii, compositions, and orbital parameters. Given that the detection of stellar pairs and exoplanets is based on the same observational methods, many binary systems are being discovered as a by-product of exoplanet surveys. On the other hand, however, the smaller dimensions of exoplanets result in much weaker signals than those produced by binary systems, reaching in some cases the limit in which the stellar noise is of the same order than the exoplanetary signal. The stellar contamination, which in some cases can mimic an exoplanetary signal, makes it difficult to reliable retrieve the signal from low mass planets orbiting around active stars, and has become one of the main limitations when aiming to detect Earth analogues. Due to this reason, developing different methods to try to distinguish between stellar and planetary signals, or at least, to mitigate the impact of stellar variability have gained interest in the recent years.

In the following sections, we present an overview of the fundamental topics and techniques that are frequently mentioned throughout this thesis, which is focused on the characterisation of multiple and planetary systems taking advantage of access to outstanding data from exoplanet surveys. In Section. 1.1 we present the basics of the two-body problem under mutual gravitational interactions following Kepler's laws. We also outline the main methods to detect binary and exoplanet systems with special emphasis on the radial velocity technique. In Section 1.2 we focus on the particular case of M-dwarf exoplanet host stars, which are the targets of the CARMENES survey. Therefore, their properties and the challenges they pose have been extensively discussed throughout this thesis. In Section 1.3, we provide the fundamental ideas under Gaussian Procession regression models that, nowadays, are commonly used in the exoplanets research field to derive planet parameters and that we have used here with different purposes. In Section 1.4 we present the CARMENES and TESS surveys, both aimed at the detection of exoplanets, but that do also provide a wealth of information of the host stars. The results presented in this thesis are based on data from these projects. Finally, in Section 1.5, we outline the main goals of this thesis and its structure.

1.1 Detection and orbital determination of two-body systems

The movement of two objects with masses m_1 and m_2 orbiting around their common centre of mass, or barycentre, under their mutual gravitational field is governed by the inverse square law of gravity. In an inertial frame of reference centered at m_1, the movement of the other object is described by a closed ellipse with the m_1 at the focus of the ellipse, as was derived by Kepler in his first law (Kepler 1609). The relative distance (r) between the objects in an elliptical orbit is given by (Hilditch 2001):

$$r = \frac{a(1 - e^2)}{1 + e \cos \nu}, \tag{1.1}$$

where a is the semi-major axis of the ellipse, e its eccentricity, and ν is the true anomaly. To have a better understanding of the main elements playing a role in orbital mechanics, we represent in Fig. 1.1 an schematic view of the relative orbit of m_2 and m_1. In this picture, the solid line

---

[2] `exoplanet.eu`, accessed on May 2021

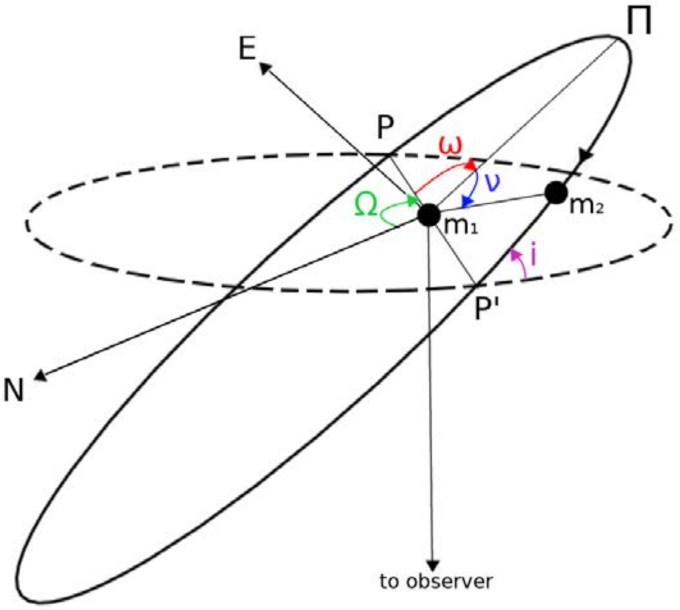

Figure 1.1: Schematic representation of the relative orbit between two point masses m_1 and m_2, and its main orbital elements.

represents the orbit of the object m_2, while the dashed line illustrates the projection of the orbit into the plane of the sky, with coordinates N and E. The inclination of the plane of the orbit with respect to the plane of the sky is given by the angle i, and the intersection between the two planes, denoted by the line PP', is called the line of nodes. The point P, at which the mass m_2 crosses the plane of the sky receding from the observer is called the ascending node, while the point P' is the descending node. The angle of the ascending node with respect to a reference direction, usually the north celestial pole N, determines the orientation of the orbit in the plane of the sky, which is called the longitude of the ascending node (Ω). The angle between the ascending node and the periastron Π is the longitude of periastron, denoted by ω. Finally, the true anomaly ν defines the angle between the periastron and the mass m_2. It is important to note that all the following equations are also valid when considering the individual orbits of the masses m_1 and m_2 around the barycenter, using the semi-major axis a_1 and a_2 instead of the semi-major axis a of the relative orbit. The size of the three orbits are in the proportions $a_1 : a_2 : a = m_2 : m_1 : (m_1 + m_2)$, and hence the semi-major axis a of the relative orbit is simply the sum of the semi-major axes of the two barycentric orbits, $a = a_1 + a_2$.

The only parameter that varies with time is the true anomaly[3], which can only be determined indirectly through other observables such as radial velocity, light curves or astrometric positions. In his second law, Kepler (1609) stated that the vector $\vec{r}$ joining the two objects sweeps equals areas during equal intervals of time, relating the true anomaly with the time. In the following paragraphs, we guide the reader through the physical interactions that leads to the derivation of the Kepler's equation, which relates the true anomaly with the time. Therefore, in an infinitesimal time interval dt, $\vec{r}$ sweeps out an infinitesimal area $dA = r^2 d\nu/2$, and since for an

---

[3] We ignore relativistic effects and tidal interactions, which are only significant for close eccentric orbits, and produces a linear change in ω with time.

entire orbit of period P the area total swept is the area of an ellipse, πab, with semi-major and semi-minor axis a and b, respectively, Kepler's second law can be expressed as:

$$\frac{d\nu}{dt} = \frac{2\pi ab}{Pr^2}, \tag{1.2}$$

where the semi-minor axis can also be written as a function of the semi-major as $b = a(1-e^2)^{1/2}$. It can be seen that at small distances, $d\nu/dt$ must be large and vice versa. Therefore, the speed of the bodies is maximum at periastron and minimum at the apoastron. A useful quantity used to simplify the relation between ν and time is the eccentric anomaly E. It is defined as the angle measured from the centre of the ellipse between the periastron and the intersection between an auxiliary circle circumscribing the orbital ellipse and a line perpendicular to the semi-major axis passing through the orbiting body. It is geometrically related to the true anomaly by the following equations:

$$\cos\nu = \frac{\cos E - e}{1 - e\cos E}, \tag{1.3}$$

and

$$d\nu = \frac{\sqrt{1-e^2}}{1 - e\cos E} dE. \tag{1.4}$$

If we now combine these two equations with Eqs. (1.1) and (1.2) we obtain

$$(1 - e\cos E)dE = \frac{2\pi}{P} dt, \tag{1.5}$$

which can be integrated, imposing that $t \equiv T_0$ at the time of periastron ($\nu = 0$, $E = 0$) to obtain Kepler's equation:

$$E - e\sin E = \frac{2\pi}{P}(t - T_0). \tag{1.6}$$

This equation describes the path of an orbiting body on the elliptical orbit as a function of time. The value of the eccentric anomaly, E, must be solved numerically given the time, t, at which the observables used to characterise the system are measured. Kepler's equation is used indirectly to determine the orbital parameters for a diversity of observables, such as radial velocities, astrometric motions, or eclipse timings. In the following paragraphs we describe the main observables and methods used to detect binary systems and exoplanets, and outline which are the orbital and physical properties that can be derived, putting special interest in the radial velocity method, which is the technique employed to obtain most of the measurements used in this work.

1.1.1 The radial velocity method

The first exoplanet detected around a main sequence star, 51 Pegasi b, was discovered using the radial velocity method, also called Doppler spectroscopy. The reflex motion of a host star being orbited by a planet or a star causes it to revolve around the centre of mass of the system with a fixed period. The radial component of this wobble, or radial velocity (hereafter, RV), can be measured by detecting periodic shifts in the spectral features of the star. As the star recedes and approaches the observer, the wavelength λ_0 of the spectral absorption and emission lines of the star are redshifted and blueshifted, respectively, according to the Doppler-Fizeau effect, as

$$\frac{\lambda - \lambda_0}{\lambda_0} = \frac{\Delta\lambda}{\lambda_0} = \frac{RV}{c}, \tag{1.7}$$

valid for $RV << c$, where c is the speed of light. Therefore, measuring the relative shift of the spectral lines at different orbital phases yields an RV curve, whose shape depends on the orbital elements. This dependence can be derived by projecting the position of the orbiting body along the line-of-sight, z, which according to the angles depicted in Fig. 1.1 is

$$z = r\sin(\omega + \nu)\sin i, \tag{1.8}$$

which we differentiate with respect to the time to obtain the expression of the RV as

$$RV = \dot{r}\sin(\omega + \nu)\sin i + r\dot{\nu}\cos(\omega + \nu)\sin i. \tag{1.9}$$

Using now Eqs. (1.1) and (1.2), after some manipulation, we obtain

$$RV = \frac{2\pi a \sin i}{P(1 - e^2)^{\frac{1}{2}}}[\cos(\nu + \omega) + e\cos\omega], \tag{1.10}$$

where the factor $2\pi a \sin(i) P^{-1}(1-e^2)^{-1/2}$ is usually written as K, and is called the semi-amplitude of the RV curve. As its name indicates, it corresponds to half of the difference between the maximum and the minimum RV of the orbit. The final expression is usually written as

$$RV = K[\cos(\nu + \omega) + e\cos\omega] + \gamma. \tag{1.11}$$

Here we added the additional parameter γ, which accounts for the RV of the barycentre of the binary system with respect to the observer. This equation relates the measured RV of the orbiting body and the time at which it is observed. The time enters the equation through the true anomaly ν, which, at the same time, is related to the eccentric anomaly E and the time through Eqs. (1.3) and (1.6). In the special case in which the eccentricity is zero, that is, a circular orbit with $r = a$, the expression for the RV curve reduces to a cosine function. With the addition of eccentricity, the velocity curve becomes more asymmetric, and therefore sampling of all the orbital phases becomes more important.

In the case of exoplanets or binary systems in which only the spectral lines of the brightest component are visible, that is, single-line spectroscopic binaries (SB1), the orbital parameters that play a role in shaping the RV curve of an orbiting body are six: the period P, the time of periastron passage T_0, the semi-amplitude K, the eccentricity e, the longitude of periastron ω, and the systemic velocity γ. An additional semi-amplitude parameter should be added for binary systems in which the lines of the two components can be detected simultaneously, called double-line spectroscopic binaries (SB2). In these cases, we obtain an additional RV curve with different semi-amplitude and a longitude of periastron differing 180 deg from that of the other component. From now on, we distinguish between the semi-amplitudes of the two components by using K_1 and K_2.

For an SB2 system it is straightforward to use the expression of the semi-amplitude to derive the projected semi-major axis of each component as

$$a_{1,2} \sin i = \frac{(1-e^2)^{1/2}}{2\pi} K_{1,2} P. \tag{1.12}$$

Another important quantity, the minimum mass of the components, can only be derived for SB2 systems. From the equation of the projected semi-major axis, using the relations $a = a_1 + a_2$ and $m_1 a_1 = a_2 m_2$, and Kepler's third law (Kepler 1619):

$$P^2 = \frac{4\pi^2 a^3}{G(m_1 + m_2)}, \tag{1.13}$$

where G is the gravitational constant, one can obtain the individual masses as a function of the orbital inclination, or minimum masses, as

$$m_{1,2} \sin^3 i = \frac{1}{2\pi G}(1-e^2)^{3/2}(K_1 + K_2)^2 K_{2,1} P. \tag{1.14}$$

An interesting outcome of Eq. (1.14) is that the mass ratio q is proportional to the ratio of RV semi-amplitudes, with the component with higher mass yielding a lower semi-amplitude and vice versa:

$$q \equiv \frac{m_2}{m_1} = \frac{K_1}{K_2}. \tag{1.15}$$

For SB1 systems, RV alone does not provide minimum masses, their ratio, or their sum, but we obtain a quantity known as the mass function, $f(m)$, as

$$f(m) \equiv \frac{m_2^3 \sin^3 i}{(m_1 + m_2)^2} = \frac{P}{2\pi G}(1-e^2)^{3/2} K_1^3. \tag{1.16}$$

This quantity gives a relation between the two masses and the orbital inclination, so to estimate the mass of the secondary we need to know the inclination of the orbit and the mass m_1 from other indirect methods as we shall see later. In the case of exoplanets, in which $m_2 << m_1$, Eq. (1.16) can be used to obtain the minimum mass of the planet, if the host star mass, m_1, is known by other means.

Usually, RVs are determined in units of kilometers per second, and the orbital period in units of days. Similarly, we normally express semi-major axes in astronomical units and masses in solar units. The expressions for Eqs. (1.12), (1.14), and (1.16) in these units are

$$\left[\frac{a_{1,2}}{au}\right]\sin i = (9.19198\times10^{-5})(1-e^2)^{1/2}\left[\frac{K_{1,2}}{\mathrm{km\ s^{-1}}}\right]\left[\frac{P}{\mathrm{d}}\right], \tag{1.17}$$

$$\left[\frac{m_{1,2}}{\mathrm{M_\odot}}\right]\sin^3 i = (1.0361\times10^{-7})(1-e^2)^{3/2}\left[\frac{(K_1+K_2)}{\mathrm{km\ s^{-1}}}\right]^2\left[\frac{K_{2,1}}{\mathrm{km\ s^{-1}}}\right]\left[\frac{P}{\mathrm{d}}\right], \tag{1.18}$$

and

$$\left[\frac{f(m)}{\mathrm{M_\odot}}\right] = (1.0361\times10^{-7})(1-e^2)^{3/2}\left[\frac{K_1}{\mathrm{km\ s^{-1}}}\right]^3\left[\frac{P}{\mathrm{d}}\right]. \tag{1.19}$$

As it can be deduced from the equations above, the amplitude of the RV variations increases with the mass of the planet, and decreases with the orbital period. Therefore, close massive planets cause large RV variations in their host-stars, of the order of 100 m s^{-1}, while planets with masses and periods similar to the Earth around solar-like stars induce variations below 1 m s^{-1}, whose detection poses an enormous challenge to modern instrumentation. Using Eq. (1.7), a RV amplitude of 1 m s^{-1} represents a variation in the wavelength of an spectral line at for example 600 nm of only 2 pm, which in modern instruments represents a shift of only a thousandth of a pixel. The determination of such small displacements usually involve a precise wavelength calibration and sophisticated pipelines and techniques that combine the spectral information spanning throughout the whole spectral range observed. Furthermore, as deduced from Eq. (1.14), the determination of masses are very sensitive to the RV semi-amplitudes, and therefore the quality and precision of RV measurements is critical for the determination of exoplanet and stellar masses.

The most widely used method to measure RV from the wavelength shift of the spectral lines is the cross-correlation function (CCF, Queloz 1995; Lafarga et al. 2020). In simple words, the CCF method consist in shifting a template spectra in small RV (or wavelength) steps and multiplying it with the observed spectrum, thus obtaining a function (the CCF) that depends on the RV shift. The template used to perform the CCF can be a spectra from a real star, a synthetic spectra, or a binary template masking absorption lines. The RV of the observed spectra corresponds to the RV shift at which the CCF is minimum, and is usually computed from the minimum of a Gaussian fit. The CCF represents a mean profile of all the lines in the spectra, and therefore its precise shape depends on several properties of the star, such as its rotational velocity, metallicity, or convective blueshift (Benz & Mayor 1981; Queloz 1995; Meunier et al. 2017).

An alternative method to the CCF is the technique of template matching (Anglada-Escudé & Butler 2012; Zechmeister et al. 2018), which is based on a least-squares matching of each observed spectrum to a coadedd high signal-to-noise spectrum derived by combining all the observations of the star. The template matching technique proved to work better than the CCF method for M-dwarfs, whose spectra contain a larger number of atomic lines and mollecular bands that can be blended, complicating the creation of binary mask templates.

Several other techniques of RV extraction have been published in the past years. Some modern and sophisticated methods include for example the jointly modelling of telluric lines and stellar spectra (Bedell et al. 2019), the selection of individual lines not affected by stellar activity (Dumusque 2018), or a template free approach based on Gaussian Processes (Rajpaul et al. 2020).

In the case of SB2 systems their spectrum is composed of the components' individual spectra, which are being Doppler-shifted in opposite directions according to their individual RVs. The resulting composite spectrum is therefore quite complex due to blends of the spectral lines, and the before-mentioned methods for RV extraction are not suited for this task, producing biased results in most of the cases. To solve this problem, alternative methods have also been proposed, although the precision achieved in the RV determination is usually lower than that reached with the methods optimized for single stars.

A common algorithm for the RV determination of SB2 systems is `todcor` (Zucker & Mazeh 1994), which is based on the CCF method, but uses instead two different templates to construct a two-dimensional CCF, from which the RVs of each component are computed. The templates are chosen accordingly to the properties of each component, and are scaled to mach the flux ratio between the stars. Another method, the spectral disentangling (Simon & Sturm 1994; Pavlovski & Hensberge 2010; Czekala et al. 2017), does not explicitly determine individual RVs, but instead the orbital elements are directly determined from the analysis of the observed composite spectra, from which RVs can be computed. This method also yields the reconstructed intrinsic spectra of the individual components, but it is computationally more demanding than the methods based on CCFs.

1.1.2 Other detection techniques

Several additional techniques have been used to discover binary systems and exoplanets, such as the transit or eclipse detection and their timing, direct imaging, astrometric precise measurements, and microlensing (Perryman 2018). We summarise below the techniques whose basic principles have been used in this work for basic purposes.

1.1.2.1 Eclipses and transits

This technique consists in the detection of a decrease in the observed flux of the star, which is produced by the pass of another star (eclipse) or a planet (transit) in front of it, as seen by the observer. Although this technique is limited to systems with the orbital plane on an almost edge-on configuration ($i \sim 90$), it has yielded almost 70 % of the exoplanet discoveries, being the most prolific exoplanet detection method thanks to space dedicated missions (e.g. CoRoT, *Kepler*, TESS). From the follow-up of transits and eclipses one can derive the orbital period and the inclination. In addition, it also provides the radius of the component stars, in the case of binary systems, or the planet radius as a function of the stellar host radius, in the case of planetary systems. The combination of these data with those from RV measurements, enables the dynamical determination of the absolute masses of the components of the binary system, or those of exoplanets as a function of the host star properties, thus yielding the exoplanet density, which provides constraints to the bulk composition of the exoplanet.

In the case of binary systems, and some exoplanets with a significant intrinsic or reflected emission, the pass of the companion behind the host star produces a secondary eclipse, allowing the determination of physical properties such as the individual radii and temperature ratio. The time of primary (t_1) and secondary (t_2) eclipse occur at true anomaly values of $\nu(t_1) = \pi/2 - \omega$ and $\nu(t_2) = 3\pi/2 - \omega$, respectively (Kallrath & Milone 2009). In circular orbits, the time difference between primary and secondary corresponds to $P/2$, however, in eccentric orbits, the phase shift between primary and secondary eclipses depends on e and ω, and is approximately given by

$$t_2 - t_1 = \frac{P}{\pi} e \cos\omega (1 + \csc^2 i) + \frac{P}{2}. \tag{1.20}$$

Therefore, precise measurements of primary and secondary eclipse timings enable the determination of orbital parameters such as the period, the eccentricity and the longitude of periastron. Besides, the follow up of eclipse timings may reveal a slow change in the longitude of periastron, also called apsidal motion. This effect is caused by relativistic effects and the lack of spherical symmetry in the shape of the components, and its measurement offer further opportunities to gain indirect insight into the internal structure of the stars (e.g. Giménez 1985; Claret & Giménez 1993; Wolf et al. 2010).

In addition, the reflex motions induced by the orbit of an additional companion in the direction of our line of sight produces variations in the light travel time of the stars. This effect can be detected as variations in of the eclipse and transit timings, and other periodic signatures such as pulsations (Irwin 1959). This effect was used to detect stars around eclipsing binary systems (Frieboes-Conde & Herczeg 1973), additional exoplanets in planetary systems (Nesvorný et al. 2012), and planets around pulsating bodies, as was the case of the first exoplanet discovered (Wolszczan & Frail 1992).

1.1.2.2 Astrometry and direct imaging

The orbital motion of two body systems around the common centre of mass can also be detected using precise astrometric measurements of the objects, which as explained in the introduction, was the method used to discover the first binary star. In addition to the orbital parameters describing a Keplerian orbit, astrometric measurements yield the longitude of the ascending node and the inclination of the orbit, which can be used to determine the individual masses of the components. In the case of exoplanets, or binary stars with a large luminosity contrast between the components, only the orbit of the brighter star can be measured, although in the case of exoplanets its detection usually involves an astrometric precision of the order of a few μas. Some exoplanets with significant intrinsic emission have been directly imaged by state-of-the art instruments, but they are usually in wide orbits, with orbital periods too large to detect any relevant change in their relative astrometric positions. Since the detection of astrometric orbits provides, among others, the determination of the orbital inclination, it can be combined with RV measurements to derive individual masses of planets and stellar companions. It is expected that tens of thousands planets are going to be discovered from astrometric measurements done by the space telescope *Gaia* (Perryman et al. 2014), becoming the most prolific method of exoplanet detection.

1.2 M dwarfs as host stars

Although M dwarfs constitute 70% of the stars in the Milky Way and 40% of its stellar mass budget (Reid & Gizis 1997; Chabrier 2003; Bochanski et al. 2010), none of them is visible to the naked eye Lépine et al. (2013). M dwarf are the coolest and lightest type of star, with effective temperatures from 2300 K to 3800 K (Reid & Hawley 2005), and a mass range that nearly expands one order of magnitude, with masses from the hydrogen burning limit at $\sim$0.072 $M_\odot$ (Chabrier et al. 2000a) to $\sim$ 0.6 $M_\odot$, covering the transition from partially to fully convective stars at $\sim$ 0.3 $M_\odot$ (Baraffe & Chabrier 2018).

Over the last years M-dwarf stars have focused the attention of many surveys searching for habitable exoplanets. The reasons for this popularity are manifold. Firstly, a planet of a certain mass and size induces a larger reflex motion and block a larger fraction of the flux orbiting around an M-dwarf than a solar-like star. Secondly, as M-dwarf stars emit less flux than solar-like stars, their habitable zones lie closer to the host star (Kopparapu et al. 2013); therefore, the induced reflex motion is larger and the transit probability increases. Finally, Earth-size planetary companions around M-dwarf stars are common (Dressing & Charbonneau 2013), hosting an average of more than 2 planets per star (Dressing & Charbonneau 2015; Gaidos et al. 2016), which makes these stars the most common potential planetary hosts.

A complete knowledge of the host star is important to precisely determine the characteristics of their companions, and to understand the potential additional signals that one may encounter in the observational data. However, M dwarfs poses other problems that may interfere with the determination of their properties, and could hamper the detection of their companions. On one hand, compared to more massive stars, M dwarfs exhibit increased levels of magnetic activity depending on their age and rotation rates. Active M dwarfs are usually linked to strong X-ray, UV, and Hα emission, flaring events, and surface inhomogeneities. All these phenomena induce large variability in photometric and spectroscopic measurements, which can mimic or hide exoplanet signals.

On the other hand, due to the low temperature of their outermost layers, the spectrum of M dwarfs is characterized by the presence of strong molecular absorption bands, such as TiO, VO, H_2, and H_2O, to the extent that the true continuum is obscured (Shields et al. 2016). The complexity of these molecular bands made nearly impossible to accurately model their opacities, and therefore synthetic spectra of M dwarfs show discrepancies with observations (Allard et al. 2012; Passegger et al. 2020). In addition, there is a disagreement between observations and stellar structure models predictions, which systematically underestimate the radii and overestimate the effective temperature of M-dwarf stars (López-Morales 2007; Morales et al. 2008, 2010), probably due to the increased magnetic activity of M-dwarf stars (Torres & Ribas 2002; Morales et al. 2010; Feiden & Chaboyer 2013).

1.2.1 Physical properties

The determination of the physical properties of exoplanets host stars are of paramount importance. As we have seen in the previous section, most of the detection methods provide the physical parameters of exoplanets as a function of those of the host star. Therefore, their uncertainties are strongly correlated and the precision at which we can measure planetary masses and radii depends on the knowledge of the host star. Additionally, the estimation of the stellar age, temperature, metallicity, and rotation, may also be necessary to understand many aspects of the nature and evolution of exoplanets, and provide insights on their habitability.

Most of the fundamental properties of a star can be measured from spectroscopic and photometric measurements. A measure of the effective temperature and metallicity can be obtained by a detailed comparison between synthetic spectra and the stellar spectrum, while a combination of distances and photometric measurements in a broad range of wavelengths yield the luminosity of the star. From effective temperatures and luminosities, using Stefan-Boltzmann's law, the stellar radius is obtained with an accuracy that can reach 2–3 % (see e.g. Schweitzer et al. 2019, for more details). Although the mass of a star is one of its fundamental properties driving its structure and evolution, its determination for isolated stars is not so straightforward. They can only be directly determined in very special cases, such as for example serendipitous approaches producing gravitational lensing events (Serenelli et al. 2020), which cannot be used to target specific stars. Therefore, the determination of the masses of host stars, and thus of their planetary companions, in most of the cases must rely on indirect methods.

One of such indirect methods to estimate the mass of an isolated star is the use of stellar structure and evolutionary models (e.g. Chabrier et al. 2000a; Spada et al. 2013; Baraffe et al. 2015; Choi et al. 2016). However, to use them some previous knowledge of certain properties of the star, such as metallicity and age, is needed, which may introduce important biases in the results. Moreover, as already mentioned, stellar model predictions still show significant differences with empirical observations of the properties of M dwarfs, which cast doubts on the reliability of masses predicted from stellar models. Another approach to estimate stellar masses is the use of empirical relationships between the stellar mass and other properties such as, for example, the luminosity, the radius, or the effective temperature of the star (Delfosse et al. 2000; Malkov 2007; Benedict et al. 2016; Mann et al. 2019; Schweitzer et al. 2019). In this work, most of the stellar masses of M dwarfs are computed using the mass–luminosity relationship by Mann et al. (2019), which uses the K_s-band absolute magnitude A_{K_s} as a proxy for the luminosity and is given by

$$\log_{10}\left(\frac{M}{\mathrm{M}_\odot}\right) = -0.642 - 0.208a - 0.000843a^2 + 0.00787a^3 + 0.000142a^4 - 0.000213a^5, \quad (1.21)$$

where $a = (A_{K_s} - 7.5)$. This empirical calibration is valid between $0.075\,\mathrm{M}_\odot$ and $0.70\,\mathrm{M}_\odot$, and yields uncertainties between 2% and 3%. For the determination of stellar radius, our main choice is the mass–radius relationship reported in Schweitzer et al. (2019):

$$\frac{R}{\mathrm{R}_\odot} = (0.0282 \pm 0.0068) + (0.935 \pm 0.015)\frac{M}{\mathrm{M}_\odot}, \quad (1.22)$$

which is valid between $0.092\,\mathrm{R}_\odot$ and $0.73\,\mathrm{R}_\odot$ with an error of 2%–3%.

For both methods, however, it is necessary to independently compute individual masses to either test the models or construct the empirical calibrations. These masses are usually taken from binary stars, for which it is possible to directly determine their individual masses from the orbital parameters. The observation of detached eclipsing binary systems, combined with the

RV amplitudes of the components, allows us to measure accurate individual masses, and have been used profusely to test stellar evolutionary models (Ribas et al. 2000; Lastennet & Valls-Gabaud 2002; Torres & Ribas 2002; Feiden & Chaboyer 2012; Higl & Weiss 2017; Tkachenko et al. 2020). Similarly, individual masses can also be determined from the reconstruction of the orbits of the components of resolved astrometric binaries. These systems are more suited to calibrate mass–luminosity empirical relations, since both individual masses and magnitudes can be derived from the same set of observations (Mann et al. 2019).

In some binary systems it is not possible to apply any of these methods to estimate individual masses of the components. This is the case of non-eclipsing and unresolved spectroscopic binaries, which only yield the minimum masses of the components and their mass ratio, and in which the luminosities of each of the components cannot be measured separately. One method to estimate such luminosities is by computing the optimal flux ratio between two templates with `todcor`. This estimate, however, depends on the wavelength range of the instrument, which is usually difficult to compare with the usual photometric band used for empirical relationships or stellar models.

1.2.2 Stellar activity

Several physical phenomena occurring on the surface of main-sequence stars can alter the shape and shift of stellar absorption lines, causing spurious RV variability at the $\mathrm{m\,s^{-1}}$ level, or jitter, on top of the true RV of the star. We refer to these effects as stellar activity, and are produced by the strong magnetic fields induced by stellar rotation, or other dynamical effects such as pulsations or motions of the outer convective envelopes. With the improving precision of high-resolution spectrographs, the measurements are now sensible to stellar variability, which have become a prominent issue in the detection of exoplanetary signals. The amplitude of stellar variability can be an order of magnitude larger than signals produced by Earth-like exoplanets. Besides, due to the semi-periodic nature of stellar signals, with timescales similar to those of exoplanets, they may difficult the disentanglement between stellar and exoplanetary signals, or they can even be mistakenly attributed to exoplanetary signals (e.g. Desidera et al. 2004; Huélamo et al. 2008; Figueira et al. 2010; Hatzes 2013; Haywood et al. 2014; Santos et al. 2014; Robertson et al. 2015; Perger et al. 2021b).

1.2.2.1 Variability sources

Stellar variability in low-mass stars is produced by three main effects with different amplitudes and frequencies: oscillations, granulation and magnetic activity (see e.g. Dumusque et al. 2011b,a).

Oscillations are expansions and contractions of the stellar envelopes produced by pressure modes (p-modes), and have typical timescales ranging between few minutes to a few hours (Dumusque et al. 2011b). This results in a variation of the velocity of the stellar surface, which is detected as spurious RV shifts of the order of 0.1–$4\,\mathrm{m\,s^{-1}}$ (Schrijver & Zwaan 2000). Theoretical models predict that the amplitude of oscillations is lower for M dwarfs and have larger timescales, although have never been detected (Rodríguez-López 2019).

On the other hand, convective motions in the outer layers of stars produces hot bubbles of plasma that rise to the surface, cool down, and sink down again into the surrounding regions (Cegla et al. 2019). Therefore, they generate a pattern of hot regions, or granules, surrounded by cool intergranular lanes, inducing velocity shifts in opposite direction. Averaged over the stellar surface, either up- or downflows can dominate the net convective shift of the star, depending on their typical size and brightness. For solar-like stars, since granules are brighter and cover a larger fraction of the stellar surface than intergranular lanes, a net convective blueshift of the order of hundreds of $\mathrm{m\,s^{-1}}$ is observed. It is found to decrease for lower mass stars (Meunier et al. 2017). For M-dwarfs, magnetohydrodynamic simulations suggest that intergranular lanes cover larger areas than in heavier stars, and that convective motions are less vigorous, producing a smaller granule velocity shift (Beeck et al. 2013a,b). This may produce a reduced net convective blueshift, or even the inversion to convective redshift. Variations of the size, brightness, and velocity of individual granules over time causes a dispersion on the net velocity shift of the order of $1\,\mathrm{m\,s^{-1}}$.

The highest contribution to stellar variability in M-dwarf stars is produced by surface inhomogeneities such as spots and faculae, produced by a local increase in the magnetic field strength. Magnetic activity strongly depends on the rotation rate of stars, which decreases with the age of the star due to magnetic braking (Mestel & Spruit 1987). Therefore, the activity level and rotation rate has been used as a clock to infer the stellar age (Douglas et al. 2016; Astudillo-Defru et al. 2017; Wright et al. 2018; Curtis et al. 2019a). In some cases, the magnetic field can be so strong that inhibits the convective motions in the region. This inhibition attenuate the heat transport to the surface, and therefore the affected area cools down and creates a so called spot (Hotta & Iijima 2020). In other cases, the magnetic field is not strong enough to inhibit completely convection, but strong enough to reduce the opacity of the photosphere, and so light from deeper layers, hotter than the stellar surface, become visible, creating the so called faculae (Berger et al. 2007). Both spots and faculae can be hundreds of degrees cooler and hotter than the surrounding photosphere, respectively. These features can cause spurious variations in the RV shift by two different mechanism. Firstly, since their brightness is different than that of the photosphere, they can change the amount of flux coming from different parts of the star, producing an imbalance between surface hemispheres receding and approaching from the observer, which are red- and blueshifted, respectively. This induces a spurious velocity shift as the star rotates. Secondly, the inhibition of convection modify the net convective shift averaged over the entire surface. As features rotate with the star, their projected surface area will change, and so will do the net convective shift. In both cases the timescale of the RV variability is of the order of the rotation period, and its amplitude can go from a few $\mathrm{m\,s^{-1}}$ for quiet stars to $\sim 100\,\mathrm{m\,s^{-1}}$ for active M dwarfs (Tal-Or et al. 2018). Additionally, the number and size of these features may vary following magnetic activity cycles of several years as in the case of the Sun, which may induce an additional long-term RV modulation (Dumusque et al. 2014).

1.2.2.2 Activity indicators

In addition to the effect on RVs, stellar activity also produces noticeable changes in spectroscopic and photometric observations, which can be measured by the so called activity indicators. They are often used to gain information about the activity level of the star and to identify the rotation period, and since they are not affected by the presence of a planet, they can be used to distinguish if a RV signal is produced by a planet or is induced by stellar activity. Several activity indicators exists, but their sensitivity to stellar activity highly depends on the characteristics of the star, such as its mass and activity level (Lafarga et al. 2021). In the following lines, we outline commonly used activity indicators.

- *Photometry*: the projected surface area of spots and faculae heavily depend on their latitude and longitude at the moment of observation. Due to the contrast temperature between the stellar photosphere and the stellar surface features, the rotation of the star causes a flux variation proportional to their projected surface area. Photometric observations of the star can capture this effect, from which the stellar rotation period can be determined. If in addition the star is observed with different photometric bands, the wavelength dependence of the contrast of stellar inhomogeneities can also be used to measure the temperature of spots and faculae (Rosich et al. 2020).
- *Chromospheric lines*: these indicators are based on a measure of the flux of activity sensitive chromospheric lines. They can be used as a measure of the activity level of the star and to measure rotation periods. Some examples of the most used lines are the Ca II H&K doublet, the Hα line, the Na I D doublet or the Ca II IRT triplet (Wilson 1968; West et al. 2004). For M dwarfs it is also common to use photospheric molecular bands, such as the TiO and VO bands (Schöfer et al. 2019).
- *CCF parameters*: the CCF profile represents the mean profile of all the lines in the spectra, and therefore its shape contain useful information about the activity of the star. Its shape can be parameterised by a Gaussian function, and a measure of its width at half maximum altitude (FWHM) and its contrast are used as common activity indicators. The bisector inverse slope (BIS), which is a measure of the asymmetries of the CCF is commonly also used with this purpose as well (Queloz et al. 2001; Lafarga et al. 2020).
- *Chromatic index*: As already mentioned, the radial velocity measurements are also affected by stellar activity. The wavelength dependence of the flux contrast between the photosphere and spots and faculae was used by Zechmeister et al. (2018) to define the chromatic index (CRX) activity indicator, which measures the dependence of the RV on wavelength. This index is defined as the slope of a linear fit to the RV as a function of the central wavelength of each order in a cross-dispersed échelle spectrum at each time step.
- *Differential line width (dLW)*: this activity indicator measures differential changes in the line width of the observed spectrum with respect to a template (Zechmeister et al. 2018), and is analogous to the FWHM but associated to the least-squares fitting method to measure the RVs.

1.2.2.3 Stellar activity mitigation

The precision improvement of RV measurements over the years have reached the limit in which the spurious RV signal induced by stellar variability poses a major problem in the detection of small planetary signals. While there are some observational strategies to mitigate the nuisance effects of oscillations and granulation (Pepe et al. 2011; Dumusque et al. 2011b), the variability of signals induced by spots and faculae, which are dominant in M dwarfs, makes them much difficult to mitigate. The timescales of these signals, comparable to those expected for exoplanets, plus the semi-periodic nature of their modulations, may mimic planetary signals and can be very challenging to disentangle them from actual planetary signals.

Over the years, there have been a considerable interest in developing new techniques to mitigate the effect of stellar variability caused by stellar inhomogeneities. A common technique to look for activity induced signals in RVs is to search for common signals or correlations between the RV measurements and the activity indicators introduced in the previous section (Queloz et al. 2001; Bonfils et al. 2007; Boisse et al. 2009; Robertson et al. 2014). There have also been an intensive use of the pre-whitening method, in which recursive sine waves are fitted to the RV data to remove the activity signal and their harmonics (Queloz et al. 2009; Dumusque et al. 2012). Analytical methods to predict RV curves have also been developed, such as the FF' method, which uses the stellar flux and its time derivative to predict RV variations (Aigrain et al. 2012).

There exist more modern techniques that are more demanding computationally, such as methods that take advantage of the different imprint of stellar activity and Keplerian motions on different absorption lines in order to construct activity indicators (Davis et al. 2017), simulations of stellar inhomogeneities to model their impact over RVs (Dumusque et al. 2014; Herrero et al. 2016), the selection of those lines less sensible to stellar activity (Dumusque 2018), or statistical methods such the Moving Average (Tuomi et al. 2013) or Gaussian Process regressions (Haywood et al. 2014; Rajpaul et al. 2015; Jones et al. 2017; Perger et al. 2021a), which have probed effective in the mitigation of the red noise induced by stellar activity. In this work, we have made use of versatile Gaussian Process regressions to characterise exoplanets as well as with different purposes. We provide some background about this technique in the following section.

1.3 Gaussian Processes

In a Bayesian framework, probability is a measure of the degree of belief about a proposition (Trotta 2008). The prior knowledge of any proposition is encoded in the prior probability distribuion, $p(\theta|M)$, where θ is the parameter vector of the model M. Once the data D are incorporated in the analysis, the prior distribution transforms into the posterior distribution, $p(\theta|D, M)$, which encodes all the information provided by the data, and updates when new data are incorporated. The relation between posterior and prior is controlled by the likelihood function, $p(D|\theta, M) \equiv \mathcal{L}(\theta)$, which describes how probable the current data are given a certain parameter vector θ (Díaz 2018).

There are only a few simple cases in which the evaluation of priors and posteriors can be carried out analytically. With the improvement in the quality of the data over years, the models used to describe the data have increased in complexity, and often require solving more complex and highly-dimensional posterior distributions. Thanks to the exponential increase in computational power over the past years, it is now feasible to apply massive numerical inference methods to evaluate posterior distributions and estimate fitting parameters, encouraging the exploitation of the power and flexibility that offer Bayesian tools (Trotta 2008). In few words, Bayesian inference is the process of updating a prior knowledge, described by a probability, based on new observations. One of such methods are Gaussian Process (hereafter GP) regressions, which have gained popularity among astronomers due to their flexibility and polyvalence.

1.3.1 Basics

A GP is a particular case of non-parametric Bayesian inference method. Conceptually speaking, a GP is a probability distribution over the infinite space of functions that offer an explanation for the observed data. Although this set of functions are not characterized with explicit sets of parameters to be inferred, they are all reduced to a single family of functions with the same underlying characteristics, such as a time scale, a smoothness, or a periodicity, which are controlled by the so called hyperparameters.

Consider now a two-dimensional Gaussian distribution defined by the variables y_1 and y_2 under the joint distribution $p(y_1, y_2)$. The observation of one of these variables, e.g. y_1, will condition the probability of y_2 as $p(y_2|y_1) = p(y_1, y_2)/p(y_1)$, which can be proven to also be normally distributed (Rasmussen & Williams 2005). A GP extends this definition to an infinite set of normal distributed variables $\boldsymbol{y} = \{y_1, y_2, ..., y_n\}$ evaluated at locations $\boldsymbol{x} = \{x_1, x_2, ..., x_n\}$, whose joint distribution is characterized by a mean vector $\mu(\boldsymbol{x})$ and a covariance matrix $\Sigma(\boldsymbol{x},\boldsymbol{x})$, such as:

$$p(\boldsymbol{y}) = \mathcal{N}(\mu(\boldsymbol{x}), \Sigma(\boldsymbol{x}, \boldsymbol{x})). \tag{1.23}$$

Therefore, once the mean vector and covariance matrix of the GP are chosen, the resulting posterior distribution over functions is defined by Eq. (1.23). If now one wants to evaluate the values of the GP $\boldsymbol{y}_*$ at some arbitrary locations $\boldsymbol{x}_*$, we start by defining the joint distribution of the observed data (consisting of $\boldsymbol{x}$ and associated values $\boldsymbol{y}$) augmented by $\boldsymbol{x}_*$ and $\boldsymbol{y}_*$ (Roberts et al. 2012),

$$p\left(\begin{bmatrix}\boldsymbol{y}\\ \boldsymbol{y}_*\end{bmatrix}\right) = \mathcal{N}\left(\begin{bmatrix}\mu(\boldsymbol{x})\\ \mu(\boldsymbol{x}_*)\end{bmatrix}, \begin{bmatrix}\Sigma(\boldsymbol{x}, \boldsymbol{x}) & \Sigma(\boldsymbol{x}, \boldsymbol{x}_*)\\ \Sigma(\boldsymbol{x}, \boldsymbol{x}_*)^{\mathrm{T}} & \Sigma(\boldsymbol{x}_*, \boldsymbol{x}_*)\end{bmatrix}\right), \tag{1.24}$$

from which we find that the GP defining the posterior distribution over functions evaluated at $\boldsymbol{x}_*$ is the normal distribution

$$f(\boldsymbol{x}_*) = \mathcal{GP}(m(\boldsymbol{x}_*), K(\boldsymbol{x}_*, \boldsymbol{x}_*)) \equiv \mathcal{N}(m(\boldsymbol{x}_*), K(\boldsymbol{x}_*, \boldsymbol{x}_*)), \tag{1.25}$$

with mean defined by

$$m(\boldsymbol{x}_*) = \mu(\boldsymbol{x}_*) + \Sigma(\boldsymbol{x}_*, \boldsymbol{x})\Sigma(\boldsymbol{x}, \boldsymbol{x})^{-1}(\boldsymbol{y} - \mu(\boldsymbol{x})) \tag{1.26}$$

and covariance matrix

$$K(\boldsymbol{x}_*, \boldsymbol{x}_*) = \Sigma(\boldsymbol{x}_*, \boldsymbol{x}_*) - \Sigma(\boldsymbol{x}_*, \boldsymbol{x})\Sigma(\boldsymbol{x}, \boldsymbol{x})^{-1}\Sigma(\boldsymbol{x}_*, \boldsymbol{x})^{\mathrm{T}}. \tag{1.27}$$

1.3.2 Kernels

From Eq. (1.25) we see that a GP is completely specified by its mean function and covariance matrix. The mean function of a GP represents any underlying physical model of the data at which the GP is applied, such as a Keplerian function, a transit model, or simply a constant value. The covariance matrix specifies the correlation between any pair of outputs. It is the most important element in a GP because it encodes our assumptions about the model which we wish to fit, and controls the characteristic shape of the family of functions from which the model will be inferred.

The formulation of a covariance matrix over arbitrarily large dimensions is done by defining a covariance kernel function (also called kernel), $\sigma(x_i, x_j)$, which provides the covariance element between two sample locations, the covariance matrix is hence defined as

$$\Sigma(\boldsymbol{x}, \boldsymbol{x}) = \begin{bmatrix} \sigma(x_1, x_1) & \sigma(x_1, x_2) & \cdots & \sigma(x_1, x_n) \\ \vdots & \vdots & \ddots & \vdots \\ \sigma(x_n, x_1) & \sigma(x_n, x_2) & \cdots & \sigma(x_n, x_n) \end{bmatrix}. \tag{1.28}$$

In the case that there are uncorrelated uncertainties ϵ_i associated to the data, we include them in the model by adding the term $\epsilon_i^2 \delta(i, j)$ to Eq. (1.28). In general, not all arbitrary functions producing the covariance matrix will be a valid kernel, but $\Sigma(\boldsymbol{x}, \boldsymbol{x})$ must be a positive semidefinite matrix (Rasmussen & Williams 2005). Usually, the points x which are close are likely to have similar associated y values, that is, the ability of past observations in explaining current data is a function of how long ago we observed them (Roberts et al. 2012). This is achieved by using stationary kernel functions, which are dependent on $|x_i - x_j|$. The most used stationary kernel function is the squared exponential function, given by

$$\sigma(x_i, x_j) = K_{\mathrm{SE}}^2 \exp\left(-\frac{|x_i - x_j|^2}{2\lambda_{\mathrm{SE}}^2}\right). \tag{1.29}$$

The squared exponential kernel is defined by two hyperparameters, K_{SE} and λ_{SE}, which govern the amplitude and the characteristic length-scale of the function, respectively. This kernel is infinitely differentiable, and thus produces smooth variations. In this work, we use the squared exponential kernel to interpolate discrete n-dimensional probability distributions, and to model the out-of-eclipse phases of eclipsing binary light curves to correct for stellar noise, instrumental drifts, and systematics.

An interesting propriety of positive semidefinite matrices, and hence of kernels, is that the sum and the product of two kernels is also a valid kernel, allowing the combination of kernels to make new ones. One example of such combination is the quasi-periodic kernel, which is the product of a squared exponential kernel with a periodic kernel, and is defined as

$$\sigma(x_i, x_j) = K_{\mathrm{QP}}^2 \exp\left(-\frac{1}{2w_{\mathrm{QP}}^2} \sin^2\left[\frac{\pi|x_i - x_j|}{P_{\mathrm{QP}}}\right] - \frac{|x_i - x_j|^2}{2\lambda_{\mathrm{QP}}^2}\right), \tag{1.30}$$

where K_{QP}, λ_{QP}, P_{QP}, and w_{QP} are the four hyperparameters defining the kernel. As for the squared exponential kernel, K_{QP} corresponds to the amplitude of the functions, while λ_{QP} is the characteristic length-scale. The hyperparameter P_{QP} is the period of the oscillations, and w_{QP} controls the smoothness/roughness within modulations. As it can be seen, as $w_{\mathrm{QP}} \to \infty$, the periodic variations are smoothed out and Eq. (1.30) becomes Eq. (1.29).

1.3.3 Applications

As said above, throughout this work we applied GP regression models in a diversity of problems due to their flexibility. They correspond to situations in which simple analytical solutions cannot always be applied. In the following lines, we briefly outline some applications of GP models in the context of this thesis.

- *Interpolator*. The evaluation of the likelihood functions to optimize the parameters of models and estimate their uncertainties are commonly done using the implementation of Bayesian methods such as Markov Chain Monte Carlo (MCMC, Hastings 1970). For problems in which numerical simulations are needed to fit the data or in which the number of parameters is large, such methods may become computationally too expensive. In those cases, an approximation of the likelihood function can be done by interpolating with a GP a limited number of likelihood function evaluations (Wang & Li 2017). The interpolation of a multi-dimensional likelihood function with a GP can be done using Eq. (1.25), but assuming now that each element of the evaluation points, $\boldsymbol{x}_*$, and input locations, $\boldsymbol{x}$, are multi-dimensional, writing their eth dimension element as $\boldsymbol{x}_*^{(e)}$ and $\boldsymbol{x}^{(e)}$. In this case, the used kernel is defined as a product of one-dimensional kernel functions over each dimension,
$$\sigma(\boldsymbol{x}_i, \boldsymbol{x}_j) = \prod_e \sigma^{(e)}(x_i^{(e)}, x_j^{(e)}). \tag{1.31}$$
We show an example of an interpolated 2-dimensional likelihood function in Fig. 1.2, in which the black dots indicate the input locations $\boldsymbol{x}$ at which the likelihood has been evaluated, and the colour code indicates the interpolated value of the likelihood function. For additional details, we refer the reader to Chapter 2.

- *Modelling of stellar light curves*. As explained before, active stars display periodic brightness variations as a consequence of their active regions. As these regions evolve, the amplitude and phase of the modulation may change, resulting in quasi-periodic variations (Angus et al. 2018). In addition, instrumental systematics can also add smooth drifts in the brightness as a function of time, caused for example by a drift in the pointing. Depending on the light curve, one may only want to model the systematics (see e.g. Gibson et al. 2011), the periodic modulations, or both. The addition of a quasi-periodic and an exponential kernels was suggested as an appropriate approach to tackle this problem (Aigrain et al. 2016). The optimization of the hyperparameters may result in a robust determination of the rotation period of the star, captured by the hyperparameter P_{QP}. As an example, in Fig. 1.3 we show the TESS light curve of the variable star GJ 207.1, together with it best GP model using this approach. We obtained the period of the modulations with an uncertainty of only 0.05%. We refer to Chapter 4 for additional details. In Chapter 5 we also used this method to detrend and normalize out-of-eclipse TESS light curves, using only a squared exponential kernel.

- *Disentangling stellar activity and planetary RV signals*. The fit of a single Keplerian model to RV data containing a planetary signal in presence of relatively large stellar activity variable modulations may yield biased orbital parameters, such as overestimated eccentricities (Stock et al. 2020). In this context, GP regression models have been used extensively over the last years to mitigate the effect of stellar activity signals on RVs, or to disentangle them from planetary signals. Different approaches have been used to that end, such as the training of the kernel hyperparameters with activity indicators or photometry (Haywood et al. 2014), or jointly modeling activity indicators and RVs with multi-dimensional GPs (Rajpaul et al. 2015; Jones et al. 2017). The most common use of GPs to disentangle planetary and activity signals is to model the activity induced RVs with an unconstrained quasi-periodic kernel (e.g. Faria et al. 2016; Damasso et al. 2020), and the planetary signal by using a Keplerian model (or an N-body Keplerian model) as the mean function ($\mu(\boldsymbol{x}_*)$ in Eq. 1.26). Using this framework, Perger et al. (2021a) analysed

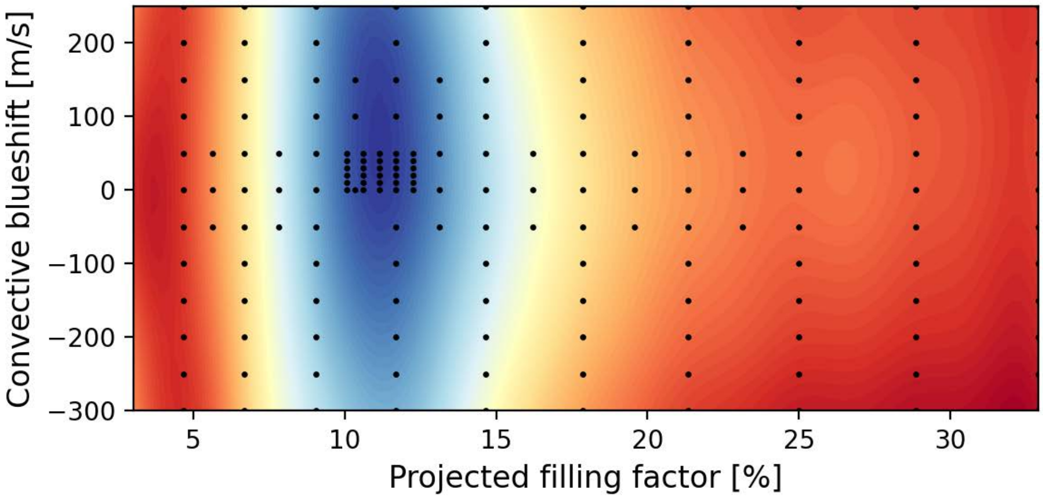

Figure 1.2: Example of a multi-dimensional likelihood function interpolated with a GP model. The colour map indicates the value of the interpolated likelihood, while the black dots, actual evaluations of the likelihood. See Chapter 2 for an explanation of the labels.

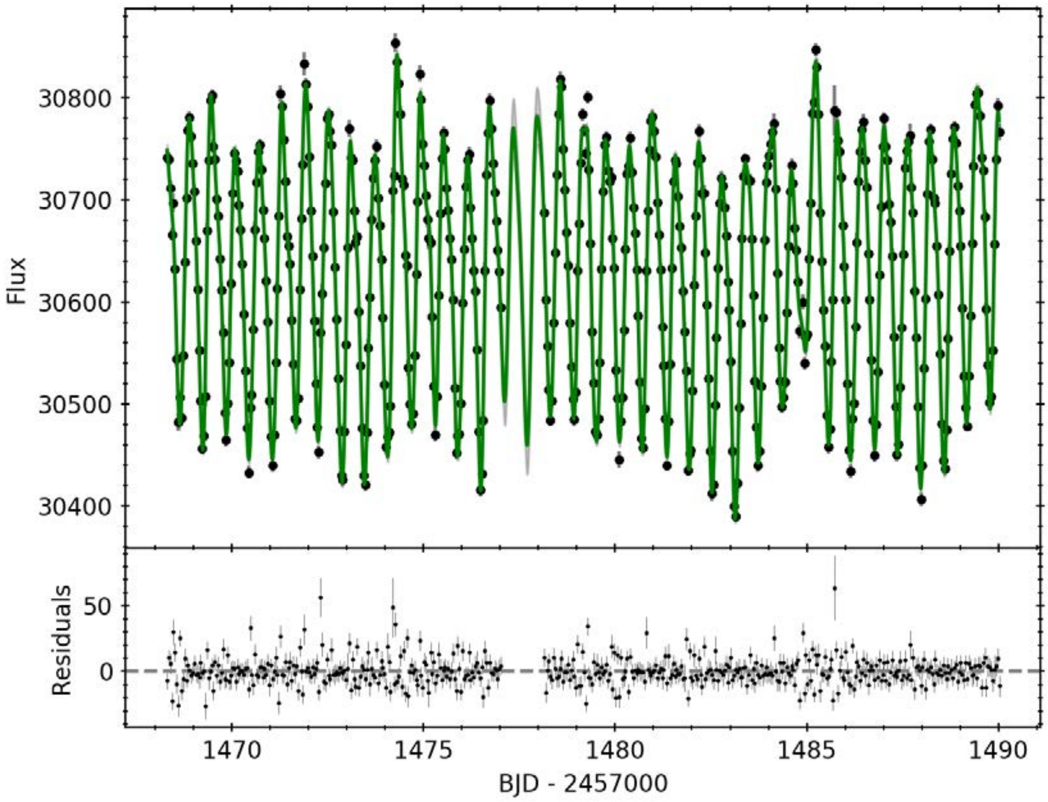

Figure 1.3: Example of a GP model (green) of a TESS light curve of the star GJ 207.1, shown as black dots. We used as a kernel the addition of a quasi-periodic and a squared exponential kernel functions. The bottom panel shows the residuals of the data after subtracting the best GP model.

the physical interpretation of the hyperparameters of the quasi-periodic kernel by modeling simulated planetary and stellar activity signals with different stellar inhomogeneities configurations. They found that the hyperparameter P_{QP} is in excellent agreement with the rotation period, that K_{QP} represents the amplitude of the activity signals, related to the filling factor of the star, and found a relation between the spot liftimes (T_{spots}) and λ_{QP}, with $T_{\text{spots}} = 1.7\lambda_{\text{QP}}$. However, they could not find a physical interpretation of the hyperparameter w_{QP}, which controls the high frequency noise in one periodicity, and recommend to maintain its value between 0.2–0.5 to avoid overfitting the planetary signal or missing the periodic component, respectively. We used this method in Chapter 3 to mitigate activity signals present in RV also containing planetary signals.

1.4 High-precision instruments

The study and mitigation of stellar activity signals, or even the detection of exoplanets, would not have been possible if there were no instruments capable of reaching high precision levels. This is the case of the CARMENES and TESS instruments, which were build with the aim of discovering low-mass exoplanets, but which are also used to gain insight into the properties of stars. The results presented in this thesis are mainly based on data from these two instruments.

1.4.1 CARMENES

CARMENES[4] (Calar Alto high-Resolution search for M dwarfs with Exoearths with Near-infrared and optical Echelle Spectrographs) is an instrument built and designed by a consortium of German and Spanish institutions to specifically conduct a large M-dwarf RV survey with a precision of $\sim 1\,\text{m}\,\text{s}^{-1}$ (Quirrenbach et al. 2016, 2018). It consists of a pair of cross-dispersed, fibre fed échelle spectrographs covering the wavelength range from 0.52 μm to 1.71 μm, which is attached to the Cassegrain focus of the 3.5 m telescope at Calar Alto observatory, Almería, Spain. The light is separated by a dichroic beam splitter centered at 0.96 μm which feeds the two spectrographs, allowing simultaneous observations. The visual (VIS) channel of CARMENES consists of a cross-dispersed échelle spectrograph covering a wavelength range from 0.52 μm to 0.96 μm with a measured spectral resolution of 94 600 and a mean sampling of 2.8 pixels per resolution element. The optical design of the near-infrared (NIR) spectrograph is similar to that of the VIS channel, but with an operating temperature of ~140 K requiring a sophisticated cooling system (Becerril et al. 2016). It covers a wavelength range from 0.96 to 1.71 μm and has a measured spectral resolution of 80 400 with a mean sampling of 2.5 pixels per resolution element. Both channels use hollow-cathode emission line lamps and Fabry-Pérot etalons for wavelength calibration (Schäfer et al. 2018).

The data reduction of CARMENES observations is carried out by the `caracal` pipeline (CARMENES Reduction And Calibration, Caballero et al. 2016b), which corrects for bias, flat-field, cosmic rays, traces échelle orders, extracts one-dimensional spectra and performs wavelength calibration. The measurement of high-precision RVs from the spectra is routinely performed by the `serval` pipeline (Zechmeister et al. 2018). The algorithm is based on the least-squares fitting of the spectra against a high signal-to-noise ratio (SNR) template, which is constructed by co-adding all available spectra of the target (Anglada-Escudé & Butler 2012). Since telluric contamination and unmasked detector defects can lead to systematic RV errors in spectral orders with low RV content, a nightly zero-point correction is applied to the RVs to

---

[4] `http://carmenes.caha.es`

track these systematics in addition to those of the instrument and/or pipeline (for more details see Trifonov et al. 2018; Tal-Or et al. 2019). In addition to RVs, `serval` also provides standard activity indicators such as the dLW, the CRX, and the emission of several chromospheric lines (e.g. Hα, Na II D, and Ca II IRT). Furthermore, for each CARMENES spectrum, their CCFs are computed using a weighted binary mask (Lafarga et al. 2020), from which the RVs, contrast, FWHM and BIS are determined.

CARMENES started scientific operations on January 2016, which also marked the beginning of the CARMENES survey. This program has observed a selection of more than 300 M dwarfs of all subtypes with the goal of detecting exoplanets. Throughout the 300 nights of guaranteed-time observations (GTO), which ended in 2020, the CARMENES survey has obtained more than 18 500 spectra with the VIS channel and almost 18 000 with the NIR adding up to more than 5 000 hours of observing time (Quirrenbach et al. 2020). The CARMENES sample of stars was selected from the CARMENES input catalogue "Carmencita" (Caballero et al. 2013, 2016a), a data base containing exhaustive information of 2 206 carefully selected M dwarfs at $\delta \geq -23°$, which is probably the most complete catalogue of bright and nearby M dwarfs. To date, the CARMENES observations have led to more than 60 scientific publications by the consortium members and collaborators, including the discovery of 30 new exoplanets (see Table A.1 for a list of published CARMENES exoplanets), the confirmation and characterisation of 20 TESS transiting planets (e.g. Luque et al. 2019; Bluhm et al. 2020; Dreizler et al. 2020; Kemmer et al. 2020), the study of exoplanet atmospheres (e.g. Nortmann et al. 2018; Alonso-Floriano et al. 2019; Yan et al. 2019; Lampón et al. 2020), the determination of the properties of M dwarfs (e.g. Passegger et al. 2018; Schweitzer et al. 2019; Cifuentes et al. 2020), or the study of stellar activity (e.g. Jeffers et al. 2018; Tal-Or et al. 2018; Schöfer et al. 2019; Lafarga et al. 2021), among others.

1.4.2 TESS

The Transiting Exoplanet Survey Satellite (TESS, Ricker et al. 2015) is an all-sky photometric survey of the nearest and brightest stars with the aim of finding hundreds of transiting planets smaller than Neptune, and whose host stars are bright enough to enable follow-up spectroscopic observations to measure planetary masses and atmospheric compositions. Over its first two years of primary mission, TESS has obtained high-precision differential photometric time-series of more than 200 000 selected stars with a 2 min cadence. In addition, TESS also provided full-frame images with a cadence of 30 min, enabling the search to any star in the field of view. The TESS detector bandpass spans from 0.60 μm to 1.00 μm, and is centered on the traditional I_C band. This wide and red bandpass is thought to reduce photon noise, and increases the sensitivity to small planets, which are easier to detect around M-dwarf stars.

The four cameras of TESS provide a field of view of 2300 deg^2, and scan almost half of the celestial sphere every one year. The halves are divided into 13 partially overlapping sectors, which are continuously observed for 27.4 days. The TESS photometric time-series, produced by the Science Process Operation Centre (SPOC, Jenkins et al. 2016), are publicly available at the Mikulski Archive for space telescopes[5]. In addition to the raw simple aperture photometry, the processed data contains the photometry corrected for instrumental variations (Smith et al. 2012; Stumpe et al. 2012, 2014), which is optimized for transit searches, but can be problematic

---

[5] `https://mast.stsci.edu/portal/Mashup/Clients/Mast/Portal.html`

for stars showing large variability. Once the data are processed and potential planetary transits are identified, selected stars are followed-up with ground-based imaging and spectroscopic instruments, such as CARMENES. These follow-up observations are used to characterise the host stars and to confirm the presence of the planet and determine their sizes and masses.

1.5 This thesis

The main purpose of this thesis is the study and characterization of exoplanets, stars, and stellar systems by analyzing data from high-precision spectroscopic and photometric surveys aimed at detecting exoplanets. In particular, Chapters 2–4 are focused on the exploitation of data from the high-resolution spectrograph CARMENES, while in Chapter 5 we use TESS photometric data to compute precise eclipse timings of well-studied eclipsing systems. TESS photometry is also used in the other chapters to look for stellar rotation periods and transit features. The contents of these four chapters have been published in five different articles in the journal *Astronomy & Astrophysics*. The CARMENES Consortium includes a large number of researchers that contributed to the preparation, implementation, and exploitation of the survey. This is reflected in the large number of co-authors in CARMENES related papers. In the following lines, we outline the contents of each chapter, describe the main changes with respect to the original publications, and detail my contributions as first or main author.

In Chapter 2 we use spectroscopic and photometric time-series of the active M dwarf YZ CMi to determine the strength of convective motions of its photosphere and the size and temperature of its active regions. With respect to the original publication by Baroch et al. (2020) we added new TESS photometric data that has been published this year. The new data confirms that active regions have evolved significantly, as was already suspected. The estimation of the bolometric luminosity, effective temperature, and radius of YZ CMi was done by C. Cifuentes and J. A. Caballero, following the method described in Cifuentes et al. (2020).

Chapter 3 reports the detection of two new exoplanets in the CARMENES data, LSPM J2116+0234 and GJ 686. During the initial analysis of the data, we became aware that Affer et al. (2019) were about to publish the discovery of an exoplanet around GJ 686, and therefore we combined their data with our CARMENES RVs to improve the determination of the orbital parameters of the planet. The results of this project were published in a collaborative work by Lalitha et al. (2019). As stated in this paper, although I am listed as the second author, my contribution to the work was equal to that of the leading author. S. Lalitha was in charge of the reduction and analysis of the photometric data, the bibliographic research of the targets, the habitability analysis and comparison with other CARMENES exoplanets. I contributed with the periodogram analysis of the RV and activity indicators, the modeling of the planetary and activity signals, and the assessment of the stability of the planetary signal. The work presented in this chapter contains a complete reanalysis of both spectroscopic and photometric data, including new data gathered after the publication, and a more detailed assesment of their habitability. We also decided not to include the data from the CARMENES NIR channel, since the planet signal was not significant and they actually reduced the accuracy in the orbital parameter determination, as seen in Table 4 in Lalitha et al. (2019).

In Chapter 4 we present the discovery and characterization of the spectroscopic orbits of all the multiple systems found in the CARMENES sample. The work done in this chapter was published in two separate articles. In Baroch et al. (2018) we determine the orbit of nine double-line binary system, whereas in Baroch et al. (2021b) we present the discovery of eight additional multiple systems, which given their orbital properties, required more observations to be characterized than those in Baroch et al. (2018). In this thesis we decided to reanalyse all the systems in Baroch et al. (2018) with the addition of new CARMENES data and archival measurements, and to remove the NIR RV from the analysis. Although the flux ratio of the stellar systems studied in this work should favour the detection of companions in the NIR channel, the presence of tellurics and the lower RV information content in the NIR resulted in RVs with a worse precision than in the VIS that do not contribute to a better determination of the orbital parameters, but rather they increase the uncertainties. The reduction of the astrometric data of GJ 282 C was done by collaborators at the Instituto the Astrofísica de Canarias (IAC), led by V. J. S. Béjar, while the estimated limits to the orbital inclination from Hipparcos astrometic data of GJ 912 and GJ 3916 were computed by S. Reffert at the Landessternwarte Königstuhl (LSW).

Chapter 5 is devoted to the analysis of TESS photometric data of well studied eclipsing binaries from which we compute precise eclipse timings with the aim of determining their apsidal motion rates. Since TESS is still providing accurate new data, we updated the results that we published in Baroch et al. (2021a) in order to improve the apsidal motion uncertainties of the systems studied in this chapter, and included new systems in the sample. Specifically, we added an additional system, EW Ori, and improved the apsidal motion determinations of four of the studied systems (KX Cnc, AL Dor, KW Hya, and V501 Mon) allowing a more robust test of general relativity. The determination of the classical apsidal motion rates required the calculation of the internal structure constants, which were provided by A. Claret using theoretical models, while A. Giménez had the original idea of recomputing apsidal motion rates of well-studied systems, selected the sample, and revised archival measurements and literature. G. Anglada-Escudé contributed with extensive discussions about different approaches to test general relativity.

Finally, in Chapter 6 we summarise and outline the main results and conclusions of the work presented in this thesis. Besides, we provide future prospects to further develop the projects presented here.

Chapter 2

Starspot constraints from chromatic radial velocities

Variability caused by stellar activity represents a challenge to the discovery and characterization of terrestrial exoplanets and complicates the interpretation of atmospheric planetary signals.

In this chapter we use a detailed stellar activity model code, `StarSim` (Herrero et al. 2016; Rosich et al. 2020), to reproduce the effect of active regions on radial velocity and photometric measurements, as well as on the chromatic index activity indicator. This aids the identification of the key parameters that have an impact on the induced variability. We analyzed the effect of stellar activity on radial velocities as a function of wavelength by simulating the impact of the properties of spots, the shift induced by convective motions, and rotation. We focused our modeling effort on the active star YZ CMi (GJ 285), which was photometrically and spectroscopically monitored simultaneously with CARMENES and the TJO telescope.

We demonstrate that a joint fit to light and radial velocity curves at different wavelengths yields determinations of key properties of active regions, including spot-filling factor, temperature contrast, and location, thus solving the degeneracy between the spot coverage area and the temperature contrast. Most notably, our model is also sensitive to convective motions, providing a novel approach to measure this parameter. The results indicate a reduced convective shift for M dwarfs when compared to solar-type stars (in agreement with theoretical extrapolations) and points to a small global convective redshift instead of blueshift.

In Sect. 2.2, we describe the model that we used to simulate time series of a rotating star with active regions, and we analyze which photospheric parameters play an important role. In Sect. 2.3, we present the spectroscopic and photometric observations of the active star YZ CMi and the results of the modeling of the spot parameters. Finally, in Sect. 2.4, we compare our results with previous parameter estimations using other methods, and summarize our findings in Sect. 2.5.

Baroch, D., Morales, J. C., Ribas, I., et al.
A&A, **641**, A69 (2020)

2.1 Introduction

Late-type dwarf stars are a strong focus of attention in the search for Earth-like planets using RVs, because the amplitude of their signals is larger than for solar-type stars (e.g., Marcy & Butler 1998; Bonfils et al. 2013; Perger et al. 2017). However, with state-of-the-art instruments reaching $\sim 1\,\mathrm{m\,s^{-1}}$ or even better uncertainties, it is not instrumental precision but astrophysical jitter that effectively limits the detection of exoplanets. This is particularly the case of some M-dwarf stars, because their intrinsic high level of magnetic activity causes the appearance of photospheric features such as stellar spots producing signals associated with the rotation period, which can hamper exoplanet detection efforts (Benedict et al. 1993). Several works discussing controversial exoplanet detections due to the stellar intrinsic jitter or spurious signals in RV curves caused by data treatment have been published (see, e.g., Robertson et al. 2014, 2015; Rajpaul et al. 2015). This reflects the difficulty of disentangling exoplanet signals from stellar jitter, even with the aid of stellar activity indices derived from spectroscopic data. However, it is also obvious that precise modeling of spot properties can help to disentangle and correct for stellar activity effects, thus enabling the detection of exoplanet signals that would otherwise be hidden within the stellar RV jitter.

A number of studies have shown that RV variability caused by stellar spots is wavelength dependent, because the flux contrast of cold spots and hot faculae is smaller toward the infrared (Desort et al. 2007; Reiners et al. 2010). Thus, in principle, measurements obtained at different spectral bands can be used to correct for intrinsic stellar RV jitter. However, the picture may be much more complicated because the effects of limb darkening, convection, and magnetic field, for instance, can cause both amplitude and phase differences between radial velocities derived from spectra at different wavelengths. On the other hand, these differential wavelength-dependent effects can be used to constrain the properties of stellar active regions.

The influence of stellar heterogeneities on RVs has been thoroughly studied in the past years by modeling the stars with surface elements at different effective temperatures representing the immaculate photosphere, spots, and faculae (see, e.g., Saar & Donahue 1997; Hatzes 2002; Lanza et al. 2007; Boisse et al. 2012). Photometric and RV variability due to stellar spots are then computed by disk-integrating the spectra corresponding to each surface element at different rotation phases. This approach only takes into account the effect of the flux dependence with effective temperature.

It is well known that the presence of magnetic fields also changes the properties of the convective layer of dwarf stars (Title et al. 1987; Hanslmeier et al. 1991). Convective cells cause significant effects on RVs, as motions produce net shifts and distortions on spectral lines (Dravins 1999; Livingston et al. 1999). For example, Gray (2009) and Meunier et al. (2017) showed that RVs derived from different spectral lines depend on the depth of the line, which also affects the shape and absolute shift of the cross-correlation function bisectors. This makes the estimation of stellar convective motions strongly dependent on the spectral lines employed and on the temperature distribution of surface elements at the time of observation. This is true even for the Sun, for which measures of convective (blue)shift range from $200\,\mathrm{m\,s^{-1}}$ to $500\,\mathrm{m\,s^{-1}}$ (Lanza et al. 2010; Meunier et al. 2010). Meunier et al. (2017) used the differential Doppler displacement between the spectral lines and their dependence on the line depth to compute the convective shift for a sample of G0 to K2 main-sequence stars, and found that the absolute value of the convective shift decreases toward cooler stars. Hydrodynamic numerical simulations performed by Allende Prieto et al. (2013) showed a similar dependence of the convective blueshift on spectral type. However, there appear to be no direct measurements of the convective shift for M dwarfs, and it is not yet certain if the decreasing trend of the convective shift continues toward late-type stars, or even if it becomes convective redshift, as some indirect measurements suggest (Kürster et al. 2003).

Regarding general active region properties, measurements of spot sizes and locations have been made using the Doppler imaging technique (Vogt & Penrod 1983), obtaining filling factors that reach ~10 % of the stellar surface (Strassmeier 2009), or even larger, as were found studying magnetic regions with Zeeman-Doppler imaging (Donati et al. 1997; Morin et al. 2008). Other techniques such as light-curve inversion (Messina et al. 1999; Berdyugina et al. 2002) can be used to retrieve spot sizes and contrast temperatures, although with this method the determination of spot temperature is strongly correlated with spot size. However, this limitation can be overcome by analyzing light curves covering a wide range of photometric bands (Mallonn et al. 2018; Rosich et al. 2020). Modeling of photometric variations of late-type active stars has revealed that cool starspots are often quite large, covering up to 20 % of the stellar surface (Berdyugina 2005). Regarding spot contrast temperatures, Berdyugina (2005) gave a representative sample of measurements suggesting values decreasing from ~2000 K for late F- and G-type stars to ~200 K for mid-M dwarfs. It should be noted that this work used a very limited and heterogeneous sample of stars, particularly M dwarfs, and combined spot temperatures determined from different methods, some of them prone to systematic biases and degeneracies.

The chromatic index (CRX) introduced by Zechmeister et al. (2018) in the context of the CARMENES survey, which measures the dependence of the radial velocity on wavelength, is ideally suited to the study of stellar activity effects. As explained in Chapter 1, this index is defined as the slope of a linear fit to the RV as a function of the central wavelength logarithm of each order in a cross-dispersed échelle spectrum at each time step. Its use as an activity indicator relies on the wavelength dependence of photospheric heterogeneities because of the temperature contrast (Barnes et al. 2011; Jeffers et al. 2014). This dependence generally causes a decrease in the activity-induced RV variations toward the reddest orders (Desort et al. 2007), although strong magnetic fields may also have a large impact at longer wavelengths due to the Zeeman effect (Reiners et al. 2013; Shulyak et al. 2019). We can make use of the CRX, together with RVs and photometric observations to constraint the properties of active regions using `StarSim`.

2.2 Modeling a spotted rotating star with `StarSim`

2.2.1 The `StarSim` model

`StarSim` is a sophisticated model used for simulating the effects of stellar spots on light and radial velocity curves. It allows us to generate precise synthetic photometric and spectroscopic time-series data of a spotted rotating photosphere. We briefly introduce the key aspects of the model here, but we refer the reader to Herrero et al. (2016) for a detailed description. The model is based on the integration of the spectral contribution of a fine grid of surface elements.

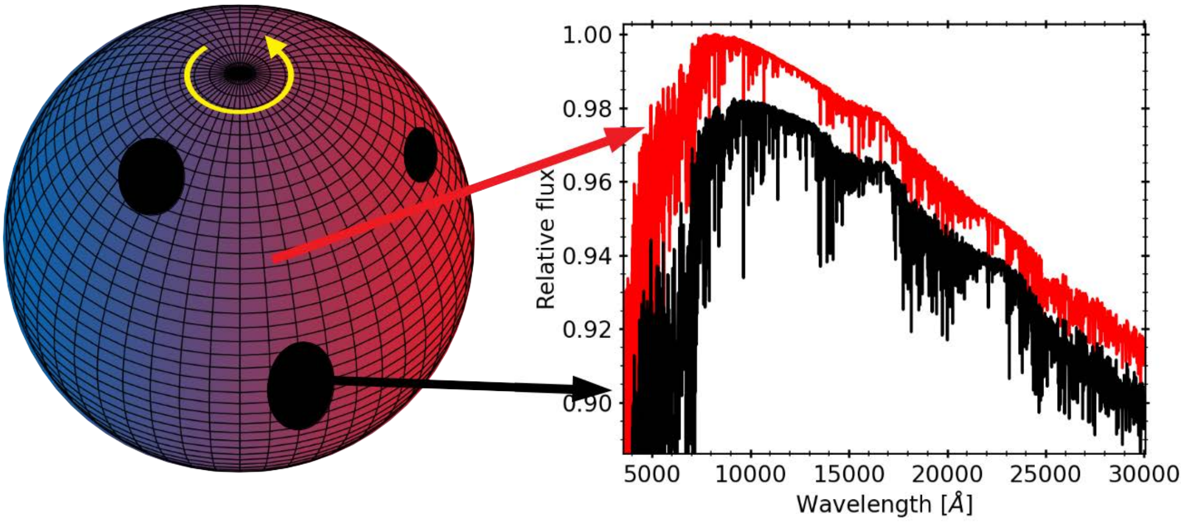

Figure 2.1: Schematic representation of the star and active regions on `StarSim`. The figure on the left shows the stellar grid of surface elements, which rotates in the direction idicated by the yellow arrow. Synthetic PHOENIX spectra of different temperatures, shown as red and black lines in the right panel, are assigned to each of the surface elements of the simulated star, here corresponding to the quiet photosphere and a spot, respectively (we omit faculae for simplicity). The spectra of each surface element is Doppler-shifted according to the projected velocity, represented by the blue and red colouring.

As seen in the schematic example shown in Fig. 2.1, synthetic PHOENIX spectra of different temperatures (Husser et al. 2013) are assigned to each of the surface elements of the star, with a different temperature depending on the properties of the region (quiet photosphere, spot, or facula), and Doppler-shifted according to the projected velocity of the surface element. Photometric light curves or RVs are then computed by integrating all surface elements. To speed up the computation of RVs and other spectral indices related to the cross-correlation function (hereafter, CCF), `StarSim` initially generates the CCFs produced from the spectrum of a single photosphere, spot, and facular element, and then integrates the entire visible surface using CCFs instead of spectra. A slow rotator template or a user-defined mask of spectral lines can be used to calculate the CCFs. Then, the contribution from each surface element is adjusted for the limb darkening computed from Kurucz ATLAS9 models (Kurucz 2017) at the specific angle with respect to the line of sight. `StarSim` defines the facular elements as circular regions around spots, whose area is controlled by the facula-to-spot area ratio. To properly account for the center-to-limb variations of convection effects in active regions, `StarSim` subtracts the bisector of the CCFs computed from the original PHOENIX spectra and then adds the bisector computed from CIFIST 3D models of a Sun-like star (Ludwig et al. 2009). The program also allows the adding of an arbitrary extra convective shift (blueshift or redshift) to the bisector of the CCFs corresponding to regions covered with spots or faculae. Finally, RV values are determined from the CCF at each epoch, which takes into account the distribution of spots and faculae and their properties, by fitting a Gaussian function.

Several stellar input parameters can be set in `StarSim`, such as the effective temperature of the star, the spot temperature, the position, size, and number of active regions, the convective shift, the stellar rotation period, the radius of the star, its surface gravity, and the inclination of the stellar spin axis with respect to the line of sight. Furthermore, one can select the wavelength range and compute time-series data of the photometry, RV, and CCF parameters.

To calculate the CRX parameter, we simulated RV curves for different wavelength ranges and measured their wavelength dependence. For this study, we used wavelength ranges matching those of the CARMENES visual channel échelle orders (i.e., 61 orders from 520 to 960 nm, Quirrenbach et al. 2016, 2018) to be consistent with our observational data. However, following Zechmeister et al. (2018), to compute the simulated CRX, we used the 40 orders (échelle orders 68 to 108) where the signal-to-noise ratio of the spectra is the highest, and thus observational RVs have lower uncertainties. The CRX is then computed as the slope of a linear fit to the RV as a function of the logarithm of the central wavelength of each order.

2.2.2 Dependence on photospheric parameters

To study the dependence of the RV and CRX time series on the properties of active regions, we ran several simulations considering a rotating spotted star. For simplicity, we assumed a single circular active region on the photosphere, and tested different values for the ratio of stellar surface covered by the spot (filling factor, *ff*), the temperature difference between the photosphere and the spot ($\Delta T \equiv T_{\rm ph} - T_{\rm sp}$), and the convective shift (CS). As explained in the previous section, `StarSim` introduces the influence of convective motions by adding a solar-like bisector to the CCF of each surface element. Thus, the solar convective blueshift is used as a reference. As an estimation of its absolute value, in our case a solar blueshift of 300 $\rm m\,s^{-1}$ (Dravins et al. 1981; Cavallini et al. 1985; Löhner-Böttcher et al. 2018) was subtracted from all CS values shown in this work. Therefore, the absolute values of CS given in this work have a dependence on the precise determination of the convective blueshift from CIFIST 3D models.

Stellar parameters such as effective temperature, surface gravity, and metallicity also have an impact on the RV and CRX time series due to their effects on stellar spectra. Besides this, the rotation of the star, its inclination, the latitude of the spot, and the presence of faculae do also play a role. However, these stellar parameters can be determined from fits to high-resolution spectra or through independent data. For this reason, we focus only on the impact of the properties of spots on RV and CRX time series.

For our simulations, we considered the case of a mid-M dwarf star approximately matching the properties of YZ CMi, which we use as a case study to compare with real observations later in Sect. 2.3. We fixed the stellar photospheric effective temperature to a value of 3100 K, the stellar surface gravity to $\log g = 5.0$, and we adopted solar metallicity. We assume an inclination of the rotation axis of $i = 90$ deg (edge-on), and we introduce a spot on the equator, with no evolution and no differential rotation. The facula-to-spot area ratio was set to zero as commonly found for active M-dwarf stars (Herrero et al. 2016; Mallonn et al. 2018; Rosich et al. 2020), and also as suggested by convection in magnetohydrodynamic simulations (Beeck et al. 2011, 2015).

Figure 2.2 illustrates the outcome of the simulations as a function of *ff*, ΔT, and CS for RV and CRX. The bottom panels show that the CRX is strongly anti-correlated with the RV. As other authors have previously shown for the case of the bisector span (see, e.g., Boisse et al. 2011a; Figueira et al. 2013), the CRX-RV anti-correlation is not a straight line, but it shows

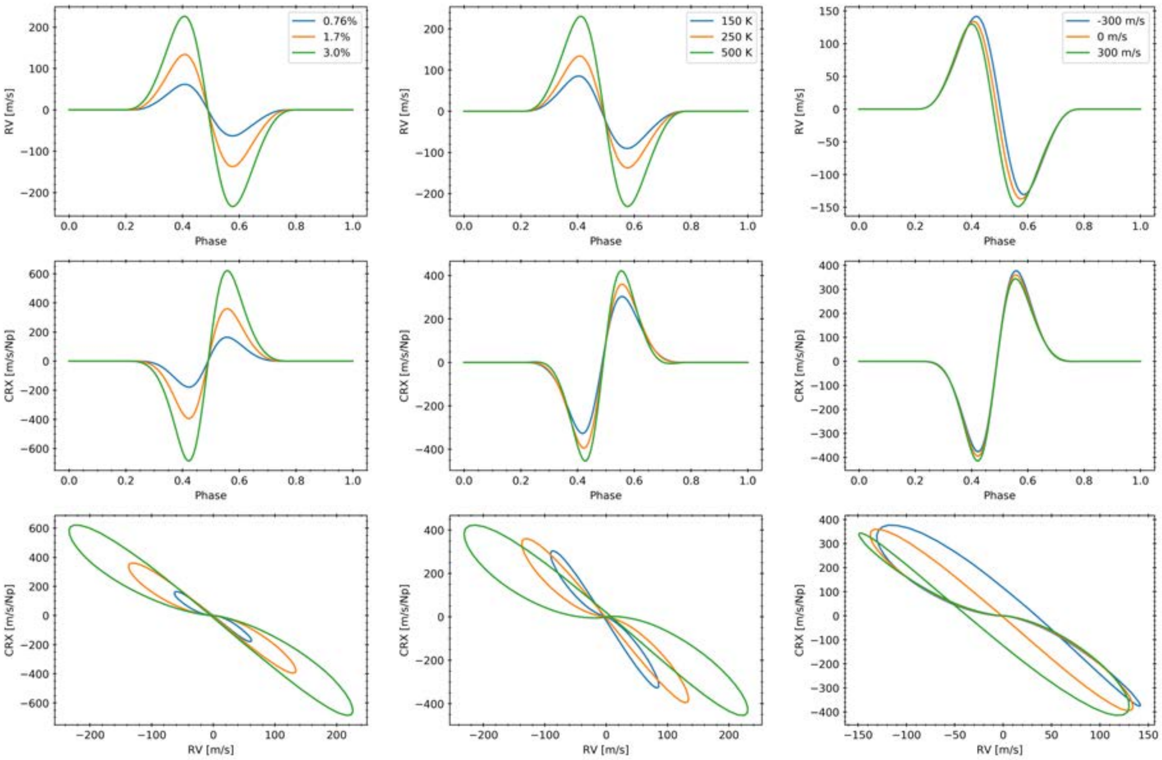

Figure 2.2: Effect of properties of stellar spots on the RV (*top panels*) and CRX (*middle panels*) phase curves and on the RV-CRX correlation (*bottom panels*) for a mid-M dwarf. Simulations of varying *ff* (*left panels*), ΔT (*middle panels*), and CS (*right panels*) are shown while keeping the other parameters constant to a set of reference values. These reference values are 1.7 % for the filling factor, 250 K for ΔT, and 0 m s^{-1} for CS. We note the different vertical scale in each plot, and that the horizontal axes are different in the bottom panels.

a lemniscate-like structure. The left panels in Fig. 2.2 show that varying *ff* mainly produces a change in the amplitude of both the RV and CRX time series, which in turn changes the scale of the correlation but preserving its slope and shape. The middle panels display the effect caused by different values of ΔT. This parameter has a much higher impact on the amplitude of the RV curve than on the CRX, producing a significant change in the slope of the correlation. Finally, CS changes the phase at which the RV peaks, and only slightly alters the asymmetry between maximum and minimum of both the RV and CRX. This change in phase does not produce any change in the scale and slope of the RV-CRX correlation, but it has a significant imprint on its shape.

The different effects of stellar spot parameters on RV and CRX data can be understood by considering the main sources of variability, which are: *(i)* the flux effect caused by the contrast between inhomogeneities and the immaculate photosphere (Dumusque et al. 2014), and *(ii)* the inhibition of convection in active regions (Dravins et al. 1981; Stein et al. 1992; Chabrier et al. 2007). Both effects cause periodic variations of the measured RV of spotted stars. However, their dependence on rotation phase (or time) is different (see Fig. 2.3, adapted from Herrero et al. 2016). The flux effect vanishes when the spot is facing the observer because the spot covers equivalent surface areas moving toward and away from the observer, hence, the net effect is canceled. Besides this, the flux effect is anti-symmetric with respect to this point, meaning it causes an RV maximum when the spot crosses the hemisphere approaching the observer, and a

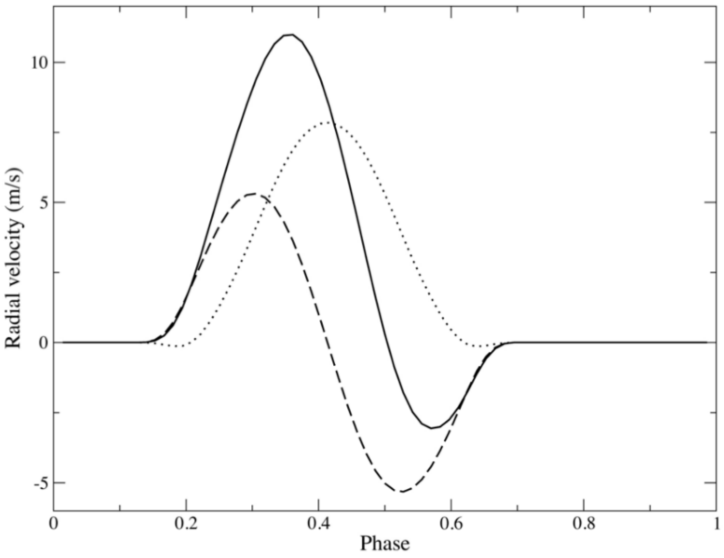

Figure 2.3: RV variability (solid line) as a function of the rotation phase, produced by a dark spot in the equator of the star. The dashed and dotted lines indicate the contribution of the flux effect and convection to the RV variability, respectively. Figure adapted from Fig. 7 in Herrero et al. (2016).

minimum on the other side. On the other hand, the convection effect is maximal at the central phase, when the projected filling factor of the spot is largest, and the RV variability is symmetric with respect to this point. The difference between the peaking phase of both effects and the dependence of the flux effect with the wavelength (the flux effect is larger when the contrast is high, which occurs at short wavelengths, while the variability from convection is constant for all frequencies) produces a phase shift of the RV peaks for different wavelengths, which is not observed in the CRX. This causes the lemniscate shape of the CRX-RV correlation, which becomes asymmetric depending on the parameters. The top-right panel in Fig. 2.2 shows that the phase shifts of RV time series are dominated by CS, while CRX remains almost unaffected (middle-right panel). The peak-to-peak amplitudes of both observables are mainly determined by the size and the temperature of the spot. This makes the analysis of chromatic radial velocities a unique tool to constrain CS, by simultaneously fitting the peak-to-peak amplitude and the phase shift of RV and CRX time series.

2.3 Fitting chromatic radial velocities of YZ CMi

The star YZ CMi (GJ 285) is a young star belonging to the β Pictoris moving group (Alonso-Floriano et al. 2015, and references therein). Its main properties are listed in Table 2.1. Maanen (1945) first announced the BY Dra-type photometric variability of the star, which was also classified as a flaring star by Lippincott (1952), showing UV Cet-type flares. Several flaring events were reported later (Andrews 1966; Sanwal 1976; Zhilyaev et al. 2011). A rotation period of 2.77 d from photometric variations was reported by Chugainov (1974) and confirmed by Pettersen et al. (1983). Recent estimations of the rotation period yielded very similar values (2.7758±0.0006 d and 2.776±0.010 d, Morin et al. 2008; Díez Alonso et al. 2019, respectively). Bondar' et al. (2019) found an activity cycle of 27.5 ± 2.0 years, estimated from more than 80 years of archival photometric observations, with peak-to-peak variations of 0.2–0.3 mag.

Estimations of the effective temperature of YZ CMi range from 3045 K (from synthetic spectra fitting; Rojas-Ayala et al. 2012) to 3600 K (from spectral color indices; Zboril 2003).

The variability of the star has been extensively studied. The large color excess of YZ CMi indicates the presence of cool spots covering a large fraction of its surface. Zboril (2003) computed spot solutions from light curves taken in different seasons, and found a typical spot coverage between 10 % and 25 % of the surface, resulting from a single spot at a co-latitude ~15–35 deg from the pole and temperature ~500 K cooler than the surrounding photosphere, all assuming an inclination ranging from 60 deg to 75 deg. Similarly, Alekseev & Kozhevnikova (2017) used 11 epochs of observations over 30 years of broad-band photometry to compute the spottedness of YZ CMi. The authors assumed an effective temperature of 3300 K and an inclination of $i = 60$ deg, obtaining two belts of spots 210 ± 70 K cooler than the photosphere, which were mainly located at latitudes of 12–15 deg, and covering up to 38 % of the stellar surface. Using Zeeman-Doppler imaging and 25 spectropolarimetric observations taken between 2007 and 2008, Morin et al. (2008) found that the visible pole is covered by a large spot, with strong axisymmetry in the magnetic energy modes, hinting toward a non-visible spot at the other hemisphere. Morin et al. (2008) also inferred negligible differential rotation ($0.0 \pm 1.8\,\mathrm{mrad\,d^{-1}}$).

The bolometric luminosity L and effective temperature $T_{\rm eff}$ of YZ CMi were homogeneously derived by CARMENES project collaborators as described in Cifuentes et al. (2020). A set of 17 broadband photometric passbands, from optical blue B_T (Tycho-2, Høg et al. 2000) to mid-infrared $W4$ (AllWISE, Cutri et al. 2013), were used. None of the measurements used, especially at the bluest passbands, seemed to be affected by strong flaring activity. To determine L and $T_{\rm eff}$, fits to the spectral energy distribution (SED) were performed employing the BT-Settl CIFIST theoretical grid of models (Baraffe et al. 2015) and the Virtual Observatory SED Analyzer (VOSA, Bayo et al. 2008). In order to recompute extreme values of bolometric luminosity, the long-term photometric variability of YZ CMi in the blue optical passband was taken into account by re-running the SED fitting at the brightness maximum and minimum, which as a conservative approach, were taken as the largest reported variability amplitude of 0.3 mag in the B band (Bondar & Katsova 2018), over a scale of decades. Those amplitudes were approximately extrapolated to 0.2 mag in the red optical, 0.1 mag in the near infrared, and 0.05 mag in the mid infrared, as observed in multiband photometric monitoring of very active M dwarfs (e.g., Caballero et al. 2006). The corresponding L and $T_{\rm eff}$ uncertainties of YZ CMi are thus larger than for invariable field M dwarfs of similar brightness. The radius was calculated using Stefan-Boltzmann's law following Schweitzer et al. (2019) and propagating the uncertainties in L and $T_{\rm eff}$.

We estimated the inclination of the stellar spin axis from the radius, the rotation period and the projected velocity, which yielded $i = 36^{+17}_{-14}$ deg. The uncertainty was computed from 10^6 random resamplings of the input parameters according to their quoted uncertainties. The lower inclination value that we find, contrary to other studies (Zboril 2003; Morin et al. 2008; Alekseev & Kozhevnikova 2017), arises from the different projected velocity and stellar radius used. In particular, projected rotational velocities of 5.0 and 6.5 $\mathrm{km\,s^{-1}}$ (Delfosse et al. 1998; Reiners & Basri 2007) and stellar radii of 0.30 and 0.37 $R_\odot$ (Pettersen 1980; Delfosse et al. 2000) were reported. Based on CARMENES data, Reiners et al. (2018b) reported $v \sin i = 4.0 \pm 1.5\,\mathrm{km\,s^{-1}}$, and we find a stellar radius of 0.369 $\mathrm{R_\odot}$ following Schweitzer et al. (2019). The resulting parameters are listed in Table 2.1.

The selection of this target for analysis of its stellar activity properties was based on two main

Table 2.1: Basic properties of YZ CMi.

Parameters	Values	Ref.
GJ	285	GJ79
Karmn	J07446+035	AF15
α (J2000)	07:44:40.17	*Gaia* DR2
δ (J2000)	+03:33:08.9	*Gaia* DR2
d [pc]	5.9874 ± 0.0021	*Gaia* DR2
G [mag]	9.6807 ± 0.0010	*Gaia* DR2
J [mag]	6.581 ± 0.024	2MASS
Sp. type	M4.5 V	PMSU
$T_{\rm eff}$ [K]	3100 ± 50	This work
$\log g$ [cgs]	5.0 ± 0.5	Lep13
$L_\star$ [$10^{-4}\,L_\odot$]	113^{+17}_{-14}	This work
$R_\star$ [$R_\odot$]	$0.369^{+0.027}_{-0.055}$	This work
pEW(Hα) [Å]	-7.097 ± 0.023	Jef18
$v \sin i$ [km s^{-1}]	4.0 ± 1.5	Rei18
$P_{\rm rot}$ [d]	2.776 ± 0.010	DA19
i [deg]	36^{+17}_{-14}	This work

References. 2MASS: Skrutskie et al. (2006); AF15: Alonso-Floriano et al. (2015); DA19: Díez Alonso et al. (2019); *Gaia* DR2: Gaia Collaboration et al. (2016, 2018); GJ79: Gliese & Jahreiß (1979); Jef18: Jeffers et al. (2018); Lep13: Lépine et al. (2013); PMSU: Hawley et al. (1996); Rei18: Reiners et al. (2018b).

points: *(i)* it is one of the M-dwarf stars with the strongest activity-induced RV variability within the CARMENES survey, with peak-to-peak amplitudes of ~300 m s^{-1}, and *(ii)* it is also one of the stars with the strongest RV-CRX correlation (Tal-Or et al. 2018), which could be indicative of large spots. Actually, CRX was recently demonstrated to be particularly useful as an activity indicator for the most active M-dwarf stars (Lafarga et al. 2021).

2.3.1 CARMENES observations

YZ CMi is one of the targets of the CARMENES survey (Reiners et al. 2018b), being observed between 2016 and 2018 at 49 epochs. To mitigate the possible effects of spot evolution, spectroscopic and photometric campaigns to sample all rotational phases were conducted between September 2016 and May 2017, yielding a total of 27 spectroscopic observations, which are used in this work. Figure 2.4 displays the RV and CRX time series, and all used data are available in Table A.2 in the Appendix. RVs and CRX are anti-correlated, as was expected given the results of the simulations in Sect. 2.2.2.

The contemporaneous photometric campaign was conducted at the Montsec Observatory in Lleida, Spain. We obtained 460 photometric measurements using a Johnson R filter with the Telescopi Joan Oró (TJO). The TJO is a fully-robotic 0.8 m Ritchey-Chrétien telescope. The

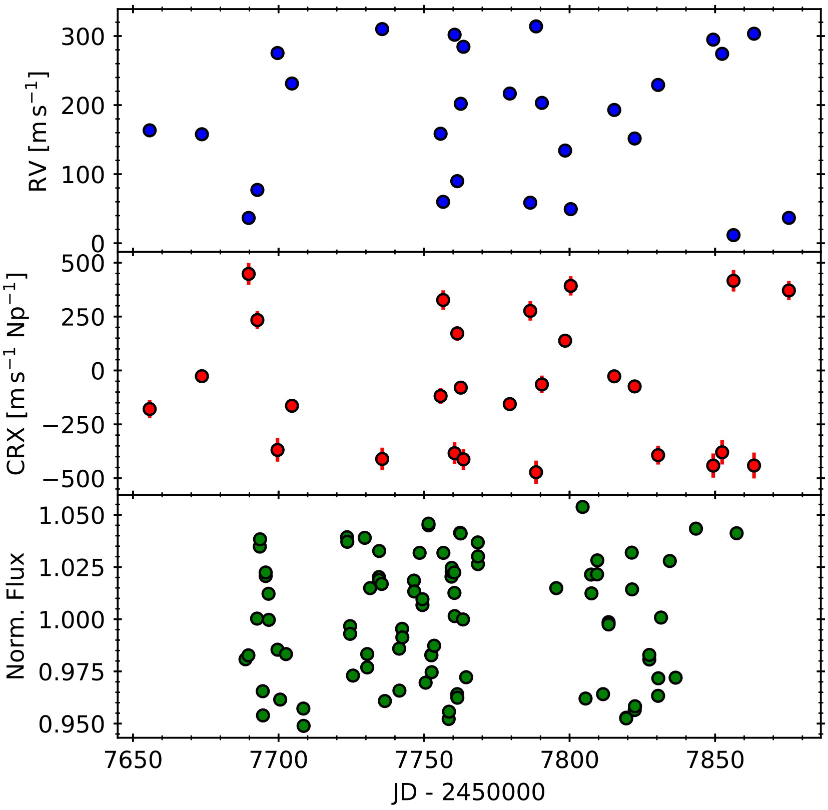

Figure 2.4: RV (*top*), CRX (*middle*), and photometric (*bottom*) time series of YZ CMi obtained with CARMENES and TJO.

photometric data were obtained with the MEIA2 instrument, an Andor 2 k×2 k CCD camera with a plate scale of 0.36 arcsec per pixel. We gathered these observations between October 2016 and April 2017. After rebinning the data with a cadence of 30 min, we performed a 2.5 σ-clipping to the residuals after a sinusoidal fit, in order to remove outliers due to flaring events, which resulted in a total of 89 photometric epochs, listed in Table A.3. The bottom panel in Fig. 2.4 displays the resulting photometric data. We also gathered publicly available data from the the Transiting Exoplanet Survey Satellite (TESS) mission (Ricker et al. 2015), which observed YZ CMi in sector 7 (January 2019) and sector 34 (January 2021). Unfortunately, none of the TESS sectors is contemporaneous to the RVs, but they could be used to understand the variability of the star.

The upper panels in Fig. 2.5 show the photometric time series from TJO and TESS in the same flux scale. We observe an obvious reduction of the photometric variability with time. Although the different filters used between TJO and TESS photometry can explain the different amplitudes between both instruments, it does not explain the reduction in amplitude between the two TESS sectors. Also, a different shape of the light curve between the two TESS epochs can be observed. In order to check the periodicities found in each dataset, we show in the lower-left panel the GLS periodogram (Zechmeister et al. 2018) of the individual time series, as well as of the combined datased. All periodograms peaks at virtually identical periods, obtaining values of 2.774 ± 0.021, 2.77 ± 0.14, and 2.7742 ± 0.0032 d for the TJO, the two TESS sectors, and the combined dataset, respectively. These values are also consistent to the value obtained by

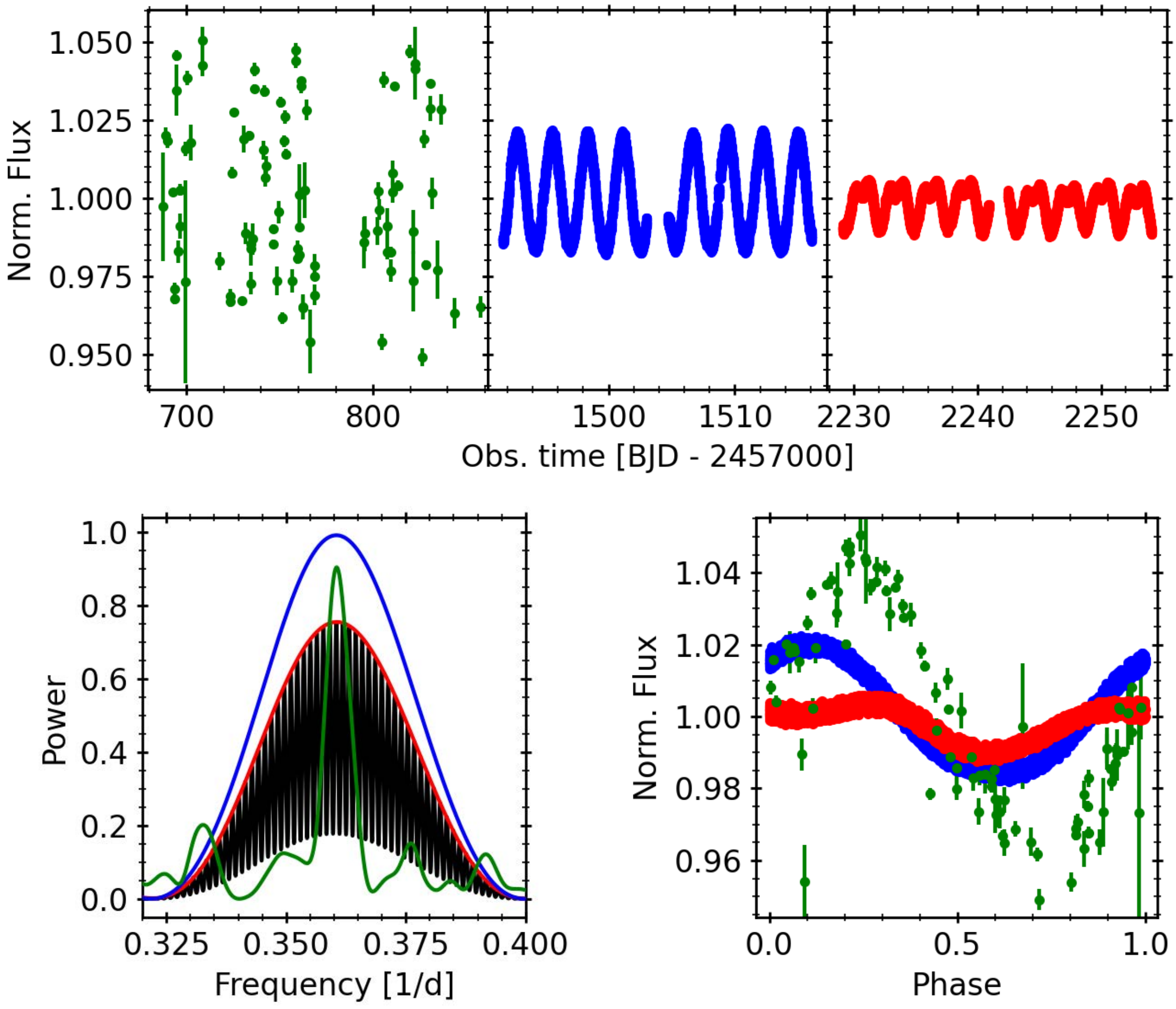

Figure 2.5: Photometric time series (top) of TJO data (green) and sectors 7 (blue) and 34 (red) of TESS data. The bottom left panel shows the GLS periodogram of the three different datasets, following the same colour scheme, and of the combined data, in black. The bottom right panel illustrates the phase folded light curves using the period derived from the combined dataset.

Díez Alonso et al. (2019), confirming the long-term stability of the rotation signal. The phase-folded light curves, using the period of 2.7742 ± 0.0032 d from the combined dataset is shown in the lower-right panel of Fig. 2.5. It shows that the TJO photometry has a slight phase shift with respect to the TESS data, while the two TESS sectors have similar phases. These results suggest that although the rotation of the star is very stable, active regions are evolving in both size and positions, producing changes in the amplitude, phase, and shape of the modulations, which highlights the importance of using contemporaneous data to simultaneously fit a shared active region map.

2.3.2 Surface distribution of the active regions

Before analyzing the impact of the size and the temperature of spots and the convective shift on the RV and CRX time series of YZ CMi, we needed to estimate the distribution of active

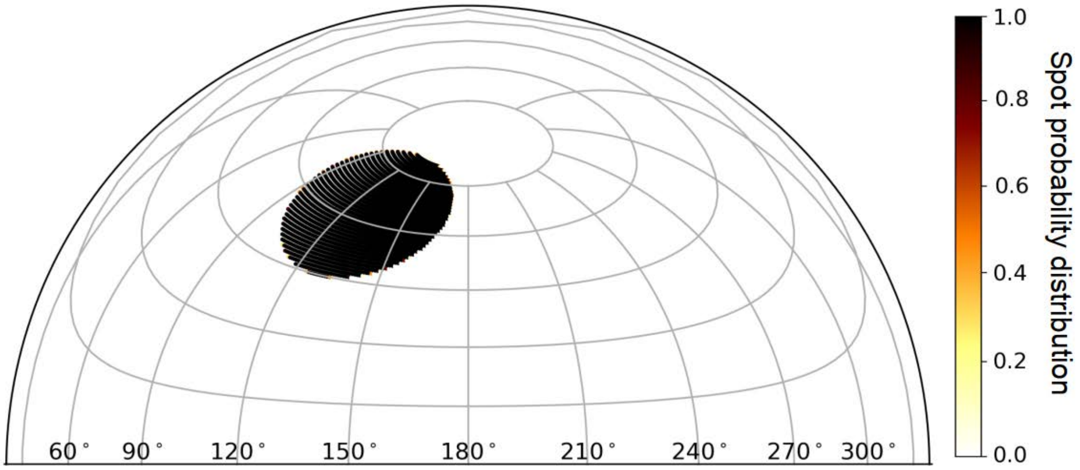

Figure 2.6: Probability distribution of the surface maps resulting from 100 inversions of the radial velocity and TJO photometry, using a temperature contrast of 200 K. Although here the image is projected in a grid representing the northern hemisphere, the datasets are not sensitive to the hemisphere in which the spots are located.

regions on the stellar photosphere, particularly their latitude. Although light curves are not strongly sensitive to the latitude of active regions, including RV data in the analysis does solve this problem. This is especially true in the case of YZ CMi, for which a constraint on the inclination of the spin axis is available. For this purpose, we made use of the implementation of the inverse problem in `StarSim`, which allows the fitting of the spot distribution that best matches light or radial velocity curves (Rosich et al. 2020). This implementation solves the inverse problem by using several small active elements on the star, which may be concentrated to reproduce spot groups. We used the stellar input parameters from Table 2.1, and estimated the latitude of active regions from the observed RV and photometric time series assuming different temperature contrast values in the range ΔT = 50–400 K. Figure 2.6 illustrates of the probability distribution of spots for 100 surface maps from the inverison of the RV and TJO data, using a temperature contrast of 200 K. We found that, while the size of active elements showed some correlation with their temperature contrast, their latitudes were always in the range 75–81 deg. The inversion of the RVs using a model with 20 active surface elements resulted in all of them concentrated around the same region. For that reason, and to speed up and simplify the fitting procedure, we decided to further model the data with a larger single non-evolving circular spot located at a latitude of $\lambda_{\rm spot} = 78$ deg.

2.3.3 Fitting spot parameters

Assuming the spot model described above, we analyzed the impact of ΔT, *ff*, and CS on the RV, CRX, and photometric time series of YZ CMi, and we determined the values that best fit all datasets simultaneously. The simulation of RV data using `StarSim` involves the computation of the CCF for each surface element of the star, a process that is computationally expensive. Therefore, we decided to fix the stellar parameters to those listed in Table 2.1, and compared our simulations with the observed RV, CRX, and light curves on a grid of the ΔT-*ff*-CS parameter space. To explore the parameter domain, the likelihood of the `StarSim` models given the

Table 2.2: Best fitting parameters and ranges introduced by the uncertainties on $T_{\rm eff}$ and i to the YZ CMi RV, CRX, and photometric datasets.

Parameters	Best model	Range	
		Min.	Max.
ff [%]	11.16 ± 0.66	9.53	13.25
ΔT [K]	199.7 ± 9.6	178.6	273.4
CS [m s^{-1}]	56 ± 37	7	237
$\Delta t_{\rm ref}$ [d]	1.9879 ± 0.0078	1.9735	2.0043
$\gamma_{\rm RV}$ [m s^{-1}]	-166.8 ± 2.5	-169.5	-163.6
$\sigma_{\rm RV}$ [m s^{-1}]	11.2 ± 2.2	8.5	17.7
$\sigma_{\rm CRX}$ [m s^{-1} Np^{-1}]	47 ± 14	33	125
$\sigma_{\rm phot}$ [$\times 10^{-3}$]	6.00 ± 0.47	5.45	6.67
$\ln \mathcal{L}$	70.8	52.0	72.8

observed datasets was first computed on a coarse grid, with 20 K, ~3.5 %, and 50 m s^{-1} steps in ΔT, ff, and CS, respectively. We subsequently defined a finer grid with step sizes divided by four to explore the regions with higher likelihood values. The likelihood at each grid point was computed by also considering an offset to the RVs ($\gamma_{\rm RV}$), and a global reference time shift to the RVs, CRX, and photometry ($\Delta t_{\rm ref}$), relating the central longitude of the star to the rotational phase. Finally, we also added jitter terms ($\sigma_{\rm RV}$, $\sigma_{\rm CRX}$, $\sigma_{\rm phot}$) to the RVs, CRX, and photometry, respectively, to account for the limitations of a single-spot model. These jitter terms are added in quadrature to the corresponding uncertainties to evaluate the likelihood function, as defined in Baluev (2009). The final model likelihood value reported is the sum of the individual likelihood values obtained for the RV, CRX, and photometry datasets.

Figure 2.7 displays the log-likelihood difference with respect to the best model, $\Delta \ln \mathcal{L}$, in the ΔT-ff plane for different values of CS. Dotted symbols correspond to the inspected grid of parameters, which is finer in the regions corresponding to the best fit of observations. The region with $\Delta \ln \mathcal{L} < 10$ corresponding to the RV, CRX, and photometry fits are independently plotted with blue, red, and green contours, respectively, while black contours indicate the joint values. Although photometric fits are independent of the convective shift, they constrain the ff and ΔT correlation very well. On the other hand, both RV and CRX are much more sensitive to CS changes, which breaks the strong ff-ΔT correlation present in the photometry fits. The different panels in Fig. 2.7 show that, in spite of the similar solution ranges for ff and ΔT, the CRX provides a stringent constraint on the upper value of CS. As a further check, we ran a test excluding the CRX dataset and we found that the uncertainty on the value of CS increases by a factor of ~2. Thus, although the filling factor and the spot temperature contrast can be determined from a simultaneous fit to the RV and photometry only, the CRX provides valuable information to constrain the convective shift. Overlap between photometry, RV, and CRX $\Delta \ln \mathcal{L}$ surfaces (i.e., best simultaneous fit to all datasets) occurs around CS ~50 m s^{-1}, suggesting a global convective redshift for YZ CMi. We note, however, that although the best solutions yield convective redshift, there are acceptable solutions ($\Delta \ln \mathcal{L} < 10$) located in the convective blueshift region.

To estimate the optimal parameters fitting the CARMENES RV and CRX data and the TJO light curve, along with their uncertainties, we interpolated the $\ln \mathcal{L}$ hypersurface over the grid

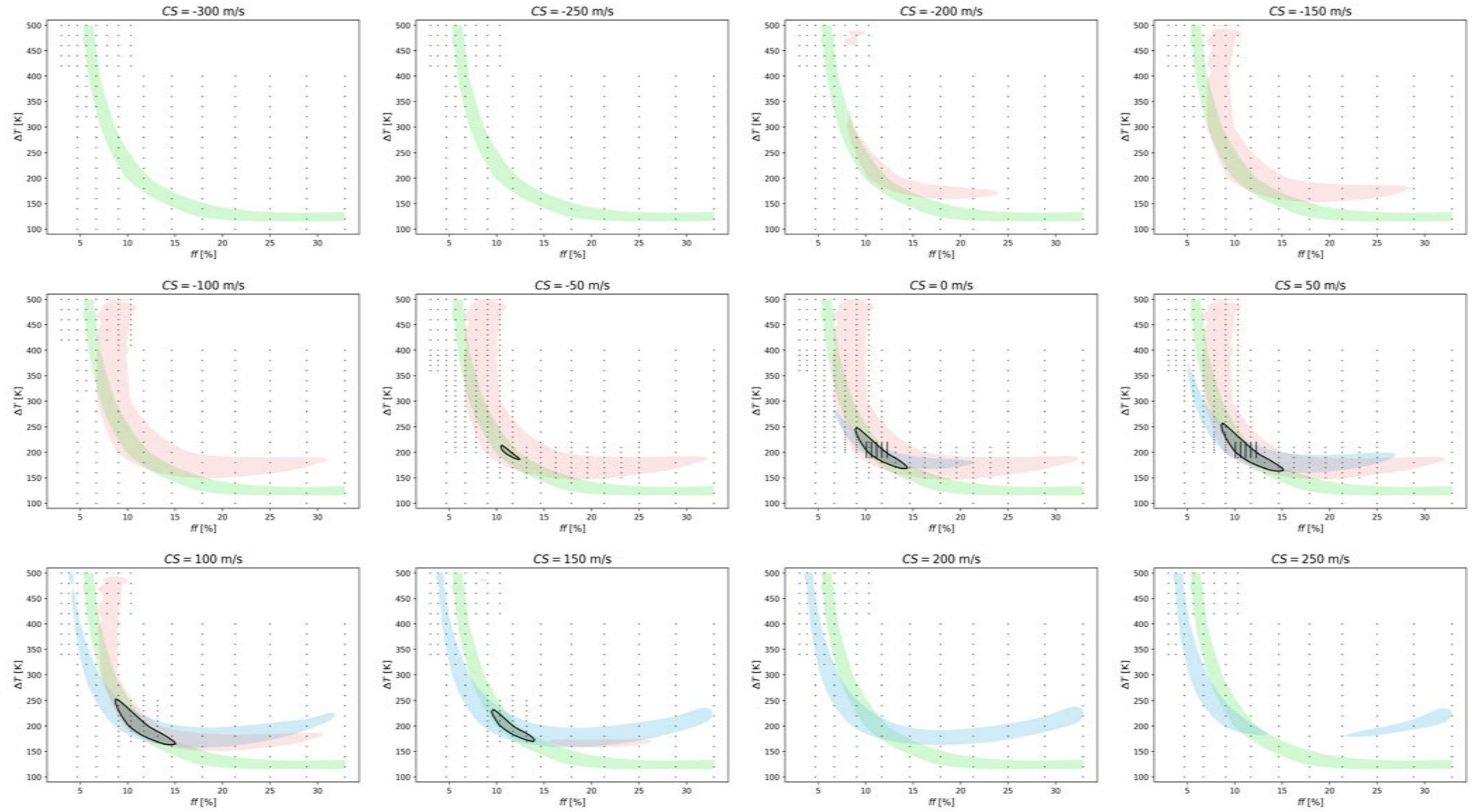

Figure 2.7: $\Delta \ln \mathcal{L}$ contour plots corresponding to the RV (*blue*), CRX (*red*), photometry (*green*), and combined (*black*) fits for different CS slices. The colored regions are within a $\Delta \ln \mathcal{L} = 10$ with respect to the best fit among all the CS slices. Black dots indicate the points of contrast temperature and filling factor used to sample the parameter space.

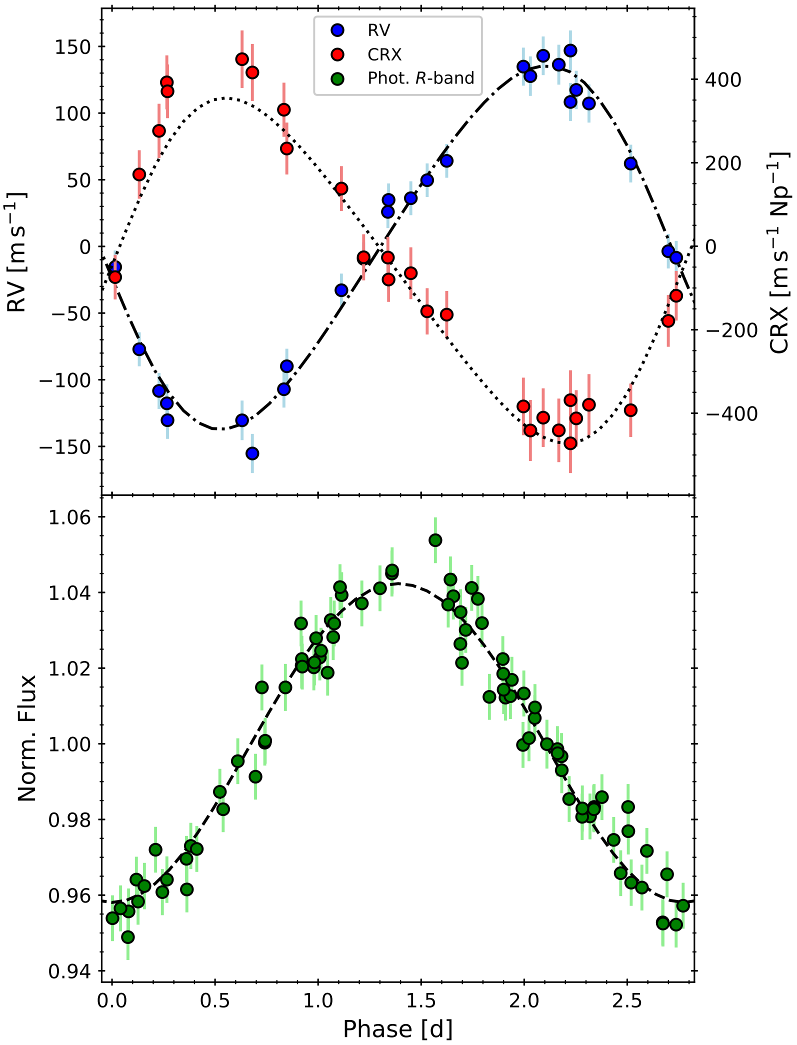

Figure 2.8: Phase-folded RV (blue circles), CRX (red circles), and photometric (green circles) data obtained for YZ CMi. In the top panel, the left and right vertical axes correspond to RV and CRX, respectively. The best models that simultaneously fit the three datasets are shown as dash-dotted (RVs) and dotted (CRX) lines, and they correspond to the values found in Table 2.2. The error bars correspond to the quadrature addition between observational uncertainties and the fit jitter parameter for each dataset.

used to search for the best solution (ΔT, *ff*, *CS*), also including the adjusted parameters ($\gamma_{\rm RV}$, $\Delta t_{\rm ref}$, $\sigma_{\rm RV}$, $\sigma_{\rm CRX}$, and $\sigma_{\rm phot}$). For this purpose, we used a multi-variate GP using a squared exponential covariance function (see Sect. 1.3), similarly to the likelihood inference explained by Wang & Li (2017) and Fleming & VanderPlas (2018). Compared to a linear interpolation, the GP interpolation produces smoother profiles, and can also infer maxima outside the evaluated points. To obtain optimal parameters, we maximized the interpolated likelihood using the Powell method inside the `scipy.optimize` Python package. Formal uncertainties were derived from the covariance matrix, computed from the Hessian evaluated at the maximum. Table 2.2 lists the parameters of the best fitting model, together with the minimum and maximum values found using other stellar parameters (see below). The best-fitting models to the RV and CRX data phase-folded to a period of 2.776 d are shown in the top panel of Fig. 2.8, while the bottom panel shows the best fit to the photometry. Figure 2.9 illustrates the correlation between RV and CRX and its best fit, showing that the cyclic evolution is well reproduced by the

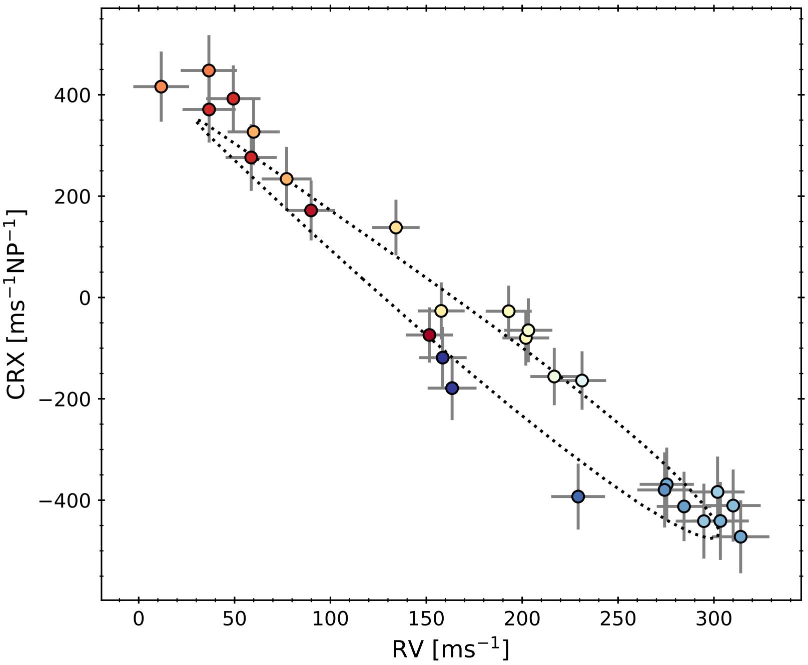

Figure 2.9: Best fit model *(dotted line)* compared to observations *(symbols)* in the RV-CRX parameter space. The colors of the symbols indicate the rotation phase at which each observation was made.

`StarSim` model. Comparing Fig. 2.9 with the bottom panels in Fig. 2.2, YZ CMi data show better consistency with the RV-CRX correlation with negative CS than with the lemniscate shape corresponding to a null CS effect. This correlation can in fact be used as a clear observable of convective blueshift or redshift thanks to the asymmetry introduced toward positive or negative velocities, respectively. Although the bottom-right panel in Fig. 2.9 shows a twisted loop, this also depends on the filling factor and temperature of spots. For YZ CMi, the CS is ~6 times smaller than in the simulations in Fig. 2.2, but the filling factor is also ~6 times larger, causing the untwisted loop.

The uncertainties of the spot parameters may be underestimated, because we assumed fixed stellar properties. We remind the reader that this is due to the computational effort needed to run the RV simulations, which prevents us from exploring solutions also including stellar properties as free parameters. To study the impact on the parameter uncertainties, we repeated the process to simultaneously fit the RV and CRX data considering a set of values for the effective temperature ($T_{\rm eff}$) of YZ CMi and its spin axis inclination (i) spanning the reported uncertainties in Table 2.1. These are the parameters identified to potentially induce changes on the simulated RV. A different $T_{\rm eff}$ could potentially change the temperature and size of spots required to reproduce the observations, while a change in i may also have an impact on the latitude and size of the spots and their imprint on RVs. Table 2.3 lists the results of the fits for the set of $\mathrm{T_{eff}}$ and i values used for this purpose. All solutions are statistically equivalent ($\Delta \ln \mathcal{L} < 10$), except for the simulations with an inclination of 52.5 deg, which start to fail at reproducing the CRX, as indicated by their relatively higher jitter. Additionally, the fit parameters span a wider range than the formal uncertainties previously reported for fixed stellar parameters. We list these additional systematic uncertainties caused by the error bars of the stellar properties in the third column of Table 2.2.

Table 2.3: Best fit parameters for every $T_{\rm eff}$-i set of models.

Model			Best fit parameters								$\ln \mathcal{L}$
$T_{\rm eff}$ (K)	i (deg)	$\lambda_{\rm spot}$ (deg)	$ff_{\rm max}$ (%)	ΔT (K)	CS (m s^{-1})	$\Delta t_{\rm ref}$ (d)	$\gamma_{\rm RV}$ (m s^{-1})	$\sigma_{\rm RV}$ (m s^{-1})	$\sigma_{\rm CRX}$ (m s^{-1} Np^{-1})	$\sigma_{\rm phot}$ ($\times 10^{-3}$)	
3050	21.5	73	11.66 ± 0.78	196 ± 12	49 ± 39	1.9932 ± 0.0080	−167.0 ± 2.4	10.9 ± 2.0	50 ± 13	5.93 ± 0.46	71.4
3050	30.0	77	11.89 ± 0.72	188.5 ± 9.9	57 ± 39	1.9930 ± 0.0080	−167.0 ± 2.5	11.1 ± 2.1	49 ± 14	5.93 ± 0.46	71.1
3050	36.0	78	11.11 ± 0.67	194 ± 10	49 ± 39	1.9869 ± 0.0079	−166.8 ± 2.5	11.4 ± 2.3	48 ± 14	6.00 ± 0.47	69.9
3050	45.0	79	10.51 ± 0.71	210 ± 13	62 ± 24	1.9839 ± 0.0079	−166.8 ± 2.6	12.0 ± 2.3	60 ± 14	6.09 ± 0.48	63.8
3050	52.5	80	9.96 ± 0.43	249.7 ± 8.8	68 ± 61	1.9821 ± 0.0086	−166.6 ± 3.0	14.4 ± 3.3	84 ± 20	6.17 ± 0.50	52.0
3100	21.5	73	11.65 ± 0.48	202.3 ± 7.2	56 ± 37	1.9941 ± 0.0078	−167.0 ± 2.4	10.9 ± 2.0	50 ± 13	5.93 ± 0.46	71.6
3100	30.0	77	12.33 ± 0.92	190.5 ± 9.6	70 ± 37	1.9931 ± 0.0081	−167.1 ± 2.4	10.7 ± 2.0	49 ± 13	5.93 ± 0.46	71.9
3100^{a}	36.0^{a}	78^{a}	11.16 ± 0.66	199.7 ± 9.6	56 ± 37	1.9879 ± 0.0078	−166.8 ± 2.5	11.2 ± 2.2	47 ± 14	6.00 ± 0.47	70.8
3100	45.0	79	10.68 ± 0.63	214.7 ± 9.4	79 ± 22	1.9855 ± 0.0080	−166.8 ± 2.5	11.5 ± 2.3	61 ± 15	6.06 ± 0.48	64.8
3100	52.5	80	10.26 ± 0.67	257 ± 14	167 ± 61	1.9869 ± 0.0089	−166.9 ± 2.5	11.6 ± 2.2	103 ± 22	6.09 ± 0.49	53.3
3150	21.5	73	11.51 ± 0.90	212 ± 14	74 ± 39	1.9962 ± 0.0081	−167.0 ± 2.4	10.7 ± 1.9	55 ± 13	5.91 ± 0.46	70.7
3150	30.0	77	12.06 ± 0.74	201.0 ± 9.8	86 ± 35	1.9947 ± 0.0079	−167.0 ± 2.4	10.6 ± 1.9	49 ± 13	5.92 ± 0.46	72.8
3150	36.0	78	11.76 ± 0.81	200 ± 11	93 ± 32	1.9930 ± 0.0078	−167.0 ± 2.3	10.4 ± 1.9	49 ± 13	5.95 ± 0.46	72.4
3150	45.0	79	11.01 ± 0.86	215 ± 13	132 ± 39	1.9932 ± 0.0083	−166.9 ± 2.3	10.4 ± 2.0	64 ± 15	5.98 ± 0.47	67.1
3150	52.5	80	10.55 ± 0.46	253.0 ± 9.5	180 ± 57	1.9881 ± 0.0082	−167.0 ± 2.5	11.3 ± 2.4	91 ± 20	6.11 ± 0.49	56.3

Notes. $^{(a)}$ Stellar parameters used as the best model in Table 2.2

2.4 Discussion

Our model for YZ CMi indicates that this active star has at least a prominent spot with a filling factor in the ~9.5–13.3 % range. The value that we found is compatible with previous values in the literature by Zboril (2003) and Alekseev & Kozhevnikova (2017), who suggested filling factors of 10–25 % and 10–38 %, respectively. The significantly broader (and less precise) ranges reported in these works most likely arise from the use of only light curves, which, as we showed in Fig. 2.7, produce a strong degeneracy in the ff-ΔT plane. However, because of the different adopted stellar inclinations, contrast temperatures, and spot models used in these two works, caution should be taken when performing comparisons. They used stellar inclinations of 60–70 deg, Zboril (2003) fixed the contrast temperature to 500 K, and Alekseev & Kozhevnikova (2017) used two spot belts. Furthermore, the spot size and latitude that we estimate are consistent with a spot covering a large fraction of the visible pole, in agreement with the results obtained by Zeeman-Doppler imaging (Morin et al. 2008).

From our analysis, we constrain the temperature difference between the photosphere and the spot to a 1σ confidence range of ~179–273 K. These values are in close agreement with the ΔT of 210 ± 70 K obtained by Alekseev & Kozhevnikova (2017), and are consistent with the commonly used empirical calibration by Berdyugina (2005) and Andersen & Korhonen (2015). However, our results are better constrained due to the simultaneous fit of photometric, RV, and CRX time series covering several wavelength bands that allow the breaking of the spot temperature and the filling factor degeneracy. Furthermore, the scarcity of spot crossing events on the ~4000 M dwarfs in the *Kepler* catalog could be indicative of a low contrast ratio for the spots on the photospheres of these stars (i.e., smaller ΔT), assuming a heterogeneous distribution of spots (Andersen & Korhonen 2015). The study of multiband photometric observations also points toward a smaller temperature difference for late-type stars than for solar-like stars (Mallonn et al. 2018; Rosich et al. 2020).

We note that differences in temperature and filling factors available in the literature may also be due to the evolution of stellar activity features, as is obvious when comparing the light curves from TESS sectors 7 and 34 in Fig. 2.5. For instance, as a further check, we compared our simulations with the TESS sector 7 photometry, obtained two years after our CARMENES dataset. Figure 2.10 shows this light curve along with the model corresponding to the best fitting parameters listed in Table 2.2, and with the range defined by all the models in Table 2.3. Although the overall aspect is similar, the TESS light curve has a lower amplitude compared to our models. This difference can be reproduced by reducing the filling factor to ~ 7.5 % or with a temperature contrast 40 K lower.

Finally, the simultaneous fit to RV, CRX, and photometric time series results in a global convective shift for YZ CMi in the range between +7 and +237 $\mathrm{m\,s^{-1}}$, in contrast with the value of −300 $\mathrm{m\,s^{-1}}$ estimated for the Sun. Interestingly, this result means that the convection effect produces a net redshift, not a blueshift, although this result must be taken with caution given the large uncertainty. Such a possibility was already suggested by Kürster et al. (2003) based on the anti-correlation between the Hα line strength and the RV for Barnard's Star, indicating an increase in the blueshift when the coverage of the star with plage regions increases. Similar conclusions are suggested by 3D hydrodynamic simulations, which also predict a very small net convective blueshift for late K-type stars that increases with the effective temperature of the star until reaching a blueshift of 300 $\mathrm{m\,s^{-1}}$ for F-type dwarfs (Allende Prieto et al. 2013).

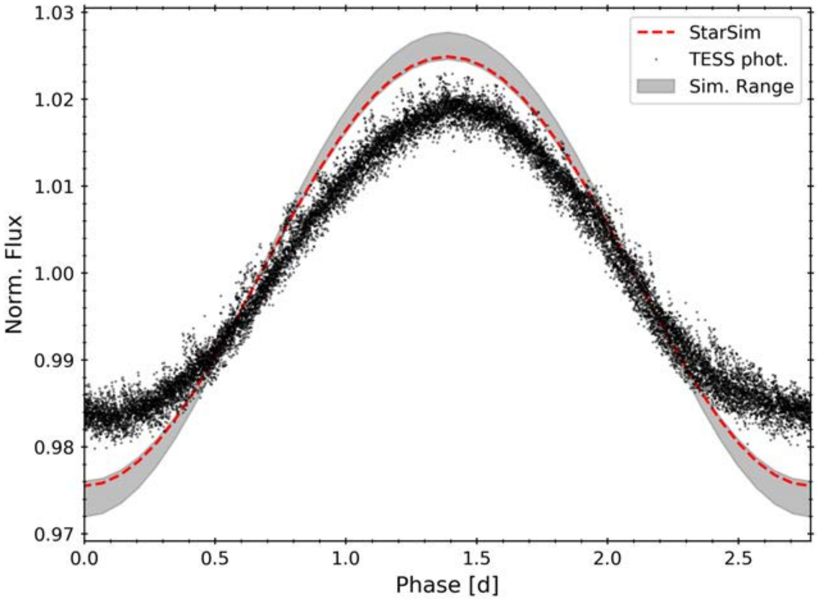

Figure 2.10: Phase-folded TESS sector 7 photometric observations (*black dots* compared to the `StarSim` simulation (*dashed line*) using the best model values and the TESS-band filter. The gray shaded region corresponds to the range defined by all the best model simulations in Table 2.3.

Meunier et al. (2017) described a similar trend from the estimation of the convective blueshift using Fe and Ti lines of 360 F7–K4 stars. For the particular case of M-dwarf stars, magnetohydrodynamic simulations suggest that convective motions are less vigorous and that the average granule velocity shift is also smaller (Beeck et al. 2013a,b).

2.5 Summary

In this chapter we took advantage of the variability induced by stellar activity on the radial velocity and photometry of stars to study not only the properties of stars, but also the convective shift on M-dwarf stars. In particular, we modeled radial velocity, chromatic index, and photometric timeseries of the active star YZ CMi using the stellar activity model code `Starsim`.

The results of our analysis highlight the importance of contemporaneous spectroscopic and photometric data to break the degeneracies between spot sizes and temperatures, while avoiding the effect of spot evolution. The simultaneous fit to light and RV curves for several wavelength bands developed in this chapter represents a novel approach to estimating not only properties of stellar activity, such as the spot filling factor and temperature difference, but also the shift of radial velocities due to convective motions. To our best knowledge, the work presented here provides the first direct determination of the convective shift of an M dwarf. In addition, since the CRX is not affected by the Keplerian orbital motion of the host star caused by exoplanets, its modeling to derive the properties of photospheric features could provide priceless information to disentangle exoplanet signals from stellar activity effects.

For the particular case of YZ CMi presented here, we obtained a spot location, size, and temperature compatible with past determinations, but with improved precision thanks to avoiding degeneracies between spot size and temperature. The estimated temperature contrast, of $\sim 200\,\mathrm{K}$, is in agreement with the decreasing contrast temperature towards late-type stars observed by other authors. We also found that the absolute convective shift of YZ CMi may be reversed toward redshift, which is consistent with the reduction of the absolute convective shift towards cooler stars obtained from the measured values of heavier stars.

Chapter 3

Planets around M dwarfs with CARMENES

Despite the spurious signals induced by their high levels of stellar activity, M dwarfs are the ideal targets to search for low-mass exoplanets in the habitable zone using the radial velocity method because their signals are larger. In the context of the CARMENES survey, more than 300 M-dwarf stars are being monitored to look for such candidates. In this chapter, we use CARMENES data of the stars LSPM J2116+0234 and GJ 686 to search for signals produced by exoplanetary companions.

We combined and analysed CARMENES and archival radial velocity measurements looking for periodic significant signals, and compared them to the signals found in photometric data and spectroscopic indicators to identify those induced by the rotation of the star. In order to obtain unbiased orbital parameters, we modeled a Keplerian orbit together with a correlated noise model describing stellar activity signals.

Based on radial velocity data from the visual channel of CARMENES, we report the discovery of a mini-Neptune companion around LSPM J2116+0234. The planet is in a 14.45 days orbit producing a radial velocity semi-amplitude of 6.0 $\mathrm{m\,s^{-1}}$, which yields a minimum mass of 12.8 $M_\oplus$. With the addition of CARMENES data to more than two decades of radial velocity data from HIRES, HARPS, and HARPS-N, we confirmed the existence of the super-Earth orbiting around GJ 686 published by Affer et al. (2019) and refined its orbital parameters, which yield an orbital period of 15.53 days and a minimum mass of 6.6 $M_\oplus$. Additionally, a planet-plus-activity model of the radial velocities revealed recurrent periodic signals at 42 and 37 days for LSPM J2116+0234 and GJ 686, respectively, also present in their photometric time series and spectroscopic indicators. We attribute these signals to the stellar rotation periods.

In Sect. 3.2, we introduce the basic properties of the host stars, and describe the spectroscopic and photometric data in Sect. 3.3. In Sect. 3.4, we present our results from the analysis of RVs, photometry and activity indicators, and model stellar activity as correlated noise using a Bayesian framework in order to find the orbital parameters and discuss the stability of the signals through time and wavelength. We summarize our findings in Sect. 3.5.

Lalitha, S., Baroch, D., Morales, J. C., et al.
A&A, **627**, A116 (2019)

3.1 Introduction

In the recent years, M-dwarf stars have gained significant attention in the field of exoplanets, with a number of surveys using the radial velocity technique searching for rocky habitable planets around these stars. The reasons for this surge of surveys focusing on M dwarfs are diverse. Firstly, compared to Sun-like stars, M dwarfs have lower mass and closer habitable zones (Kasting et al. 1993; Kopparapu et al. 2013), and as a consequence, potentially habitable planets would induce larger RV signals and be easier to detect. Secondly M-dwarfs host an average of more than 2 planets per star (Dressing & Charbonneau 2015; Gaidos et al. 2016), making them the most common potential planetary hosts.

On the other hand, the downside of surveying M-dwarf stars with high-resolution spectrographs is their high levels of magnetic activity. Large inhomogeneities such as dark spots and bright faculae could be produced on the stellar surface due to the activity, which in turn affect the spectral line profile, inducing a Doppler-shift in the spectrum (Vogt & Penrod 1983). Consequently, stellar activity can induce large-amplitude RV variations which may have periodicities close to the stellar rotation period, and as a result, they can be misinterpreted as planetary signals. The spot- and facula-induced RV amplitude generally tends to decrease toward longer wavelengths (Desort et al. 2007), while in stars with a strong magnetic field the relative importance of the Zeeman effect increases with wavelength (Reiners et al. 2013). In addition, M dwarfs emit the bulk of their spectral energy at wavelengths redward of 1 μm (Reiners et al. 2010, and references therein). Hence, in theory, observations at wavelengths around 700–900 nm are ideal for both reducing the effect of stellar activity on RVs and minimizing the exposure time when surveying M dwarfs (Reiners et al. 2018b). The CARMENES spectrograph was specifically designed to cover this wavelength range, extending further into the NIR than most high-precision spectrographs to cover the range where M dwarfs emit the bulk of their spectral energy.

Performing a fit of a planetary signal in presence of significant activity-induced RV variability may yield biased orbital parameters. To solve that problem, several techniques have been developed over the past years to disentangle activity-induced variations from planetary signals. Some of these techniques are based on the study of correlations between activity indicators and RVs (see e.g. Queloz et al. 2001; Boisse et al. 2011b; Oshagh et al. 2017; Zechmeister et al. 2018), the selection of individual spectral lines less affected by activity (Dumusque 2018), or the simulation of stellar inhomogeneities to model the effects over RVs. One method that has gained popularity on the recent years, thanks to the steadily increase in computational power, is the use of Bayesian inference models such as Gaussian Processes (Haywood et al. 2014; Rajpaul et al. 2015; Faria et al. 2016; Jones et al. 2017; Perger et al. 2021a). The flexibility of such models allows the simultaneous fit of the activity-induced quasi-periodic variability and planetary signals, while yielding physical interpretations of stellar variability, such as the filling factor of the star, the rotation period, and the mean spot lifetimes (Perger et al. 2021a).

In this chapter, we analyze the RV data of two similar M dwarfs, LSPM J2116+0234 and GJ 686, monitored as part of the CARMENES Guaranteed Time Observations (GTO) M-dwarf survey. The data reveal the presence of a mini-Neptune around LSPM J2116+0234 with a period of 14.4 d, and a super-Earth with a period of 15.5 d around GJ 686. However, Affer et al. (2019, hereafter Aff19) reported the detection of the 15.5 d planet around GJ 686 while we were still analysing our data, and we decided to combine CARMENES and archival data to publish a refinement of the orbital parameters of GJ 686b, instead of reporting its discovery. In

Table 3.1: Basic properties of the host stars.

Parameters	LSPM J2116+0234	GJ 686	Ref.
Karmn[a]	J21164+025	J17378+185	
α (J2000)	21:16:27.55	17:37:54.39	*Gaia*
δ (J2000)	+02:34:50.76	+18:35:45.92	*Gaia*
$\mu_\alpha \cos\delta$ [mas a^{-1}]	247.356 ± 0.021	926.638 ± 0.016	*Gaia*
μ_δ [mas a^{-1}]	−39.763 ± 0.015	984.455 ± 0.018	*Gaia*
ϖ [mas]	56.691 ± 0.022	122.555 ± 0.018	*Gaia*
d [pc]	17.6394 ± 0.0068	8.1596 ± 0.0012	*Gaia*
G [mag]	10.8595 ± 0.0008	8.7390 ± 0.0006	*Gaia*
J [mag]	8.219 ± 0.032	6.360 ± 0.023	2MASS
Sp. Type	M3.0 V	M1.0 V	PMSU
$T_{\rm eff}$ [K]	3393 ± 54	3645 ± 54	Pas19
$\log g$ [cgs]	4.60 ± 0.06	4.74 ± 0.06	Pas19
[Fe/H] [dex]	−0.13 ± 0.19	−0.10 ± 0.19	Pas19
L [L$_\odot$]	0.0247 ± 0.0003	0.0293 ± 0.0007	Schw19
R [R$_\odot$]	0.430 ± 0.013	0.427 ± 0.013	Schw19
$M_\star$ [M$_\odot$]	0.430 ± 0.017	0.426 ± 0.017	Schw19
pEW (Hα) [Å]	0.102 ± 0.006	−0.066 ± 0.007	Schf19
$v \sin i$ [km s^{-1}]	< 2	< 2	Rei18
$\log R'_{HK}$	···	−5.42 ± 0.05	Sua18
U [km s^{-1}]	−24.06 ± 0.02	−33.68 ± 0.02	Cor19
V [km s^{-1}]	−18.21 ± 0.02	35.29 ± 0.02	Cor19
W [km s^{-1}]	−5.17 ± 0.02	−21.27 ± 0.01	Cor19

Notes. (a) CARMENES identifier.

References. 2MASS: Skrutskie et al. (2006); Cor19: Cortés-Contreras (2021, in prep); *Gaia*: Gaia Collaboration et al. (2016, 2018); Jef18: Jeffers et al. (2018); Rei18:Reiners et al. (2018b); PMSU: Hawley et al. (1996); Pas19: Passegger et al. (2019); Sch19: Schweitzer et al. (2019); Sua18: Suárez Mascareño et al. (2018); UCAC4: Zacharias et al. (2013).

Sect. 3.2, we introduce the basic properties of the host stars, and we describe the spectroscopic and photometric data in Sect. 3.3. In Sect. 3.4, we present our results from the analysis of RVs, photometry and activity indicators. We model activity as correlated noise using a Bayesian framework in order to find the orbital parameters and discuss the stability of the signals through time and wavelength. We conclude and summarize our work in Sect. 3.5.

3.2 Targets

A summary of the basic stellar properties of both targets is presented in Table 3.1. The photospheric parameters such as the effective temperature $T_{\rm eff}$, surface gravity $\log g$, and metallicity [Fe/H] of the targets were determined in the CARMENES framework by Passegger et al. (2019) using the PHOENIX-ACES model grid (Husser et al. 2013). The stellar masses, radii, and luminosities were determined based on the photospheric parameters and a mass-radius relation (Schweitzer et al. 2019).

LSPM J2116+0234 (Karmn J21164+025) is an M3.0 V star at a distance of 17.6394 ± 0.0068 pc (Gaia Collaboration et al. 2016, 2018). It was discovered by Lépine & Shara (2005) as a northern star with a proper motion larger than 250 mas a^{-1}, and characterized photometrically and spectroscopically by Lépine & Gaidos (2011) and Lépine et al. (2013). LSPM J2116+0234 has been identified as a nearby potential target for planet searches (Finch et al. 2014), activity analyses (Rodríguez et al. 2010; Jeffers et al. 2018), and determination of photospheric stellar parameters (Passegger et al. 2018).

Figure 3.1 shows the galactocentric space-velocity components U, V, and W of known members of young moving groups from Montes et al. (2001), together with the space-velocity of LSPM J2116+0234 computed by a CARMENES collaborator using the *Gaia* second data release astrometric data and the absolute radial velocity computed by Lafarga et al. (2020). The obtained space-velocity is consistent with membership to the young disk population and to the IC 2391 stellar kinematic group, which has an estimated age of 50 ± 5 Ma as inferred by Barrado y Navascués et al. (2004) using lithium depletion and Hα emission. However, the *ROSAT* All Sky Survey did not detect X-ray emission for LSPM J2116+0234. This imposes an estimated upper-limit luminosity $L_{\rm X} < 10^{27}$ erg s^{-1}, much lower than the expected value of 10^{29} erg s^{-1} found for the members with similar spectral type of the IC 2391 and other older young open clusters such as the Pleiades or Hyades (Patten & Simon 1996). Furthermore, the tentative rotational period of LSPM J2116+0234 obtained in this work, of about ~42 d (see Section 3.4.1), is longer than those of the IC 2391 cluster members (Patten & Simon 1996) and those of the

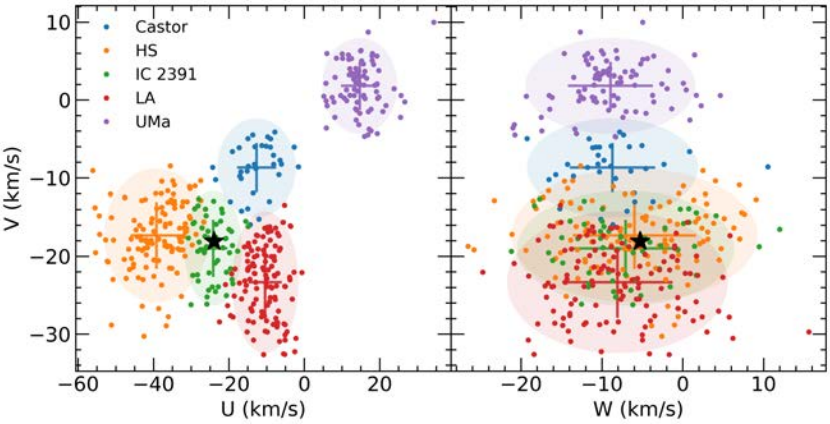

Figure 3.1: (U, V) and (W, V) planes of young moving groups along with LSPM J2116+023 (star symbol). The crosses indicate the 1σ uncertainties for each moving group while the ellipses represent a 2σ uncertainty.

members of the older Pleiades open cluster (110–130 Ma, Stauffer et al. 1998; Dahm 2015), which have typical rotational periods of less than 10 days (Rebull et al. 2016). Therefore, although LSPM J2116+0234 shares the same kinematics as the IC 2391 supercluster, the X-ray emission and the rotation period indicate that the object is older than 50 Myr. In fact, from the gyrochronologic relation in Barnes (2007), we estimate an age for this star of $\sim$ 2 Ga, using its rotation period and $B - V$ color, of 1.474 ± 0.014 mag (Zacharias et al. 2013).

GJ 686 (BD+18 3421, Karmn J17378+185) is an M1.0 V star, located in the Hercules constellation, at only 8.1596 ± 0.0012 (Gaia Collaboration et al. 2016, 2018). Because of its earlier spectral type and closer heliocentric distance, GJ 686 is also brighter than LSPM J2116+0234. In particular, its bright visual magnitude $V \approx 9.6$ mag (Koen et al. 2010; Zacharias et al. 2013) enabled the star to be tabulated in the "Bonner Durchmusterung des südlichen Himmels" by Schönfeld (1886), and its parallax to be measured more than 100 years ago (Barnard 1913; Adams et al. 1926; Osvalds 1957). It was one of the first late-type stars for which RV and metallicity were measured (Wilson 1953; Tokovinin 1990) and one of the first M-type standard stars (Henry et al. 1994). Later, GJ 686 took on greater relevance with the investigation of its moderate activity level (Stauffer & Hartmann 1986; Stephenson 1986; Herbst & Layden 1987; Rutten et al. 1989; Panagi & Mathioudakis 1993), which was confirmed by later comprehensive studies (Delfosse et al. 1998; Wright et al. 2004; Isaacson & Fischer 2010; Jeffers et al. 2018). This activity level is consistent with its kinematic classification as a thin-disk star (Cortés-Contreras 2016). In the past 20 years several spectra were taken with HIRES (Vogt et al. 1994) on the Keck-I telescope to search for extrasolar planets around it. Using these data, Butler et al. (2017) found a signal at 15.5303 ± 0.0030 d with an amplitude of 3.46 ± 0.56 m s^{-1}, which they listed as a signal requiring confirmation. Contemporaneously to our analysis, Aff19 combined the HIRES RV data from Butler et al. (2017) with high-precision RV data from HARPS (Mayor et al. 2003) and HARPS-N (Cosentino et al. 2012), yielding the detection of a super-Earth orbiting GJ 686. The planetary companion was reported to have a minimum mass of $7.1 \pm 0.9\,\mathrm{M}_{\oplus}$, orbiting its host star with a period of 15.5321 d and a semi-major axis of 0.091 au. Furthermore, they also analyzed the activity indicators of HIRES, HARPS and HARPS-N, from which they estimated a rotation period of 37 d and an activity cycle of ~2000 d.

3.3 Observations

3.3.1 Spectroscopic data

High-resolution spectroscopic observations of both targets were obtained with the VIS and NIR channels of the CARMENES spectrograph. RV were computed by the `serval` pipeline (Zechmeister et al. 2018), which were corrected for systematic RV errors by applying a nightly zero-point correction (Trifonov et al. 2018; Tal-Or et al. 2019). The median magnitude of these corrections are 1.79 m s^{-1} and 1.78 m s^{-1} for the VIS and NIR channel data of LSPM J2116+0234, respectively, and 1.86 m s^{-1} for the VIS channel data of GJ 686. In addition, we also retrieved activity indicators computed by `serval` and from the CCF properties.

LSPM J2116+0234 was monitored between 30 Jun 2016 and 2 May 2019, obtaining 84 high-resolution spectra from each of the CARMENES channels. In total, the observations cover a time span of 1036 d, with typical exposure times of 1800 seconds.

Table 3.2: Basic information of archival and CARMENES spectroscopic observations.

Target	Instrument	N_{obs} (N_{used}) [#]	Δt [d]	*rms* [m s^{-1}]	$\overline{\sigma}$ [m s^{-1}]
LSPM J2116+0234	CARM-VIS	84(79)	1036	5.35	1.48
	CARM-NIR	84(80)	896	8.47	5.49
GJ 686	HIRES	114(112)	5947	4.09	1.85
	CARM-VIS	108(103)	1060	3.19	1.62
	HARPS-N	64(61)	1347	3.02	0.71
	HARPS	20(19)	2299	2.42	0.69

For GJ 686, 108 CARMENES spectra from the VIS channel are available, which were obtained between 22 Feb 2016 and 29 Nov 2018, covering 987 d. Since the internal RV precision of the NIR channel is larger than the expected RV signal of the planet, we decided not to use the NIR RVs. Additionally, as outlined in Aff19, other instruments have monitored GJ 686 during the past 21 years, adding an additional 198 precise RVs. With respect to the original publication by Lalitha et al. (2019), here we used 9 and 25 additional RVs of LSPM J2116+0234 from the VIS and the NIR CARMENES channel, respectively, and 7 new CARMENES RVs of GJ 686, which were gathered and processed after the submission date.

Finally, to avoid using RV epochs contaminated by flares, or spectra with a low SNR, we applied a 3σ clipping to both the RVs and uncertainties of each individual dataset, removing a total of 11 RVs from GJ 686 (3.6%, 7 with large uncertainties and 4 with a large dispersion) and 9 from LSPM J2116+0234 (5.4%, 5 with large uncertainties and 4 with a large dispersion). In general, the discarded CARMENES RVs come from spectra with problems in the wavelength calibration, or with low SNR due to observations under partially cloudy conditions. In Table 3.2, we provide a summary of the total number of available RVs, the time span of the data, standard deviation and median internal uncertainty $\overline{\sigma}$. Figure 3.2 shows the RV time series of both targets. The radial velocities for LSPM J2116+0234 and GJ 686 are listed in Table A.4 and A.5, respectively.

3.3.2 Photometric data

In order to constrain the rotation period of the stars and to search for planetary transits, we searched for photometric time-series from public archives of photometric surveys. For LSPM J2116+0234, we found photometric data from ASAS[1] (Pojmanski 1997), Catalina Sky Survey[2] (Drake et al. 2009), and NSVS[3] (Woźniak et al. 2004). For GJ 686, we found archival photometry from TESS[4] (Ricker et al. 2015) and ASAS. We note here that the light curves from TESS and NSVS were not included in the original publication by Lalitha et al. (2019). Along with the archival photometry, we have monitored GJ 686 with the following facilities:

---

[1] `http://www.astrouw.edu.pl/asas/`

[2] `https://catalina.lpl.arizona.edu`

[3] `https://skydot.lanl.gov/nsvs/nsvs.php`

[4] `https://mast.stsci.edu/portal/Mashup/Clients/Mast/Portal.html`

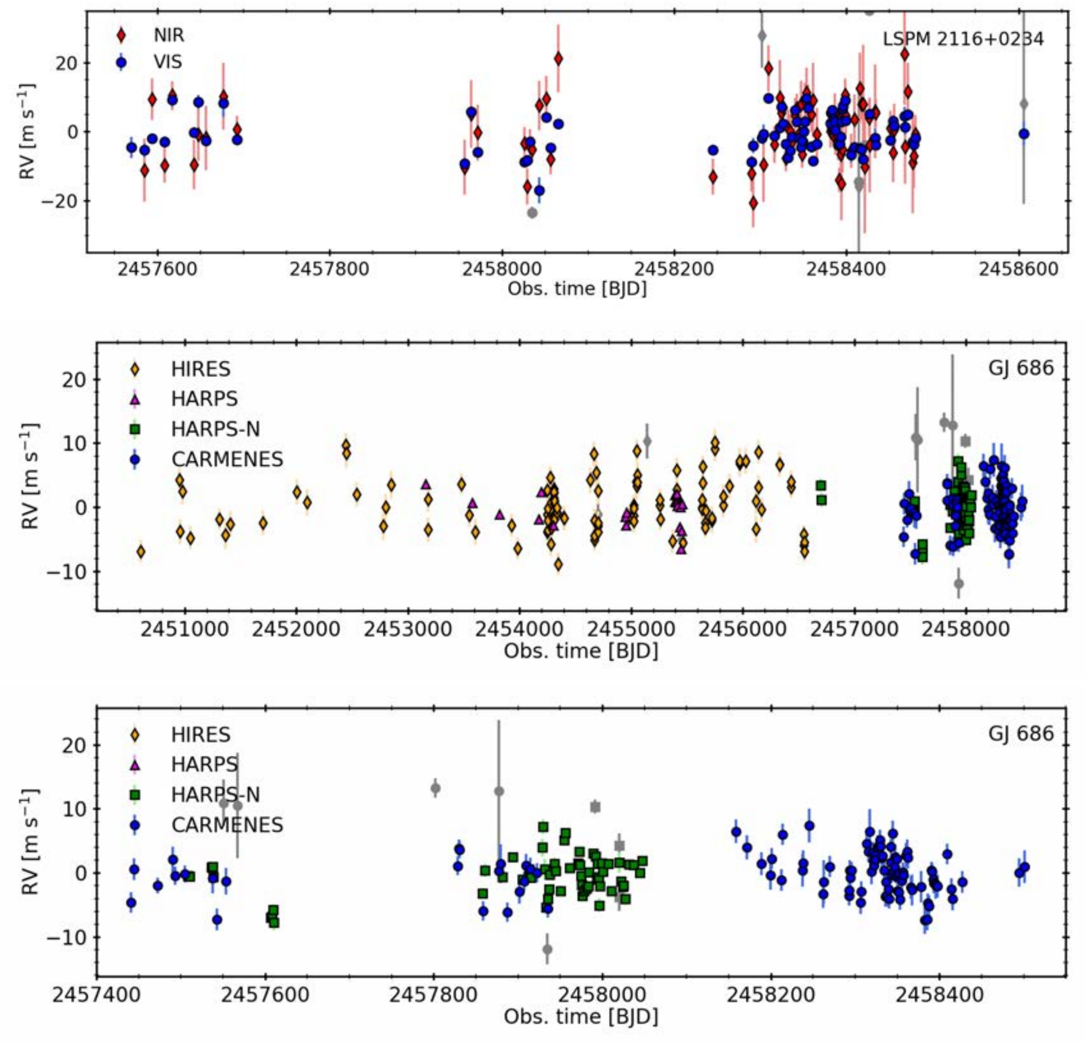

Figure 3.2: RV time series of the M-dwarf stars LSPM J2116+0234 (*top*), GJ 686 (*middle*) and a highlight to the data with JD>2457000 of GJ 686 (*bottom*). The grey symbols correspond to the clipped RVs.

- MONET: the MONET 1.2 m telescope located at the Sutherland station of the South African Astronomical Observatory (SAAO). It is equipped with a 2k × 2k CCD with a plate scale of 0.36 arcsec per pixel.
- OSN: the T90 telescope located at Sierra Nevada Observatory, Spain is a 0.9 m Ritchey-Chrétien telescope. It is equipped with a CCD camera VersArray 2k × 2k with a plate scale of 0.38 arcsec per pixel (Rodríguez et al. 2010).
- TJO: the Joan Oró telescope is located at the Montsec Astronomical Observatory (OAdM), Spain. It is a fully robotic 0.8 m Ritchey-Chrétien telescope equipped with Andor 2k × 2k CCD camera with a plate scale of 0.36 arcsec per pixel.
- LCO: the Las Cumbres Observatory Global Telescope is a network of robotic telescopes deployed at several sites around the globe. The observations were performed using the 0.4 m telescopes in Haleakala, Hawai'i, the Teide Observatory in Tenerife, the McDonald Observatory in Texas, the South African Astronomical Observatory, and the Cerro Tololo

Table 3.3: Basic information of photometric observations.

Target	Instrument	Filter	$N_{\rm obs}$ ($N_{\rm used}$) [#]	Δt [d]	rms [mmag]	$\overline{\sigma}$ [mmag]
LSPM J2116+0234	ASAS	V	388(375)	3 269	48	25
	Catalina	V	268(258)	3 106	160	51
	NSVS	R	147(143)	221	32	11
GJ 686	MONET-S	B	10 225(9 734)	55	5.2	1.5
	OSN	V	713(705)	58	3.9	2.4
	OSN	R	716(710)	58	4.6	3.6
	TJO	R	558(544)	87	12	13
	LCO	B	387(370)	93	5.5	0.7
	LCO	V	1 661(1 603)	93	8.5	1.5
	TESS	T	17 096(17 043)	25	0.65	0.41
	ASAS	V	585(571)	2 397	14	12

Interamerican Observatory. The telescopes have a plate scale of 0.57 arcsec per pixel.

The MONET, TJO and OSN photometric data were reduced and analyzed by CARMENES collaborators with standard packages and tasks of the Image Reduction and Analysis Facility (IRAF[5]). The LCOGT images were reduced by the BANZAI pipeline (McCully et al. 2018). To minimise the effect of possible flares and the systematics, we applied a 3σ clipping to all the photometric data. In Table 3.3, we give a summary of the photometric observations, including the number of photometric epochs before and after (in parentheses) filtering, the time-span (Δt) and scatter (rms) of the data, and the median internal uncertainty ($\overline{\sigma}$).

3.4 Analysis and results

3.4.1 LSPM J2116+0234

To investigate the RV variability of LSPM J2116+0234, we first computed the generalized Lomb-Scargle (GLS) periodogram (Zechmeister et al. 2009) of the RVs from the individual VIS and NIR CARMENES channels and from the combined dataset. In Fig. 3.3a, the resulting periodograms are plotted together with the window function (WF) of the combined dataset (top panel). We computed the false alarm probability (hereafter, FAP) levels of 0.1% using 10 000 bootstrap randomizations of the input data. The signal is considered significant if it reaches a FAP level < 0.1%. The VIS data periodogram (Fig. 3.3a, second panel) displays a significant and isolated signal at 14.451 d (0.0692 d^{-1}), accompanied by the two yearly aliases at ±0.0027 d^{-1} (~365 d) from the central peak, as suggested by the WF. The NIR data, shown in the third panel of Fig. 3.3a also show a signal at 14.455 d (0.0692 d^{-1}), although not significant. Because of the larger errors of the NIR RVs, the periodogram of the combined dataset

---

[5] IRAF is distributed by the National Optical Astronomy Observatory, which is operated by the Association of Universities for Research in Astronomy under a cooperative agreement with the National Science Foundation. `http://iraf.noao.edu/`

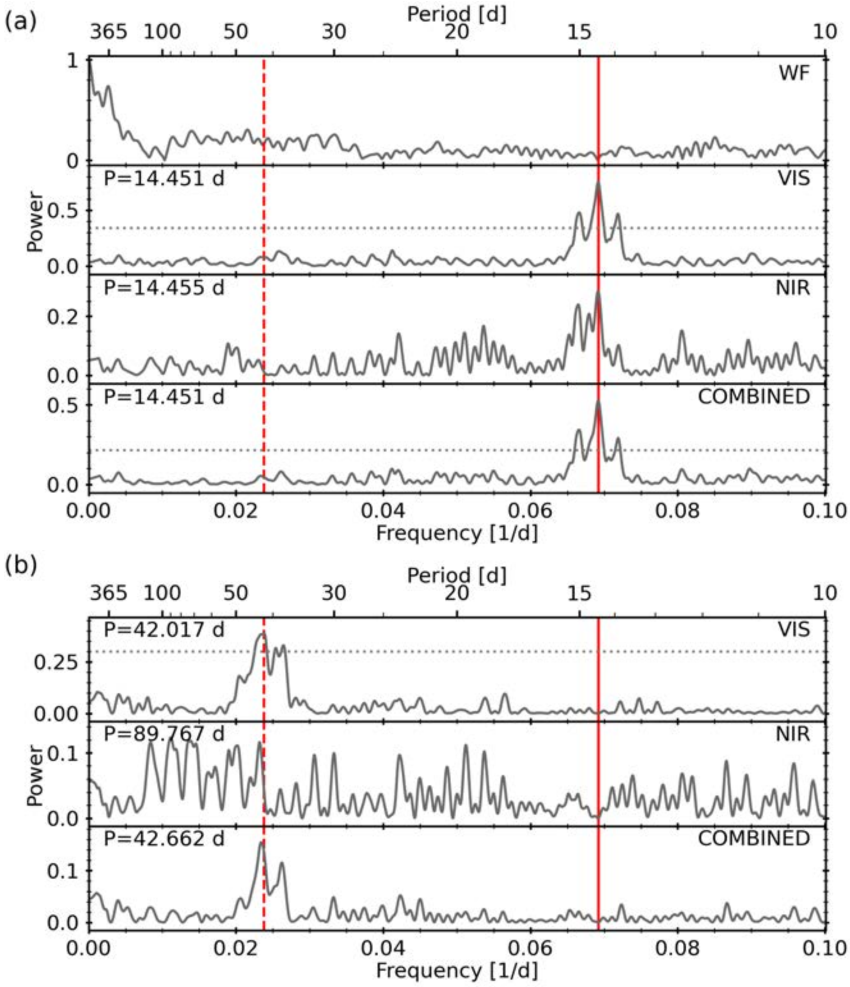

Figure 3.3: (a) GLS periodograms of LSPM J2116+0234 RV data. The top panel shows the WF of the combined dataset. The next two panels correspond to the VIS and the NIR CARMENES channels, respectively, while the bottom panel shows the periodogram of the combined data set. The horizontal line represent the bootstrapped FAP levels of 0.1%. The periods reported in each panel refer to the highest peak. The vertical solid and dashed red lines indicate the period of the proposed planet and the estimated stellar rotation period at 14.45 and ~42 d, respectively. Although we have inspected the periodogram for significant signals at frequencies up to 1 d^{-1}, for visual purposes, we only show the region from 0 to 0.1 d^{-1} in all the periodograms. (b) GLS periodograms of the RV residuals after removing a sinusoid with the period found in (a).

(Fig. 3.3a, bottom panel) is very similar to the periodogram of the VIS channel. The combined periodogram also has a significant peak at 14.451 d. Furthermore, in all three cases we also found prominent signals at a period of 1.07 d, which is the expected period of a daily alias of the 14.451 d signal.

We analyzed the periodograms of the residuals after subtracting the main signal from the RV periodograms to investigate if there are significant RV variations remaining. The residual periodograms are shown in Fig. 3.3b. They show a significant peak in the VIS data at 0.0238 d^{-1} (42.0 d), and the both the NIR and combined data have excess power at 42.7 d, although they do not reach the 0.1% FAP level.

Furthermore, we carried out a periodogram analysis of the activity indicators to investigate if the signals at ∼14.45 d and ~42 d in the RV data may have a stellar origin. Figure 3.4 depicts the GLS periodograms of the dLW, CRX, the Hα, calcium infrared triplet (Ca II IRT a, b and c), and sodium D doublet (Na I D a and b) indices, and the contrast, FWHM and bisector span (BIS) of the CCFs, as introduced in Sect. 1.2.2.2. None of the periodograms show any significant peak at 14.45 d (vertical solid line). The Hα line, as well as two of the calcium lines and the FWHM show significant peaks between 42 and 48 d, which are close to the significant peak in the residual RV periodogram, while the sodium lines have significant peaks at 1 year. In addition, the CRX has excess power at ~42 d. After subtraction of these signals, the residuals do not show any significant peaks in their periodograms at 14.45 d (see Fig. B.1 in the appendix). Thus, we attribute the signals at ~42 d in the RV residuals and the activity indices to be related to the rotation period of the star.

We investigated if there is any significant correlation between the RVs and various activity indicators, as shown in Fig. B.2 in the appendix, but none of the indicators show a correlation above the significance limit, which we set to a p-value of 0.01 or lower. We also observe that there are indicators that despite having significant signals in the periodogram, they show no correlation with the RV, which could be indicative of a shift in phase between the indices and the activity-induced RV.

The analysis of the CARMENES RVs of LSPM J2116+0234 was complemented with almost 15 years of archival photometric data from ASAS, NSVS, and the Catalina Sky Survey. The GLS periodograms of the photometric data are depicted in Fig. 3.5. We do not find any prominent signal in the ASAS photometry, while the NSVS data has a significant signal at 44 ± 4 d with a semi-amplitude of 28 mmag, and the Catalina data at 160 ± 1 d with an semi-amplitude of 73 mmag. After removing this signals, no prominent period can be found in the data at the 14.45 d signal found in the RVs. Additionally, we used the available photometric data to search for a possible planetary transit signature. Given the orbital parameters, the transit probability of LSPM J2116+0234 b is 2.3%, with a transit duration of ∼ 2.7 h. The expected transit depth for a planet of 3 $M_\oplus$ (assuming a 100% water world) is of ∼ 5 mmag, but we did not find any evident transit signature. This result was somewhat expected, given that the expected signal depth is much lower than the dispersion of the lights curves, of 48 mmag, 32 mmag, and 114 mmag for ASAS, NSVS, and Catalina, respectively.

To summarize, based on CARMENES VIS and NIR RV data we identify a strong signal at ∼14.45 d with no counterpart in the activity indicators nor photometric data, which we attribute to a planetary origin. We also find significant signals at ~42 d in the residuals of the RV data. This signal is also significant in some activity indicators and in the NSVS photometric data, and thus we relate it to the rotation period of the star.

3.4.1.1 Radial velocity modeling

Assuming that the strong signal at 14.45 d present in the VIS RVs has planetary origin, we determined the orbital parameters of the signal by fitting a Keplerian model with period (P), semi-amplitude (K), time of periastron passage[6] (T_0), eccentricity (e) and longitude of periastron (ω) through $e\sin\omega$ and $e\cos\omega$, and an RV offset (γ) as free parameters. Furthermore, we also allowed an adjustable RV jitter ($\sigma_{\rm jit}$) in the fit, as defined by Baluev (2009). Since the NIR

---

[6] For a circular orbit, we define it as the time of maximum RV.

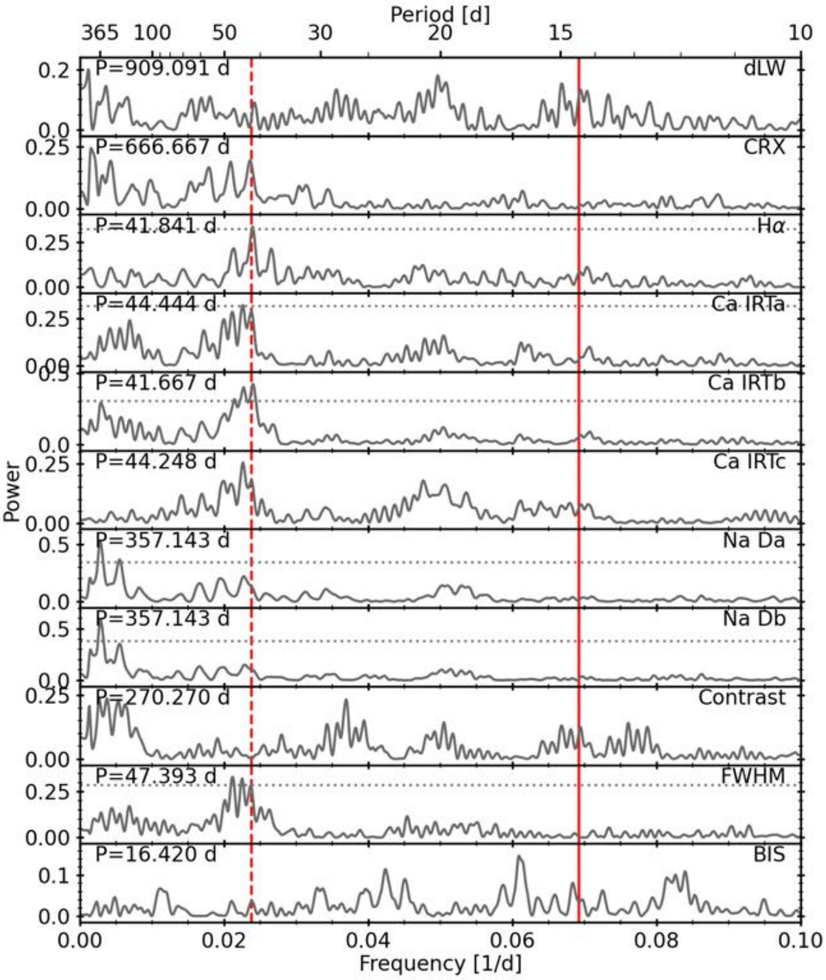

Figure 3.4: GLS periodograms of the activity indicators of LSPM J2116+0234. The vertical red solid line indicates the period of the suggested planet, while the vertical red dotted indicates the stellar rotation period. The periods reported in each panel refer to the highest peak. Horizontal lines represent the bootstrapped 0.1% FAP levels.

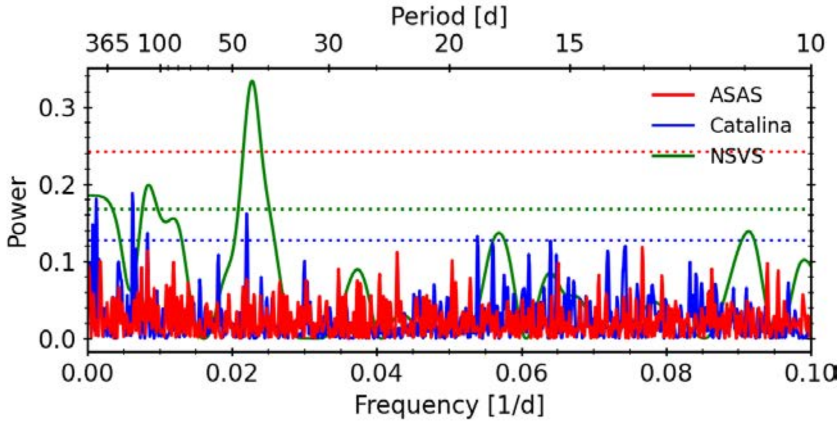

Figure 3.5: GLS periodograms of the ASAS (red), NSVS (blue), and Catalina (green) photometric time series of LSPM J2116+0234. The horizontal dotted lines of each colour indicate the corresponding 0.1 % FAP levels.

Table 3.4: Best-fit parameters to different models of the planetary system LSPM J2116+0234b.

	LSPM J2116+0234 b					
	Null model	Circular	Keplerian	GP + Circular	GP + Keplerian	Prior
Orbital parameters						
P [d]	···	$14.4466^{+0.0090}_{-0.0090}$	$14.4472^{+0.0085}_{-0.0090}$	$14.4483^{+0.0078}_{-0.0082}$	$14.4481^{+0.0071}_{-0.0081}$	$\mathcal{U}(10, 20)$
T_0 [BJD-2457000]	···	$574.19^{+0.43}_{-0.43}$	$573.5^{+1.3}_{-1.2}$	$574.19^{+0.37}_{-0.39}$	$572.86^{+0.85}_{-0.83}$	$\mathcal{U}(550, 590)$
K [m s^{-1}]	···	$5.77^{+0.40}_{-0.39}$	$5.91^{+0.42}_{-0.41}$	$5.80^{+0.37}_{-0.35}$	$6.02^{+0.38}_{-0.40}$	$\mathcal{U}(0, 20)$
$e \sin \omega$	···	0 (fixed)	$-0.041^{+0.077}_{-0.075}$	0 (fixed)	$-0.089^{+0.051}_{-0.047}$	$\mathcal{U}(-1, 1)$
$e \cos \omega$	···	0 (fixed)	$0.142^{+0.066}_{-0.066}$	0 (fixed)	$0.147^{+0.058}_{-0.054}$	$\mathcal{U}(-1, 1)$
RV offsets and jitter						
γ [m s^{-1}]	$0.5^{+3.3}_{-3.0}$	$-0.20^{+0.30}_{-0.30}$	$-0.30^{+0.30}_{-0.29}$	$-0.67^{+0.65}_{-0.64}$	$-0.77^{+0.64}_{-0.67}$	$\mathcal{U}(-100, 100)$
$\sigma_{\rm jit}$ [m s^{-1}]	$2.01^{+0.31}_{-0.28}$	$2.13^{+0.28}_{-0.25}$	$2.08^{+0.28}_{-0.26}$	$0.50^{+0.42}_{-0.34}$	$0.35^{+0.36}_{-0.25}$	$\mathcal{U}(0, 10)$
Hyperparameters						
$K_{\rm QP,VIS}$ [m s^{-1}]	$4.8^{+2.3}_{-1.3}$	···	···	$2.07^{+0.52}_{-0.41}$	$2.09^{+0.54}_{-0.39}$	$\mathcal{U}(0.001, 10)$
$\lambda_{\rm QP}$ [d]	1600^{+4000}_{-1200}	···	···	134^{+95}_{-59}	133^{+89}_{-52}	$\mathcal{U}(5, 500)$
$w_{\rm QP}$	$0.52^{+0.28}_{-0.18}$	···	···	$0.33^{+0.23}_{-0.15}$	$0.34^{+0.19}_{-0.11}$	$\mathcal{U}(0.05, 1)$
$P_{\rm QP}$ [d]	$14.451^{+0.016}_{-0.015}$	···	···	$41.8^{+2.1}_{-1.7}$	$42.7^{+2.0}_{-1.7}$	$\mathcal{U}(10, 60)$
Derived parameters						
e	···	0 (fixed)	$0.167^{+0.062}_{-0.063}$	0 (fixed)	$0.182^{+0.048}_{-0.050}$	···
ω [deg]	···	0 (fixed)	344^{+28}_{-30}	0 (fixed)	329^{+18}_{-18}	···
$a \sin i$ [AU]	···	$0.0876^{+0.0022}_{-0.0021}$	$0.0876^{+0.0022}_{-0.0020}$	$0.0876^{+0.0021}_{-0.0021}$	$0.0876^{+0.0022}_{-0.0020}$	···
$m_{\rm p} \sin i$ [M$_\oplus$]	···	$12.5^{+1.0}_{-1.1}$	$12.6^{+1.0}_{-1.1}$	$12.6^{+1.0}_{-1.0}$	$12.8^{+1.0}_{-1.0}$	···
Fit quality						
$\sigma_{\rm O-C}$ [m s^{-1}]	2.70	2.63	2.54	1.40	1.36	···
$\ln \mathcal{L}$	−202.8	−187.2	−184.8	−169.1	−162.7	···
$\Delta \ln \mathcal{L}$	0	15.6	18.0	33.7	40.1	···

RVs do not show a significant signal at the orbital period in the GLS periodogram, we did not use these data to compute the orbital parameters.

We computed the uncertainties and final orbital parameters by running the Markov Chain Monte Carlo (MCMC) sampler `emcee` (Foreman-Mackey et al. 2013), with the natural logarithm of the model likelihood as the objective function. We run 500 chains of 25 000 steps each, with a burn-in of 20 000. The uncertainties were derived from the 1σ (68.27%) confidence interval of the posterior parameter distribution. We chose uniform priors with conservative ranges as those shown in the last columns in Table 3.4, with a period prior centered at the period found in the GLS periodogram.

The best-model parameters can be found in Table 3.4, for both a circular and an eccentric orbit model, with the corresponding log-likelihood statistic ($\ln \mathcal{L}$), which is the probability distribution of the data fitting the model and depends on the adopted noise model (see e.g. Baluev 2013). All the orbital parameters obtained with the two models are compatible within their respective uncertainties. The best fit parameters of the eccentric model yield a period of $14.4472^{+0.0085}_{-0.0090}$ d with an eccentricity of $0.167^{+0.062}_{-0.063}$ and an RV semi-amplitude of $5.91^{+0.42}_{-0.41}$ m s^{-1}. Given the mass of the host star, of 0.430 ± 0.017 M$_\oplus$, these orbital parameters correspond to a planet with a minimum mass of $12.6^{+1.0}_{-1.1}$ M$_\oplus$.

To check that the planetary signal found in the VIS RVs is consistent with the NIR data, we fixed all the parameters to the orbital parameters found for the Keplerian model (fourth column in

Table 3.4) except for the semi-amplitude, the RV offset and the jitter term, which were sampled with an MCMC. We obtain an RV semi-amplitude of $4.7 \pm 1.0\,\mathrm{m\,s^{-1}}$, which is compatible with the value found from the VIS RVs within mutual uncertainties.

To test the statistical significance of the eccentric model over the circular model, we used the likelihood ratio statistic. In the case of a nested model, that is, when one model is a special case of the other, as in this case, the likelihood ratio asymptotically behaves as (Wilks 1938):

$$\ln\left(\frac{\mathcal{L}_{\mathrm{Keplerian}}}{\mathcal{L}_{\mathrm{Circular}}}\right) = \Delta\ln\mathcal{L} = \frac{\chi_p^2}{2} \tag{3.1}$$

where p is the difference in free parameters between the two models. Therefore, the difference in $\Delta\ln\mathcal{L}$ of 2.8 indicates that the eccentric model is preferred over the circular one with a significance of 93% ($\sim 2\sigma$).

We also tested if there are other possible models explaining the data, apart from the planetary hypotesis. To do so, we evaluated the statistical significance of our models by computing the improvement in $\Delta\ln\mathcal{L}$ with respect to a null model. We note here that in this case we cannot approach the likelihood ratio test as a χ^2 distribution, since the tested models are not nested. For our null model, we assume that the observed variability is only produced by correlated noise coming from stellar activity, and we model it using a GP, an RV offset, and a jitter term. Rasmussen & Williams (2005) described many different covariance functions governing a GP (see Sect 1.3 for more details), among which the quasi-periodic kernel has been widely used to disentangle planetary signals from stellar activity signals (Haywood et al. 2014; Mortier et al. 2018; Perger et al. 2019) or even to infer stellar rotation periods (Angus et al. 2018). As defined in Eq. (1.30), this kernel is characterized by four hyperparameters: (1) the output-scale amplitude, K_{QP}, which contains the amplitude of the RV variations due to the activity and information about the filling factor of the star, (2) the decay time, λ_{QP}, which is related to the lifetime of the active regions, (3) the smoothing parameter, w_{QP}, which controls the high-frequency noise, and may be related to the number of spots and/or facule in the photosphere, and (4) the periodicity of the correlations, P_{QP}, which is interpreted as the rotation of the star (Perger et al. 2021a). Another kernel that was used in the original publication by Lalitha et al. (2019), and whose results we do not reproduce in this work, is the simple harmonic oscillator implemented in `celerite` (Foreman-Mackey et al. 2017). The reason for not including these results in this work is the recent advise by Perger et al. (2021a) against using this kernel when studying correlations caused by stellar activity, given the unreliable estimates of the rotation period and the lower quality fits obtained with this kernel.

The GP models with the quasi-periodic kernel are implemented using the `george` python library (Ambikasaran et al. 2015). All the parameters have been optimized simultaneously, and their solutions and uncertainties have been computed from the MCMC posterior distribution. We choose a uniform prior for the periodic component P_{QP} ranging from 10 d to 60 d, covering the two significant signals found in the periodogram. We consider a model as tentative or as statistically significant over the null model if it reaches a FAP level of 1% or 0.1%, respectively. These values corresponds to $\Delta\ln\mathcal{L}$=15.1 and 18.7, which are computed from a bootstrap randomization of 5000 permutations of the datapoints.

The best-fit parameters of the null model are shown in the second column of Table 3.4. We obtained a periodicity of $P_{\mathrm{QP}} = 14.451^{+0.016}_{-0.015}$ d, and a decay time larger than the time span of the data, indicating the long-term stability of this signal. We take the best-fit $\ln\mathcal{L}$, of −202.8, as the base value to compute the $\Delta \ln \mathcal{L}$ of the other models in Table 3.4. With a value of $\Delta \ln \mathcal{L} = 18.0$, we obtain that the eccentric model is just above the significance threshold of 0.1%.

Additionally, we investigated the influence of the activity-induced RV variations on the determination of the orbital parameters by modeling together a Keplerian orbit and an activity term defined by the same GP model used in the null model. The best fit parameters of the activity plus Keplerian model, using both a circular and an eccentric orbit, are listed in the fifth and sixth columns of Table 3.4, respectively. The orbital parameters in both cases are very similar to the values obtained with the respective models without the GP term. We note that all the parameters agree within 1σ uncertainties, except for the jitter terms, which are smaller. This is expected since we are adding an extra term modeling the activity, which was previously absorbed by the jitter term. A drastic reduction of the dispersion of the residuals with respect to the null model and the planet models is also observed. We note that the eccentric model with activity term is significantly favoured over the null model and over the eccentric model alone, with a $\Delta \ln \mathcal{L}$ of 40.1 and 22.1, respectively. Also, as done for the models without GP terms, we can use the likelihood ratio between the eccentric and circular models to asses their statistical significance through Eq. (3.1). With a $\Delta \ln \mathcal{L}$ of 6.4, the eccentric model is preferred over the circular one with a significance of 99.8% (3σ). We therefore conclude that the model that is better explaining the observed data is the activity plus eccentric orbit model.

The best orbital parameters of the activity plus eccentric model correspond to an orbital period of $14.4481^{+0.0071}_{-0.0081}$ d with an eccentricity of $0.182^{+0.048}_{-0.050}$ and a RV semi-amplitude of $6.02^{+0.38}_{-0.40}\,\mathrm{m\,s^{-1}}$, which is slightly larger but compatible with that obtained with the Keplerian model alone. The orbital parameters yield a minimum mass for the planet of $12.8^{+1.0}_{-1.0}\,\mathrm{M}_{\odot}$. As for the GP hyperparameters, we find an amplitude of the activity-induced RV variations of $2.09^{+0.54}_{-0.39}\,\mathrm{m\,s^{-1}}$, and a decay time of 133^{+89}_{-52} d. Although we used a broad prior to sample the periodicity, we obtain $\mathrm{P_{QP}} = 42.7^{+2.0}_{-1.7}$ d, which is very similar to the periodicities found in the activity indicators, photometry, and RV residuals. Hence, we consider the period of ~42 d as the rotation period of the star. The top panel in Fig. 3.6 shows the best-fitting activity plus Keplerian model to the RVs on a densely sampled region, for clarity. We also show the GP contribution to the fit with a clear periodic modulation of 42.7 d and an amplitude of $\sim 2\,\mathrm{m\,s^{-1}}$. The two bottom panels show the Keplerian part of the model as a function of the orbital phase, before (left) and after (right) the GP model is subtracted from the data. The histograms of the posterior distribution (see Fig. B.3 in the appendix) suggest that all the orbital parameters follow a well behaved normal distribution, except for the expected correlation between T_0 and $e \sin \omega$ and $e \cos \omega$ due to their proximity to the degenerate solution at zero eccentricity, and the log-normal distributions of some hyperparameters.

Finally, to provide more evidence against a potential activity-induced origin of the signals, we checked the stability of the signal throughout the wavelength range covered. We used the RVs from each spectral order of CARMENES to compute the RV semi-amplitude and uncertainties of a Keplerian orbit with P, T_0, e, ω, and GP hyperparameters fixed to the best solution listed in the sixth column in Table 3.4. We estimated the value of K and their uncertainties from the final posterior distribution of an MCMC sample of 500 walkers and 1000 steps. In Fig. 3.7, we show the resulting semi-amplitude of the eccentric orbit as a function of the logarithm of the wavelength at the center of each CARMENES order. All the values are consistent within 2σ of the semi-amplitude found with the RVs of all the orders combined. Further, we do not see a decrease in amplitude toward longer wavelength, as would be expected if the signal is activity-induced (Desort et al. 2007). Therefore, we conclude that the signal at the ~14.45 d period in

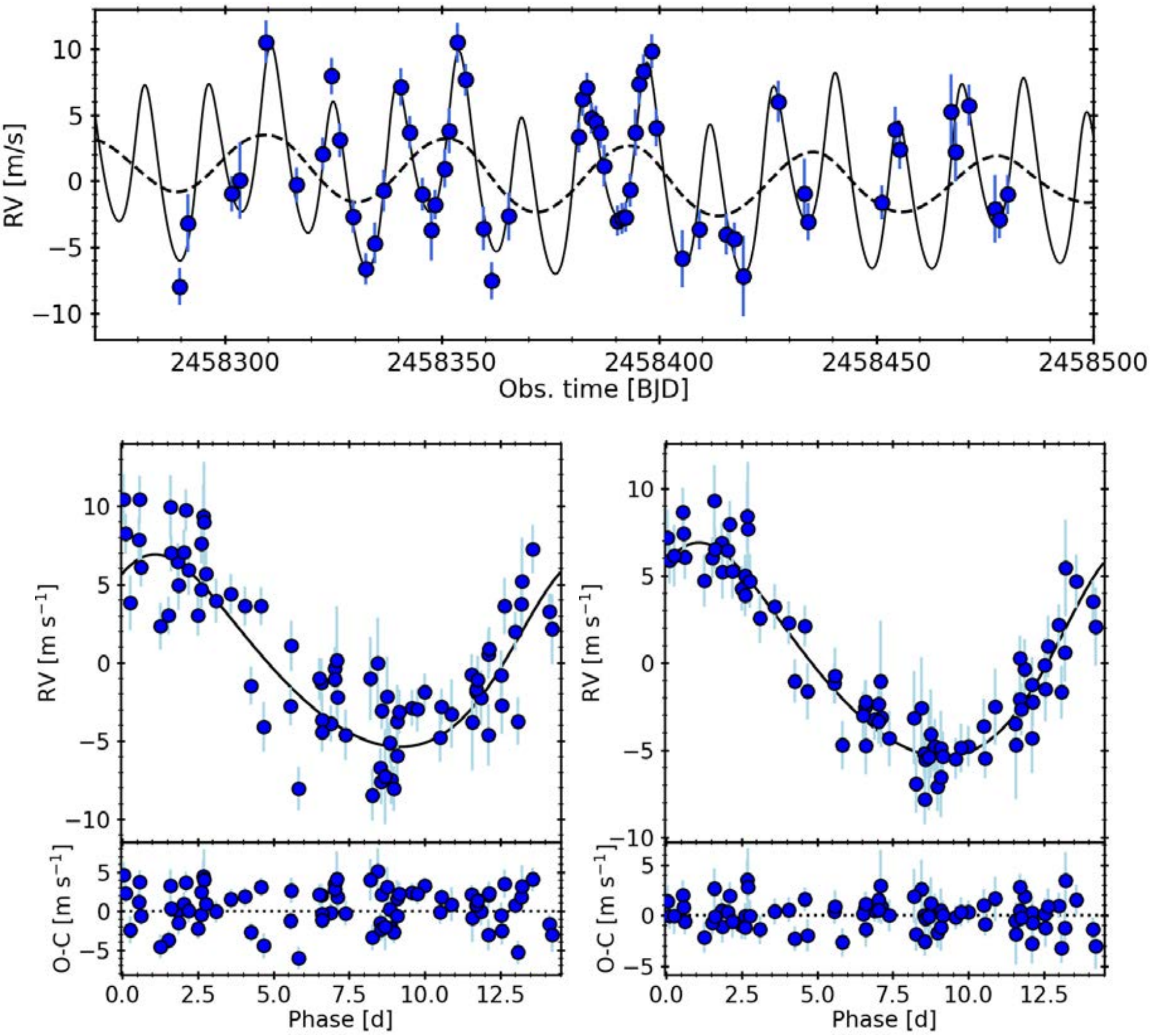

Figure 3.6: *Top*: highlight of a densely sampled region of the CARMENES RVs of LSPM J2116+0234. The solid line correspond to the best orbital and activity model. The dotted line illustrates only the contribution of the GP model. *Bottom*: RVs of LSPM J2116+0234 as a function of the orbital phase, along with the Keplerian part of the model before (*left*) and after (*right*) the GP model is subtracted from the data.

LSPM J2116+0234 is consistent with the planet hypothesis.

3.4.2 GJ 686

We computed the GLS periodograms of the HIRES, HARPS, HARPS-N and CARMENES RV measurements of GJ 686 to investigate its variability. Figure. 3.8a (top to bottom) shows the WF of the combined dataset, the periodograms of the HIRES, HARPS, HARPS-N, and CARMENES RVs, and of all data combined. We subtracted the mean value of each RV dataset to compute the periodogram of the combined dataset. The horizontal dotted line indicates the 0.1% bootstrapped FAP level.

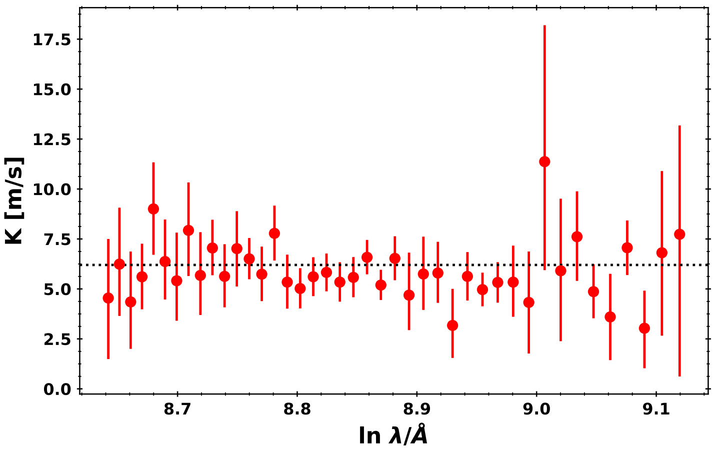

Figure 3.7: Semi-amplitude of a Keplerian orbit fit to the RVs from individual echelle orders of LSPM J2116+0234, as a function of the logarithm of the wavelength at the center of the order. The black dotted line indicates the semi-amplitude found when using the RVs from the entire VIS channel.

Except for HARPS, all the instruments have the strongest signal at a period of 15.5 d with FAP $< 0.1\%$. The HARPS dataset shows a non-significant signal around 16.0 d, although we also notice an excess power at ~15.5 d. The periodogram of the combined dataset has a highly significant signal at 15.53 d (0.06439 d^{-1}). We notice an additional peak at 16.22 d (0.06165 d^{-1}) with high significance, owing to one yearly alias of the main signal, which is clearly observed in the WF.

Signals at ~49 d in HIRES, at ~ 37 d in HARPS-N, and at ~41 d in the combined datasets become significant once the main signal is removed, as shown in Fig. 3.8b. Further subtracting these signals of the residuals, the combined dataset shows two non-significant signals at ~120 d and ~1100 d. These signals were detected at the 1% FAP level by Lalitha et al. (2019), speculating that they could be produced either by a long term activity cycle or an offset mismatch between datasets, or by a long period planet. With the addition of new CARMENES data in this work, the signals are now above the 10% FAP level, and therefore are not significant anymore (see Fig. B.4 in the appendix).

Further, we searched for periodic signals in the GLS periodograms of the CARMENES activity indicators and photometric data, in order to investigate the possibility of the periodic RV variations being produced by stellar activity. As before, we consider a signal to be significant when it reaches a FAP below the 0.1% level. We show the resulting GLS periodograms of the activity indicators and the properties of the CCFs in Fig. 3.9. There are several activity indicators with significant signals, among which there is a recurrence of signals between 36 and 40 d. However, neither of the activity indices show any significant signals at or near 15.53 d. The detected periods are in agreement with those previously reported by Aff19 while we were working in the analysis of this system. In particular, they found significant signals at 37 and 45 d in the Hα data from HARPS-N and HIRES, respectively, and a significant signal at 38 d in the S-index from HIRES, which is a measure of the flux in the Ca II H and K lines. Furthermore, most of the activity indices during the last ~100 d of CARMENES observations also present a modulation of the signals at ~38 d (see Fig. B.6 in the appendix). The modulation may be caused by an epoch of high stellar activity. Additionally, we also see significant signals in the CRX at 365 d caused by a combination of the WF and a long-period trend. The GLS periodograms of the residuals of

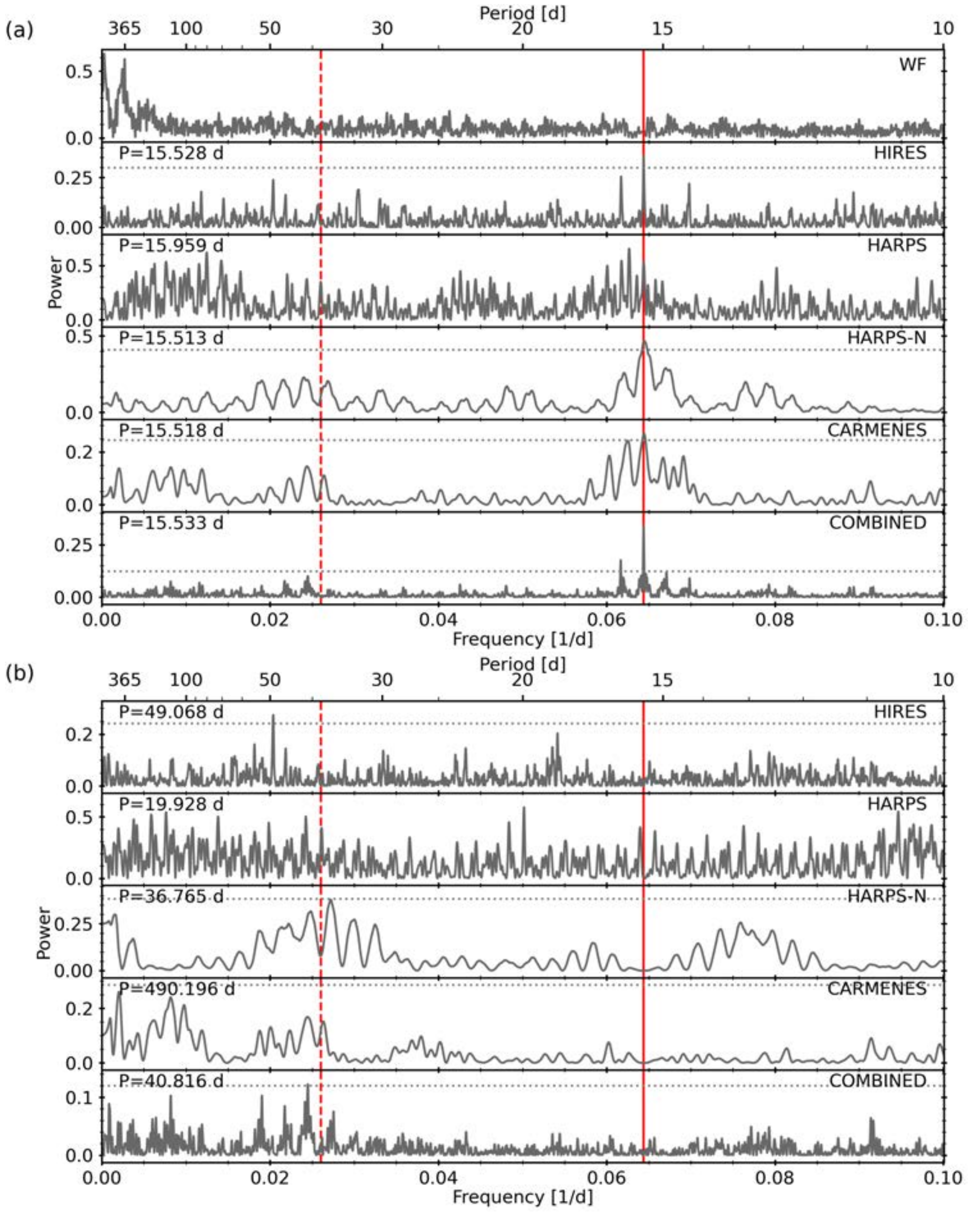

Figure 3.8: (a) GLS periodograms of GJ 686 RV data. The top panel shows the WF of the combined dataset. The next four panels represent the HIRES, HARPS, HARPS-N, and CARMENES data, respectively, and the bottom panel shows the periodogram of the combined dataset. The periods reported in each panel refer to the highest peak. Horizontal dotted lines represent the bootstrapped FAP level of 0.1%. The vertical solid and dashed red lines indicate the period of the proposed planet and estimated stellar rotation period at 15.53 and ~38 d, respectively. (b) GLS periodograms of the RV residuals after removing a sinusoid with the period found in (a).

the activity indicators (Fig. B.5 in the appendix), only show significant signals at long periods in Hα, and a signal just above the 0.1% FAP in the CRX. We further investigate the correlations between several activity indicators and the RV (see Fig. B.8 in the appendix). Although none of the indicators have a significant correlation with RV (absolute p-value below 0.01), in some indicators we observe a concentration of measures with a similar phase (similar colours), which may be due to a phase shift between the indicators and the RVs (Perger et al. 2019). Given that the signals at ~38 d are present in both RV and activity indicators, we attribute this variability to the stellar rotation period.

To further investigate the stellar rotation period of GJ 686 we performed GLS periodograms to the available photometric data and show them in Fig. 3.10. All photometric time series except ASAS have peaks below the 0.1 % FAP threshold. We obtain significant signals at 34^{+19}_{-7} d (MONET, amplitude of 4.0 mmag), 30^{+5}_{-6} d (TJO, amplitude of 11.1 mmag), 24^{+7}_{-6} d (OSN-R, amplitude of 2.0 mmag), 58^{+18}_{-8} (LCO-B, amplitude 2.7 mmag), and 64^{+23}_{-11} (LCO-V, amplitude 5.5 mmag). As seen in the periodogram, the photometric data from the V-band of OSN and from TESS only impose lower limit periods of 25 d and 17 d, respectively. The disparity in their periodicities and amplitudes, which are much larger than the TESS dispersion, of 0.6 mmag, may be an indication of either an evolution of stellar variability or that the signals have different and not clear natures. Therefore, we cannot conclude that the rotation signal of GJ 686 is detected in its photometric data.

As a summary, based on the signals found in the activity indicators, the rotation period of the star most likely lies within the range 36–40 d. Further, we have not found any significant and recurrent signal at ~15.53 d in the activity indicators or photometry. Therefore, this signal is probably not produced by stellar activity, and might have a planetary origin.

3.4.2.1 Radial velocity modeling

Assuming a planetary origin of the 15.5 d signal, we fit a Keplerian and a circular orbit model to the combined RVs. We computed the orbital parameters and uncertainties using an MCMC to infer the posterior distribution of the fitted parameters. The best-fit orbital parameters and their uncertainties are shown in the fourth and fifth column of Table 3.5, respectively, and in the last column we show the priors used, which in all cases consisted in conservative uniform priors, with the period centered around the signal found in the RV periodogram. As we have done for LSPM J2116+0234, we can asses the statistical significance of adding eccentricity to the model by computing the likelihood ratio statistic, which is $\Delta \ln \mathcal{L} = 0.1$. From this value, the circular model is favoured over the eccentric model with a significance of 90%. The final parameters of the circular orbit give a planet with a period of $15.5309^{+0.0016}_{-0.0015}$ d, which produces an RV semi-amplitude of $2.77^{+0.23}_{-0.22}$ m s^{-1}. Using the stellar mass given in Table 3.1, we derive a minimum planet mass of $m_p \sin i = 6.06^{+0.51}_{-0.53}$ M$_\oplus$.

As for the case of LSPM J2116+0234 (see Sect. 3.4.1.1), we defined our null model using a GP with a quasi-periodic kernel to account for the presence of correlated noise, and used it to evaluate the statistical significance of our models. We modeled the RVs of each instrument with separate GPs, sharing all the parameters except the amplitude $K_{\rm QP}$ describing the activity-induced variations, which should be different for instruments working in different wavelength ranges. Since HARPS and HARPS-N work in the same wavelength range, we modeled their RVs with the same amplitude $K_{\rm QP,HARPS}$.

The null model solution for GJ 686 is listed in the third column of Table 3.5. The best-fit null model yields a periodicity of $31.66^{+0.77}_{-0.83}$ d which is the second harmonic of the periodogram signal at 15.5 d, and we obtain a time decay $\lambda_{\rm QP}$ of $33.2^{+6.8}_{-5.6}$, meaning that the fitted signals are not stable in the long term. The best solution yields a $\ln \mathcal{L}$ of −714.7, which we use as a reference to compare the $\Delta \ln \mathcal{L}$ against other models. For this star, the $\Delta \ln \mathcal{L}$ corresponding to a FAP of 1% and 0.1% are 13.4 and 17.4, respectively, as computed from a bootstrap randomization

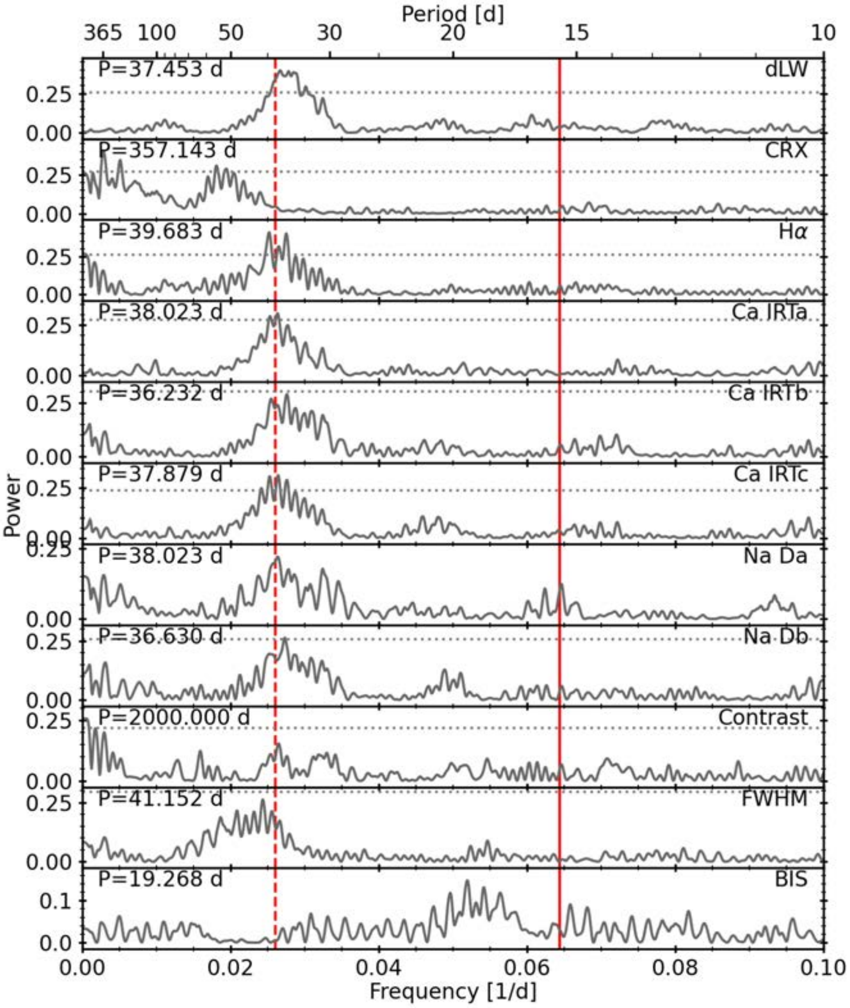

Figure 3.9: GLS Periodograms of the CARMENES activity indicators of GJ 686. The vertical solid line indicates the period of the suggested planet, while the vertical red dotted line marks the period attributed to the rotation. The periods reported in each panel refer to the highest peak. Horizontal dotted lines represent the bootstrapped 0.1% FAP level.

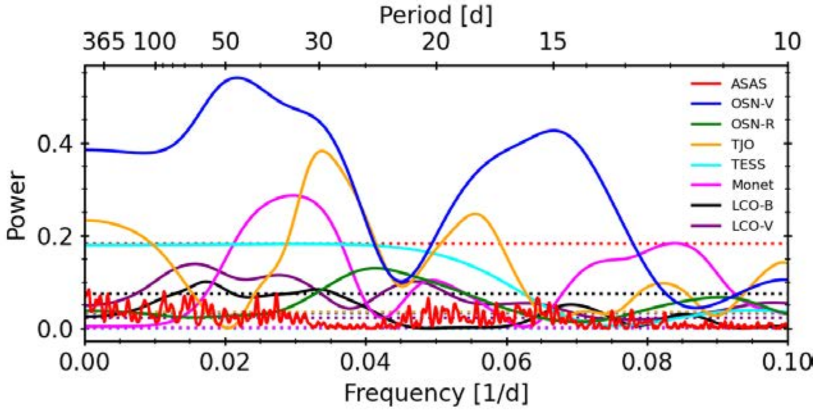

Figure 3.10: GLS periodograms of the ASAS (red), OSN (V-band in blue, R-band in green), TJO (orange), TESS (cyan), and MONET (magenta) photometric time series of GJ 686. The horizontal dotted lines of each colour indicate the corresponding 0.1 % FAP levels.

Table 3.5: Best-fit parameters to different models of the planetary system Gl 686 b.

	Gl 686 b						
	Aff19	This work					
	GP + Circular	Null model	Circular	Keplerian	GP + Circular	GP + Keplerian	Prior
Orbital parameters							
P [d]	$15.5321^{+0.0017}_{-0.0017}$	···	$15.5309^{+0.0016}_{-0.0015}$	$15.5306^{+0.0018}_{-0.0017}$	$15.5315^{+0.0014}_{-0.0015}$	$15.5311^{+0.0014}_{-0.0014}$	$\mathcal{U}(10, 20)$
T_0 [JD-2450000]	$7805.69^{+0.28}_{-0.28}$	···	$610.90^{+0.62}_{-0.62}$	$606.6^{+2.3}_{-2.1}$	$610.58^{+0.63}_{-0.61}$	$606.5^{+1.4}_{-1.5}$	$\mathcal{U}(585, 625)$
K [m s^{-1}]	$3.29^{+0.31}_{-0.32}$	···	$2.76^{+0.23}_{-0.23}$	$2.77^{+0.23}_{-0.22}$	$2.94^{+0.20}_{-0.20}$	$2.97^{+0.20}_{-0.20}$	$\mathcal{U}(0, 20)$
$e \sin \omega$	···	···	···	$-0.092^{+0.066}_{-0.079}$	···	$-0.118^{+0.055}_{-0.058}$	$\mathcal{U}(-1, 1)$
$e \cos \omega$	···	···	···	$-0.025^{+0.082}_{-0.077}$	···	$-0.015^{+0.057}_{-0.061}$	$\mathcal{U}(-1, 1)$
RV offsets and jitter							
$\gamma_{\rm HIRES}$ [m s^{-1}]	$0.65^{+0.52}_{-0.49}$	$-0.31^{+0.60}_{-0.61}$	$0.42^{+0.32}_{-0.31}$	$0.41^{+0.33}_{-0.32}$	$0.54^{+0.57}_{-0.53}$	$0.59^{+0.56}_{-0.57}$	$\mathcal{U}(-100, 100)$
$\gamma_{\rm HARPS}$ [m s^{-1}]	$-0.33^{+0.60}_{-0.61}$	$0.20^{+0.84}_{-0.83}$	$-0.64^{+0.42}_{-0.42}$	$-0.72^{+0.44}_{-0.42}$	$-0.13^{+0.61}_{-0.64}$	$-0.18^{+0.65}_{-0.64}$	$\mathcal{U}(-100, 100)$
$\gamma_{\rm HARPS-N}$ [m s^{-1}]	$-0.41^{+0.53}_{-0.63}$	$-0.08^{+0.71}_{-0.78}$	$-0.33^{+0.29}_{-0.29}$	$-0.29^{+0.28}_{-0.29}$	$-0.67^{+0.61}_{-0.68}$	$-0.62^{+0.63}_{-0.64}$	$\mathcal{U}(-100, 100)$
$\gamma_{\rm CARM}$ [m s^{-1}]	···	$-0.47^{+0.64}_{-0.65}$	$-0.18^{+0.27}_{-0.27}$	$-0.18^{+0.27}_{-0.27}$	$-0.62^{+0.65}_{-0.63}$	$-0.63^{+0.67}_{-0.68}$	$\mathcal{U}(-100, 100)$
$\sigma_{\rm jit,HIRES}$ [m s^{-1}]	$0.51^{+0.47}_{-0.35}$	$0.60^{+0.52}_{-0.42}$	$2.82^{+0.29}_{-0.26}$	$2.85^{+0.29}_{-0.27}$	$0.64^{+0.46}_{-0.42}$	$0.66^{+0.47}_{-0.43}$	$\mathcal{U}(0, 10)$
$\sigma_{\rm jit,HARPS}$ [m s^{-1}]	$0.67^{+0.46}_{-0.41}$	$0.96^{+0.70}_{-0.55}$	$1.67^{+0.39}_{-0.30}$	$1.70^{+0.44}_{-0.30}$	$0.76^{+0.44}_{-0.38}$	$0.89^{+0.47}_{-0.40}$	$\mathcal{U}(0, 10)$
$\sigma_{\rm jit,HARPS-N}$ [m s^{-1}]	$1.44^{+0.29}_{-0.26}$	$0.95^{+0.29}_{-0.29}$	$2.10^{+0.24}_{-0.21}$	$2.05^{+0.24}_{-0.21}$	$1.10^{+0.25}_{-0.23}$	$1.07^{+0.22}_{-0.22}$	$\mathcal{U}(0, 10)$
$\sigma_{\rm jit,CARM}$ [m s^{-1}]	···	$0.61^{+0.34}_{-0.37}$	$2.13^{+0.26}_{-0.24}$	$2.14^{+0.25}_{-0.24}$	$0.63^{+0.32}_{-0.37}$	$0.59^{+0.33}_{-0.36}$	$\mathcal{U}(0, 10)$
Hyperparameters							
$K_{\rm QP,HIRES}$ [m s^{-1}]	$3.16^{+0.44}_{-0.40}$	$4.00^{+0.51}_{-0.43}$	···	···	$3.20^{+0.49}_{-0.43}$	3.24^{+49}_{-43}	$\mathcal{U}(0.001, 10)$
$K_{\rm QP,HARPS}$ [m s^{-1}]	$1.76^{+0.31}_{-0.28}$	$2.69^{+0.37}_{-0.31}$	···	···	$1.69^{+0.33}_{-0.28}$	$1.70^{+0.33}_{-0.29}$	$\mathcal{U}(0.001, 10)$
$K_{\rm QP,CARM}$ [m s^{-1}]	···	$2.83^{+0.42}_{-0.38}$	···	···	$2.26^{+0.43}_{-0.35}$	$2.25^{+0.45}_{-0.35}$	$\mathcal{U}(0.001, 10)$
$\lambda_{\rm QP}$ [d]	23^{+31}_{-18}	$33.2^{+6.8}_{-5.6}$	···	···	39^{+11}_{-9}	41^{+11}_{-9}	$\mathcal{U}(5, 500)$
$w_{\rm QP}$	$0.48^{+0.31}_{-0.18}$	$0.311^{+0.050}_{-0.047}$	···	···	$0.53^{+0.16}_{-0.13}$	$0.55^{+0.16}_{-0.13}$	$\mathcal{U}(0, 1)$
$P_{\rm QP}$ [d]	$37.0^{+5.5}_{-14.6}$	$31.66^{+0.77}_{-0.83}$	···	···	$37.9^{+2.3}_{-1.6}$	$38.2^{+2.9}_{-1.6}$	$\mathcal{U}(10, 60)$
Derived parameters							
e	···	···	···	$0.126^{+0.055}_{-0.070}$	···	$0.134^{+0.050}_{-0.055}$	···
ω	···	···	···	263^{+41}_{-55}	···	264^{+29}_{-27}	···
$a \sin i$ [AU]	0.091 ± 0.004	···	$0.0917^{+0.0012}_{-0.0012}$	$0.0917^{+0.0012}_{-0.0012}$	$0.0917^{+0.0012}_{-0.0012}$	$0.0917^{+0.0012}_{-0.0012}$	···
$m_{\rm p} \sin i$ [M$_\oplus$]	7.1 ± 0.9	···	$6.09^{+0.51}_{-0.53}$	$6.06^{+0.51}_{-0.53}$	$6.50^{+0.47}_{-0.47}$	$6.50^{+0.46}_{-0.47}$	···
Fit quality							
σ_{O-C} [m s^{-1}]	···	1.23	2.87	2.88	1.48	1.43	···
$\ln \mathcal{L}$	···	−714.7	−715.4	−715.3	−664.1	−662.2	···
$\Delta \ln \mathcal{L}$	···	0	−0.7	−0.6	50.6	52.5	···

of 5000 permutations of the input data. The obtained $\Delta \ln \mathcal{L}$ of the models only fitting a planet are negative and close to zero. This means that the null model is preferred over the only-planet models, and may be indicating that the activity-induced signal has an amplitude comparable to that produced by the planet.

To disentangle the two terms, we jointly modeled the planetary signal and the activity term of GJ 686 for both the circular and eccentric cases, using a GP with a quasi-periodic function as the covariance matrix of the activity term. We list the best-fit orbital parameters to the models in the sixth and seventh column of Table 3.5. The $\Delta \ln \mathcal{L}$ values with respect their respective models without the activity term are 51.3 and 53.2 for the circular and eccentric cases, and 50.6 and 52.5 with respect the null model, respectively. All the values are well below the 0.1% FAP level, justifying the jointly modeling of planet and activity in both cases. Regarding the addition of eccentricity, the $\Delta \ln \mathcal{L}$ between both models, of 1.9, favours the eccentric model with a 85% significance.

With a period of 15.5311 ± 0.0014 d, the planetary signal has an eccentricity of $0.134^{+0.050}_{-0.055}$ and an RV semi-amplitude of 2.97 ± 0.20 m s^{-1}, which is slightly lower than the amplitude found in

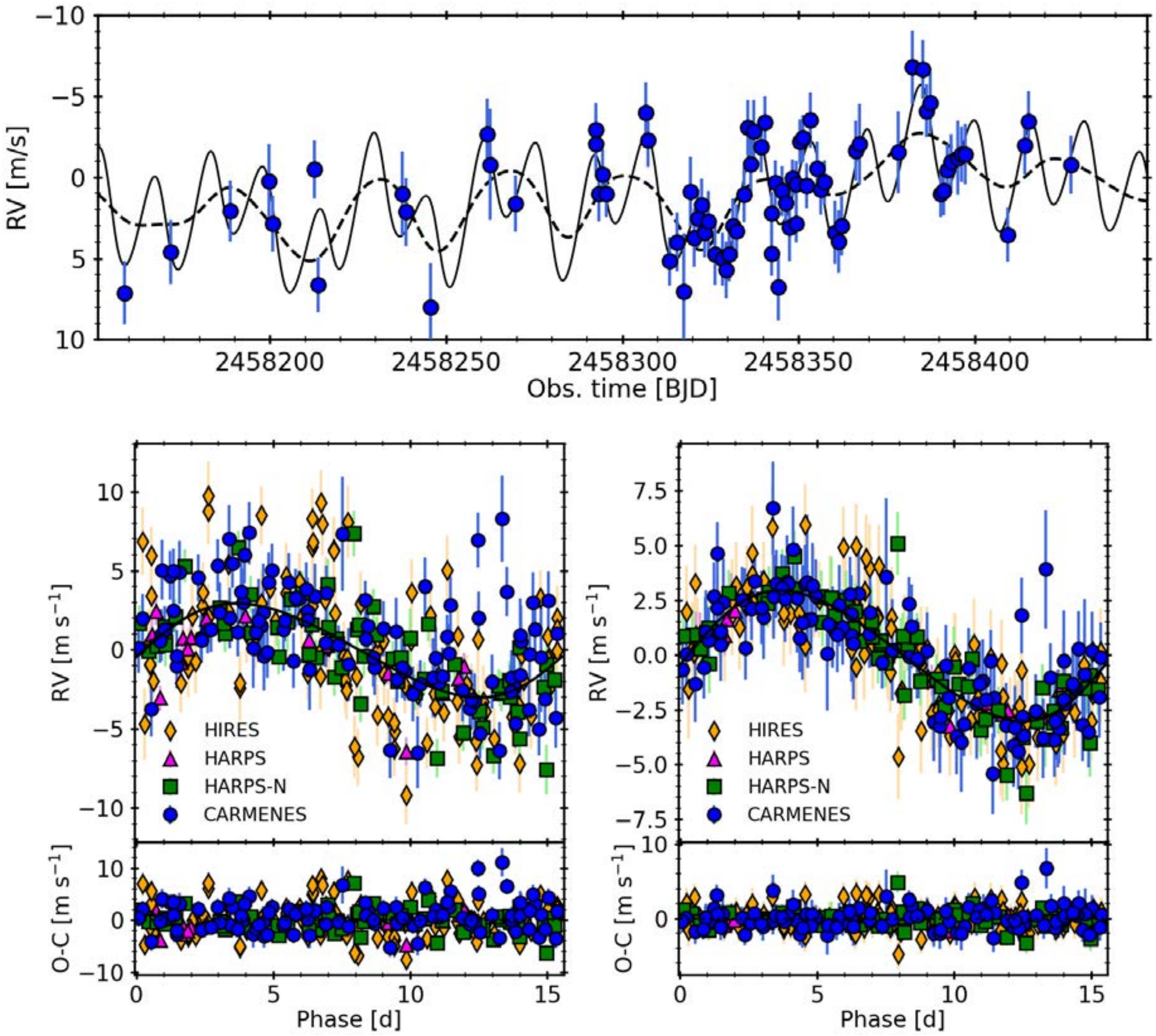

Figure 3.11: *Top*: highlight of a densely sampled region of the CARMENES RVs of GJ 686. The solid line correspond to the best orbital and activity model. The dotted line illustrates only the contribution of the GP model. *Bottom*: RVs of GJ 686 from HIRES, HARPS, HARPS-N, and CARENES, as a function of the orbital phase, along with the Keplerian part of the model before (*left*) and after (*right*) the GP model is subtracted from the data.

Aff19, but consistent within the mutual uncertainties. Consequently, we also derived a smaller minimum mass of $6.50 \pm 0.47\,M_{\oplus}$. All the other orbital parameters are consistent within the respective uncertainties. As it happened for LSPM J2116+0234, the obtained planetary minimum masses are larger for the joint model than for the only-planet model, which is an indication that the presence of stellar activity may bias the derived parameters. We found a strong periodicity at $38.2^{+2.9}_{-1.6}$ d in the GP hyperparameters, reducing significantly the uncertainties obtained in Aff19. This periodicity is in agreement with the signals found in the activity indicators, and therefore we consider 38.2 d as the rotation period of the star. We obtain semi-amplitudes of the activity term of the order of $\sim 2\,\mathrm{m\,s^{-1}}$, which are comparable to the planetary signal.

The top panel in Fig. 3.11 illustrates the best-fitting model on a densely sampled region of the

CARMENES data, together with the best model and the GP component tracing the activity-induced RV modulation. The bottom panels show the Keplerian part of the activity plus Keplerian model, before (left) and after (right) subtracting the GP contribution to the RVs. The periodicity of 38.2 d and the semi-amplitude of 2.26 m s^{-1} of this modulation can be observed, which is highly correlated with the variability of the activity indicators illustrated in Fig B.6 in the appendix. The posterior distributions shows that all the orbital parameters follow a well behaved normal distribution and there are no strong correlations between parameters, except for the correlation between $e \sin \omega$ and $e \cos \omega$ with T_0 (see Fig. B.7 in the appendix).

When comparing the best model found by Aff19 and our equivalent model (GP + circular), we note a small decrease in the RV semi-amplitude with respect to that found in Aff19, and a further decrease when comparing our semi-amplitude to the tentative signal found in Butler et al. (2017), of 3.46 ± 0.56 m s^{-1}, although in both cases they are consistent within their respective uncertainties. Therefore, in order to prove the consistency of the signal in all datasets, we decided to check the stability of the signal over time. For simplicity, we used a circular model, with the RV offsets and jitter terms fixed to the values found in the fourth column of Table 3.5. We iteratively added RV datapoints in chronological order and computed the final parameters and uncertainties from the parameter distribution of an MCMC chain of 1000 steps. The results are shown in Fig. 3.12, with each color representing the instrument with which the RV measurement was made and the grey shaded regions indicating the uncertainties. As observed, the amplitude is almost always compatible within uncertainties, and the period and time of periastron passage are stable after the addition of the ~60th measurement. As for LSPM J2116+0234, we also tried to check the stability of the signal at different wavelength ranges, but given the lower amplitude of the planetary signal, we could only detect it significantly in only two of the CARMENES spectral orders.

Finally, we used the derived orbital parameters of the Keplerian plus activity model to investigate in detail for a possible planetary transit signature in the TESS photometric data. The transit probability of GJ 686 b is 2.3%, and the transit duration would be ~2.5 h. Assuming chemical compositions ranging from a 100% iron planet (1.3 $R_\oplus$) to 100% water world (2.3 $R_\oplus$), the transit depth at $i = 90$ deg would range from 0.078% to 0.24% of the total flux. In Fig. 3.13 we show the phase-folded TESS photometric data in the region around the expected transit time, extended to cover the uncertainties in T_0 and P, together with the theoretical transits produced by these two different compositions at $i = 90$ deg. None evident transit feature is present within the observed range. Additionally, we performed a Box-fitting Least Square periodogram (Kovács et al. 2002), but any significant signal was found. From the dispersion of the TESS photometry, we could put a detection limit to a transit depth of 0.05%.

3.4.3 Discussion

As shown in Fig. 3.14, aside from their minimum masses, the two exoplanets found in this work have very similar characteristics, orbiting their host stars at nearly the same period, distance and with a similar eccentricity. In addition, the same mass and comparable luminosities of LSPM J2116+0234 and GJ 686 suggest that the two planets receive a very similar insolation, of 3.2 and 3.5 times that received by the Earth, respectively. According to Kopparapu et al. (2013, 2014), both stars have very similar habitable-zone locations, with inner limits at 0.16 au

---

[7] `exoplanets.eu`

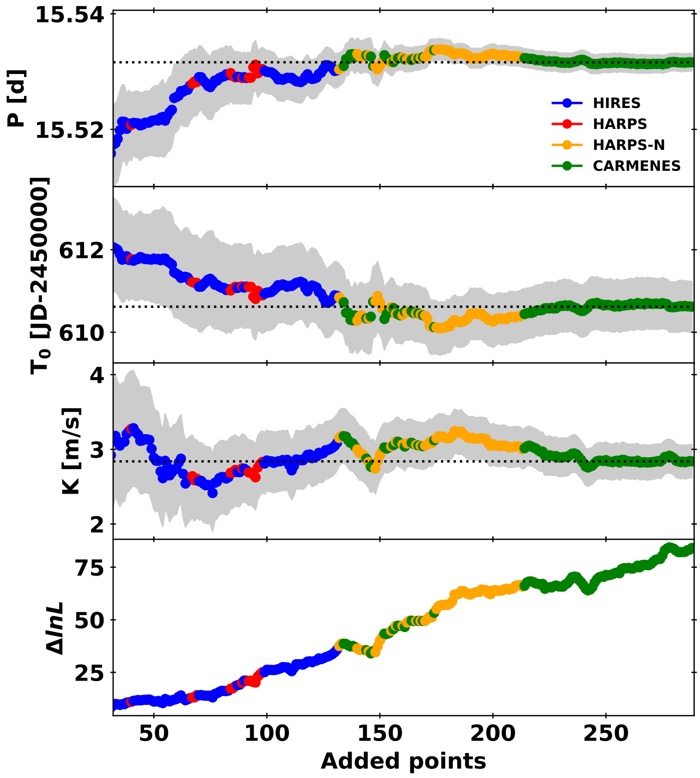

Figure 3.12: Orbital parameters of a circular orbit and $\Delta\ln\mathcal{L}$ as a function of the number of RV points, which are added chronologically. Each color represents a different instrument, and the gray shaded regions indicate the uncertainties computed from the MCMC posterior distribution. The first three panels show the period, time of maximum RV and semi-amplitude, respectively. The bottom panel shows the increment in $\ln\mathcal{L}$ with respect to a fit to the mean value. The black dotted line indicates the orbital parameters obtained from the combined RVs.

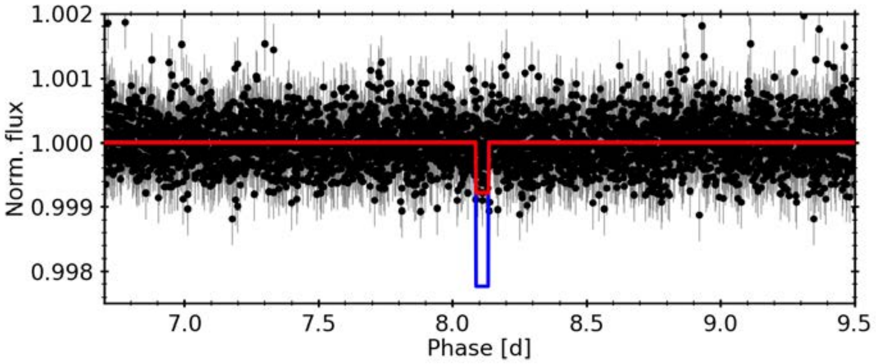

Figure 3.13: TESS photometric data of GJ 686 phase-folded to period of 15.53 d. The red and blue solid lines depict the theoretical transit models for planets with a radius of 1.3 and 2.3 $M_\oplus$, respectively, and an orbital inclination of 90 deg.

and 0.17 au from the host stars for LSPM J2116+0234 and GJ 686, respectively. The inner limit of the habitable zone is defined as the distance at which the surface temperature of the planet produces an increase of the water vapour in the stratosphere of more than an order of magnitude, triggering a dramatic increase in the surface temperature. A more conservative limit, defined as the distance at which the oceans evaporates completely, places the inner edge of

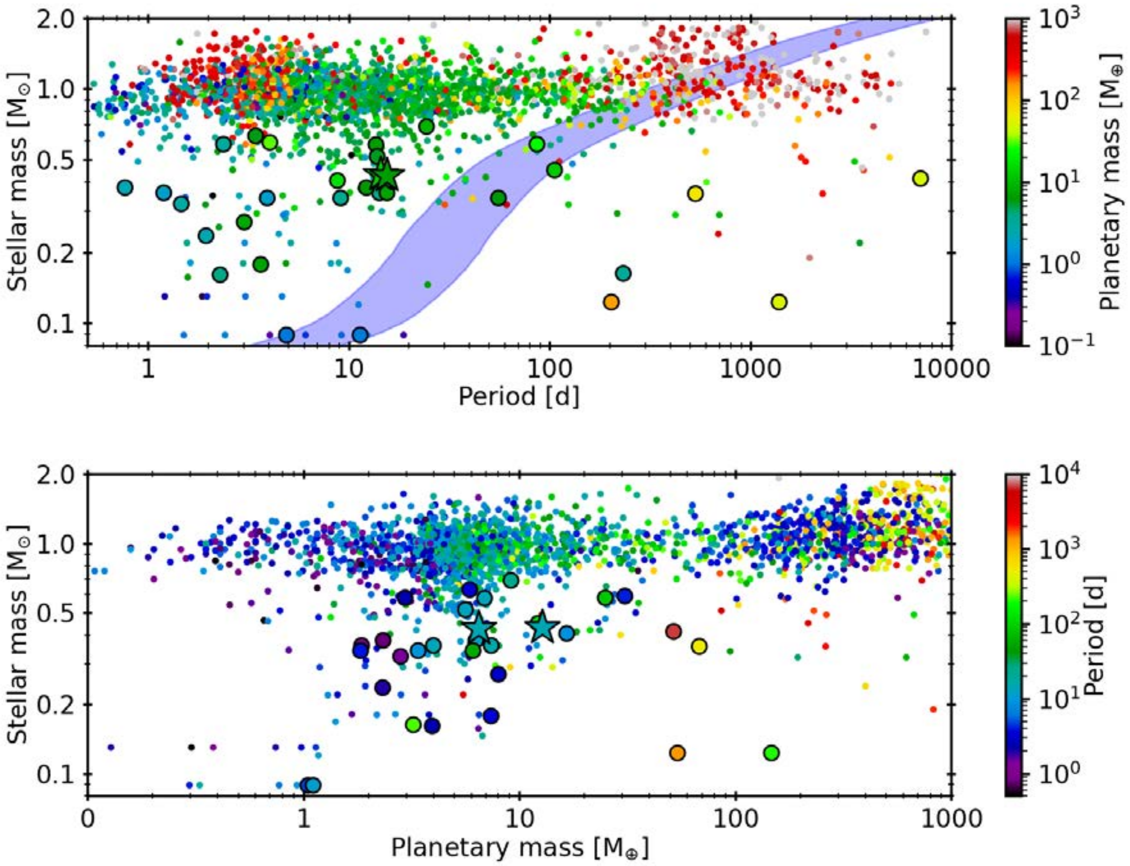

Figure 3.14: Parameters of all known exoplanets as listed in the `exoplanets.eu`[7] database. CARMENES discoveries (see Table A.1 in the appendix) are shown as circles with black contours, while the two planetary systems discussed in this chapter are shown as stars. *Top:* Host star mass as a function of the orbital period. The blue band marks the position of the optimistic habitable zone (Kopparapu et al. 2014), while the colour code indicates the planetary mass. *Bottom:* Host star mass as a function of the mass of the planet. The color code indicates the orbital period of the planets.

the habitable zone of LSPM J2116+0234 and GJ 686 at 0.13 au and 0.14 au, respectively. With semi-major axes of 0.088 au for the mini-Neptune around LSPM J2116+0234 and 0.092 au for the super-Earth around GJ 686, the two planets are closer to the host star than the conservative habitable-zone limits, as it can be seen in the top panel in Fig. 3.14, which illustrates the optimistic habitable zone of a 5 $M_\odot$ planet (Kopparapu et al. 2014). The inner edge of the habitable zone, however, strongly depends on the atmospheric and planetary parameters such as gravity, pressure, relative humidity or surface albedo. Considering for example a reduced greenhouse effect (relative humidity lower than 1%) and and increased surface albedo, the habitable zone can be pushed inwards to $\sim$ 0.08 au (Zsom et al. 2013), reaching the positions of GJ 686 b and LSPM J2116+0234 b.

As seen in Fig. 3.14, most of the discovered exoplanets are orbiting stars with masses above 0.5 $M_\odot$. With host star masses lower than this value, both LSPM J2116+0234 b and GJ 686 b increases the number of exoplanets discovered in this region. These diagrams also demonstrates the capability of CARMENES as an ideal instrument to discover low-mass planets on both short and long orbits around M dwarfs, with a considerable amount of the planets with host stars masses below 0.5 $M_\odot$ discovered by this instrument. Actually, CARMENES has doubled the number of planets around stars with masses lower than 0.2 $M_\odot$. Nearly ~75% of CARMENES discoveries are super-Earths or mini-Neptunes at a wide range of periods, but it has also found massive planets around very cool stars, populating a region of the parameter space that until now was not sampled. A close look at the upper panel of Fig. 3.14 reveals that the two small planets reported in this paper are part of a rather large population of CARMENES planets with similar masses and periods between 11-16 d, representing more than a 20% of all the CARMENES planetary discoveries. An concentration of planetary systems with periods between 10 d and 20 d has also been found in the HADES survey of exoplanets around M dwarfs (Affer et al. 2016, 2019), confirming this characteristic behaviour of M dwarf planetary systems.

3.5 Summary

In this chapter we analyzed 79 and 80 RV measurements of the M3.0 V star LSPM J2116+0234 taken with the visible and near-infrared channels of the high-resolution CARMENES échelle spectrograph, respectively. We also confirmed and refined the orbital parameters of the super-Earth around the M1.0 V star GJ 686 reported in Affer et al. (2019) with the addition of 103 new RV CARMENES measurements.

The analysis of the RVs from LSPM J2116+0234 revealed a signal at ~14.44 d, which is not present in any of the activity indicators or the photometric data, and is consistent between all wavelength orders. We interpret this signal as being caused by a planet with a minimum mass of 12.8 ± 1.0 $M_\oplus$ and a minimum semi-major axis of $0.0876^{+0.0022}_{-0.0020}$ au.

We also combined archival RV data from HIRES, HARPS, and HARPS-N with the CARMENES RVs to refine the orbital parameters and properties of GJ 686 b derived in Affer et al. (2019). We derived a slightly smaller and more precise RV semi-amplitude of 2.97 ± 0.20 m s^{-1}, resulting in a lower minimum mass of the planet of $6.64^{+0.46}_{-0.47}$ $M_\oplus$. The orbital period of ~15.53 d and the maximum semi-major axis of 0.0917 ± 0.0012 au are consistent with those derived in Affer et al. (2019). In contrast to this work, our model suggests a non-zero eccentricity, with a value of $0.134^{+0.050}_{-0.055}$.

Finally, we used photometric measurements and activity indices to confirm that additional signals present in the RV data are produced by stellar activity, obtaining an estimate of the rotation period for both LSPM J2116+0234 and GJ 686. For both targets, a non-parametric stellar variability model was adopted to account for correlated noise caused by stellar magnetic activity. We simultaneously modeled the stellar variability and the planetary signals to obtain a self-consistent planetary solution. From this model, we determined the stellar rotation period to be 42.7 d for LSPM J2116+0234 and 38.2 d for GJ 686, and found that the activity-induced variability of GJ 686 has an amplitude comparable to that of the planetary signal. With the data currently available, the RV time series favour a single eccentric planet model for both LSPM J2116+0234 and GJ 686.

Chapter 4

Multiple stellar systems in CARMENES

M dwarfs are ideal targets to the search for Earth-size planets in the habitable zone using the radial velocity method. This has attracted the attention of many ongoing surveys such as the CARMENES project, which, as already said, is surveying more than 300 M dwarf stars in search for exoplanets. Among the target stars, spectroscopic binary systems have been discovered, which can be used to measure fundamental properties of stars. Using spectroscopic observations from CARMENES, we newly characterise the spectroscopic orbits and physical properties of 17 systems by analysing their radial velocity curves. We derive the radial velocities of the stars using two-dimensional cross correlation techniques and template matching. The measurements are modelled to determine the orbital parameters of the systems.

Out of the 349 stars selected for the CARMENES survey, 17 have been found to be spectroscopic multiple systems. The sample is composed of five single-line binaries, ten double-line binaries, and two triple-line spectroscopic triple systems. The companions of two of the single-line binaries, GJ 3626 and GJ 912, have minimum masses below the stellar boundary and, thus, could be brown dwarfs. We find a new white dwarf in a close binary orbit around the M star GJ 207.1, located at a distance of 15.79 pc. From a global fit to radial velocities and astrometric measurements, we are able to determine the absolute masses of the components of GJ 282 C, which is one of the youngest systems with measured dynamical masses. We estimate absolute masses of the double-line binaries from mass-luminosity calibrations, obtaining masses ranging between 0.1 $M_\odot$ and 0.6 $M_\odot$.

In Sect. 4.2 we list the studied stars and describe the observations used in our analysis, including available data in public archives. Section 4.3 explains the method used to measure the RVs from observations and to obtain the orbital parameters and rotation periods. In Sect. 4.4 we present the results for each system, while in Sect. 4.5 we discuss the peculiarities of some of them and estimate individual masses of double-line spectroscopic binaries. Finally, we give the concluding remarks in Sect. 4.6.

Baroch, D., Morales, J. C., Ribas, I., et al.
A&A, **619**, A32 (2018)

Baroch, D., Morales, J. C., Ribas, I., et al.
A&A, accepted (2021)

4.1 Introduction

M dwarfs constitute the majority of stars in the Galaxy, in both number and mass (Gizis et al. 2002), and comprise almost 75 % of the stars in the solar neighbourhood (Henry et al. 2006). Over 40 % of M dwarfs are found in multiple systems (Cortés-Contreras et al. 2017; Winters et al. 2019), making them a key ingredient to our understanding of the stellar population as a whole. Statistical studies of their properties, such as the distribution of mass ratio and orbital elements, provide crucial tests for star formation theories and evolutionary models (see e.g. Tohline 2002; Duchêne & Kraus 2013). Depending on their orbital architecture, dynamical analyses of binary systems can yield fundamental properties such as the individual masses and radii with a precision of a few percent, independently from calibrations and stellar models (Andersen 1991; Torres et al. 2010; Southworth 2015). These masses and radii enable critical comparisons with stellar model predictions, as well as to determine empirical calibrations that can be applied to derive the fundamental properties of single stars (Baraffe et al. 2015; Benedict et al. 2016; Mann et al. 2019; Schweitzer et al. 2019).

Apart from their interest as a major galactic population, M dwarfs have also gained significant attention in the field of exoplanets. A number of surveys searching for rocky habitable planets using radial velocities (RVs) and the transit technique focus on M-dwarf stars, in which Earth-size planetary companions are common (Dressing & Charbonneau 2013). Moreover, compared to Sun-like stars, M dwarfs have the critical advantages of having a lower mass and closer habitable zones (Kasting et al. 1993; Kopparapu et al. 2013). This means that potentially habitable planets would induce larger RV signals and would be easier to detect than around earlier-type stars. As a benefit of these exoplanet surveys, a large number of new stellar binary systems have also been discovered (e.g. Irwin et al. 2009, 2010; Irwin et al. 2011; Kirk et al. 2016; Dittmann et al. 2017; Baroch et al. 2018; Sperauskas et al. 2019).

The CARMENES survey (Quirrenbach et al. 2018, 2020) is an example of one of such exoplanet surveys. It is observing more than 300 M-dwarf stars searching for exoplanets in their habitable zones, and already discovered ∼30 planets (see Table A.1). In addition to these new planets, several spectroscopic multiple systems were identified with the first observations of the sample, and they were followed-up for their characterization.

The stellar systems discovered with CARMENES are especially interesting because the number of known M dwarf multiple systems is still scarce (see e.g. the Ninth Catalogue of Spectroscopic Binary Orbits, hereafter SB9[1]; Pourbaix et al. 2004). The distribution of mass ratios and orbital elements may help to understand the formation and evolution of low-mass stars, brown dwarf, or giant planets in M dwarf stellar systems. Besides, they are also valuable to constrain the properties of M dwarfs, which still show some discrepancies with stellar model predictions (Morales et al. 2010; Tal-Or et al. 2013; Feiden & Chaboyer 2014).

---

[1] `http://sb9.astro.ulb.ac.be/`

4.2 Sample selection and data

4.2.1 Spectroscopic data

A simple search for stars in the CARMENES sample showing RV excursions greater than $\sim$0.5 km s^{-1} revealed 17 new multiple stellar system candidates. A total of 421 high-resolution spectra of these stars were obtained from January 2016 to December 2020 with the visual channel of the CARMENES spectrograph. Table 4.1 lists the main properties of the stars studied here. It includes their common names and CARMENES identifiers, their equatorial coordinates, distances, and proper motions, their G- and K_s-band magnitudes, and different spectroscopic properties, all computed assuming non-binarity, and therefore subject to some bias. The astrometric properties of all systems are from the *Gaia* Early Data Release 3 (Gaia Collaboration et al. 2016, 2018, 2021).

We also collected additional high-resolution spectroscopic observations from public archives in order to complement our observations for long-period systems. We found a total of 115 additional observations, 60 taken with the HARPS spectrograph at La Silla Observatory (Mayor et al. 2003), 42 with the FEROS spectrograph also at La Silla Observatory (Kaufer et al. 1999), 6 spectra with the UVES spectrograph at Paranal Observatory (Dekker et al. 2000), 6 with the HARPS-N spectrograph (Cosentino et al. 2012) at the Roque de los Muchachos Observatory , and, 1 with the CAFE spectrograph at Calar Alto Observatory (Aceituno et al. 2013), obtained by Jeffers et al. (2018) as part of the characterisation of the CARMENES input catalogue of stars.

After the publication of the orbital parameters in Baroch et al. (2018) of nine of the SB2 analysed in this chapter, Winters et al. (2020) and Sperauskas et al. (2019) published 40 new radial velocities from the TRES and CORAVEL spectrographs, respectively, of three of our targets, GJ 1029, Ross 59, and GJ 1182, and determined their orbital parameters independently to our measurements. Since the spectra of these observations are not publicly available for analysis, we gathered the radial velocities from the original publications and added them to our analysis. In total, we gathered and computed the radial velocities of 576 high-resolution spectra for the seventeen systems studied in this chapter, with a time span of up to 15 years for some of the targets. A summary of the number of observations available from each instrument is given in Table 4.2.

4.2.2 Photometric data

In order to check for possible eclipses or rotational variability, we collected photometric time series from public archives of surveys such as TESS (Ricker et al. 2015), ASAS (Pojmanski 1997), NSVS (Woźniak et al. 2004), MEarth (Berta et al. 2012), and SWASP (Pollacco et al. 2006). We refer to Díez Alonso et al. (2019) for details on these surveys. Within the context of the CARMENES spectroscopic survey, photometric follow-up was triggered from ground-based observatories for some interesting candidates. In particular, we collected R-band photometric data of GJ 207.1 at the Montsec Astronomical Observatory[2] using the Telescopi Joan Oró (TJO) and the MEIA2 instrument. TJO is a fully robotic 0.8 m Ritchey-Chrétien equipped

---

[2] `www.oadm.cat`

Table 4.1: Astrometric, photometric, and spectroscopic properties of the 17 systems studied in this work.

Name Karmn	α (J2016)^a δ (J2016)^a	$\mu_\alpha \cos\delta$ [mas a^{-1}]^a μ_δ [mas a^{-1}]^a	ϖ [mas]^a d [pc]^a	G^a [mag] $K_s{}^b$ [mag]	Sp. T $T_{\rm eff}$ [K]	$M_\star$ [M$_\odot$]^f $R_\star$ [R$_\odot$]^f	$v \sin i$ [km s^{-1}] pEW(Hα) [Å]^l
EZ Psc	00:16:14.63	+714.63(5)	65.11(4)	10.909(3)	M4.0 V^c	···	4.0(1.6)^j
J00162+198 W	+19:51:37.5	−761.97(4)	15.359(10)	7.087(23)	···	···	−4.16(6)
GJ 1029	01:05:37.64	1917.7(3)	79.9(3)	12.950(3)	M5.0 V^d	···	4.1(8)^k
J01056+284	+28:29:33.6	−187.26(22)	12.51(4)	8.550(20)	···	···	−0.116(17)
GJ 207.1	05:33:44.55	−231.54(5)	63.36(5)	10.3762(7)	M2.5 V^d	0.488(20)	9.8(1.5)^i
J05337+019	+01:56:41.0	−153.99(4)	15.783(12)	6.855(21)	3419(51)^f	0.485(15)	−5.00(4)
Ross 59	05:53:14.06	156.7(5)	47.7(5)	9.933(3)	M1.5 V^d	···	$< 3^h$
J05532+242	+24:15:31.8	−605.1(3)	20.95(22)	6.633(21)	···	···	−0.034(10)
UCAC4 355-020729	07:00:07.00	+145.47(3)	33.53(3)	12.3039(7)	M5.0 V^c	0.598(24)	3.8(1.5)^i
J07001−190	−20:58:34.9	−89.66(3)	29.83(3)	8.091(17)	3100(50)^f	0.589(19)	−6.99(4)
GJ 282 C	07:36:07.15	+74.13(14)	70.27(13)	9.142(3)	M1.0 V^c	0.585(25)	3.1(1.5)^i
J07361−031	−04:53:16.6	−293.12(10)	14.23(3)	5.934(18)	3894(51)^g	0.577(21)	−0.860(14)
LP 427-016	09:14:03.02	−146.56(5)	43.52(5)	11.101(2)	M3.0 V^e	0.473(19)	$< 2^i$
J09140+196	+19:40:03.2	−160.42(4)	22.98(3)	7.535(21)	3493(51)^g	0.471(15)	−0.101(12)
LP 790-2	10:18:13.84	−396.41(4)	39.49(4)	12.320(3)	M4.5 V^c	···	···
J10182−204	−20:28:41.1	114.40(5)	25.32(3)	8.145(23)	···	···	−7.63(9)
GJ 3612	10:35:26.99	−1653.64(25)	78.6(3)	10.7196(28)	M3.5 V^d	···	$< 3^h$
J10354+694	+69:26:58.7	−641.5(3)	12.73(5)	7.161(20)	···	···	+0.070(8)
GJ 3626	10:50:26.07	+52.00(22)	44.27(20)	11.7962(6)	M4.0 V^d	0.418(18)	$< 2^i$
J10504+331	+33:05:54.3	−636.21(21)	22.59(10)	8.012(16)	3393(51)^g	0.419(14)	+0.092(14)
GJ 1182	14:15:32.55	−744.4(5)	72.9(4)	12.655(3)	M5.0 V^d	···	6.8(5)^k
J14155+046	+04:39:31.5	−769.5(3)	13.89(7)	8.618(25)	···	···	+0.10(10)
UU UMi	15:41:20.01	+805.1(4)	73.3(3)	11.0493(9)	M3.0^d	···	$< 3^h$
J15412+759	+75:59:22.9	−716.3(4)	13.65(6)	7.442(23)	3430(51)^g	···	−0.11(2)
GJ 3916	15:47:24.22	−309.0(6)	62.5(3)	10.2077(4)	M2.0 V^d	0.506(21)	$< 3^h$
J15474−108	−11:06:07.0	−370.8(5)	16.00(7)	6.743(18)	3528(51)^g	0.503(16)	−0.028(18)
LP 395−8	20:19:49.26	83.565(19)	33.90(3)	11.023(3)	M3.0 V^e	···	11.8(1.5)^h
J20198+229	+22:56:36.4	106.536(20)	29.501(23)	7.283(18)	···	···	−3.03(25)
GJ 810 A	20:55:37.75	1416.6(4)	84.9(5)	11.0620(28)	M4.0 V^d	···	$< 3^h$
J20556−140N	−14:02:08.0	−472.4(3)	11.78(7)	7.37(3)	···	···	−0.02(7)
GJ 912	23:55:39.28	−480.24(6)	55.92(4)	10.1368(8)	M2.5 V^d	0.510(20)	$< 2^i$
J23556−061	−07:51:20.8	−378.89(3)	17.883(14)	6.715(24)	3694(51)^g	0.506(15)	+0.074(11)
GJ 4383	23:58:32.74	+82.5(4)	59.1(3)	10.6312(4)	M3.0 V^d	0.472(20)	$< 2^i$
J23585+076	+07:39:25.2	−315.35(16)	16.92(8)	7.063(21)	3471(51)^g	0.470(16)	+0.042(10)

References. *a*: Gaia Collaboration et al. (2016, 2018, 2021); *b*: Skrutskie et al. (2006); *c*: Alonso-Floriano et al. (2015); *d*: Reid et al. (1995); *e*: Zacharias et al. (2013); *f*: Schweitzer et al. (2019); *g*: Passegger et al. (2018); *h*: Jeffers et al. (2018); *i*: Reiners et al. (2018b); *j*: Fouqué et al. (2018); *k*: Jenkins et al. (2009); *l*: Schöfer et al. (2019).

with an Andor 2k × 2k CCD camera with a plate scale of 0.36 arcsec pixel^{-1}. We also collected *R*-band photometric data of GJ 282 C from the Sierra Nevada Observatory (OSN), Spain, using the 0.9 m Ritchey-Chrétien telescope equipped with a VersArray 2k × 2k CCD camera, and a plate scale of 0.38 arcsec pixel^{-1} (Rodríguez et al. 2010).

To minimise the effect of flares and the systematics, photometric data were binned in equal time intervals. For the SWASP data, in which multiple observations were taken each night, we first checked for the presence of short-duration eclipses and then performed a nightly binning, except for the short-period system GJ 207.1. We binned the TESS high-cadence data in 1 h bins for stars with visible short-term modulations, such as GJ 207.1, GJ 282 C, UCAC4 355-020729, LP 790-2, and LP 398-8, while for GJ 3612 and UU UMi, which have a smoother light curve,

Table 4.2: Number of spectroscopic observations and their time spans (in days), and photometric epochs after and before (in parentheses) filtering and binning.

System	Spectroscopic data[a]					Photometric data			
	C	H	F	Others	Δt [d]	TESS	ASAS	SWASP	Others
EZ Psc	11	···	5	···	2003	···	···	···	6357(6520)^j
GJ 1029	21	···	···	13^b	496	···	···	136(4695)	843(869)^j
GJ 207.1	14	1	2	···	5010	1051(30645)	452(463)	3699(3853)	539(560)^g
Ross 59	19	···	···	19^{c,d}	6090	···	306(318)	254(2116)	···
UCAC4 355–020729	27	···	···	···	738	480(14580)	553(572)	···	···
GJ 282 C	43	38	3	···	2464	542(16279)	476(504)	209(15238)	1705(1715)^h
LP 427–016	22	···	2	···	2830	···	320(335)	65(3821)	196(199)^i
LP 790-2	14	···	···	···	359	520(15369)	···	168(14814)	···
GJ 3612	21	···	···	···	686	158(54819)	···	···	148(163)^i
GJ 3626	42	···	···	···	2830	···	···	96(5090)	···
GJ 1182	22	···	···	14^b	816	···	···	···	1067(1109)^j
UU UMi	30	···	···	1^e	2794	329(121486)	···	···	2696(2803)^j
GJ 3916	38	3	23	6^f	5609	···	457(472)	376(73874)	···
LP 395–8	14	···	···	···	501	607(17539)	···	908(979)	···
GJ 810 A	29	···	···	···	557	···	388(409)	···	5364(5673)^j
GJ 912	28	9	3	···	4107	···	304(311)	256(90025)	···
GJ 4383	26	9	4	···	3425	···	234(241)	239(22787)	···

Notes. $^{(a)}$ The spectroscopic instruments are labeled as C (CARMENES), H (HARPS), and F (FEROS); $^{(b)}$ TRES; $^{(c)}$ HARPS-N; $^{(d)}$ CORAVEL; $^{(e)}$ CAFE; $^{(f)}$ UVES; $^{(g)}$ TJO; $^{(h)}$ OSN; $^{(i)}$ NSVS; $^{(j)}$ MEarth.

we chose longer bins of 12 h. In addition, we applied a 3σ clipping filter to all datasets. We list the final number of photometric epochs for each photometric survey and system, after applying this filter (total number of measurements in parentheses), in the last three columns of Table 4.2.

4.2.3 Direct imaging data

A bibliographical search revealed that the system GJ 282 C was observed and spatially resolved by Kammerer et al. (2019, see their Fig. 10) in an adaptive optics search for companions with the NAOS-CONICA imager (NACO; Lenzen et al. 2003; Rousset et al. 2003). NACO is an adaptive optics-assisted instrument that provides imaging, imaging polarimetry, and coronography in the 1–5 μm range. The adaptive optics system, NAOS, is equipped with both visible and infrared wavefront sensors, and contains several dichroics that split the light from the telescope between CONICA and one of the NAOS wavefront sensors. CONICA is the infrared camera and spectrometer attached to NAOS and is equipped with an Aladdin 1024 × 1024 pixel InSb array detector. Observations were performed on 22 January 2015 and 26 March 2016 in the L_p filter and on 2 February 2016 in the $IB_{2.18}$ filter. The plate scale of NACO during these observations was 27.19 mas pixel^{-1} for the L_p filter and 13.27 mas pixel^{-1} at 2.18 μm, which provided fields of view of 28 × 28 arcsec^2 and 14 × 14 arcsec^2, respectively. Short individual exposure times of 0.2 s in the L_p filter and 0.5 s at 2.18 μm were used to avoid saturation of the primary star. We downloaded these data from the European Southern Observatory archive[3], and were reduced and analysed consistently by CARMENES project collaborators using routines within `IRAF` (Tody 1986, 1993). Individual images were sky-subtracted and flat-field corrected using

---

[3] `http://archive.eso.org/cms.html`

Table 4.3: Astrometric positions of GJ 282 C computed from NACO observations.

Obs. date	ρ [mas]	θ [deg]	Δm [mag]^a
2015-01-22	516.0 ± 3.0	134.87 ± 0.38	2.400 ± 0.050 (L_p)
2016-02-02	455.3 ± 1.6	135.02 ± 0.15	2.560 ± 0.010 ($IB_{2.18}$)
2016-03-26	442.5 ± 2.6	133.77 ± 0.32	2.360 ± 0.050 (L_p)

Notes. [(a)] Δm refers to the magnitude difference between the stars at the band indicated in parenthesis.

a superflat model, aligned, and combined to produce the final image. Aperture photometry of both stars in this combined image was performed with `daophot` to determine the magnitude difference between the primary and secondary. The pixel position of the stars was determined in each individual image using the `imcentroid` routine. The average value and the standard error of the mean were adopted as the final value and its error bars. The detector positions were transformed into the sky positions using the average position angle during observations in the L_p band and the plate scale and orientation from the image header. We list the astrometric positions derived from these observations in Table 4.3.

4.3 Data analysis

4.3.1 Radial velocity measurements

After the selection of the multiple system candidates based on excursions greater than $\sim 0.5\,\mathrm{km\,s^{-1}}$ of the RVs provided by the CARMENES pipeline `serval` (Zechmeister et al. 2018), we searched for the signature of companion stars in the spectra using `todmor` (Zucker et al. 2003), a new implementation of the two-dimensional cross-correlation method `todcor` (Zucker & Mazeh 1994) for multi-order spectra. This technique uses two different template spectra for each component, scaled according to their flux ratio. The two spectra are simultaneously Doppler-shifted, constructing a two-dimensional cross-correlation function (CCF) from which the RVs of the two components can be computed. The flux ratio α of the system in the wavelength range of the observations can also be obtained. As templates for the calculation of the CCFs, we employed synthetic PHOENIX stellar models (Husser et al. 2013). For each system, we explored a grid of values for the effective temperature of each component, flux ratios in the observed wavelength band, and the spectral-line broadening v_{br} (to account for rotation velocity) to look for the combination that maximised the CCF peak. Spectral orders with a signal-to-noise ratio of their CCFs below 5 or with telluric contamination were discarded beforehand. To obtain the final RVs of each system in a consistent way, we optimised the template parameters using the spectrum with highest SNR among the spectra with well resolved CCF peaks. Spectra obtained at orbital phases close to conjunction, where the radial velocities of the components cannot be disentangled due to rotational broadening and a low flux ratio, were not considered in this analysis.

In general, we prefer to use synthetic spectra over high SNR spectra of real stars as templates because the latter are prone to systematics due to the uncertainty of the absolute RVs of the different template stars and by residual contamination due to tellurics on the co-added spectra.

However, the molecular bands of the coolest stars modeled by synthetic spectra show discrepancies with observations due to inaccurate or incomplete molecular opacities (Allard et al. 2012; Passegger et al. 2020), and for this reason, the use of real templates could reveal signals from a secondary body that otherwise, with synthetic spectra, could not be resolved. Therefore, for those stars for which the signature of the secondary component was not detected with synthetic spectra, we used high signal-to-noise co-added data from the CARMENES stars GJ 752 A (V1428 Aql, Karmn J19169+051N; M2.5 V) and GJ 1253 (Wolf 1069, Karmn J20260+585; M5.0 V) as fiducial templates of mid and late M-dwarf stars. The main cases in which real spectra were used as templates correspond to stars with a small RV difference between the components (UU UMi and GJ 810 A) and in those with a low flux ratio (GJ 4383). We computed the absolute RVs of the template stars by cross-correlating them with synthetic spectra.

For the GJ 3916 and GJ 4383 systems, the `todmor` analysis revealed three different signals in the CCF. In these cases, we first fitted the template to the component with the highest flux, setting the flux of the secondary component to zero, and subtracted it from the observed spectra. Then, we analysed all the residuals with `todmor` again, and extracted the RVs of the other two components. These RVs were consistent with these stars being hierarchical triple systems. However, due to their configuration, there were orbital phases in which the RVs of the primary and one of the two secondary stars almost overlapped, in which case the RV of the dimmer component could not be extracted.

Finally, for systems where the signature of the secondary component was not found in the spectra, that is, SB1s, we used the RVs provided by the CARMENES pipeline `serval` (Zechmeister et al. 2018). In this case, the spectra of the primary component is not significantly affected by the much fainter companion and `serval` provided a significantly better RV precision than `todmor`. Several observations of the star are needed to produce the high signal-to-noise ratio template used by `serval`. We set this limit to five, thus allowing us to measure RVs using `serval` for CARMENES spectra and for the HARPS data of GJ 282 C and GJ 912. A small number of FEROS and HARPS spectra are also available for four of the five analysed SB1 systems, some of them taken ~10 years before the CARMENES observations. Although isolated, they are crucial for the characterisation of long-period systems. However, two difficulties arise when trying to use these data. On the one hand, the RV offset between the different instruments needs to be computed. On the other hand, the small number of observations does not allow us to derive precise RVs using `serval`. To solve this issue, we computed the RVs of the two FEROS spectra and the single HARPS spectrum of GJ 207.1 with `todmor` using the one-dimensional configuration (i.e. setting the flux ratio to zero), which gives an absolute RV with respect to the synthetic spectra. In order to constrain the RV zero point of these measurements from `todmor`, we also computed the CARMENES RVs with `todmor`. We then corrected the RV offset as the difference with respect to `serval` RVs.

Table 4.4 shows the optimised parameters of the templates for each target, used to obtain the radial velocities of the systems with `todmor`. For UU UMi, GJ 810 A, and GJ 4383, we provide the effective temperatures of the stars used as templates obtained by Passegger et al. (2019). The list of computed RVs and uncertainties for each system and instrument, together with the method used to compute them, either `todmor` (T) or `serval` (S), are listed in Tables A.6–A.8. For the analysis done in Baroch et al. (2018) we also computed the RVs of the components using the NIR channels of CARMENES, which in theory should have better resolving power than the VIS channel due to the larger flux ratios at longer wavelengths. However, the low RV information content in the NIR and the presence of large telluric bands resulted in a reduced

Table 4.4: Spectral properties of the templates used to derive the radial velocities with TODCOR.

Name	$T_{\rm eff,1}$ [K]	$T_{\rm eff,2}$ [K]	$v_{\rm br,1}$ [km s^{-1}]	$v_{\rm br,2}$ [km s^{-1}]	α
			SB1s		
GJ 207.1	3600	···	11.50	···	0.00
GJ 282 C	3900	···	4.25	···	0.00
LP 427-016	3700	···	3.00	···	0.00
GJ 3626	3500	···	2.50	···	0.00
GJ 912	3700	···	2.75	···	0.00
			SB2s		
EZ Psc	3300	2900	6.75	7.25	0.10
GJ 1029	3100	2900	3.50	5.50	0.36
Ross 59	3900	3600	1.50	0.00	0.10
UCAC4 355-020729	3100	3000	4.50	0.00	0.24
LP 790-2	3000	3000	5.25	6.00	0.50
GJ 3612	3500	3300	2.50	4.50	0.24
GJ 1182	3300	2900	2.25	5.00	0.24
UU UMi[a]	3583	3158	0.75	0.00	0.26
LP 395-8	3600	3100	14.75	12.50	0.16
GJ 810 A[a]	3583	3583	0.00	0.25	0.66
			ST3s		
GJ 3916[b]	3600	3300	4.50	0.00	···
GJ 4383[a,b]	3583	3158	1.25	0.00	···

Notes. (a) Real templates are used instead of synthetic. Effective temperatures from Passegger et al. (2019). (b) For ST3 we set the flux ratio to zero in a first step to extract the RVs of the primary component, and reanalyse the residuals using the same templates with a flux ratio of one to compute the RVs of the other two components.

capability to resolve the two components at small relative RVs and in a worse RV precision than the obtained with the VIS. We therefore preferred not to include the NIR RVs in the analysis presented here.

4.3.2 Orbital parameter determination

We determined the orbital parameters of each system by fitting an N-body Keplerian model to the RVs of all the components simultaneously. For binary systems, we fitted the five parameters (six for SB2 systems) defining a spectroscopic Keplerian orbit: the period P, the semi-amplitude of the components K_A (and K_B for SB2), the time of periastron passage T_0, the eccentricity e, and the argument of periastron ω, using $e\sin\omega$ and $e\cos\omega$ as actual parameters. Additionally, we fitted an RV offset for each instrument ($\gamma_{\rm Inst.}$), except for the corrected FEROS RVs, which was fixed as explained above. We defined the systemic velocity γ as $\gamma_{\rm CARM}$ plus the offset between the CARMENES observations computed with `serval` and `todmor`, and their uncertainties were propagated accordingly. We also allowed an adjustable RV jitter term for each instrument ($\sigma_{\text{Inst.}}$), which was added in quadrature to the errors as described in Baluev (2009). This jitter term represents unaccounted error sources in the estimation of the uncertainties of the measurements. We employed a hierarchical model for the triple systems (i.e. an inner binary, and a more distant star, orbiting around the centre of mass of the inner binary, without mutual interactions). We use the subscripts 'AB' to refer to the wide orbit of the inner-system centre of mass around the outer and brighter component 'A', and 'B' to refer to the inner system, while we use 'Ba' and 'Bb' for the two inner components (there are no 'Aa' and 'Ab' components).

For GJ 282 C, we also included in the analysis the three astrometric measurements and performed a simultaneous fit of the RVs, the relative astrometric positions, and a combination of the proper motions from the Hipparcos-*Gaia* Catalog of Accelerations (hereafter HGCA, Brandt 2018) using the `orvara` software (Brandt et al. 2021). In addition to the parameters that define the RV curve of an SB1 system, the astrometric orbit model adds three more parameters: the inclination of the system (i), the longitude of the ascending node (Ω), and the semi-major axis of the orbit (a). The HGCA accelerations also provided the proper motion ($\mu_\alpha \cos\delta$ and μ_δ) and parallax (ϖ) of the barycentre.

We computed the orbital parameters and uncertainties by sampling the posterior probability distribution with the `emcee` sampler (Goodman & Weare 2010; Foreman-Mackey et al. 2013), an implementation of the affine-invariant ensemble sampler Markov chain Monte Carlo (MCMC). We sampled the posterior distribution with 250 walkers and 5 000 steps, after a burn-in of 5 000 samples, unless indicated otherwise for some specific cases. Parameter uncertainties were derived from the 68.27 % credibility interval of the resulting posterior parameter distribution. For systems with orbits larger than the time span of the observations, we placed broad and uninformative priors in all parameters, uniformly sampling the period up to 100 000 d and the eccentricity to 0.9.

From the orbital parameters of the systems we derived the projected semi-major axes, $a_{\text{A,B}} \sin i$, and the minimum masses $M_{\text{A,B}} \sin^3 i$ for SB2 systems, or the binary mass functions $f(M)$ for SB1 systems, which were computed with Eqs. (1.12), (1.14), and (1.16), respectively. For SB1 systems, for which we cannot directly compute the value of $M_{\text{A,B}} \sin^3 i$, we computed the secondary minimum mass, $M_{\text{B,min}}$, by numerically solving Eq. (1.14) for M_{B} with $i = 90$ deg and assuming the primary mass listed in Table 4.1.

4.3.3 Photometric analysis

To fully characterise the systems, we also analysed the photometric data searching for eclipses and for variability due to stellar rotation. The dominant periodicity were determined by computing the GLS periodogram (Zechmeister et al. 2009) of each photometric dataset. Uncertainties are estimated as half the full width at half maximum of the periodogram peak, as a conservative approach. To assess the significance of the signals found, we computed the false alarm probability (FAP), which measures the probability that the signal randomly arises from white noise. We measured the FAP level of the signal with a bootstrap randomisation of the input data, and considered a signal as significant if it reached a value $< 0.1\%$.

For GJ 282 C, the high precision of the TESS photometric data revealed clear deviations from a strictly periodic sinusoid and a low-period modulation of lower amplitude. To improve the accuracy of the rotational period determination of this system, we inferred the periodicity in the light curves by using a GP with a sum of two quasi-periodic covariance functions (Eq. 1.30, see Sect 1.3 for more details on GPs) to model two modulations of different periodicities. The hyperparameters and their uncertainties were computed by sampling the posterior probability with the `emcee` MCMC sampler. We attributed the hyperparameters controlling the periodicity in each kernel term to the rotation period of the individual components.

We searched for eclipses in the light curves using two different approaches: in the case of systems with well determined periods from radial velocities, we folded the light curve of each target in a phase-magnitude diagram using the orbital period found in Sect. 4.4, and checked for a decrease in brightness within a narrow phase region compatible with the radial velocity orbit. We also made use of the Box-fitting Least Squares (hereafter BLS; Kovács et al. 2002) to identify eclipses with depth similar to the photometric scatter of each curve. BLS was also used in the case of binary systems with poorly constrained periods, although the eclipse probability is very small for long period systems. Both methodologies yielded negative results in all cases and, therefore, we concluded that none of the seventeen multiple systems analysed in this chapter is an eclipsing system within the limits of the sampling and measurement accuracy of the photometric data.

4.4 Results

We report in this section the result of the orbital fitting analysis and its interpretation for each of the seventeen systems separately. This includes five SB1, ten SB2, and two ST3.

4.4.1 Single-line spectroscopic binaries (SB1s)

4.4.1.1 GJ 207.1

GJ 207.1 is an M2.5 V star located at 15.783 ± 0.012 pc. Also known as Wachmann's Flare Star, it was first classified as a variable flaring star by Wachmann (1939), and has been repeatedly detected as an extreme-ultraviolet and soft X-ray source by wide-field surveys (Pounds et al. 1993; Lampton et al. 1997; Ansdell et al. 2015). It is listed as a member of the young disc population (Montes et al. 2001), with an estimated age of 100 Ma (Lowrance et al. 2005). However, these estimates are based on its high level of activity and on its Galactic space-velocity components, which could be affected by binarity, therefore biasing the kinematic and age assignments. A projected rotation velocity of $v \sin i = 9.8 \pm 1.5\,\mathrm{km\,s^{-1}}$ was reported by Jeffers et al. (2018) using CARMENES spectra. It was classified by Reiners et al. (2012) as a possible spectroscopic binary. High-resolution images ruled out companions beyond 0.2 arcsec with $\Delta I > 1$ mag and beyond 0.5 arcsec $\Delta I > 3$ mag (Jódar et al. 2013), and planets with masses $>10\,M_{\mathrm{Jup}}$ beyond 12.3 au (Biller et al. 2007), assuming an age of 100 Ma.

A total of 14 CARMENES spectra were taken between November 2016 and November 2018. Three additional spectra are publicly available in the HARPS and FEROS archives, which were taken between 9 and 12 years before the CARMENES measurements. Although the `serval` RVs showed a large dispersion of $\sim 60\,\mathrm{km\,s^{-1}}$, no companion was detected with `todmor` in any of the three datasets, either using synthetic or observed template spectra. Therefore, we used the RVs provided by the CARMENES pipeline. As explained in Sect 4.3.1, to put the HARPS and

Table 4.5: Computed and derived parameter for the SB1 systems.

Parameter	System			
	GJ 207.1	GJ 912	GJ 3626	LP 427-016
Orbital parameters				
P [d]	$0.60417356^{+0.00000024}_{-0.00000026}$	5188^{+58}_{-55}	2996^{+31}_{-30}	>6 400 <29 000
T_0 [BJD-2457000]	$867.06173^{+0.00016}_{-0.00015}$	$3\,099^{+47}_{-44}$	$1\,033^{+3}_{-3}$	...
K_A [km s^{-1}]	$35.133^{+0.032}_{-0.031}$	$1.356^{+0.084}_{-0.074}$	$0.9444^{+0.0051}_{-0.0048}$	>0.25 <1.4
$e \sin \omega$	0 (fixed)	$-0.4949^{+0.0046}_{-0.0049}$	$-0.4172^{+0.0032}_{-0.0033}$	0 (fixed)
$e \cos \omega$	0 (fixed)	$-0.380^{+0.021}_{-0.020}$	$-0.0785^{+0.0065}_{-0.0066}$	0 (fixed)
e	0 (fixed)	$0.6239^{+0.0098}_{-0.0097}$	$0.4246^{+0.0024}_{-0.0024}$	0 (fixed)
ω [deg]	0 (fixed)	$232.5^{+1.8}_{-1.6}$	$259.34^{+0.92}_{-0.94}$	0 (fixed)
$\gamma_{\rm CARM}$ [km s^{-1}]	$30.994^{+0.024}_{-0.023}$	$0.009^{+0.027}_{-0.029}$	$-0.6004^{+0.0015}_{-0.0016}$	>0.0 <0.9
$\gamma_{\rm HARPS}$ [km s^{-1}]	...	$-0.734^{+0.025}_{-0.027}$	...	...
γ^a [km s^{-1}]	$30.836^{+0.024}_{-0.024}$	$17.479^{+0.031}_{-0.029}$	$-59.870^{+0.017}_{-0.017}$	>13.2 <14.0
$\sigma_{\rm CARM}$ [km s^{-1}]	$0.079^{+0.026}_{-0.018}$	$0.00346^{+0.00077}_{-0.00062}$	$0.00201^{+0.00045}_{-0.00041}$	...
$\sigma_{\rm HARPS}$ [km s^{-1}]	$0.35^{+0.38}_{-0.25}$	$0.0056^{+0.0045}_{-0.0029}$	...	...
$\sigma_{\rm FEROS}$ [km s^{-1}]	$0.46^{+0.35}_{-0.32}$	$0.22^{+0.30}_{-0.16}$	$0.0088^{+0.0098}_{-0.0062}$	...
Derived parameters				
$a_A \sin i$ [au]	$0.0019511^{+0.0000018}_{-0.0000017}$	$0.505^{+0.032}_{-0.028}$	$0.2355^{+0.0012}_{-0.0011}$	>0.14 <3.8
$f(M)$ [M$_\odot$]	$0.0027146^{+0.0000074}_{-0.0000072}$	$0.00063^{+0.00011}_{-0.00009}$	$0.0001941^{+0.0000017}_{-0.0000016}$	>0.000009 <0.008
$M_{\rm B,min}$ [M$_\odot$]	$0.0979^{+0.0025}_{-0.0025}$	$0.0589^{+0.0030}_{-0.0036}$	$0.0331^{+0.0011}_{-0.0011}$	0.012
Estimated parameters				
$P_{\rm rot}$ [d]	0.60435 ± 0.00026	41.8 ± 1.3	...	36 ± 3
i [deg]	$13.8^{+2.2}_{-2.2}$	> 17	> 19	...
a_A [au]	$0.0082^{+0.0015}_{-0.0011}$	>0.5 <3.0	>0.235 <0.656	...
a [au]	$0.01454^{+0.00085}_{-0.00060}$	>4.5 <6.0	>3.08 <3.49	...
$M_{\rm B}$ [M$_\odot$]	$0.63^{+0.20}_{-0.13}$	>0.06 <0.21	>0.033 <0.11	>0.012 <0.13
$q \equiv M_B/M_A$	$1.29^{+0.42}_{-0.26}$	>0.115 <1.0	>0.08 <0.25	>0.024 <0.27
K_B [km s^{-1}]	$27.2^{+6.9}_{-6.6}$	>1.4 <11.8	>3.78 <11.46	...
Fit quality				
rms [km s^{-1}]	0.48	0.041	0.0024	0.042

Notes. $^{(a)}$ Parameter adopted as the barycentre RV. Corresponds to $\gamma_{\rm CARM}$ plus the RV shift between the CARMENES RVs computed with `serval` and with `todmor` .

FEROS `todmor` measurements to the same level as the CARMENES RVs, we subtracted from them the mean difference between the CARMENES observations computed with `serval` and `todmor`, of −0.158 ± 0.007 km s^{-1}. This correction, added to the RV zero point of the `serval`

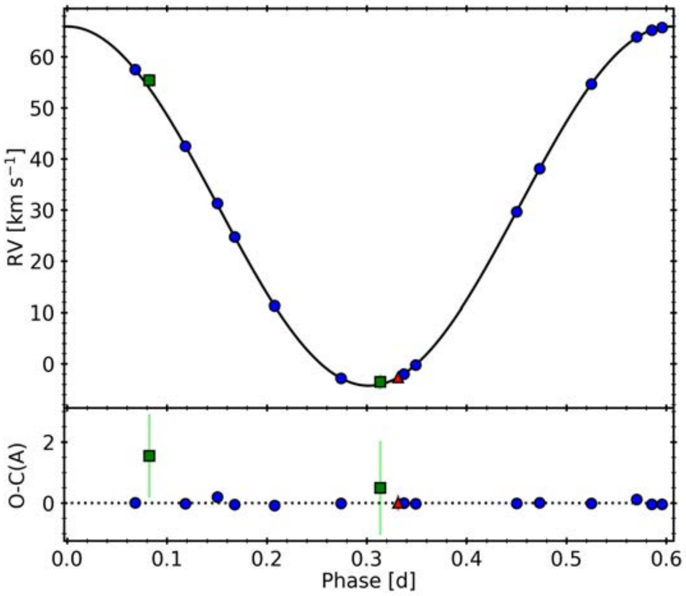

Figure 4.1: Best orbital fit to the RVs of GJ 207.1 from CARMENES (blue circles), HARPS (red triangle), and FEROS (green squares), phase folded to the period of the system. The bottom panel shows the residuals from the fit.

measurements from CARMENES ($\gamma_{\rm CARM}$) was assigned as the absolute RV of the barycentre of the system (γ).

We list the orbital parameters of the system in the second column of Table 4.5, and we show in Fig. 4.1 the best fit to the RVs as a function of the orbital phase. Although the solution with non-zero eccentricity has a slightly better likelihood, it was not significantly different from a circular solution within the errors, putting a 1σ upper limit of $e = 0.0017$. Therefore, we decided to keep $e \sin \omega$ and $e \cos \omega$ fixed to zero. We found a sub-day orbital period of 0.60417356 d, with an uncertainty of less than 0.1 s, and a semi-amplitude of the RV signal of $35.133^{+0.032}_{-0.031}$ km s^{-1}. Given that the tidal circularisation timescale is small for orbital periods below 10 days, assuming a circular orbit for this system is further justified (Mazeh 2008). From this solution and the estimated mass of the primary component in Table 4.1, we solved Eq. 1.16 to obtain a minimum secondary mass of 0.0979 ± 0.0025 $M_\odot$, which is equivalent to a minimum mass ratio of 0.2.

We analysed the available photometric data listed in Table 4.2 to look for significant signals in the GLS periodograms. We found no significant periods in the ASAS photometry. However, as shown in the top panel in Fig. 4.2, we found very significant signals at 0.6042 ± 0.0012, 0.6043 ± 0.0003, and 0.60460 ± 0.00013 d in the TJO, SWASP, and TESS photometry, respectively, very similar to the orbital period of the system. We also found the same significant period at 0.605 ± 0.007 d when analysing the TESS data separately for sectors 6 and 32. After removal of the main signal, the residuals of the combined data still show an accumulation of significant peaks around 0.6 d. This accumulation could be an indication that the signal, while maintaining the same period, slightly changed its phase between the two sectors, producing an interference pattern in the periodogram. The periodograms of the residuals of the individual sectors, however, do not show any significant signal around 0.6 d, but they do at the first harmonic at about 0.3 d, as can be seen in the bottom panel in Fig. 4.2.

Tidal evolution theory predicts that the synchronisation and alignment timescales should be two

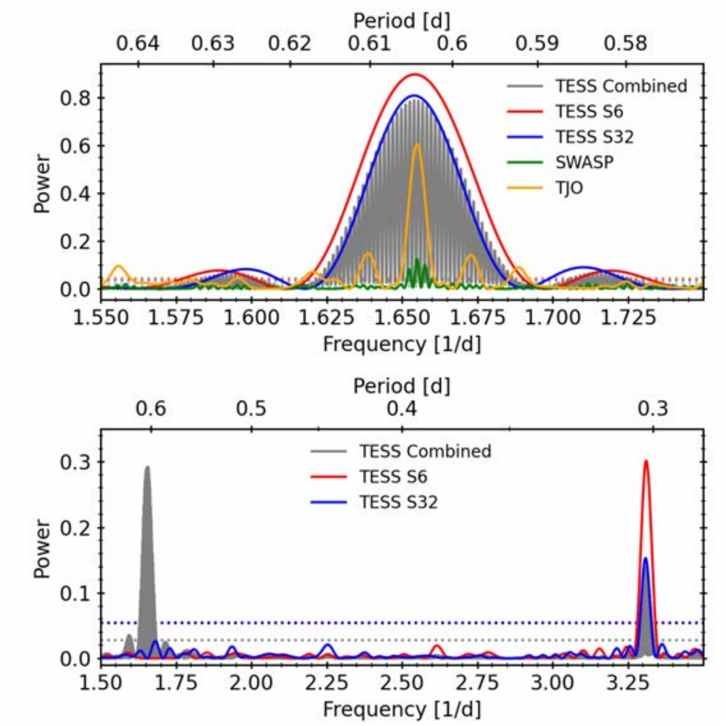

Figure 4.2: *Top:* GLS periodogram of the combined TESS data (grey) and individual sectors 6 (red) and 32 (blue), SWASP (green), and TJO (orange) photometry of GJ 207.1. *Bottom:* GLS periodogram of the residuals of the combined TESS data (grey) and their sectors 6 (red) and 32 (blue) after the removal of the significant signals. The horizontal dotted lines of the corresponding colors indicate the corresponding 0.1 % FAP level.

or three orders of magnitude shorter than the circularisation timescale (Zahn & Bouchet 1989; Mazeh 2008). Given that the orbit of GJ 207.1 is already circularised, and that the orbital and rotation periods are virtually identical, one may expect that spin-orbit alignment should have already been achieved. If that is the case, we can estimate the orbital inclination by combining the measured $v \sin i$ (9.8 km^{-1}, Table 4.1) of the star together with the measured rotation period (0.60435±0.00026 d, Table 4.5) and the stellar radius (0.485±0.015 $R_\odot$, Table 4.1). This yields a significantly pole-on orbital inclination of $i = 13.8^{+2.2}_{-2.2}$ deg.. This inclination yields a companion mass of $0.63^{+0.20}_{-0.13}\,M_\odot$ with an RV semi-amplitude of $27.2^{+6.9}_{-6.6}$ km s^{-1}.

The measured $v \sin i$ of GJ 207.1 may be biased due to its short orbital period. Indeed, we estimate that the RV shifts during the exposure time of the CARMENES spectroscopic observations, which varies between 8 and 30 min, can reach up to 7.6 km s^{-1}, depending on the orbital phase at which the observation was taken. This shift produces a broadening of the spectral lines that causes an overestimation of the true $v \sin i$ from the spectral analysis. However, we can estimate the effect of this RV shift over the measured $v \sin i$ taking into account that the variance of the observed line profile is the addition of the variances of the kernels defining the true line profile and the RV shift. The kernel of both the observed and true line profiles can be defined, to first order, by a Wigner semicircle distribution (Gray 2005) with radius equal to the projected rotational velocity and variance $(v \sin i)^2/4$, while the RV shift effect is defined by a rectangular function with length l equal to the shift and variance $l^2/12$. Therefore, the true projected rotational velocity, $v_T \sin i$, is defined by $v_T \sin i = 2\sqrt{(v \sin i)^2/4 - l^2/12}$. Even in the worst case scenario, where the RV shift caused by the exposure time is $l = 7.6$ km s^{-1}, this equation yields a minimum value of $v_{\rm T}\sin i = 8.8\,{\rm km\,s^{-1}}$ which is well within the uncertainty of the measured $v\sin i = 9.8 \pm 1.5\,{\rm km\,s^{-1}}$.

In general, the light curves of short-period binary systems present photometric modulations induced by the presence of a close companion. These include the reflection modulation and the beaming effect, which modulate the stellar brightness with orbital periodicity, and the ellipsoidal variation effect, which causes cyclic modulations at half the orbital period (Zucker et al. 2007; Mazeh 2008; Faigler & Mazeh 2011). These modulations carry information about the secondary component and can be approximated by sinusoidal functions, with harmonic periods and phase differences well defined with respect to the time of conjunction, and with constant amplitudes. Although these effects should be readily visible in the TESS photometry, it actually appears to be dominated by activity-induced variations. This hypothesis is further favoured by the phase change observed between the two TESS sectors.

The theoretically predicted amplitudes of the Doppler beaming, ellipsoidal, and reflection effects can be computed as given in Faigler & Mazeh (2011):

$$A_{\rm beam} = \alpha_{\rm beam} 4\frac{K_A}{c} = 27\alpha_{\rm beam}\left(\frac{M_A}{{\rm M}_\odot}\right)^{-2/3}\left(\frac{P}{1{\rm d}}\right)^{-1/3}\left(\frac{M_B\sin i}{10{\rm M}_{\rm Jup}}\right)\ {\rm ppm}, \tag{4.1}$$

$$A_{\rm ellip} = \alpha_{\rm ellip}\frac{M_B\sin i}{{\rm M}_\odot}\left(\frac{R_A}{a}\right)^{3}\sin i = 128\alpha_{\rm ellip}\sin i\left(\frac{R_A}{{\rm R}_\odot}\right)^{3}\left(\frac{M}{{\rm M}_\odot}\right)^{-2}\left(\frac{P}{1{\rm d}}\right)^{-2}\left(\frac{M_B\sin i}{10{\rm M}_{\rm Jup}}\right)\ {\rm ppm}, \tag{4.2}$$

and

$$A_{\rm refl} = \alpha_{\rm refl}0.1\left(\frac{R_B}{a}\right)^{2}\sin i = 57\alpha_{\rm refl}\sin i\left(\frac{M}{{\rm M}_\odot}\right)^{-2/3}\left(\frac{P}{1{\rm d}}\right)^{-4/3}\left(\frac{R_B}{{\rm R}_{\rm Jup}}\right)^{2}\ {\rm ppm}, \tag{4.3}$$

where the coefficients α are of order unity. Using these equations, and the stellar and orbital parameters listed in Tables 4.1 and 4.5, we obtain theoretical amplitudes of $A_{\rm beam}$ ~670 ppm, $A_{\rm ellip}$ ~780 ppm, and $A_{\rm refl}$ ~0.7 ppm. While we can neglect the reflection effect due to its low amplitude, the amplitudes of the Doppler beaming and ellipsoidal effects should be visible in the TESS photometry shown in Fig. 4.3, and therefore we can model them. To do so, we assumed the activity-induced variability to be a sinusoidal modulation at the orbital period (P = 0.60435 d, Table 4.5) and different phases and amplitudes between the two sectors. To model the Doppler beaming and ellipsoidal effect, we assumed two cosine functions with periods P (for the Doppler beaming) and $P/2$ (for the ellipsoidal effect), with a reference time fixed to the maximum of the radial velocities and with the same amplitude in both sectors. The full model that we adopted to describe the variability in each TESS sector j is defined by

$$A_j = C + a_j\cos\left(\frac{2\pi}{P}T + \delta_j\right) + A_{\rm beam}\cos\left(\frac{2\pi}{P}T\right) + A_{\rm ellip}\cos\left(\frac{4\pi}{P}T\right), \tag{4.4}$$

where a_j and δ_j are the amplitude and phase of the activity-induced modulations in each sector, and T is defined as $t - t_{\rm ref}$, where $t_{\rm ref}$ is the time of maximum radial velocity. In addition to the orbital period, we also fixed the amplitude of the Doppler beaming modulation, since it depends on the well-constrained RV semi-amplitude $K_{\rm A}$, while we left C, δ_i, a_i, and $A_{\rm ellip}$ as free parameters. We computed the parameters and uncertainties by sampling the posterior probability distribution using `emcee`. The best-model fit is shown in Fig 4.3. We obtain amplitudes of $a_6 = 4557 \pm 67$ ppm and $a_{32} = 2023 \pm 60$ ppm for the activity-induced variability of TESS

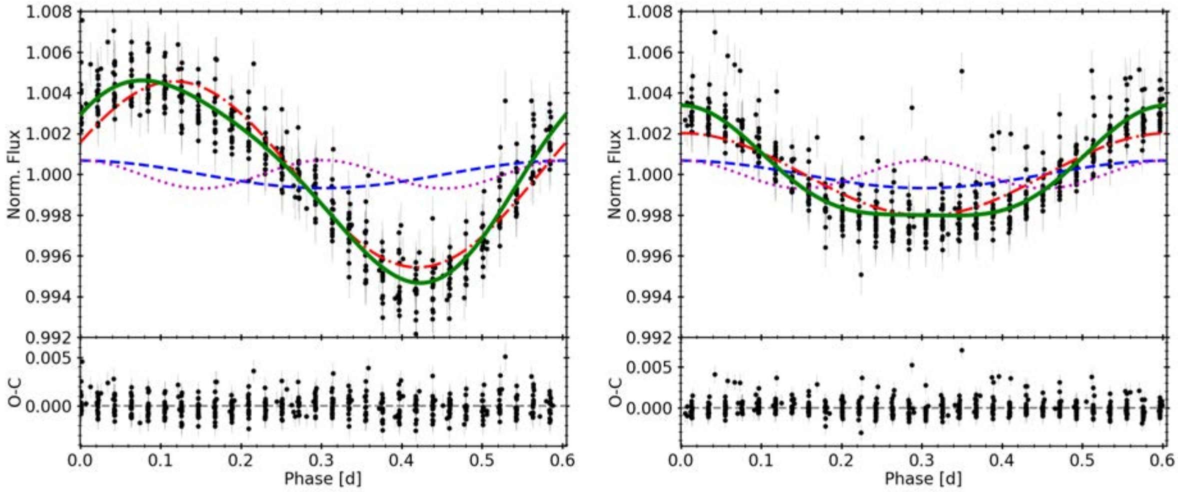

Figure 4.3: Hourly binned photometry of GJ 207.1 from TESS sectors 6 (*left*) and 32 (*right*), phase folded to the orbital period. We show the best fit, described by Eq. 4.4, as a green solid line. The activity-induced variability is shown as a dash-dotted red line, while the magenta dotted line and the dashed blue line describe the ellipsoidal and the Doppler beaming effects, respectively. The bottom panels show the residuals of the best fit.

sectors 6 and 32, respectively, with a shift between them of 1.19 ± 0.03 rad. We obtained an amplitude of the ellipsoidal effect of $A_{\rm ellip}$ = 694 ± 47 ppm, slightly lower than the predicted value of 780 ppm. From Eq.(4.2), and using the computed $A_{\rm ellip}$ and the estimated inclination, we derive a secondary mass of about 0.56 $M_\odot$, which is in good agreement with the mass derived from RVs, within uncertainties. Since the photometric amplitude of the ellipsoidal effect is larger for inclinations closer to 90 degrees, it is possible to put constraints on the inclination of the system independently of our former assumption about spin-orbit alignment. To do so, we estimated the amplitude $A_{\rm ellip}$ at which the model is no longer compatible with the observed photometry. By setting a log-likelihood decrease of 15 with respect to the best-fit as the limit of an acceptable fit, we obtained the maximum $A_{\rm ellip}$ amplitude at ~1000 ppm. This upper limit rules out orbital inclinations higher than 20 deg, and therefore excludes companions with masses below 0.37 $M_\odot$. For such a massive companion, the spectral lines of the two components of the system should be easily detected using `todmor` if it were a normal main-sequence M dwarf.

All the evidence points towards an underluminous companion to GJ 207.1 A. Interestingly, the absolute mass of the unseen component derived from the RVs under the assumption of zero obliquity of $0.63^{+0.20}_{-0.13}$ $M_\odot$ lies in the middle of the white dwarf mass distribution (Catalán et al. 2008). Therefore, we conclude that the secondary component of GJ 207.1 is most likely a white dwarf. We estimate that the progenitor star could have had a mass of $2.1^{+1.6}_{-1.4}$ $M_\odot$, as computed from initial-to-final mass relationships (Catalán et al. 2008). The time required for an object in this mass range to become a white dwarf is at least $0.59^{+22}_{-0.45}$ Ga (Marigo et al. 2001). However, the absolute masses and radii used to determine the mass of the white dwarf progenitor should be taken with caution. This binary system has probably suffered episodes of mass transfer during the red giant phase of the secondary, and the M dwarf could have truncated the evolution of the white dwarf precursor when it was ascending the giant branch. This truncation would produce a white dwarf with a lower mass than if it were isolated (Iben & Livio 1993; Rebassa-Mansergas et al. 2019) and may have changed the properties of both stars (Rebassa-Mansergas et al. 2011).

Bar et al. (2017) conducted a spectroscopic search for white dwarfs around nearby M dwarfs. For GJ 207.1, they set an upper limit of 8000 K for the temperature of any existing white dwarf in the system, estimated from the non-detection of any flux contribution from a companion in an X-SHOOTER (Vernet et al. 2011) spectrum down to 300 nm. From the cooling sequences of hydrogen white dwarfs (Chabrier et al. 2000b), we estimate that it takes at least 1 Ga for a 0.6 $M_\odot$ white dwarf to cool down to a temperature of ~8000 K, and even more for more massive white dwarfs. All this evidence points towards an age older than 1 Ga for this system, in contradiction with the young age proposed in previous works (Lowrance et al. 2005).

To investigate this disagreement, we recomputed the Galactic space-velocity components determined by Montes et al. (2001) using the absolute RV of the system determined in this work and the newly available *Gaia* proper motions and parallax. These new parameters yield space velocity components U, V, and W of −21.4, −10.5, and −28.6 km s^{-1}, respectively (Johnson & Soderblom 1987), which place the system in the thin disc population (Bensby et al. 2003), and outside the young disc population limits (Leggett 1992). Other stellar youth indicators for GJ 207.1, such as its UV and X-ray overluminosity, relatively strong Hα emisson, and flaring activity can be explained by the fast rotation of the M-dwarf component caused by the spin-orbit synchronisation at the short orbital period of the binary. The characteristic age of the thin disc population is younger than ~8 Ga (Fuhrmann 1998), which is compatible with the cooling age of the putative white dwarf. The upper limit of ~8 Ga on the age, set by the kinematics of the system, and the lower limit of ~1 Ga, set by the cooling time of the white dwarf, mean that the main-sequence phase of the progenitor star should not have lasted more than ~7 Ga. Only stars with masses $\gtrsim 0.9\,M_\odot$ would reach the white dwarf stage within that time (Marigo et al. 2001) and would yield a final mass $\gtrsim 0.52\,M_\odot$ (Catalán et al. 2008).

4.4.1.2 GJ 912

GJ 912 is a high proper motion M2.5 V star located at a distance of 17.81 ± 0.03 pc. From its galactocentric space-velocity computed by Hawley et al. (1996), this system could be a member of the thin disc population, with an estimated age younger than 8 Ga (Fuhrmann 1998). No companions were found at angular separations between 0.1 arcsec and 3.5 arcsec with AstraLux (Jódar et al. 2013), or at wider separations using low-resolution imaging (Winters et al. 2019). The sensitivity of these surveys at small separations depended, however, on the flux ratio of the components. The rotation period estimated from the $R'_{\rm HK}$ index of the star, $\log(R'_{\rm HK}) = -5.01 \pm 0.19$, is of the order of 42 d (Astudillo-Defru et al. 2017).

Twenty-eight measurements for GJ 912 were obtained with CARMENES between July 2016 and November 2020. Nine archival observations from HARPS and three from FEROS taken between August 2009 and November 2013 are also available. An inspection of all the spectra with `todmor` revealed no secondary peaks in the CCF, indicating either an extreme flux ratio or a small relative RV between the two components. As for GJ 207.1, we used the difference between the CARMENES RVs computed with `serval` and with `todmor` to correct the offset of the FEROS `todmor` RVs, obtaining a value of 17.475 ± 0.002 km s^{-1}.

The orbital parameters resulting from the MCMC analysis are shown in the third column of Table 4.5. The best-fit solution corresponds to a period of 5188^{+58}_{-55} d (about 14.2 a), with an RV semi-amplitude of $1.356^{+0.084}_{-0.074}$ km s^{-1}. The orbit is highly eccentric, $e = 0.6239^{+0.0098}_{-0.0097}$. The RVs and the best-fit solution are shown in Fig. 4.4 as a function of the orbital phase. Using

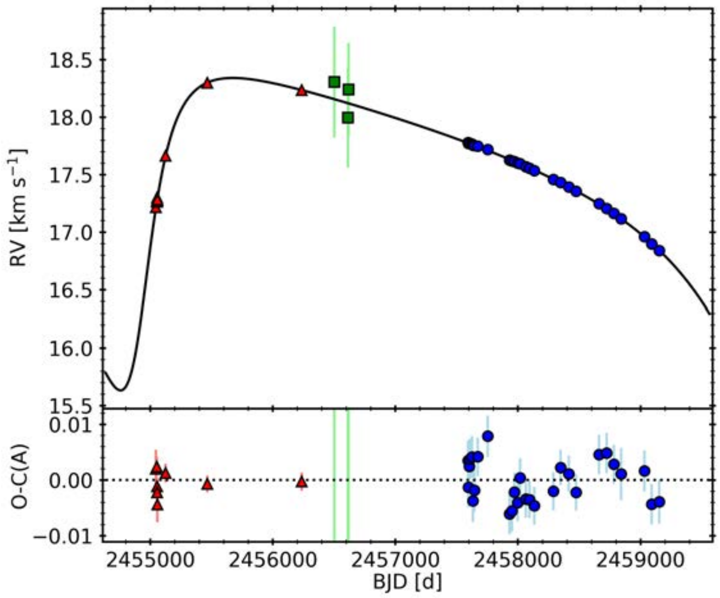

Figure 4.4: Best orbital fit to the RVs of GJ 912 from CARMENES (blue circles), HARPS (red triangles), and FEROS (green squares) as a function of time. Residuals from the best fit are depicted in the bottom panel. Those corresponding to the FEROS observations are outside the Y-axis scale.

the derived mass function $f(M)$ and the estimated mass of the primary component (0.510 M$_\odot$, Table 4.1), we determine a minimum companion mass of $0.0600^{+0.0030}_{-0.0036}$ M$_\odot$, which is compatible with a brown dwarf (i.e. mass lower than 0.072 M$_\odot$, Chabrier et al. 2000a) for inclinations above ~50 deg. Assuming an inclination probability distribution uniform in $\cos i$ (which implies a companion mass function favouring lower-mass companions), this corresponds to a probability of ~63 %. An inspection of the RV residuals of the best fit yielded no significant signals.

We also analysed the available photometry of this object to search for signals of its rotation period. We binned the available SWASP data in nightly bins in order to reduce the scatter. Furthermore, we discarded observations made after BJD = 2 456 000, since they have systematic nightly deviations of more than three magnitudes, and the median of the errors is ten times higher than that of the previous data. This reduced the number of individual epochs in the light curve from 90 025 to only 256. The GLS periodogram shows a significant peak at 165 d. However, the long period was similar to the time span of each season of observation and, after its removal, a significant peak at 41.8 d arises, as shown in Fig. 4.5. Therefore, we attributed the 41.8 ± 1.3 d signal to the rotation period of the star, which is consistent with the period estimated by Astudillo-Defru et al. (2017). No significant signals were found in the ASAS data. Based on the rotation period of this system, we can safely assume that this system is older than, for example, the objects of the cluster NGC 6811, which has an estimated age of 1 Ga (Curtis et al. 2019b,a).

Finally, a constraint on the inclination of the system and, therefore, on the maximum mass of the companion, can be set by using 3.1 years of astrometric data from Hipparcos (Perryman et al. 1997; van Leeuwen 2007). In addition to the five standard astrometric parameters, an astrometric orbit was fitted to the Hipparcos abscissa residuals by a CARMENES project collaborator following the methods described in Reffert & Quirrenbach (2011), from which the inclination and ascending node of GJ 912 were determined via a least squares minimisation. An astrometic orbit was detected with 94 % probability, and the inclination was constrained to be larger than

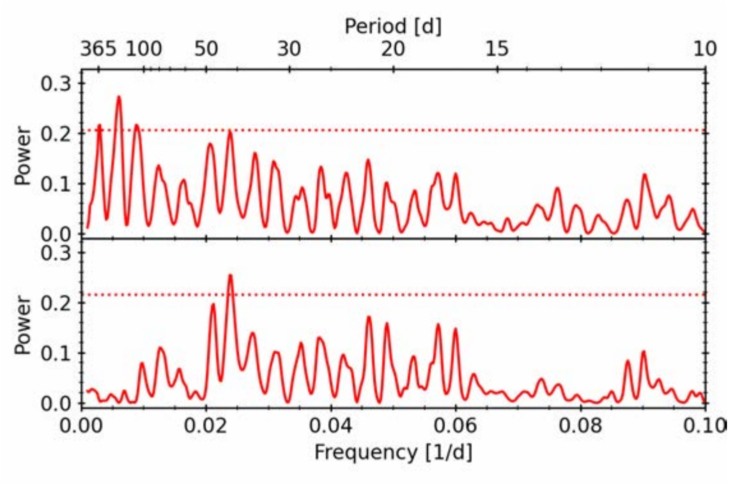

Figure 4.5: GLS periodogram of the SWASP photometry of GJ 912 (*top*) and of the residuals after the removal of the significant signal (*bottom*). The horizontal dotted lines indicate the corresponding 0.1 % FAP level.

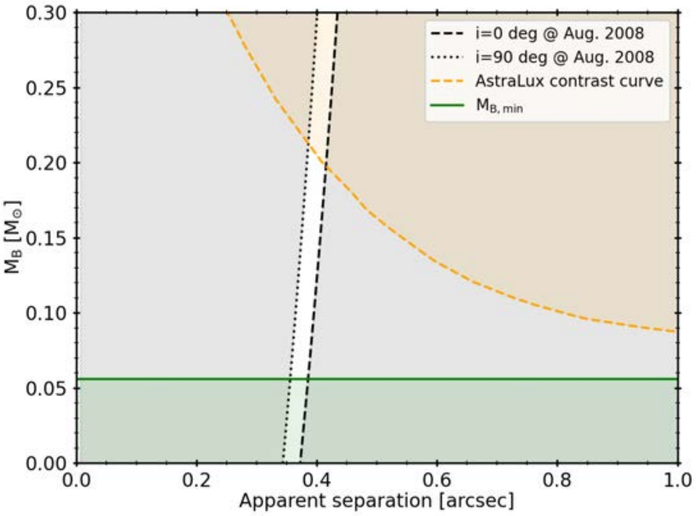

Figure 4.6: Constraint on the mass of the secondary star in GJ 912 as a function of the apparent angular separation of the two components. The orange dashed line represents the contrast curve of the AstraLux observation by Jódar et al. (2013). The green solid line indicates the minimum mass limit computed from our RVs. The dashed and dotted black lines are constraints from RVs on the angular separation at the time of the observation, assuming inclinations between 0 deg (dashed) and 90 deg (dotted). The shaded regions indicate mass values that are not compatible with the observations.

5.5 deg at 1σ. An even more constraining limit can be set from the non-detection of a companion in the AstraLux observation by Jódar et al. (2013), made in August 2008. Assuming the 5 Ga stellar evolutionary model from Baraffe et al. (2015, hereafter BHAC15) and the estimated primary mass ($0.510 \pm 0.020\,M_\odot$, Table 4.5), we converted the brightness contrast curve shown in Fig. 3 by Jódar et al. (2013) into mass detection limits, and show it in Fig. 4.6 as a function of the angular separation. We also show in Fig 4.6 the minimum mass allowed by the radial velocities, and the range of possible angular separations between the components at the date of observation, at any inclination between 0 and 90 deg. We can therefore determine that any companion with a mass above $0.21\,M_\odot$ should be detected in the AstraLux observation, assuming

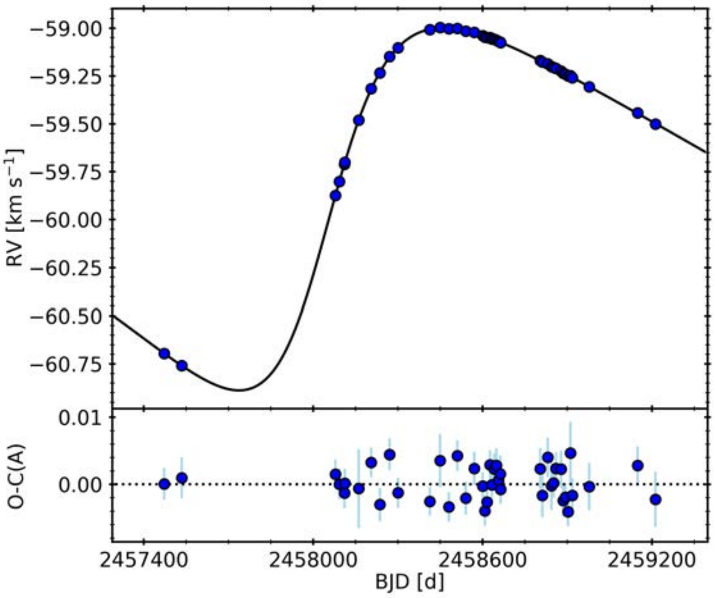

Figure 4.7: Best orbital fit to the RVs of GJ 3626 from CARMENES as a function of time. The residuals from the fit are shown in the bottom panel.

that the companion is a main-sequence star. This limits the inclination to values above ~17 deg, which pushes the probability of the secondary being a brown dwarf up to ~66 %.

4.4.1.3 GJ 3626

Located at a distance of 22.61 ± 0.06 pc, GJ 3626 is an M4.0 V high proper motion star. It has a low activity level, with an Hα pseudo-equivalent width pEW(Hα) = 0.092±0.014 Å (Schöfer et al. 2019), and an upper limit to the projected rotational velocity of 2 km s^{-1} (Reiners et al. 2018b). No rotation period has been reported for this star. In the context of the sample selection of the CARMENES input catalogue, Cortés-Contreras et al. (2017) searched for low-mass companions to this star using the high-resolution lucky imaging instrument FastCam. From these observations, performed in March 2012, they excluded the presence of companions with $\Delta I < 4$ mag between 0.2 and 2 arcsec, and with $\Delta I < 5$ mag beyond 2 arcsec. In addition, observations taken for the Robo-AO adaptative optics M-dwarf multiplicity survey (Lamman et al. 2020), performed in January 2016, put limits on companions with $\Delta i' < 2$ mag beyond 0.1 arcsec, $\Delta i' < 3$ mag beyond 0.5 arcsec, and $\Delta i' < 4$ mag beyond 1 arcsec.

We observed GJ 3626 with CARMENES between March 2016 and November 2020, obtaining 42 spectra. We searched for the signature of a secondary component in the spectra using `todmor`, but no additional peaks in the CCF were detected. Therefore, we used the high-precision RVs computed with `serval` to determine the orbital parameters of the system as an SB1. However, to measure the absolute centre-of-mass RV, we used the RVs computed with `todmor` using synthetic spectra.

We show in Fig. 4.7 the best-fitting orbital solution; the parameters are listed in Table 4.5. The solution corresponds to a rather eccentric ($e = 0.4257^{+0.0029}_{-0.0028}$) orbit with a period of 3009^{+37}_{-35} d (about 8.24 a) and a semi-amplitude of $0.9431^{+0.0053}_{-0.0053}$ km s^{-1}. From the mass function computed from the orbital parameters and the primary component mass (0.418 ± 0.018 M$_\odot$; Table 4.1),

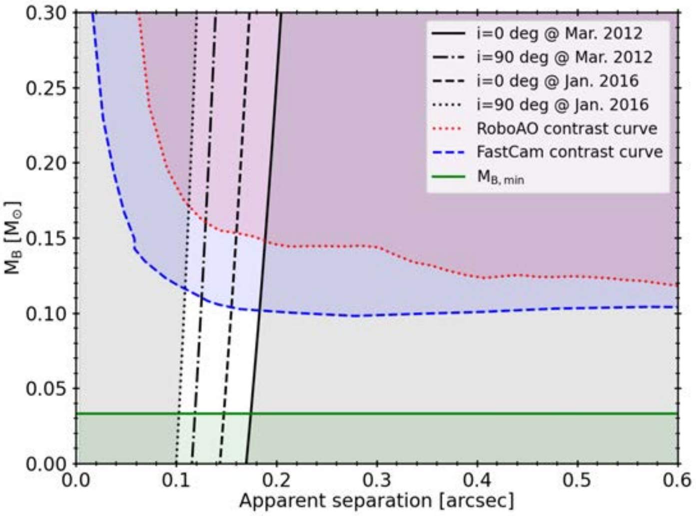

Figure 4.8: Constraints on the mass of the secondary star in GJ 3626 as a function of the apparent angular separation of the two components. The red dotted and blue dashed lines represent the contrast curves of the Robo-AO and FastCam observations, respectively. The green solid line indicates the minimum mass limit computed from RVs. The solid and dot-dashed lines, and the dashed and dotted lines are constraints from RVs on the angular separation at the time of the FastCam and Robo-AO observations, respectively, for orbital inclinations between 0 and 90 deg. The shaded regions indicate mass values that are not compatible with the observations.

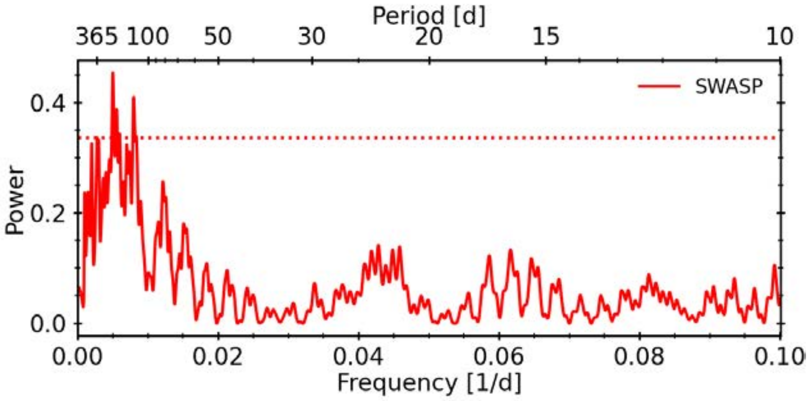

Figure 4.9: GLS periodogram of the SWASP photometry of GJ 3626. The horizontal dotted line indicate the corresponding 0.1 % FAP level.

we calculate a minimum mass of $0.0331^{+0.0010}_{-0.0011}\,M_\odot$ for the secondary component, well below the brown dwarf mass limit. We sampled the posterior distribution of minimum masses for 10^5 random values of the inclination, assuming a uniform distribution in cos i, and estimated a true secondary mass of $0.039^{+0.025}_{-0.005}\,M_\odot$ and an 87 % chance of it being a brown dwarf.

As an additional constraint, and as we did for GJ 912, we used the Robo-AO (Lamman et al. 2020) and the FastCam (Cortés-Contreras et al. 2017) contrast curves. Using the 5 Ga BHAC15 stellar evolutionary model and the estimated primary mass, we again converted the brightness contrast curves into mass detection limits, which are shown in Fig. 4.8 as a function of the orbital separation. We also illustrate in Fig. 4.8 the possible range of apparent angular separations of the two components, given any inclination between 0 and 90 deg, at the time of the FastCam and RoboAO observations. It can be seen from this figure that a companion with a mass above 0.11 $M_\odot$ would have been detected in the FastCam observations. Using this limit as an upper bound to the companion mass, we set a lower bound to the inclination of the system to 19 deg, pushing the probability of the secondary component being a brown dwarf up to 93 %.

We also analysed the available photometry from SWASP to look for signals induced by rotation. We first removed outliers using a 3 σ clipping procedure and binned the light curve into nightly bins, resulting in 96 epochs between May 2004 and June 2007. The GLS periodogram, shown in Fig. 4.9, shows a significant peak at 199 d. However, the photometry is divided into two different subsets of less than 200 days, with ~1 000 days in between, which makes the interpretation of this signal difficult. Therefore, it is unclear whether this signal may be due to rotation. As a further check, we analysed the residuals from the fits to the RV curve and the CARMENES activity indicators in order to look for significant rotation signals, but none was found.

4.4.1.4 LP 427-016

LP 427-016 is an M3.0 V star located at a distance of 22.98 ± 0.03 pc. From its galactocentric space velocity, it was classified as a member of the Local Association kinematic group (Cortés-Contreras 2016), with an estimated age between 10 and 150 Ma (Bell et al. 2015). The Hα emission shows low levels of chromospheric emission, pEW(Hα) = -0.10 ± 0.01 Å, and the spectroscopic observations are consistent with slow rotation, $v \sin i$ <2 km s^{-1} (Schöfer et al. 2019; Jeffers et al. 2018). Furthermore, Díez Alonso et al. (2019) reported a rotation period of 89.9 ± 2.0 d using ASAS photometry, although with a poor FAP of 1.8 %. Considering its hypothetical young age, the star would be expected to be magnetically active (Terndrup et al. 2000; West et al. 2008; Fang et al. 2018) and to have a shorter rotation period (Barnes 2003; Curtis et al. 2019b). However, this is not supported by the measured activity indicators or the rotation period of this star, pointing towards an age of the system older than suggested by its kinematic assignation (see López-Santiago et al. 2009, for an assessment of the contamination by old stars in purely kinematic searches of members of nearby young moving groups).

No close companions with $\Delta I < 3$ mag at an angular separation greater than 0.2 arcsec were found in observations from the FastCam high-resolution lucky imager (Cortés-Contreras et al. 2017). In addition, observations from the Robo-AO adaptative optics M-dwarf multiplicity survey (Lamman et al. 2020) ruled out companions with $\Delta i' < 1$ mag beyond 0.1 arcsec, and $\Delta i' < 5$ mag beyond 1 arcsec.

This object was spectroscopically observed with CARMENES for a total of 22 times, between March 2016 and November 2020. Two FEROS observations, obtained two years before those of CARMENES, are also available. The RVs for this system are listed in Table A.6, and shown in Fig. 4.10. The CARMENES RVs show an unambiguous long-term trend indicating binarity, but no companion was detected with `todmor`. In order to move the FEROS RVs to the same offset level as the CARMENES RVs, we again used the difference between the CARMENES RVs computed using `todmor` and `serval`. An attempt to determine the best orbital fit resulted in the MCMCs diverging towards long periods, as expected. The best circular orbit fit, shown in Fig. 4.10, corresponds to a period of ~35 500 d (97 a), although the circular model is compatible ($\Delta \ln \mathcal{L} < 15$) with orbital periods between ~6 400 d (17.5 a) and ~100 000 d (274 a). We therefore adopt 6 400 d as the shortest possible period for a circular orbit, which yields a semi-amplitude of 0.25 km s^{-1} and a minimum secondary mass of 0.012 $M_\odot$.

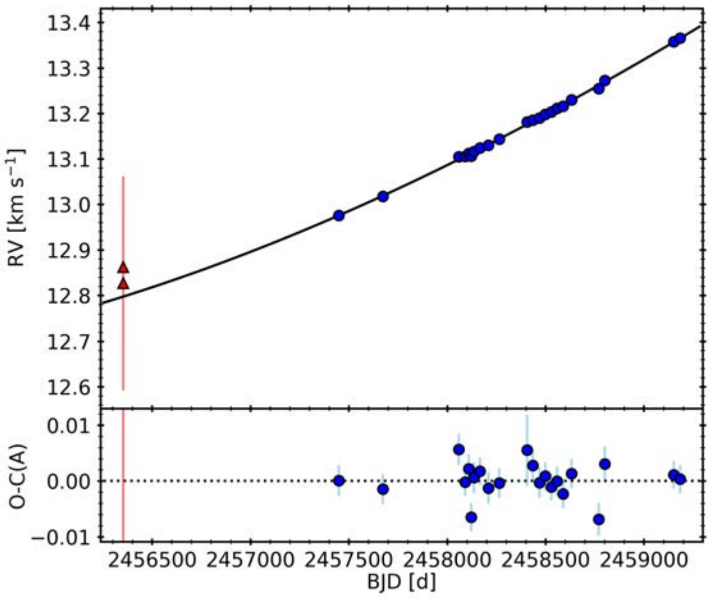

Figure 4.10: Best fit to the RVs of LP 427-016 taken with CARMENES (blue circles) and FEROS (red triangle), assuming a circular orbit. The bottom panel shows the residuals from the fit. Those corresponding to FEROS observations are outside the Y-axis scale.

More stringent bounds can be derived from the available observations with high-resolution imaging. Figure 4.11 shows the contrast curves obtained from the FastCam and Robo-AO high-resolution observations. We used the BHAC15 5 Ga evolutionary models to estimate the mass limit of the secondary component from the magnitude difference of the contrast curves and the mass of the primary component as for GJ 912. We also plot the minimum mass corresponding to the minimum allowed period derived from the RVs and the lower limit to the apparent separation (all assuming $e = 0$) computed with Kepler's third law and the lower bound to the period. From this figure, we conclude that any main-sequence companion with a mass higher than ~0.13 $M_{\odot}$ would have been detected in high-resolution imaging observations. From this value, we obtain an upper bound to the period of ~29 000 d (79 a). We suggest that the secondary component may have a mass in the range 0.011–0.13 M$_{\odot}$, at an angular separation between 0.5 arcsec and 1.3 arcsec. We list in Table 4.5 all the limits to the orbital parameters resulting from this analysis.

Allowing for non-zero eccentricity would affect the lower limit of the period, which could be as small as the time span of the data, ~3 000 d. Extreme values of the eccentricity would also allow very small apparent projected separations, increasing the upper limit to the mass of the companion.

LP 427-016 was photometrically monitored by the ASAS, NSVS, and SWASP surveys. As shown in Fig. 4.12, the GLS periodogram shows significant signals at periods of 33.2 ± 1.3 d and 38.9 ± 4.8 d for the NSVS and SWASP data, respectively, which are compatible within their errors. The second highest peak in the periodogram of the NSVS data, also significant and consistent with the window aliasing of the 33.2 ± 1.3 d period, is at a period of 37.2 ± 1.3 d, coincident with the signal found in the SWASP data. In the ASAS data, we find excess power at a period of 89.9 d as claimed by Díez Alonso et al. (2019), but with a significance much lower than our 0.1 % FAP threshold. Given that the time-span of the SWASP data is five times longer than that of NSVS, although less precise, we attribute the 38.9 ± 4.8 d signal to the rotation

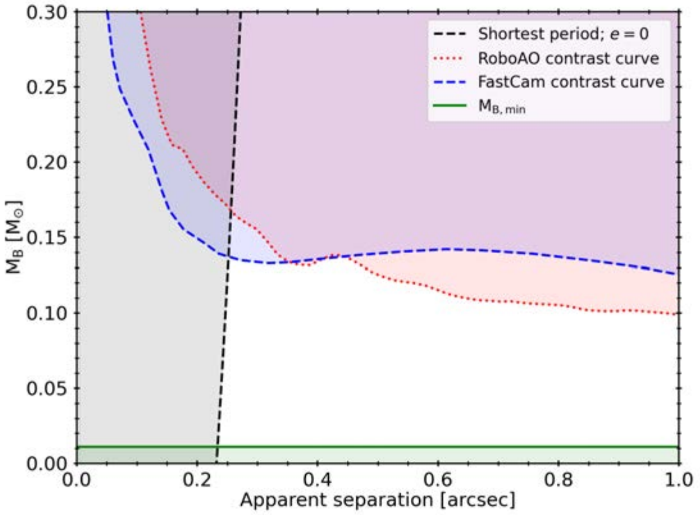

Figure 4.11: Constraints on the mass of the secondary star in LP 427-016 as a function of the apparent separation of the two components. The red dotted and blue dashed lines depict the contrast curves of the RoboAO and FastCam observations, respectively. The green line indicates the minimum mass limit computed from RVs, of 0.011 $M_\odot$. The black dashed line is the apparent separation for the lower limit to the period, assuming a circular orbit and $i = 90$ deg. The shaded regions indicate solutions that are not consistent with the observations.

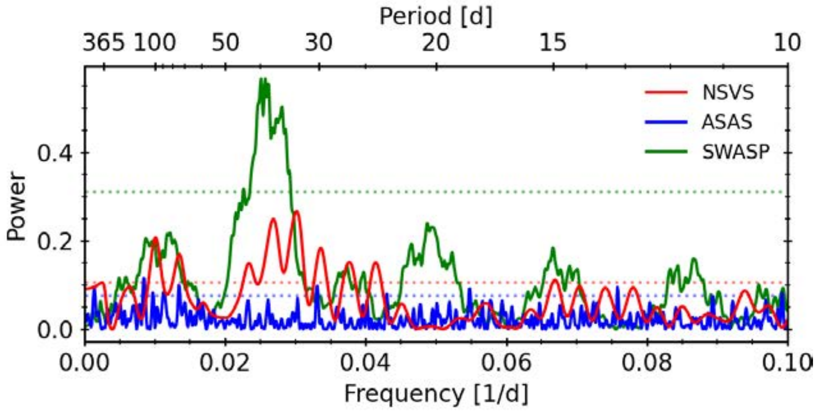

Figure 4.12: GLS periodogram of the NSVS (red), ASAS (blue), and SWASP (green) photometry of LP 427–016. The horizontal dotted lines of each colour indicate the corresponding 0.1 % FAP level.

period of the more massive star. As in the case of GJ 912, based on the rotation period of this system, we can safely assume that it is older than the objects of the cluster NGC 6811, with an estimated age of 1 Ga (Curtis et al. 2019b,a), and therefore, rule out its membership to the Local Association kinematic group as suggested by its space velocity, which, incidentally, could be biased by the binarity of the system.

4.4.1.5 GJ 282 C

GJ 282 C is an M1.0 V star located at a distance of 14.23 ± 0.03 pc. It is active, with pEW(Hα) = −0.86 ± 0.01 Å (Schöfer et al. 2019), and also a bright X-ray source as observed by the *ROSAT* satellite (Voges et al. 1999; Kiraga 2012). Díez Alonso et al. (2019) reported a rotational period of 12.2±0.1 d, based on ground-based photometry from ASAS. The projected rotational velocity is 3.1 ± 1.5 km s^{-1} (Reiners et al. 2018b). Cortés-Contreras et al. (2017) observed this object with the FastCam high-resolution lucky imager, but no companions were detected. Poveda et al. (2009) determined that GJ 282 C is bound to the GJ 282 AB system, a pair of K3 V and K7 V stars (Reid et al. 1995; Montes et al. 2018), based on their small projected and radial separations, 55 300 and 25 000 au, respectively, their similar proper motions and RVs, and their identification as X-ray sources in the *ROSAT* catalogue. Nevertheless, Poveda et al. (2009) could not attribute the small discrepancies observed between the values of the proper motions and the RVs to the A–B orbit. From the kinematics of GJ 282 A, and therefore also GJ 282 C, Tabernero et al. (2017) classified this system as a member of the Ursa Major moving group, with an estimated age of about 300 Ma (Soderblom & Mayor 1993).

In recent years, several works claimed the detection of a secondary companion to GJ 282 Ca (called GJ 282 Cb), although none of them provides a robust determination of the orbital parameters and masses. In order to determine the presence of perturbing objects in nearby stars, Kervella et al. (2019) searched for proper motion anomalies between the long-term proper motion vector, computed from the difference in the astrometric position between Hipparcos and *Gaia* and the proper motion measurements from the two catalogues. From this study, Kervella et al. (2019) obtained a lower limit to the secondary mass, normalised at an orbital radius of 1 au, of $35.4^{+9.9}_{-3.8}\,\mathrm{M_{Jup}\,au^{-1/2}}$. Furthermore, from high-contrast imaging observations made with NACO at the VLT, Kammerer et al. (2019) detected a companion at 441.5 ± 0.02 mas, with an L_p-band contrast of 2.619 ± 0.005 mag, which they classified as a candidate stellar-mass companion. Assuming a primary mass of 0.585 $\mathrm{M_\odot}$, as listed in Table 4.1, and using the 300 Ma BHAC15 models, this contrast would correspond to a ∼0.18 $\mathrm{M_\odot}$ companion. Finally, Grandjean et al. (2020) reported the detection of a low-mass stellar companion from the analysis of the HARPS RV data, in which they found a long-term trend with an amplitude of 700 m s^{-1} and also a short-term variation with an amplitude of 50 m s^{-1}. Although they attributed the short-term variation to magnetic activity, they modelled the data with two Keplerian terms, obtaining a long period of 8500 ± 1900 d and an eccentricity of 0.55 ± 0.04, corresponding to a companion with a minimum mass of $29^{+18}_{-16}\,M_{\mathrm{Jup}}$, and a period of 22 d for the short-term signal. However, this short period is not consistent with the rotation period of 12.2 d reported from photometry (Díez Alonso et al. 2019), which would be the expected variability timescale for activity-related signals.

We observed GJ 282 C with CARMENES between January 2016 and November 2020, gathering a total of 42 spectra. Additionally, we retrieved 38 and 3 spectra from the HARPS and FEROS archives, respectively. A preliminary analysis of the RVs obtained with `todmor` revealed a clear long-period modulation with an amplitude of ∼4 km s^{-1}. No signature of the companion was found in the spectra. As for the other systems, we used the difference between the CARMENES RVs derived with `todmor` and the RVs from `serval`, of −17.4637±0.0009 km s^{-1}, to correct the offset of the FEROS RVs, which could not be computed with `serval`. As mentioned, in addition to the RVs, three high-contrast images acquired with NACO in January 2015, February 2016, and March 2016, were also analysed by CARMENES project collaborators to derive the angular separations and position angles of the two components, which we list in Table 4.3, together with the measured magnitude differences.

We simultaneously fitted the RVs and the differential astrometry using the code `orvara`, which also uses the acceleration on the plane of the sky from the Hipparcos-*Gaia* Catalog of Accelerations. To avoid systematic effects due to the different filters used in the astrometric observations,

Table 4.6: Orbital parameters for the astrometric binary GJ 282 C.

Parameter	System
Orbital parameters	
P [d]	6591^{+136}_{-177}
T_0 [BJD]	2460004^{+90}_{-91}
K_{Ca} [km s^{-1}]	$2.66^{+0.12}_{-0.12}$
$e \sin \omega$	$-0.0109^{+0.0054}_{-0.0057}$
$e \cos \omega$	$-0.213^{+0.010}_{-0.010}$
e	$0.213^{+0.010}_{-0.010}$
ω [deg]	$183.0^{+1.5}_{-1.4}$
Ω [deg]	$136.95^{+0.46}_{-0.46}$
a [au]	$6.224^{+0.081}_{-0.080}$
i [deg]	$93.96^{+0.55}_{-0.55}$
$\gamma_{\rm CARM}$ [km s^{-1}]	$+0.89^{+0.11}_{-0.12}$
$\gamma_{\rm HARPS}$ [km s^{-1}]	$-0.20^{+0.11}_{-0.12}$
γ [km s^{-1}]	$-18.35^{+0.11}_{-0.12}$
$\sigma_{\rm ALL}{}^{a}$ [m s^{-1}]	$10.52^{+0.80}_{-0.71}$
Derived parameters	
M_{Ca} [$M_\odot$]	$0.554^{+0.058}_{-0.049}$
M_{Cb} [$M_\odot$]	$0.1881^{+0.0048}_{-0.0047}$
q	$0.340^{+0.034}_{-0.034}$
K_{Cb} [km s^{-1}]	$7.83^{+0.49}_{-0.41}$
$\mu_\alpha \cos \delta$ [mas a^{-1}]	$+60.72^{+0.38}_{-0.29}$
μ_δ [mas a^{-1}]	$-278.61^{+0.32}_{-0.44}$
ϖ [mas]	$71.053^{+0.027}_{-0.027}$
Estimated parameters	
$P_{\rm rot,Ca}$ [d]	12.15 ± 0.02
$P_{\rm rot,Cb}$ [d]	0.3257 ± 0.0002
Fit quality	
rms [km s^{-1}]	0.037

Notes. $^{(a)}$ `orvara` code only fits a single jitter term to all the RV sets.

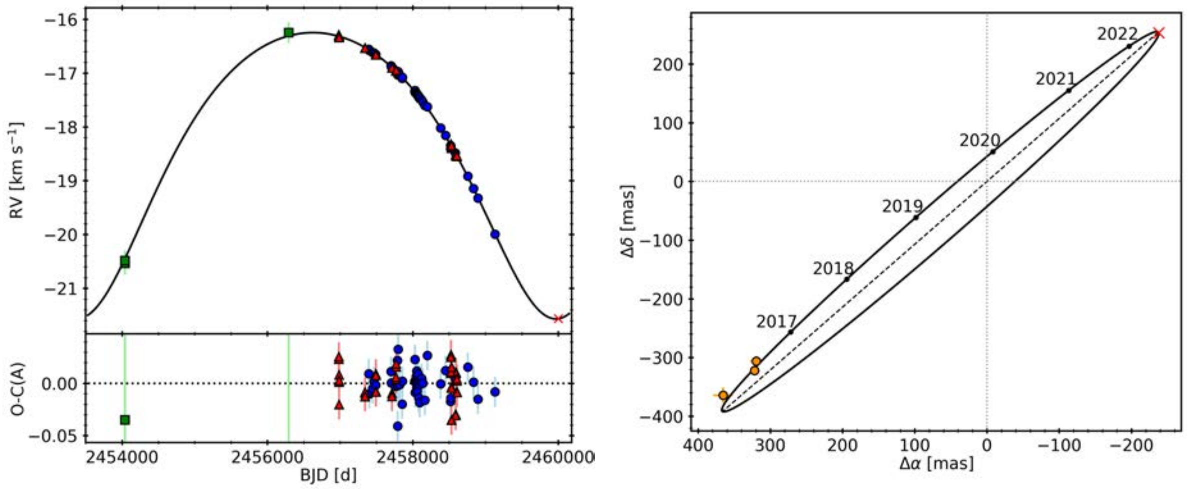

Figure 4.13: Best joint orbital fit to the spectroscopic data and differential astrometry of GJ 282 C. *Left*: RVs of GJ 282 C from CARMENES (blue cicles), HARPS (red triangles) and FEROS (green squares), as a function of time. The residuals from the fit are shown in the bottom panel, except for FEROS, which are outside the Y-axis scale. *Right:* Differential astrometry between GJ 282 Ca and GJ 282 Cb. Orange circles show the astrometric relative position measured from NACO observations. The red cross depicts the position of periastron, while the dashed line indicates the line of nodes.

we scaled the errors of the separation and position angle listed in Table 4.3 by a constant value of 3.7 and 4.5, respectively, so that the reduced χ^2 statistic of the astrometric fit was approximately one. The orbital parameters resulting from the MCMC analysis are listed in Table 4.6, and the best fit to the RVs and to the relative astrometric orbit are shown in Fig. 4.13. The best-fitting model has a period of 6591^{+136}_{-177} d with an eccentricity of $0.213^{+0.010}_{-0.010}$, and an almost edge-on orbit with i =$93.96^{+0.55}_{-0.55}$ deg. From the computed orbital parameters, we derive absolute dynamical masses of $0.554^{+0.058}_{-0.049}$ $M_\odot$ and $0.1881^{+0.0048}_{-0.0047}$ $M_\odot$ for the primary and secondary components, respectively. The mass of the primary is in agreement with the mass derived by Schweitzer et al. (2019), of 0.585 ± 0.025 $M_\odot$, from empirical mass-luminosity calibrations. In addition, the luminosity contrast corresponding to these two masses in the *L*- and *K*-band, estimated from the 300 Ma BHAC15 models, are 2.45 and 2.56, respectively, which are very similar to those computed from the NACO observations, listed in Table 4.3, although their filters do not exactly match those available from the models. The estimated contrast in the *I*-band is 3.0, which lies right at the detection limit of the FastCam high-resolution imaging observations made in March 2014 by Cortés-Contreras et al. (2017), with a predicted angular separation of 500 mas. We find an additional significant signal at 12.1 d in the RV residuals of the best fit, which is in agreement with the rotation period found by Díez Alonso et al. (2019). No more significant signals are found in the data.

We analysed the available photometry, listed in Table 4.2, to search for rotational signals. As shown in the GLS periodograms in Fig. 4.14, we found significant periods at 12.15 ± 0.03 d, 12.21 ± 0.09 d, 12.27 ± 0.6 d, and 12.2 ± 2.5 d in the ASAS, SWASP, OSN, and TESS data, respectively, confirming the period found by Díez Alonso et al. (2019) using the ASAS photometry only. We also found short-period modulations of small amplitude in the TESS data, which could be produced by the companion. To compute their period, we fitted the TESS light curve with a GP, using a sum of two quasi-periodic kernels as a covariance function. We show the TESS photometry with the best-fit GP model in Fig. 4.15. We obtained periods of

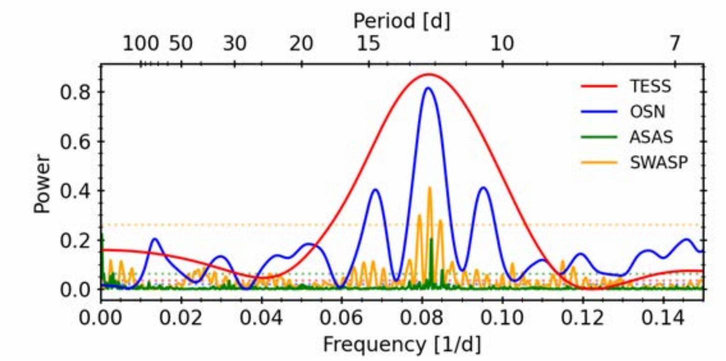

Figure 4.14: GLS periodogram of the TESS (red), OSN (blue), ASAS (green), and SWASP (orange) photometry of GJ 282 C. The horizontal dotted lines of each colour indicate the corresponding 0.1 % FAP level.

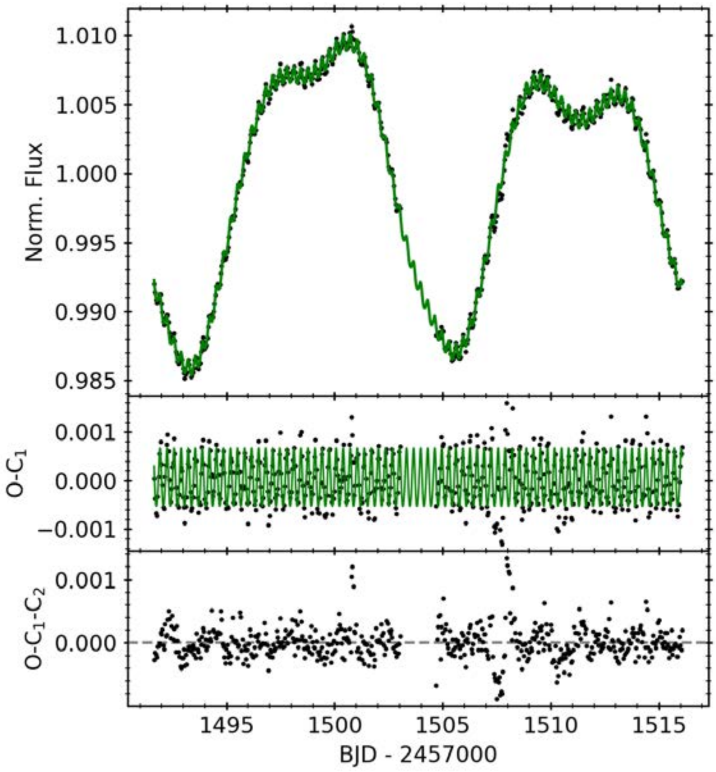

Figure 4.15: *Top*: TESS photometry of GJ 282 C with an hourly binning and the GP fit using as covariance function the sum of two quasi-periodic kernels, in green. *Middle:* Residuals and best short-period GP model after subtracting the long-period model. *Bottom:* Residuals of the TESS data.

12.41 ± 0.10 d and 0.32574 ± 0.00018 d for the large- and small-amplitude modulations, respectively. The estimated contribution of the companion to the total flux in the TESS band, based on the luminosity contrast measured by direct imaging, is around 3 %. The short-period modulations, with an amplitude of 0.12 % (see in the middle panel of Fig. 4.15), could thus be explained by 4 % modulations on the brightness of the companion. Another possibility is that the modulation is produced by a background star located within the TESS photometric mask around this object (Gaia EDR3 3060789275061364480). This star has a TESS-band magnitude of T = 12.0 mag, and it is thus brighter than GJ 282 Cb, which has an estimated T of ~12.6 mag. The background star accounts for 7 % of the total flux, which means that variations of 1.7 % in its brightness would be required to produce the observed modulation. With an effective temperature for the background star of 6000 K estimated from *Gaia* data, such variations would be highly unusual (McQuillan et al. 2012). Given the young age and strong activity of GJ 282 C, we suggest that the short-period photometric signal is plausibly produced by the low-mass companion rather than the background star. We attribute the 12.2 d signal to the rotation of the primary component. In this case, we adopt the period from the ASAS photometry because the light curve covers a large number of cycles, thus leading to a tighter constraint.

Finally, using the systemic radial and astrometric properties derived from our analysis, listed in Table 4.6, we recalculated the galactocentric velocity, obtaining 25.1, −2.5, and −7.8 km s^{-1} for the U, V, and W components, respectively. These values are very similar to those of GJ 282 A listed by Tabernero et al. (2017) and compatible with members of the Ursa Major moving group (Montes et al. 2001), which supports the physical association of the quadruple system. Moreover, the absolute value of pEW(Hα) of GJ 282 C is similar to or larger than the values for members of the Hyades (~650–800 Ma; Douglas et al. 2019, and references therein) measured by Terndrup et al. (2000) and Fang et al. (2018). Likewise, the X-ray luminosity $\log L_X = 29.29 \pm 0.17$ erg s^{-1} (Voges et al. 1999) is also compatible with members of the Hyades (Núñez & Agüeros 2016), even if we assume that the Ca and Cb components have similar levels of X-ray emission. The rotational periods of GJ 282 Ca and Cb are longer than those measured by Rebull et al. (2016) for members of the Pleaides (~110–130 Ma; Stauffer et al. 1998; Dahm 2015), but shorter than for Praesepe stars (~600–750 Ma; Douglas et al. 2019, and references therein) as measured by Douglas et al. (2016). All this information supports the membership of GJ 282 C to the Ursa Major moving group that, considering the age of this association, makes this one of the youngest multiple stellar systems with known ages and dynamical masses (Lodieu et al. 2020). Furthermore, the masses are comparable with field objects of similar spectral type (Benedict et al. 2016, and references therein), which indicates that these low-mass stars in the mass range of 0.2–0.5 M$_\odot$ have already arrived to the main-sequence phase at the age of the moving group (Zapatero Osorio et al. 2014).

4.4.2 Double-line spectroscopic binaries (SB2s)

4.4.2.1 EZ Psc

Located at a distance of 15.359 ± 0.010 pc, EZ Psc is an M4.0 V star with a large proper motion. It shows high levels of magnetic activity, with pEW(Hα)=-4.16 ± 0.06 Å, and several detected flaring events (Gershberg et al. 1999; Rodríguez Martínez et al. 2020). Furthermore, it is also an extreme ultraviolet source (Christian et al. 1999), and an X-ray bright source as detected by the Einstein Slew Survey (Elvis et al. 1992) and *ROSAT* (Voges et al. 1999). Norton et al. (2007) and Newton et al. (2016) measured a rotation period of 4.79 d using photometric data from SWASP and MEarth, respectively, consistent with the rotation period of 4.83 ± 0.06 d derived by Díez Alonso et al. (2019) from the same dataset. Using spectroscopic youth indicators such as surface gravity-sensitive indices, lithium absorption and Hα emission, Shkolnik et al. (2009) derived an age upper limit to EZ Psc of 300 Ma. Additionally, it is a common proper motion companion to the M4.0 V star G 32–7 (Heintz 1987; Weis 1991), which was determined to be a bound companion located at an angular separation of 25 arcsec (Lépine & Bongiorno 2007; Poveda et al. 2009), equivalent to 384 au using the parallax from *Gaia*.

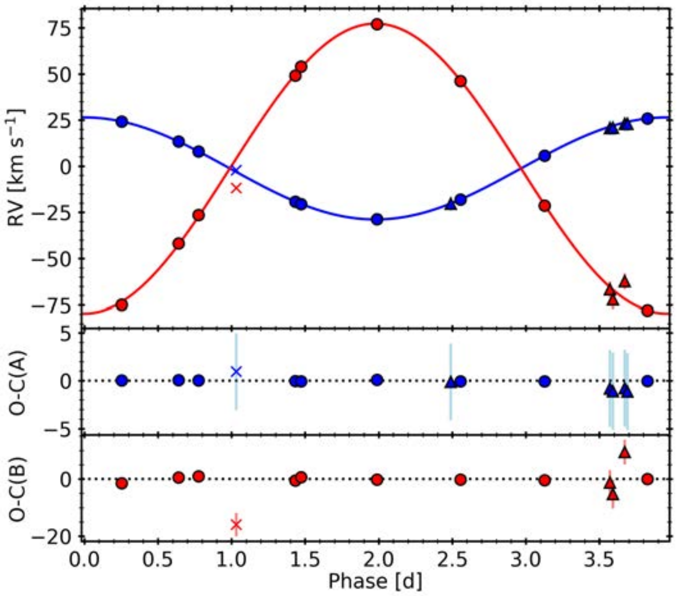

Figure 4.16: Best-fitting model to the `todmor` RV curves of EZ Psc as a function of the orbital phase. Blue and red colours correspond to the primary and secondary components, respectively. Circular and triangular symbols correspond to the RVs from CARMENES and FEROS, respectively, while the crosses indicate data points not used in the fit. The residuals from the fit are shown in the bottom panels.

We took 11 spectroscopic observations of EZ Psc with the CARMENES spectrograph between July 2016 and December 2018. Additionally, we gathered five spectra from FEROS which were not included in Baroch et al. (2018), expanding the time span of the data to 5.5 years. A first inspection of the spectra with TODCOR revealed a faint secondary companion with a flux ratio of 0.10, close to the detection limit of TODCOR. Due to the low exposure time of one spectrum, we could not detect the secondary component, and obtained a highly uncertain primary RV. In another spectrum, the blending of lines due to the small RV difference between the two components resulted in biased RV measurements, as shown by the cross symbols in Fig. 4.16. We discarded these two spectra for further analysis. We could only detect the secondary signal in three out of the five FEROS spectra, obtaining much larger uncertainties than with CARMENES. This is probably caused by the lower flux ratio at the wavelength range of FEROS and because some spectra have a lower SNR. The combined analysis of the RVs from CAMRENES and FEROS resulted in the orbital parameters listed in Table 4.7, and in the best orbital fit shown in Fig. 4.16. For the analysis, we assumed both circular and eccentric orbits, resulting in solutions with non-significant likelihood differences, $\Delta \ln \mathcal{L}$=0.1. From the likelihood ratio test (see Sect. 3.4.1.1), we can reject the eccentric hypothesis with a 90 % confidence. The best circular orbit fit yields an orbital period of $3.956511^{+0.00072}_{-0.00073}$ d and minimum masses of $0.3620^{+0.0037}_{-0.0037}$ $M_{\odot}$ and $0.12757^{+0.00089}_{-0.00090}$ $M_{\odot}$, resulting in a mass ratio of 0.3524 ± 0.0016. These results are in perfect agreement with those published in Baroch et al. (2018), in which we left the eccentricity as a free parameter, obtaining a negligible eccentricity $e = 0.00220^{+0.00096}_{-0.00090}$.

Finally, we searched for rotation signals in the photometric data of EZ Psc by doing a GLS periodogram of the MEarth light-curve, which we show in Fig. 4.17. We obtain a clear and very significant peak at 4.80 ± 0.10 d, which produces a modulation in the light curve with a semi-amplitude of 5.5 mmag. The period found in the periodogram is consistent with the periods found by Norton et al. (2007), Newton et al. (2016), and Díez Alonso et al. (2019).

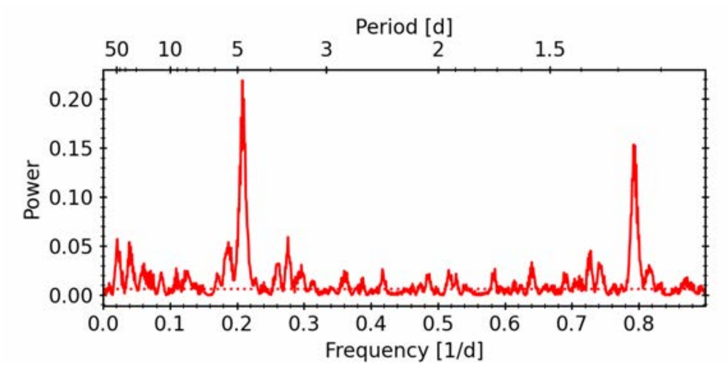

Figure 4.17: GLS periodogram of the MEarth photometry of EZ Psc. The horizontal dotted line indicates the corresponding 0.1% FAP level.

Given the low flux ratio determined with `todmor`, we consider the period of 4.80 ± 0.10 d as the rotation period of the brightest component. Although we would expect that an evolved system with an orbital period lower than 8–10 d have its rotation period synchronized with the orbital period (Mazeh 2008), this is not the case for EZ Psc, which may be an indication of the youth of the system, as indicated by the age upper limit of 300 Ma derived by Shkolnik et al. (2009). In addition, given the semi-major axis of the system, the probability of having eclipses is of ~10%, but none was found in the available light curves.

4.4.2.2 GJ 1029

The object GJ 1029, located at a distance of 12.51 ± 0.04 pc, is an M5.0 V star with one of the largest known proper motions (Giclas et al. 1961), with a value larger than 1.9 arcsec a^{-1}. It is an inactive star, with pEW(Hα)=−0.116 ± 0.017 Å and no excess emission in X-ray or NUV, from which Schneider et al. (2011) put an bottom limit to its age of 600 Ma. Newton et al. (2016) determined a rotation period of 23.2 d from the analysis of the MEarth photometry. No companions with $\Delta z > 3$ mag were found beyond 100 mas with the imager AstraLux (Janson et al. 2014). Furthermore, in the context of the CARMENES input catalogue, Cortés-Contreras et al. (2017) observed GJ 1029 with the imaging instrument FastCam, from which they excluded the presence of companions with $\Delta I > 4$ mag beyond 0.2 mas.

We gathered 21 high resolution spectra of GJ 1029 from CARMENES, which were taken between August 2018 and October 2019. Using `todmor`, we detected the spectroscopic signal of two different components, which yielded a flux ratio of 0.36. We could detect the secondary signal in all observations. However, the proximity in RV between the two components in 7 spectra introduced a systematic bias in the RVs of the secondary component, as illustrated by the cross markers in Fig. 4.18. We did not use these secondary radial velocities in our analysis. Furthermore, an additional 13 pairs of radial velocities were obtained by Winters et al. (2020) from spectra taken with the TRES spectrograph in 2017, using TODCOR and a spectra of Barnard star as a template. Using these RVs alone, Winters et al. (2020) computed orbital parameters of GJ 1029 compatible to those obtained in Baroch et al. (2018).

We jointly analysed the RVs from CARMENES and from Winters et al. (2020). We obtained a period of $95.586^{+0.076}_{-0.077}$ d and an eccentricity of $0.3742^{+0.0039}_{-0.0040}$. The minimum masses derived from the orbital parameters are 0.01926 ± 0.00054 and 0.0142 ± 0.0025 $M_{\odot}$, which yield a mass

Table 4.7: Computed and derived parameters for the SB2 systems.

Parameter	System									
	EZ Psc	GJ 1029	Ross 59	UCAC4 355-020729	LP 790-2	GJ 3612	GJ 1182	UU UMi	LP 395-8	GJ 810 A
Orbital parameters										
P [d]	$3.956511^{+0.000072}_{-0.000073}$	$95.586^{+0.076}_{-0.077}$	$725.3^{+2.2}_{-2.0}$	$6.56025^{+0.00030}_{-0.00029}$	$5.922756^{+0.000076}_{-0.000072}$	$119.388^{+0.048}_{-0.048}$	$154.031^{+0.031}_{-0.032}$	5240^{+410}_{-290}	$1.1293284^{+0.0000077}_{-0.0000073}$	$672.92^{+0.59}_{-0.58}$
T_0 [BJD−2 450 000]	$7708.9422^{+0.0017}_{-0.0019}$	$7857.47^{+0.28}_{-0.28}$	$8003.5^{+1.3}_{-1.2}$	$8002.367^{+0.054}_{-0.054}$	$8007.47^{+0.14}_{-0.13}$	$7718.26^{+0.77}_{-0.80}$	$7867.930^{+0.068}_{-0.067}$	5220^{+160}_{-220}	$620.098^{+0.051}_{-0.053}$	$7805.06^{+0.99}_{-0.99}$
K_A [km s^{-1}]	$27.645^{+0.057}_{-0.058}$	$6.867^{+0.036}_{-0.035}$	$2.869^{+0.034}_{-0.035}$	$2.157^{+0.012}_{-0.012}$	$32.496^{+0.065}_{-0.066}$	$10.689^{+0.039}_{-0.037}$	$11.969^{+0.024}_{-0.025}$	$3.82^{+0.44}_{-0.43}$	$36.634^{+0.099}_{-0.098}$	$5.432^{+0.016}_{-0.016}$
K_B [km s^{-1}]	$78.45^{+0.32}_{-0.32}$	$9.31^{+0.12}_{-0.12}$	$8.75^{+0.12}_{-0.12}$	$2.510^{+0.019}_{-0.019}$	$56.19^{+0.14}_{-0.14}$	$20.91^{+0.12}_{-0.12}$	$17.927^{+0.093}_{-0.093}$	$6.42^{+0.73}_{-0.71}$	$65.14^{+0.23}_{-0.22}$	$6.403^{+0.021}_{-0.021}$
$e\sin\omega$	0 (fixed)	$-0.1798^{+0.0060}_{-0.0060}$	$0.4787^{+0.0094}_{-0.0093}$	$0.0226^{+0.0060}_{-0.0060}$	$-0.0122^{+0.0018}_{-0.0018}$	$-0.3589^{+0.0032}_{-0.0032}$	$-0.5329^{+0.0014}_{-0.0014}$	$0.056^{+0.019}_{-0.021}$	$-0.0002^{+0.0021}_{-0.0023}$	$-0.1904^{+0.0019}_{-0.0020}$
$e\cos\omega$	0 (fixed)	$-0.3281^{+0.0047}_{-0.0046}$	$-0.1513^{+0.0080}_{-0.0093}$	$-0.1055^{+0.0057}_{-0.0058}$	$0.0048^{+0.0017}_{-0.0018}$	$0.0521^{+0.0029}_{-0.0031}$	$0.0577^{+0.0024}_{-0.0024}$	$-0.304^{+0.086}_{-0.068}$	$0.0077^{+0.051}_{-0.053}$	$-0.1515^{+0.0024}_{-0.0024}$
e	0 (fixed)	$0.3742^{+0.0039}_{-0.0040}$	$0.5034^{+0.0085}_{-0.0085}$	$0.1080^{+0.0058}_{-0.0057}$	$0.0132^{+0.0017}_{-0.0016}$	$0.0633^{+0.0035}_{-0.0035}$	$0.5360^{+0.0014}_{-0.0014}$	$0.310^{+0.069}_{-0.087}$	$0.0080^{+0.0028}_{-0.0025}$	$0.2433^{+0.0021}_{-0.0021}$
ω [deg]	0 (fixed)	$208.7^{+1.0}_{-1.0}$	$107.5^{+1.2}_{-1.0}$	$167.9^{+3.2}_{-3.2}$	$291.2^{+8.2}_{-8.1}$	$325.5^{+2.3}_{-2.5}$	$276.18^{+0.26}_{-0.25}$	$169.5^{+3.2}_{-3.7}$	359^{+16}_{-17}	$231.50^{+0.54}_{-0.54}$
$\gamma_{\rm CARM}$ [km s^{-1}]	$-1.324^{+0.033}_{-0.033}$	$-11.319^{+0.035}_{-0.034}$	$27.512^{+0.014}_{-0.014}$	$13.9593^{+0.0088}_{-0.0091}$	$13.596^{+0.037}_{-0.038}$	$-62.159^{+0.023}_{-0.025}$	$-0.800^{+0.018}_{-0.018}$	$-41.28^{+0.09}_{-0.10}$	$-26.680^{+0.068}_{-0.070}$	$-142.1423^{+0.0078}_{-0.0079}$
$\gamma_{\rm FEROS}$ [km s^{-1}]	$1.2^{+1.5}_{-1.5}$	...	...	...	...	...	...	...	...	...
$\gamma_{\rm TRES}$ [km s^{-1}]	...	$-11.187^{+0.039}_{-0.038}$	...	...	...	...	$-0.608^{+0.024}_{-0.024}$	...	...	...
$\gamma_{\rm HARPS-N}$ [km s^{-1}]	...	...	$27.328^{+0.049}_{-0.050}$	...	...	...	...	...	...	...
$\gamma_{\rm CORAVEL}$ [km s^{-1}]	...	...	$27.29^{+0.29}_{-0.25}$	...	...	...	...	...	...	...
$\sigma_{\rm CARM}$ [km s^{-1}]	$0.043^{+0.055}_{-0.031}$	$0.091^{+0.035}_{-0.033}$	$0.031^{+0.015}_{-0.013}$	$0.010^{+0.011}_{-0.007}$	$0.054^{+0.053}_{-0.037}$	$0.067^{+0.038}_{-0.037}$	$0.018^{+0.020}_{-0.013}$	$0.0067^{+0.0070}_{-0.0047}$	$0.11^{+0.12}_{-0.08}$	$0.0072^{+0.0081}_{-0.0050}$
$\sigma_{\rm FEROS}$ [km s^{-1}]	$4.0^{+2.0}_{-1.3}$	...	...	...	...	...	...	...	...	...
$\sigma_{\rm TRES}$ [km s^{-1}]	...	$0.049^{+0.052}_{-0.035}$	...	...	...	...	$0.030^{+0.032}_{-0.021}$	...	...	...
$\sigma_{\rm HARPS-N}$ [km s^{-1}]	...	...	$0.028^{+0.034}_{-0.020}$	...	...	...	...	...	...	...
$\sigma_{\rm HARPS-N}$ [km s^{-1}]	...	...	$0.79^{+0.36}_{-0.29}$	...	...	...	...	...	...	...
Derived parameters										
$q \equiv M_B/M_A$	$0.3524^{+0.0016}_{-0.0016}$	$0.737^{+0.010}_{-0.010}$	$0.3280^{+0.0034}_{-0.0035}$	$0.8593^{+0.0082}_{-0.0080}$	$0.5784^{+0.0017}_{-0.0017}$	$0.5112^{+0.0034}_{-0.0035}$	$0.6677^{+0.0036}_{-0.0036}$	$0.593^{+0.040}_{-0.035}$	$0.5624^{+0.0022}_{-0.0022}$	$0.8484^{+0.0032}_{-0.0032}$
$a\sin i$ [au]	$0.038585^{+0.000021}_{-0.000021}$	$0.13184^{+0.00020}_{-0.00020}$	$0.6693^{+0.0013}_{-0.0013}$	$0.0027974^{+0.0000073}_{-0.0000072}$	$0.048276^{+0.000036}_{-0.000036}$	$0.34607^{+0.00042}_{-0.00040}$	$0.35734^{+0.00027}_{-0.00027}$	$4.70^{+0.10}_{-0.09}$	$0.010564^{+0.000010}_{-0.000010}$	$0.71004^{+0.00089}_{-0.00087}$
$M_A\sin^3 i$ [M$_\odot$]	$0.3620^{+0.0037}_{-0.0037}$	$0.01926^{+0.00054}_{-0.00054}$	$0.0572^{+0.0016}_{-0.0016}$	$0.00003650^{+0.00000061}_{-0.00000061}$	$0.2711^{+0.0016}_{-0.0016}$	$0.2567^{+0.0036}_{-0.0036}$	$0.1539^{+0.0018}_{-0.0018}$	$0.315^{+0.061}_{-0.056}$	$0.07893^{+0.00070}_{-0.00065}$	$0.05706^{+0.00042}_{-0.00042}$
$M_B\sin^3 i$ [M$_\odot$]	$0.12757^{+0.00089}_{-0.00090}$	$0.01420^{+0.00025}_{-0.00025}$	$0.01877^{+0.00042}_{-0.00042}$	$0.00003136^{+0.00000043}_{-0.00000043}$	$0.15679^{+0.00080}_{-0.00079}$	$0.1312^{+0.0013}_{-0.0013}$	$0.10272^{+0.00074}_{-0.00073}$	$0.187^{+0.037}_{-0.034}$	$0.04438^{+0.00033}_{-0.00030}$	$0.04841^{+0.00032}_{-0.00032}$
$P_{\rm rot}$ [d]	4.80 ± 0.10	15–25	14.3 ± 0.7	...	7.33 ± 0.04	> 27	8.94 ± 0.25	90 ± 10	1.129 ± 0.010	138 ± 9
Fit quality										
rms_A [km s^{-1}]	0.84	0.11	0.03	0.13	0.09	0.09	0.06	0.03	0.17	0.03
rms_B [km s^{-1}]	3.17	0.59	0.22	0.26	0.27	0.31	0.41	0.04	0.48	0.03

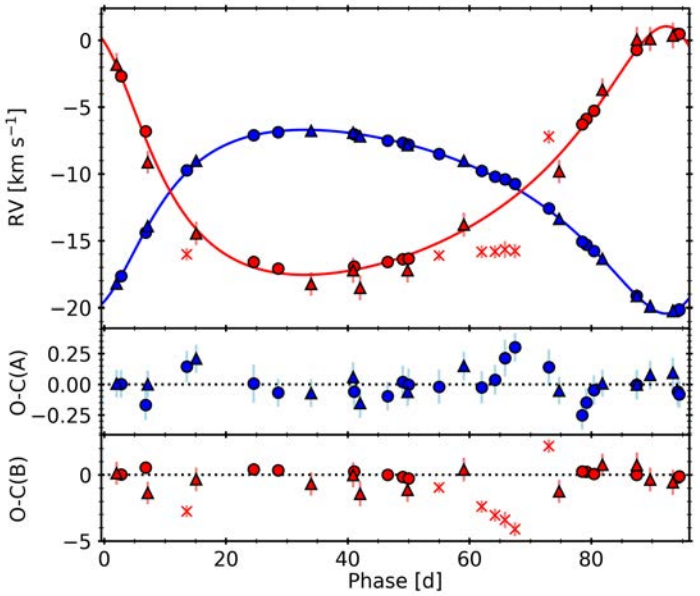

Figure 4.18: Best-fitting model to the `todmor` RV curves of GJ 1029 as a function of the orbital phase. Blue and red colours correspond to the primary and secondary components, respectively. Circular and triangular symbols correspond to the RVs from CARMENES and TRES, respectively, while crosses indicate data points not used in the fit. The residuals from the fit are shown in the bottom panels.

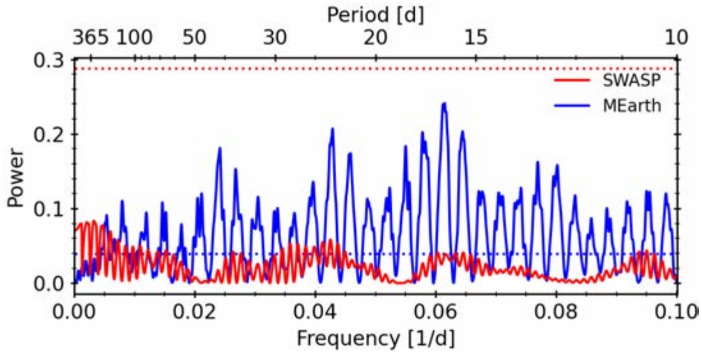

Figure 4.19: GLS periodogram of the SWASP (red) and MEarth (blue) photometry of GJ 1029. The horizontal dotted lines of each color indicate the corresponding 0.1 % FAP level.

ratio of 0.737 ± 0.010. Table 4.7 lists the orbital parameters and uncertainties of the best fit, which we show in Fig. 4.18. The orbital parameters determined in this analysis are compatible within mutual uncertainties with those presented by Baroch et al. (2018). Only the eccentricity is slightly smaller, although consistent within 2σ with respect to the value reported in Baroch et al. (2018). This small difference may be explained by the addition of the data from Winters et al. (2020) and the removal of the RVs from the NIR channel of CARMENES, which improved considerably the fit.

Finally, in order to search for rotation signals, we analyzed the available photometric data from MEarth and SWASP with a GLS periodogram, which we show in Fig. 4.19. We do not find any signal in the SWASP data above the 0.1 % FAP level. The MEarth photometric data shows a significant signal at 16.26±0.24 d, which differs from the rotation period determined by Newton et al. (2016), of 23.2 d using a subset of the same data. We do find a significant peak at 23.3 d, which is the second strongest signal as seen in Fig. 4.19. Given the inconsistencies between these determinations, and the large amount of significant peaks, we cannot confirm any rotation period for GJ 1029, although it may probably be located between 15 and 25 d.

4.4.2.3 Ross 59

The M1.5 V star Ross 59 is a high proper motion object located at a distance of 20.95 ± 0.22 pc. It has a low chromospheric activity, with pEW(Hα)=-0.034 ± 0.010 Å, and a slow projected rotational velocity. Several searches for companions to Ross 59 have been carried out with the use of the imaging instruments FastCam, AstraLux, and RoboAO. No companions beyond 200 mas with $\Delta i' > 1$ are detected in the observations with Robo-AO (Lamman et al. 2020), or with $\Delta I > 3$ beyond 500 mas using AstraLux and FastCam observations (Cortés-Contreras et al. 2017; Jódar et al. 2013).

We observed Ross 59 with the CARMENES spectrograph between January 2016 and April 2018, gathering 19 spectra. An inspection of the spectra with `todmor` revealed a faint companion signal at few km s^{-1} of the main signal. After a grid search for optimal parameters of the templates, we obtained a flux ratio between the components of 0.10. The low rotational broadening applied to both templates allowed us to resolve the signal of the two components even at small relative RVs. Only one secondary RV is significantly affected by blended lines, as indicated by the cross symbol in Fig. 4.20, which we removed from the analysis. Six additional spectra observed with HARPS-N are also available, from which we obtained the RVs of the two components. We also considered an additional 13 RVs of the primary component obtained with the CORAVEL spectograph and measured by Sperauskas et al. (2019), from which they determined an orbital period of 700 d, although no other orbital parameters were given. From a combined analysis of all the available RV datasets, we obtained an orbital period of $725.3^{+2.2}_{-2.0}$ d with an eccentricity of 0.5034 ± 0.0085. The system has the lowest mass ratio of the SB2s studied in this work, $q = 0.3280^{+0.0034}_{-0.0035}$. Minimum masses are 0.0572 ± 0.0016 M$_\odot$ and 0.01877 ± 0.00042 M$_\odot$. All the orbital parameters are compatible with those reported in Baroch et al. (2018) within mutual uncertainties. Although we added additional RVs from CORAVEL, with a time-span of more than 6000 d, we obtain similar uncertainties in the period determination. This may be due to the much lower precision of the CORAVEL measurements compared to those from CARMENES and HARPS-N.

We gathered archival photometric observations of Ross 59 from SWASP and ASAS, which we analysed searching for periodic signals from rotation. As seen in Fig. 4.21, the GLS periodogram of the SWASP photometry have a significant peak at 14.3 ± 0.7 d, just below the 0.1 %, while the ASAS data do not show any significant periodicity, although the highest peak is located at ~28 d, close to the first harmonic of the signal found in the SWASP data. Given that the semi-amplitude of the signal found by SWASP, of 5.4 mmag, is much lower than the dispersion of the ASAS photometry (24 mmag) and than the semi-amplitude of the highest signal (16 mmag), we think improbable that the signal found in ASAS is produced by the star. We therefore assume the 14.3 ± 0.7 d signal to probably be the rotation period of the more massive and brighter component. This rotation period is slightly lower than those found for the objects in Praesepe or NGC 6811 (Curtis et al. 2019b), which have estimated ages of ~700 Ma and ~ 1Ga, respectively (Douglas et al. 2019), and therefore we estimate an age upper limit to Ross 59 of 1 Ga.

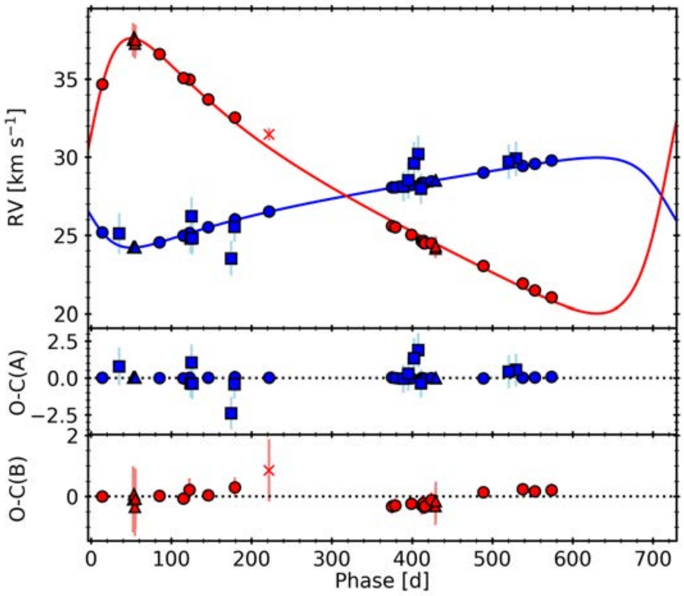

Figure 4.20: Best-fitting model to the `todmor` RV curves of Ross 59 as a function of the orbital phase. Blue and red colours correspond to the primary and secondary components, respectively. Circular, triangular, and square symbols correspond to the RVs from CARMENES, HARPS-N, and CORAVEL, respectively, while crosses indicate data points not used in the fit. The residuals from the fit are shown in the bottom panels.

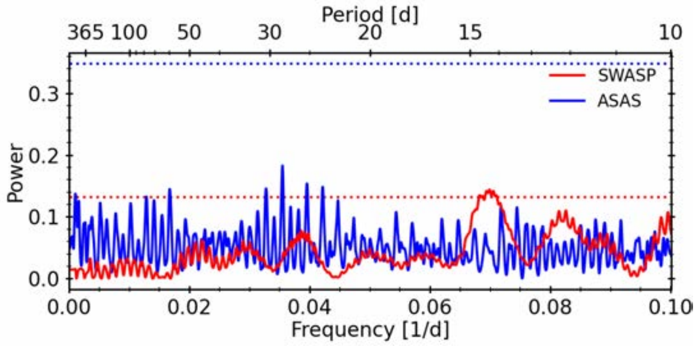

Figure 4.21: GLS periodogram of the SWASP (red) and ASAS (blue) photometry of Ross 59. The horizontal dotted lines of each color indicate the corresponding 0.1 % FAP level.

4.4.2.4 UCAC4 355–020729

UCAC4 355–020729 is an M5.0 V star located at a distance of 29.83 ± 0.03 pc. Catalogued as a bright X-ray source in the *ROSAT* bright source catalogue (Voges et al. 1999; Haakonsen & Rutledge 2009), it is an active star, with pEW(Hα) = −6.99 ± 0.04 Å, despite the relatively low value of its projected rotational velocity of 3.1 ± 1.5 km s^{-1}.

We observed this system with CARMENES between November 2016 and November 2018, obtaining a total of 27 spectra. The analysis of the spectra using `todmor` shows a secondary peak with a flux ratio of 0.24. Given the small relative RV separation between the two signals, we decided to fix the line-broadening of the secondary template to zero, to minimise the effects of line blending. Although we could detect two signals in all spectra using `todmor`, the resulting RVs near the conjunctions are affected by systematics produced by blended lines due to the small RV

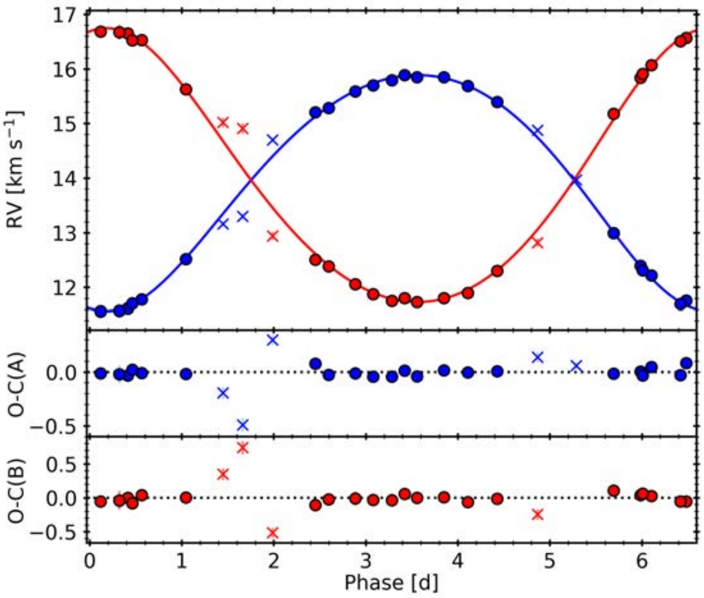

Figure 4.22: Best-fitting model to the `todmor` RV curves of UCAC4 355–020729 as a function of the orbital phase. Blue and red circles correspond to the primary and secondary components, respectively, while the crosses indicate data points not used in the fit. The residuals from the fit are shown in the bottom panels.

difference between the two signals, as can be seen in Fig. 4.22. We therefore removed these RVs from our orbital analysis. Table 4.7 lists the orbital parameters corresponding to the best-fitting solution to the RVs, while in Fig. 4.22 we show the RVs phase folded to the best orbital period. The best-fitting solution yields a slightly eccentric orbit, with $e = 0.1123 \pm 0.0054$, and an orbital period of $P = 6.56045 \pm 0.00028$ d. The semi-amplitudes of the RVs yield a mass ratio of $0.8603^{+0.0082}_{-0.0081}$, and minimum masses of $3.650 \pm 0.061 \times 10^{-5}$ M$_{\odot}$ and $3.136 \pm 0.043 \times 10^{-5}$ M$_{\odot}$ for the primary and secondary components, respectively. The very low minimum masses obtained could be an indication of an almost pole-on orientation of the orbit. Assuming a mass of ~0.25 M$_{\odot}$ for the primary star, given its M5.0 spectral type, and using the obtained minimum mass, the orbital inclination should be below ~3.0 deg. This low inclination would be consistent with the low value of the measured projected rotational velocity. This argument is even more convincing considering that this value is probably overestimated because of the blending of the spectral lines.

Finally, we analysed the photometry and activity indicators in search for stellar rotation signals, although the low inclination of the system might probably reduce the amplitude of any possible modulation due to stellar spots. No significant signal was found in any of the activity indicators, aside from signals at the orbital period in the CRX and dLW that can be attributed to the blending of the two component spectra. The light curve from TESS (top panel in Fig. 4.23) reveals several flaring events during the 27 d of continuous monitoring, as expected from the high activity of the star. After removing the flares with a sigma clipping and a rebinning of 1 h, the GLS periodogram (bottom panel in Fig 4.23) shows three signals just above the 0.1 % FAP level, at periods of 0.97, 1.46, and 2.82 d, which are not related to the 6.56 d by any alias or harmonic. We also found excess power at the orbital period, although the signal is not significant. There are no significant signals in the ASAS photometry. Given these results, we can not confirm any rotational period for the components of this system at present. With the orbital period lower than

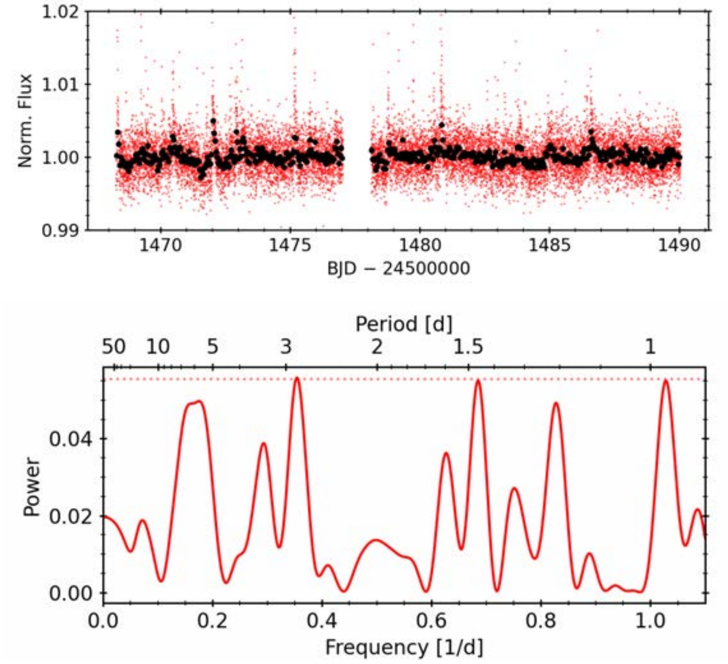

Figure 4.23: *Top panel:* TESS photometry of UCAC4 355–020729 (red) and its 1 hour binning (black). *Bottom panel:* GLS periodogram of the hourly binned TESS photometry. The horizontal dotted line indicates the 0.1% FAP level.

8–10 days, we should expect a synchronisation of the rotation period with the orbital motion (Mazeh 2008) for evolved stars. However, the X-ray and Hα emissions, and the flaring activity of this system, may be an indication of the young age of the system, and therefore their rotation periods may have not reached yet synchronization.

4.4.2.5 LP 790-2

LP 790-2 is an M4.5 V star located at a distance of 25.32 ± 0.03 pc. It is considered a variable star, with variations of 12 mmag observed in the I-band photometry (Hosey et al. 2015), which are also present and clearly visible in the TESS photometry, in addition to several flaring events. LP 790-2 is very active, with the strongest Hα emission in our sample (pEW(Hα)=−7.63 ± 0.09 Å), and catalogued as a bright X-ray source using ROSAT data (Haakonsen & Rutledge 2009). It is a comoving companion of the fainter late M-dwarf LP 790-1 (Luyten 1979; Schneider et al. 2019), which is located at 31.5 arcsec, corresponding to a projected distance of 800 au.

We gathered spectroscopic observations of LP 790-2 with CARMENES between December 2016 and December 2017, obtaining 14 spectra. The analysis of the spectra with `todmor` show two well-resolved signals, with an optimal flux ratio of 0.50. The orbital modeling of the RVs of the system resulted in an eccentric solution with e $=0.0132^{+0.0017}_{-0.0016}$ and a period of $5.922756^{+0.000076}_{-0.000072}$ d. The orbital parameters yielded minimum masses of $0.2711^{+0.0016}_{-0.0016}$ and $0.15679^{+0.00080}_{-0.00079}\,M_{\odot}$, with a mass ratio of 0.5784 ± 0.0017. All the orbital parameters are listed in Table 4.7, and the best fitting model is shown in Fig. 4.24.

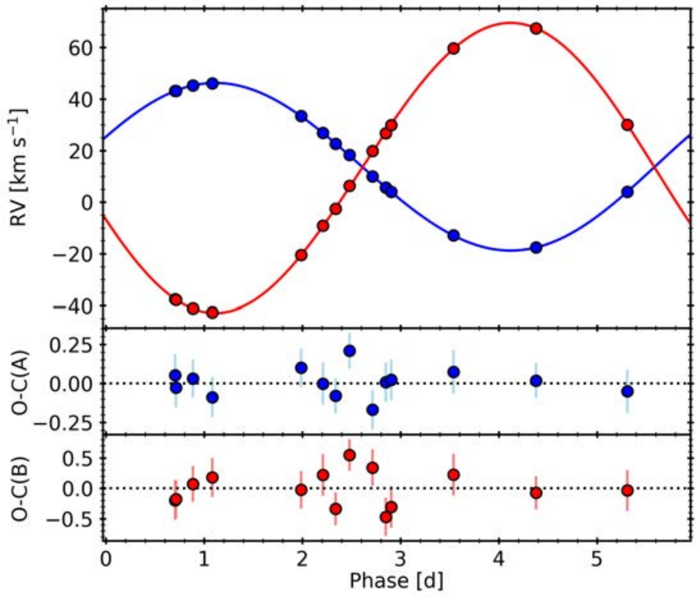

Figure 4.24: Best-fitting model to the `todmor` RV curves of LP 790-2 as a function of the orbital phase. Blue and red colours correspond to the primary and secondary components, respectively. The residuals from the fit are shown in the bottom panels.

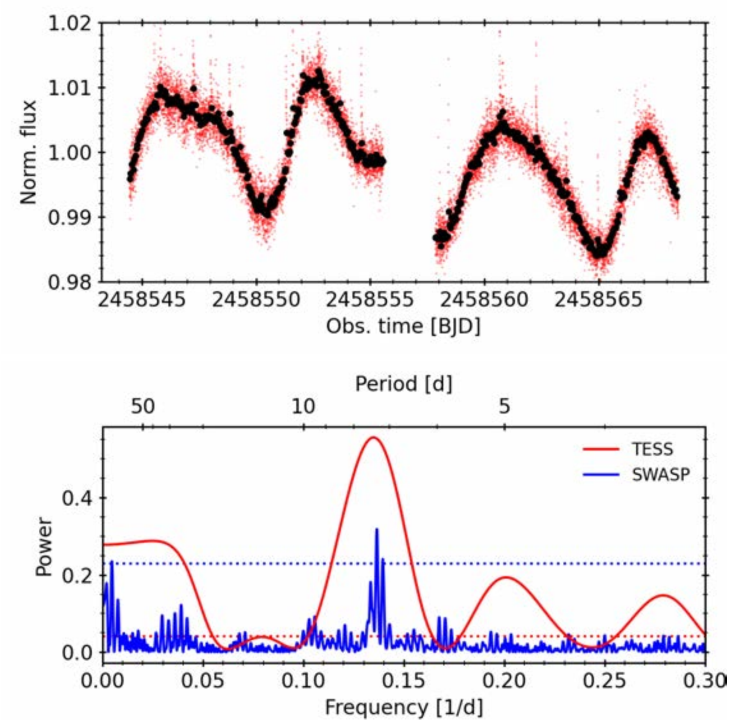

Figure 4.25: *Top panel:* TESS photometry of LP 790-2 (red) and its 1 hour binning (black). *Bottom panel:* GLS periodogram of the hourly binned TESS (red) and SWASP (blue) photometry of LP 790-2. The horizontal dotted lines of each color indicate the corresponding 0.1 % FAP level.

Given that for orbital periods below 8–10 d the circularisation timescale is small, we also modeled the RVs with a circular orbit to see if the addition of eccentricity improves the fit significantly. However, the statistical significance of a circular fit is much lower than an eccentric one, with $\Delta \ln \mathcal{L}$ =~50. This result, together with the high activity of the system, may be indicative of the young age of the components, which may have not yet reached circularisation. An alternative possibility to the eccentricity of the system may be the presence of a third body perturbing the system through the Lidov-Kozai mechanism (Lidov 1962; Kozai 1962), although no clear evidences are seen in the radial velocities.

Finally, we analyzed the available photometry of LP 790-2 from SWASP and TESS searching for variability signals. As mentioned above, the TESS light curve shows evident modulations with an amplitude of 12 mmag and several flaring events. The GLS periodogram shown in Fig. 4.25 indicate that these modulations have a periodicity of 7.4 ± 1.0 d, and are very significant. The SWASP photometry, which spans 2 years, has a significant signal coincident with that of TESS, at a period of 7.33 ± 0.04 d. Given the longer time-span covered by SWASP, we assume 7.33 ± 0.04 d as the rotation period of the brightest component of LP 790-2. We observe that synchronization between rotation and orbital periods has not yet been achieved, which supports the young age hypothesis based on its high activity and eccentric orbit.

4.4.2.6 GJ 3612

The object GJ 3612 is an M3.5 V star located at a distance of 12.73 ± 0.05 pc. It is a rather inactive star, with pEW(Hα)=0.070±0.008 Å and a projected rotational velocity below 3 km s^{-1}, which agrees with the long rotation period of 118 ± 10 d suggested by Díez Alonso et al. (2019) based on photometric observations from NSVS.

It has been observed between February 2016 and December 2017 with CARMENES, obtaining 21 spectra. The analysis with `todmor` yields a flux ratio of 0.24 between the two templates. We clearly resolve the signal of the two components in most of the cases, except for two spectra

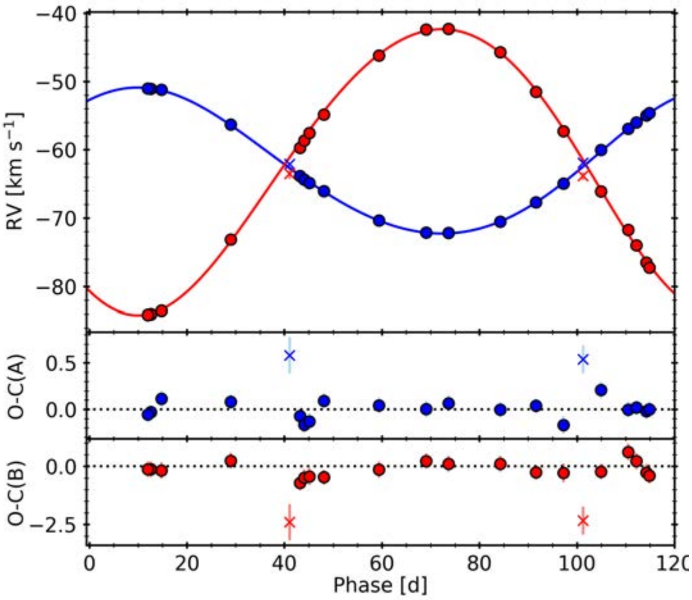

Figure 4.26: Best-fitting model to the `todmor` RV curves of GJ 3612 as a function of the orbital phase. Blue and red colours correspond to the primary and secondary components, respectively, while the crosses indicate data points not used in the fit. The residuals from the fit are shown in the bottom panels.

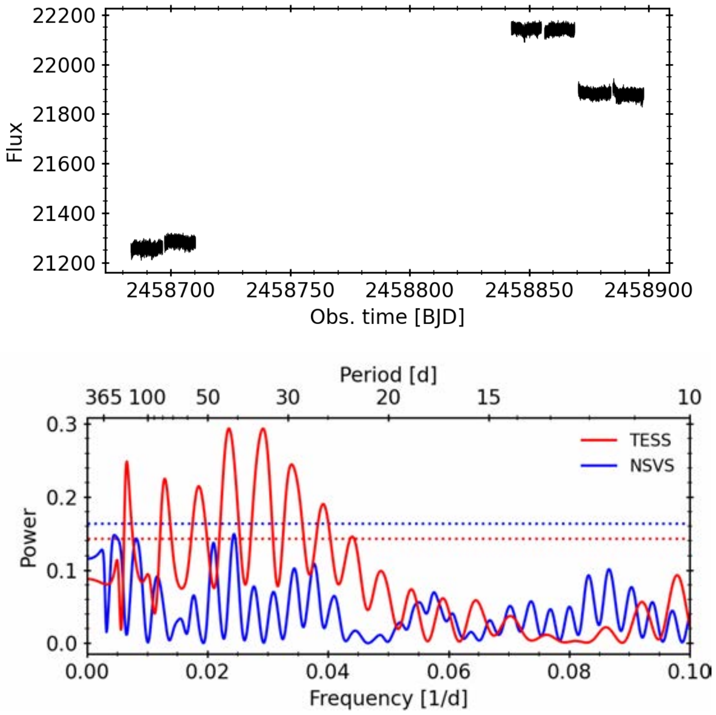

Figure 4.27: *Bottom panel:* TESS photometry of GJ 3612 before normalizing. *Bottom panel:* GLS periodogram of the TESS (red) and NSVS (blue) photometry of GJ 3612. The horizontal dotted lines of each color indicate the corresponding 0.1 % FAP level.

which were taken close to conjunction and therefore the blending of the lines produced biased RVs, as shown by the cross markers in Fig. 4.26. We removed these two spectra from the analysis. We modeled the remaining 19 RV pairs with a Keplerian orbit, obtaining the parameters listed in Table 4.7. We determine an orbital period of 119.388 ± 0.048 d with a low eccentricity of 0.0633 ± 0.0035, and obtain minimum masses of 0.2567 ± 0.0036 and 0.1312 ± 0.0013 $M_\odot$ for the primary and secondary components, respectively, which yield a mass ratio of $0.5112^{+0.0034}_{-0.0035}$. The best orbital fit is shown in Fig. 4.26.

We searched for the signals of rotation in the photometric data from TESS and NSVS by computing their GLS periodogram, which we show in Fig. 4.27. Although Díez Alonso et al. (2019) found a significant peak at 118 ± 10 d in the NSVS data, we obtain the highest peak at ~41 d, although with a similar power than the signal at 118 d. Nevertheless, both signals do not reach the required 0.1 % FAP threshold. The TESS photometry has a significant peak at 42.6 ± 3.0 d, which coincides with the the highest peak seen in the NSVS data. We note however that although the periods coincide, the amplitude of the modulation is much larger in the NSVS data, ~12 mmag, while in the TESS data is of ~0.3 mmag. Also, the derived period is longer than the TESS sector time-span, and although we have data from three sectors spanning 200 d, the normalization of the photometry has to be performed individually, as shown in the top panel in Fig. 4.27. Therefore, potential biases could be introduced in this process leading to spurious long period signals. As a conservative approach, we assume that the rotation period of the brightest component is longer than the time span of one TESS sector, that is, 27 d.

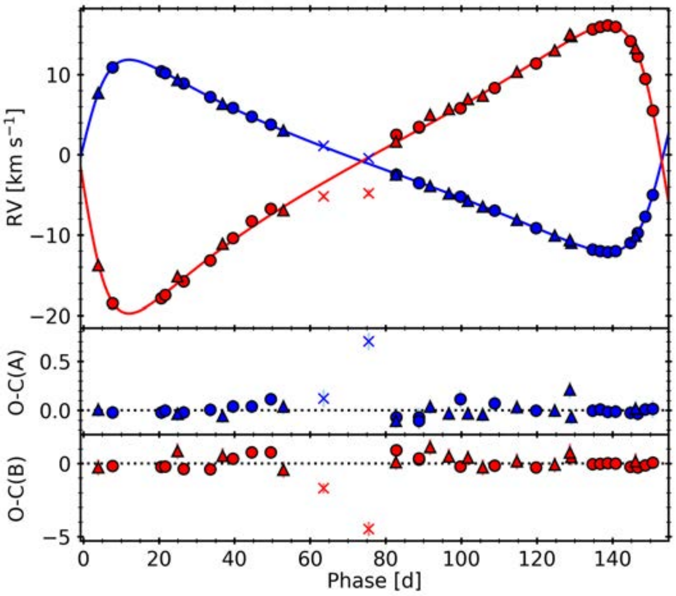

Figure 4.28: Best-fitting model to the `todmor` RV curves of GJ 1182 as a function of the orbital phase. Blue and red colours correspond to the primary and secondary components, respectively. Circular and triangular symbols correspond to the RVs from CARMENES and TRES, respectively, while crosses indicate data points not used in the fit. The residuals from the fit are shown in the bottom panels.

4.4.2.7 GJ 1182

The M5.0 V star GJ 1182 is an inactive object (pEWH(α)=0.10 ± 0.10 Å) located at a distance of 13.89 ± 0.07 pc. Newton et al. (2016) determined a rather suspicious rotation period of 0.998 d using MEarth photometry, which coincides with the highest peak of the window function of the data. It was imaged by Cortés-Contreras et al. (2017) and Lamman et al. (2020) for companions using the imagers FastCam and Robo-AO, from which they discarded companions with $\Delta I >$ 3.0 beyond 200 mas and with $\Delta z > 2$ beyond 70 mas, respectively. As a part of a survey of rotational velocities of M-dwarfs, Jenkins et al. (2009) took a medium-resolution spectra of GJ 1182, from which they determined a projected rotational velocity of 6.8 ± 0.5 km s^{-1} and found weak evidences for binarity. It has also been spectroscopically observed with the TRES spectrograph by Winters et al. (2020), who detected the signal of the two components and determined orbital parameters in agreement with those reported in Baroch et al. (2018).

We analyzed with `todmor` a total of 22 spectra, which were taken with CARMENES between April 2016 and July 2017. The signal of the two components are detected in all spectra, obtaining a flux ratio of 0.24. Two spectra were discarded for further analysis given the biased RVs due to line blending. Additionally, we added to the analysis the 14 RVs computed by Winters et al. (2020). The complete list of RVs are shown in Table A.7. The best orbital solution to the available RVs corresponds to an eccentric orbit (e = 0.5360 ± 0.0014) with a period of $154.031^{+0.031}_{-0.032}$ d. Using the orbital parameters listed in Table 4.7, we derive minimum masses of 0.1539 ± 0.0018 M$_\odot$ for the primary component and $0.10272^{+0.00074}_{-0.00073}$ M$_\odot$ for the secondary, yielding a mass ratio of 0.6677 ± 0.0036. All orbital parameters agree within mutual errors with those reported in Baroch et al. (2018) and Winters et al. (2020), except for the orbital period, which is compatible within 2σ. The addition of the RVs by Winters et al. (2020), doubling the time-span of the CARMENES data, enabled us to significantly reduce the uncertainties in the

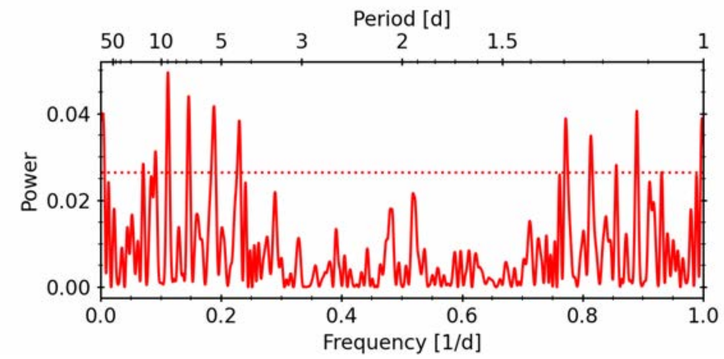

Figure 4.29: GLS periodogram of the MEarth photometry of GJ 1182. The horizontal dotted line indicates the corresponding 0.1 % FAP level.

orbital period. We show the best orbital fit and the RVs of GJ 1182 in Fig. 4.28.

We finally analyzed the available MEarth photometry to look for the signature of stellar rotation. We performed a GLS periodogram to the data, which we show in Fig. 4.29. The highest significant peak is at a period of 8.94 ± 0.25 d causing a semi-amplitude of 1.8 mmag, although there are several other signals with a significance below the 0.1 % FAP level, including the period reported by Newton et al. (2016) at ∼1 d. We therefore consider 8.94 d as the tentative rotation period of the brightest component. As for the cases of GJ 912 and GJ 282 C, the rotation period of GJ 1182 is shorter than those found for the objects in Praesepe or NGC 6811 (Curtis et al. 2019b), from which we estimate an upper limit to its age of 1 Ga.

4.4.2.8 UU UMi

Catalogued as the high proper-motion star Ross 1057 (Ross 1939), UU UMi is an M3.0 V star located at a distance of 14.6±0.3 pc. It is a rather inactive system, with pEW(Hα) = −0.10±0.10 Å and a measured projected rotational velocity below 3 km s^{-1}. Newton et al. (2016) reported a probable rotation period of 91 d from MEarth photometry, while Díez Alonso et al. (2019) found 83.4 ± 10.4 d using the same dataset. A first indication of its binarity was suggested by Lippincott (1981), who found evidence of variable proper motion in the residuals of plate series taken between 1970 and 1979, showing a perturbation with a period of 10–15 years and an amplitude of 0.04 arcsec. Heintz (1993) expanded the study including plates up to 1990, and found UU UMi to be an unresolved binary with a large astrometric variation amplitude and a companion mass of about 0.10 M$_\odot$. The authors derived a circular orbit with a period of 14.5 years, an inclination of i = 92 deg, an amplitude of a = 0.0745 arcsec, and longitude of the ascending node of Ω = 21 deg.

A first inspection of the spectra with TODCOR revealed the signal of both components, although their proximity in RV made impossible to obtain unbiased RVs in any of the observations, using synthetic templates. We therefore decided to use as templates the coadded spectra of two CARMENES stars, GJ 752 A and GJ 1253. With the use of real templates, the companion was detected spectroscopically in all exposures, obtaining in all the cases unblended RVs and a flux ratio 0.26. In our previous study of UU UMi (Baroch et al. 2018) we were not able to discern between a circular and an eccentric orbit and, therefore, the eccentricity was fixed to zero. Here, we update this analysis with eight additional CARMENES observations, adding

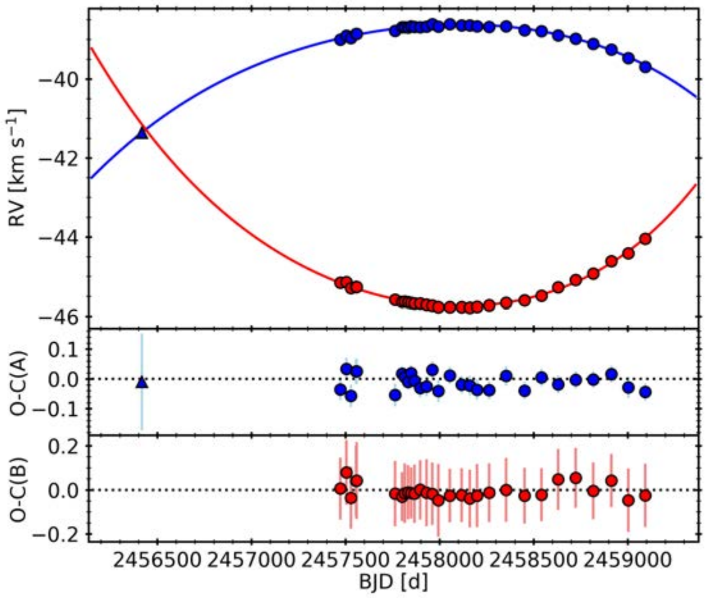

Figure 4.30: Best fit to the `todmor` RVs of UU UMi as a function of time. Blue and red colours correspond to the primary and secondary components, respectively. Circular and triangular symbols correspond to the RVs from CARMENES and CAFE, respectively. The residuals from the best fit are shown in the bottom panels.

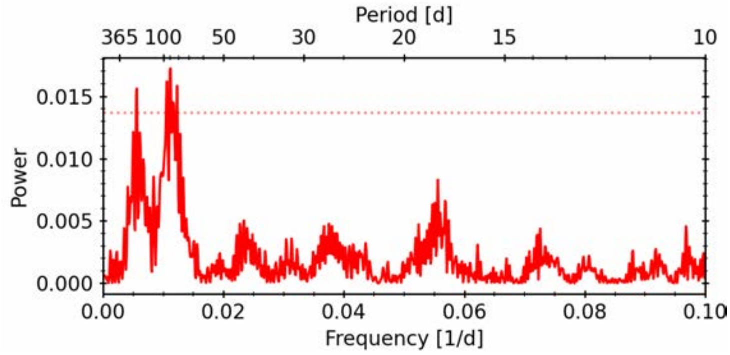

Figure 4.31: GLS periodogram of the MEarth photometry of UU UMi. The horizontal dotted line indicates the corresponding 0.1% FAP level.

up to a total of 30 spectra taken between March 2016 and December 2020, and one archival measurement taken with the CAFE spectrograph in May 2013. Although only the primary star can be resolved in this latter case, the almost equal RV of both spectra is a useful information to constrain the systemic velocity and the time of conjunction. Table A.7 lists the full set of RVs used in this analysis for UU UMi.

From a Keplerian fit to the RVs of this system, which is shown in Fig. 4.30, we obtained a period of 5240^{+410}_{-290} d with an eccentricity of $0.310^{+0.069}_{-0.087}$ and a mass ratio of $0.593^{+0.040}_{-0.035}$. The eccentric orbit is significantly favoured over a circular one, with $\Delta \ln \mathcal{L} = 14.2$. Interestingly, the fitted period of $14.3^{+1.1}_{-0.8}$ years is in agreement with that in Heintz (1993). Using the almost edge-on inclination derived by Heintz (1993), $i = 92$ deg, we derived absolute masses of $0.32 \pm 0.06\,M_\odot$ and $0.19 \pm 0.04\,M_\odot$ for the primary and secondary components, respectively. We note here that the uncertainties of the individual masses are propagated from the RV parameters only, and therefor may be underestimated due to the lack of any reported error bar for the inclination.

Besides, we inspected the activity indices computed with `serval` to look for signs of stellar rotation, but without succes. We also analysed the TESS photometry with equally unsuccsesful results, although as in the case of GJ 3612, the normalization of the photometry has to be performed for each sector individually, introducing potential biases in the process. In the GLS periodogram of the seven years of MEarth photometry, which we show in Fig. 4.31, we found a signal below the 0.1 % FAP level at a period of 90 ± 10 d with an amplitude of 1 mmag, which was already reported by Newton et al. (2016) and Díez Alonso et al. (2019). This signal could be a product of the stellar rotation of one of the components and indicates an age of the system older than 1 Ga (Curtis et al. 2019b). Finally, we also reanalysed the HIPPARCOS photometry (Perryman et al. 1997) from which this object was catalogued as variable (Kazarovets et al. 1999; Adelman 2001). We found that all the points leading to the classification of UU UMi as a variable star were actually flagged as bad quality measurements.

4.4.2.9 LP 395-8

LP 395-8 is an M3.0 V star located at a distance of 29.501 ± 0.023 pm. It is an active star, with pEW(Hα)=-3.03 ± 0.25 Å, and was catalogued in the ROSAT survey as a bright X-ray (Motch et al. 1998; Haakonsen & Rutledge 2009) and flaring (Fuhrmeister & Schmitt 2003) source. Besides, it is a rapid rotator, with a rotation period of 1.13 ± 0.01 d (Díez Alonso et al. 2019).

We observed LP 395-8 with the CARMENES spectrograph between June 2016 and December 2017, gathering 14 spectra. The analysis using `todmor` allowed us to clearly resolve signals of both components, obtaining a flux ratio value of 0.16. We obtained the largest values of the rotational broadening among the stars in this chapter, with 14.75 and 12.50 km s^{-1} for the primary and secondary templates, respectively. These values are close to the value derived by Jeffers et al. (2018), of 11.8 ± 1.5 km s^{-1}.

We fitted a Keplerian orbit to the obtained CARMENES RVs. The orbital parameters are listed in Table 4.7, and the best-fitting orbital solution is shown in Fig. 4.32. We obtained a short orbital period of $1.1293284^{+0.0000073}_{-0.0000077}$ d and a small eccentricity of $0.0080^{+0.0028}_{-0.0025}$. Using the orbital parameters we derived minimum masses of $0.07893^{+0.00070}_{-0.00065}$ and $0.04438^{+0.00033}_{-0.00030}$ M$_\odot$, yielding a mass ratio of 0.5624 ± 0.0022. Although with such a small period an evolved binary system should have already achieved orbital circularization of the orbit (Mazeh 2008), the eccentric solution likelihood is significant over a circular orbit, with $\Delta \ln \mathcal{L} = 3.3$ (i.e. 2σ significance). This fact along with the high activity, X-ray emission, and flaring rate, may be an indication of the young age of the system. Another possible explanation for the high activity of the system is that the rapid rotation of the stars is induced by spin-orbit synchronization (see below) instead of being a product of its young age. As for the case of LP 790-2, the eccentricity of the system may be produced by the Lidov-Kozai mechanism, induced by the perturbations caused by a possible third body.

In order to confirm the rotation period found by Díez Alonso et al. (2019), we analyzed the available light curves of LP 395-8 from SWASP and TESS. The TESS light curve shows evident modulations with an amplitude of 14 mmag and several flaring events. We show in Fig. 4.33 the GLS periodogram of the photometric data, which reveals clear and significant peaks in both datasets at 1.129 ± 0.02 and 1.129 ± 0.01 d for TESS and SWASP data, respectively, which perfectly match with the value in Díez Alonso et al. (2019) and also with the orbital period (1.1293284 d). This confirms that spin-orbit synchronization have been already achieved, and

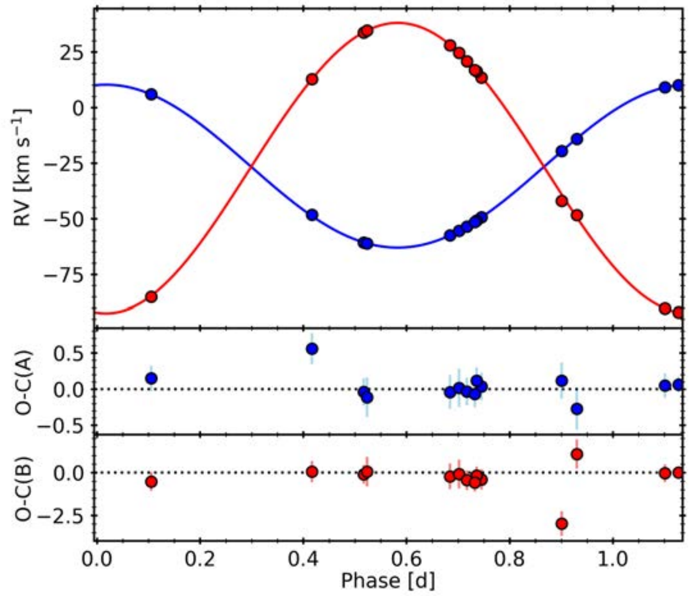

Figure 4.32: Best-fitting model to the `todmor` RV curves of LP 395-8 as a function of the orbital phase. Blue and red colours correspond to the primary and secondary components, respectively. The residuals from the fit are shown in the bottom panels.

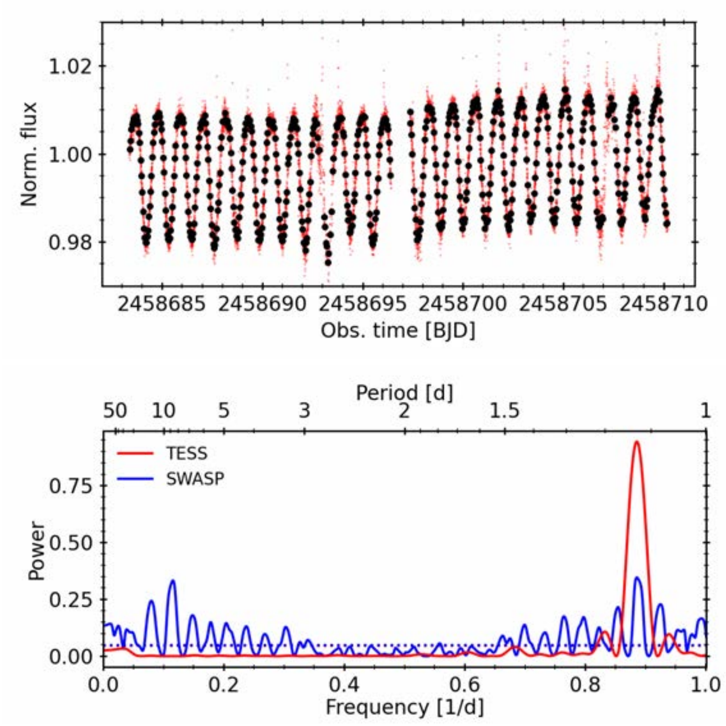

Figure 4.33: *Top panel:* TESS photometry of LP 395-8 (red) and its 1 hour binning (black). *Bottom panel:* GLS periodogram of the TESS (red) and SWASP (blue) photometry of LP 395-8. The horizontal dotted lines of each color indicate the corresponding 0.1 % FAP level.

may be an alternative explanation of the high activity level of the star, which could be induced by the rapid rotation of the components. The probability of being an eclipsing binary is ~40%, as computed from the semi-major axis in Table 4.7 and the estimated individual radius in Table 4.9. However, no eclipses are found in any photometric time series.

4.4.2.10 GJ 810 A

The object GJ 810 A is an M4.0 V star located at a distance of 11.78 ± 0.07 pc. It is a common proper motion companion of the M5.0 V star GJ 810 B (Luyten 1979; Poveda et al. 2009), which is at an angular distance of 107.1 arcsec, corresponding to a projected distance of 1262 au (Jao et al. 2003). The rotation period estimated from the $R'_{\rm HK}$ index of the star, $\log(R'_{\rm HK}) = -5.57$, is of the order of 101 d (Astudillo-Defru et al. 2017), while Newton et al. (2018) determined a value to be 137.4 d using MEarth photometry. A first indication of the binary nature of GJ 810 A was suggested by Jao et al. (2011), who found perturbations in the astrometric residuals spanning more than 10 years of observations. These perturbations were also reported by Vrijmoet et al. (2020) with observations spanning 20 years, but they were not able to resolve the system and obtain an orbital solution. The tentative close companion to GJ 810 A was neither detected in the imaging observations made by Cortés-Contreras et al. (2017) in July 2012 with the FastCam lucky imager, from which companions with $\Delta I < 3$ mag between 0.2 and 2 arcsec were discarded.

We gathered 29 spectra of GJ 810 A with CARMENES between September 2016 and November 2018. An inspection of the spectra with `todmor` reveals the signals of two different components with similar fluxes. However, the proximity in RV between the signals resulted in biased RVs in most of the cases, and the few remaining observations were not enough to compute the orbital parameters. Therefore, as in the case of UU UMi, we used as templates the coadded spectra of the CARMENES M2.5 V star GJ 752 A, obtaining an optimal fit with a flux ratio of 0.66. The analysis of RVs resulted in a long orbital period of $672.92^{+0.59}_{-0.58}$ d with an eccentricity of 0.2433 ± 0.0021. All orbital parameters are listed in Table 4.7, from which we derived minimum masses of 0.05706 ± 0.00042 and 0.04841 ± 0.00032 $M_\odot$ for the primary and secondary components, respectively, yielding a mass ratio of 0.8484 ± 0.0032. The orbital best fit to the phase folded RVs is shown in Fig. 4.34. The resulting orbital period is 140 d shorter and two orders of magnitude more precise than that reported in Baroch et al. (2018), and we also obtain a significative smaller eccentricity. This is mainly due to the addition of four new observations made after the publication of this paper, which expanded 350 d the time-span of the observations, and also to the use of real spectra templates in this new analysis, which reduced the bias of the RVs close to conjunction and enabled us to add seven additional observations that were not resolved previously.

Finally, and to indepently confirm the rotation period reported by Newton et al. (2018), of 137.4 d, we analyzed the photometry from ASAS and MEarth searching for significant periodic signals in the data. We show in Fig. 4.35 the GLS periodogram of the MEarth photometry of GJ 810 A, which display a significant peak at a period of 138 ± 9 d with a semi-amplitude of 1.5 mmag, coincident with the signal found by Newton et al. (2018). We do not find any significant peak in the ASAS photometry. As in the cases of GJ 912 and LP 427-016, based on the long rotation period of this system, we can safely assume that it is older than the objects of the cluster NGC 6811, with an estimated age of 1 Ga (Curtis et al. 2019b,a).

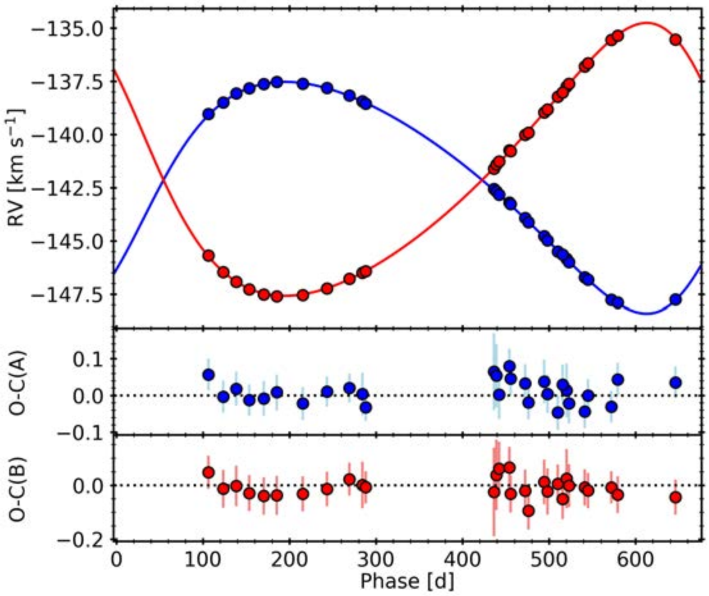

Figure 4.34: Best-fitting model to the `todmor` RV curves of GJ 810 A as a function of the orbital phase. Blue and red colours correspond to the primary and secondary components, respectively. The residuals from the fit are shown in the bottom panels.

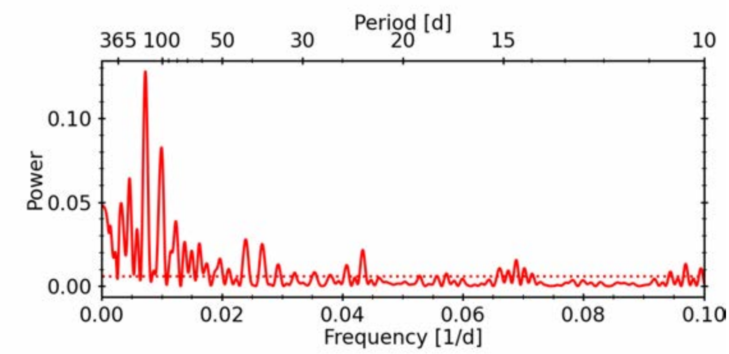

Figure 4.35: GLS periodogram of the MEarth photometry of GJ 810 A. The horizontal dotted line indicates the corresponding 0.1 % FAP level.

4.4.3 Triple-line spectroscopic triples (ST3s)

4.4.3.1 GJ 3916

GJ 3916 is catalogued as an M2.0 V high-proper motion star (Luyten 1955), located at a distance of 16.00 ± 0.07 pc. It is a quiet star, with pEW(Hα) = −0.03 ± 0.02 Å and a projected rotational velocity below 3 km s^{-1}. Using empirical relationships, Astudillo-Defru et al. (2017) estimated a rotation period of 78 d from the emission strength of the Ca II H&K lines.

The first indication of the binarity of this system was deduced from HIPPARCOS astrometric data through the detection of an accelerated proper motion (Makarov & Kaplan 2005; Frankowski et al. 2007). More recently, Kervella et al. (2019) reported a difference in the proper motion between HIPPARCOS and *Gaia*, from which they obtained a lower limit to the secondary mass, normalised to an orbital separation of 1 au, of $144^{+40}_{-15}\,\mathrm{M_{Jup}}\,\mathrm{au}^{-1/2}$. The presence of a companion to GJ 3916 was spectroscopically confirmed by Zechmeister et al. (2009), who reported a $4.1\,\mathrm{km\,s^{-1}\,a^{-1}}$ trend in six high-precision RVs obtained as part of the planet search programme with VLT+UVES (Dekker et al. 2000). Moreover, Houdebine & Mullan (2015) detected the signal of the secondary companion by cross-correlation in three high-resolution spectra taken with HARPS. They also obtained projected rotational velocities of 1.24 ± 0.14 and $3.51 \pm 0.05\,\mathrm{km\,s^{-1}}$ for the primary and secondary signals, respectively.

We collected 32 spectra of GJ 3916 between April 2016 and August 2019 with CARMENES. We also used 23 spectra taken between March 2007 and July 2013 with the FEROS spectrograph, along with the UVES and HARPS spectra mentioned above. An inspection of the CARMENES spectra with `todmor`, using synthetic spectra, revealed a clear signal from a tertiary component in the system, in addition to the two expected signals. We proceeded as explained in Sect. 4.3.1 and extracted the RVs of the three signals in the spectra. We repeated the same process for the observations from UVES, FEROS, and HARPS, where the third signal was not so evident as in the CARMENES data. From the available 32 archival spectra, we could only detect all three signals in 11 of them, two signals in 17, and only the signal from the brightest companion in 4. This effect was mostly due to the unfavourable orbital position of some of the components and the lower exposure time of the HARPS, UVES, and FEROS observations with respect to those from CARMENES. We list the RVs in Table A.8.

The RVs suggest a hierarchical triple system configuration, with the most massive star, A, tracing out a long-period orbit around the common barycentre with the two other stars, Ba and Bb, which in turn are orbiting each other with a shorter orbital period. The best fit to the hierarchical Keplerian model used to describe this system is shown in Fig. 4.36. The top panel depicts the RVs of the three components. In the bottom-left, we show the long-period orbit of components A around the Ba+Bb system after subtracting the RVs of the short-period orbit. In the bottom-right panel, we show the orbital motion of Ba and Bb after subtracting the orbital motion of their centre of mass around component A. The fitted parameters are reported in Table 4.8. The outer orbit has a period of 3028 ± 23 d with an eccentricity of 0.458 ± 0.026, while the inner orbit has a period of $132.959^{+0.013}_{-0.014}$ d and an eccentricity of $0.1104^{+0.0049}_{-0.0047}$. The minimum masses are $0.328^{+0.033}_{-0.028}$, $0.1511^{+0.0025}_{-0.0025}$, and $0.1353^{+0.0031}_{-0.0030}\,\mathrm{M_\odot}$ for the components A, Ba, and Bb, respectively.

Additionally, as for GJ 912, the inclination of the system was constrained by using the astrometric observations from Hipparcos. This was done by a CARMENES collaborator following the method described in Reffert & Quirrenbach (2011). Using the orbital solution in Table 4.8, an astrometric orbit was fitted to the Hipparcos data, determining an inclination of $i_{AB} = 99 \pm 8$ deg and an ascending node of $\Omega = 304 \pm 8$ deg at $1\,\sigma$ level. The astrometric orbit fitted here corresponds to the orbit of the photocentre, not of component A. As a result, the true apparent orbit would depend on the flux ratio between the most and least massive (i.e. brightest and faintest) components, although this effect only affects the amplitude of the apparent orbit, and not the derived inclination. From the inclination of the outer orbit and the relation between $\sin i_{AB}$ and $\sin i_B$ we measured a difference between the inner and outer inclinations of $\Delta i = 13 \pm 7$ deg, consistent with coplanarity within 2σ. We also used the estimated outer inclination, the minimum masses, and the mass ratios to compute the absolute individual masses, which are $0.352 \pm 0.047\,\mathrm{M_\odot}$, $0.195 \pm 0.026\,\mathrm{M_\odot}$, and $0.174 \pm 0.024\,\mathrm{M_\odot}$ for the A, Ba, and Bb components, respectively, which yields a mass ratio between the three components very close to 2:1:1.

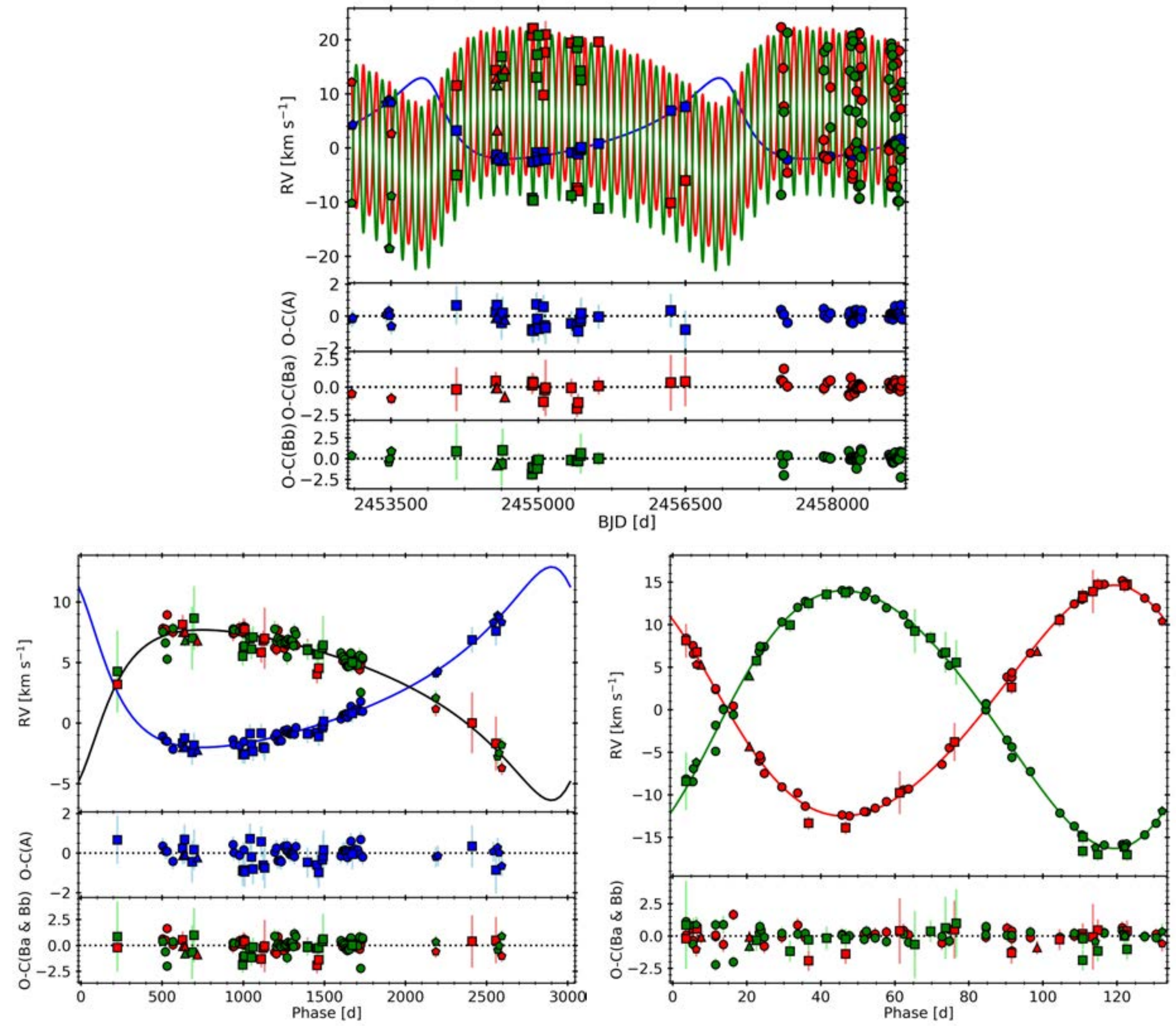

Figure 4.36: *Top panel*: Fit to the RVs of the three components of GJ 3916 as a function of time. *Middle panel*: Same fit but phase folded to the period of the outer orbit and with the inner orbit subtracted. *Bottom panel*: Fit to the inner orbit of the components Ba and Bb with outer orbit subtracted. Blue, red, and green symbols indicate the RVs of components A, Ba, and Bb, respectively. Measurements from CARMENES, FEROS, UVES, and HARPS are plotted as circular, squared, pentagonal, and triangular symbols, respectively.

We finally used the available photometry from ASAS and SWASP to search for signals of the rotation period of the components. No significant signals in the ASAS photometry could be detected as already reported by Díez Alonso et al. (2019). Although not significant, the highest peak in the periodogram of the SWASP data, shown in Fig. 4.37, is at ~78 d with an semi-amplitude of 1.4 mmag, identical to the one estimated by Astudillo-Defru et al. (2017) from the emission of the Ca II H&K lines. Using only the first two epochs of the SWASP data, which have half the dispersion and uncertainty than the rest, the peak at 78.1 ± 8.6 d becomes significant and with a semi-amplitude of 2.4 mmag. Therefore, we attributed the 78.1 ± 8.6 d signal to the rotation period of star A, given the small expected flux of the other components. Based on the long rotation period of this system, which is much larger than the typical values found for the objects of the cluster NGC 6811, we can safely assume that GJ 3916 is older than this cluster, with an estimated age of 1 Ga (Curtis et al. 2019b,a).

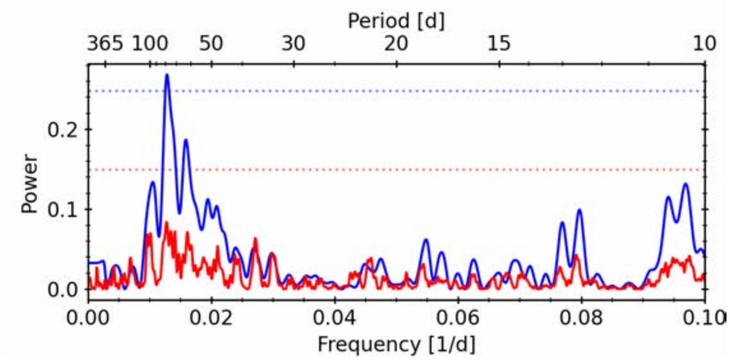

Figure 4.37: GLS periodogram of the SWASP photometry of GJ 3916, using the entire dataset (red) and the first two epochs (blue). The horizontal dotted lines of each color indicate the corresponding 0.1% FAP level.

4.4.3.2 GJ 4383

GJ 4383 is an M3.0 V star located at a distance of 16.43 ± 0.07 pc. It is a rather inactive star, showing the Hα line in absorption with pEW(Hα) = +0.04 ± 0.01 Å, and a projected rotational velocity below 2 km s^{-1}. Using the measured $R'_{\rm HK}$ index, Astudillo-Defru et al. (2017) estimated a rotation period of 67 d, while Díez Alonso et al. (2019) did not find any significant signal in the ASAS photometry that could be associated with rotation. Although the HIPPARCOS astrometry does not show an acceleration in the astrometric measurements, Makarov & Kaplan (2005) found discrepancies between the proper motions in the HIPPARCOS and Tycho-2 (Høg 2000) catalogues and concluded that GJ 4383 could be an astrometric binary. Likewise, Kervella et al. (2019) found differences between the proper motions of HIPPARCOS and *Gaia*, from which a lower limit to the mass of the companion, normalised to 1 au, was set to 83^{+23}_{-9} M$_{\rm Jup}$ au$^{-1/2}$.

We observed GJ 4383 with CARMENES between July 2016 and December 2020, gathering 26 high-resolution spectra. We also retrieved nine and four spectra from the HARPS and FEROS public databases, respectively. A first inspection of the spectra with `todmor` using synthetic spectra only revealed the signal of one component, whose RVs exhibit a sinusoidal-like shape, probably produced by a companion. To attempt to resolve the suspected companion, we used the coadded spectra of the CARMENES observations of GJ 752 A and GJ 1253 as templates. With this approach, we resolved the signal of not only one but two additional components. From the 26 CARMENES spectra, we were able to detect the signal of the three components in 11 cases, two components in 10 spectra, and one component in 5. We did not detect the companions in any of the HARPS and FEROS spectra due to the lower SNR of their observations with respect to those from CARMENES. We list the RVs in Table A.8.

The architecture of the RVs of this system is very similar to that of GJ 3916: two low-mass stars orbiting each other with a relatively short period, which in turn are orbiting a heavier star in a much wider orbit. We therefore fitted the same physical model to the RVs, which yielded the parameters listed in the third column of Table 4.8. We show in Fig 4.38, from top to bottom, the orbital best fit to the RVs of GJ 4383 (top panel) and the same fit phase folded to the A–B (bottom-left) and Ba–Bb (bottom right) orbital periods. We measured a wide orbit between A and the pair Ba–Bb with an orbital period of 4646 ± 17 d and an eccentricity of 0.1068 ± 0.0049. The close orbit between the Ba and Bb components has a period of $216.07^{+0.13}_{-0.14}$ d and an eccentricity of $0.283^{+0.012}_{-0.011}$. From the RV semi-amplitudes, we derived an approximately 4:1:1

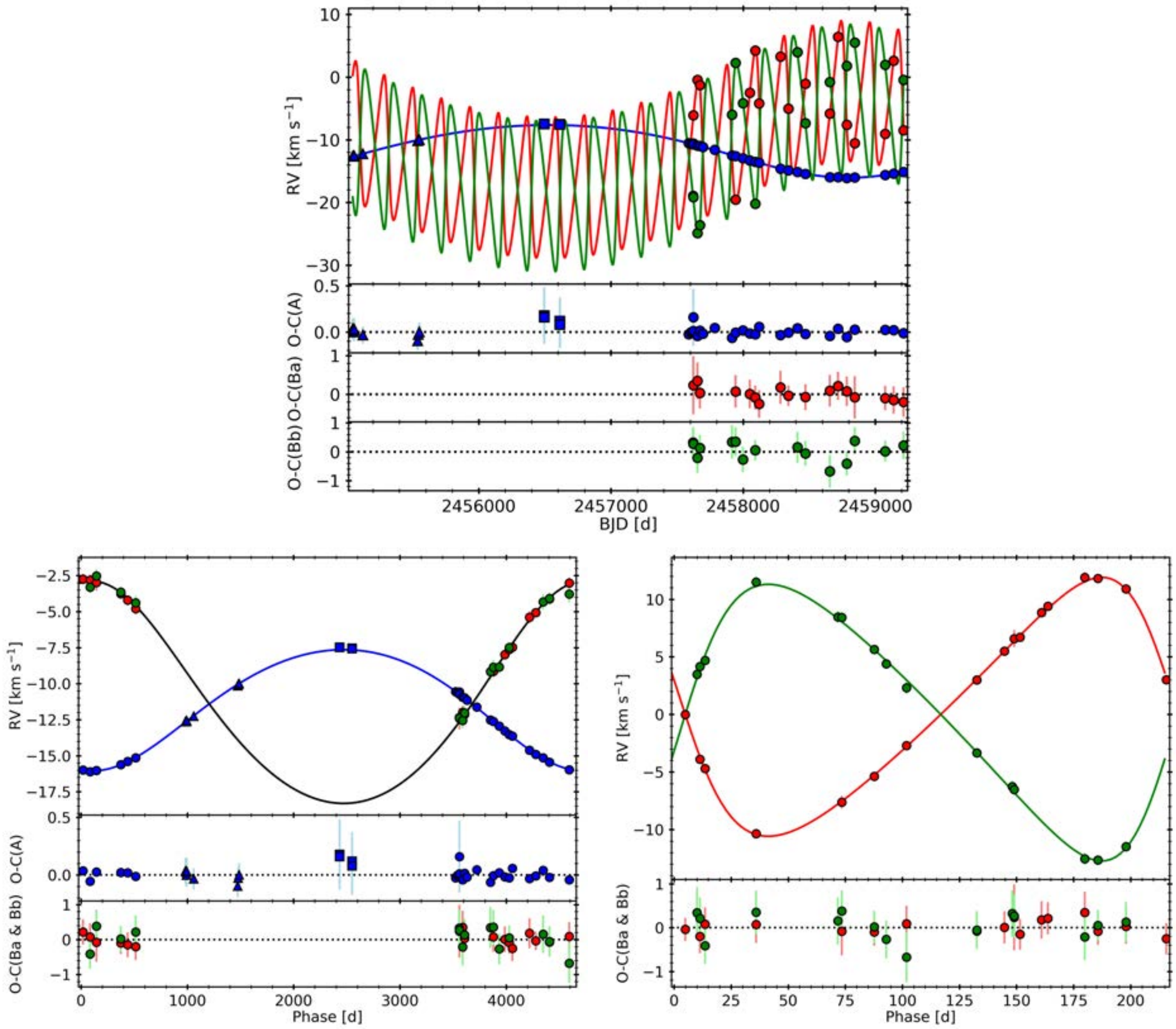

Figure 4.38: Same as Fig. 4.36, but for GJ 4383.

mass ratio between the components, with minimum masses of $0.509^{+0.017}_{-0.016}\,M_\odot$, $0.1206^{+0.0040}_{-0.0040}\,M_\odot$, and $0.1130^{+0.0048}_{-0.0049}\,M_\odot$ for components A, Ba, and Bb, respectively. The value of the minimum mass of the component A deviates only 1σ from the estimated value from mass-luminosity calibrations in Schweitzer et al. (2019), $0.472 \pm 0.020\,M_\odot$. This fact points at an almost edge-on orbit with respect to the line of sight.

Finally we searched for significant signals in the available ASAS and SWASP photometry. No significant periods were found in the ASAS photometry, which has a dispersion of 35 mmag. However, the periodogram of the SWASP photometry, shown in Fig. 4.39, has a significant signal at 52.5 ± 1.8 d with a semi-amplitude of 8.2 mmag, which we attributed to the rotation period of the most massive star, expected to be brighter. As for previous cases, we can assume that this system is older than 1 Ga, based on the rotation period much longer than that of the objects of NGC 6811 (Curtis et al. 2019b,a).

Table 4.8: Computed and derived parameters for the ST3 systems GJ 3916 and GJ 4383.

Parameter	System	
	GJ 3916	GJ 4383
Orbital parameters		
P_{AB} [d]	3028^{+23}_{-23}	4634^{+17}_{-17}
$T_{0,\mathrm{AB}}$ [BJD]	2456972^{+39}_{-38}	2458700^{+39}_{-36}
K_A [km s^{-1}]	$7.43^{+0.37}_{-0.32}$	$4.206^{+0.037}_{-0.036}$
K_B [km s^{-1}]	$7.07^{+0.35}_{-0.32}$	$7.66^{+0.11}_{-0.11}$
$e_{AB} \sin \omega_{AB}$	$0.318^{+0.023}_{-0.023}$	$0.0176^{+0.0061}_{-0.0066}$
$e_{AB} \cos \omega_{AB}$	$0.328^{+0.031}_{-0.030}$	$-0.1052^{+0.0050}_{-0.0048}$
e_{AB}	$0.458^{+0.026}_{-0.026}$	$0.1068^{+0.0049}_{-0.0049}$
ω_{AB} [deg]	$44.1^{+3.6}_{-3.6}$	$170.4^{+3.6}_{-3.3}$
P_B [d]	$132.959^{+0.013}_{-0.014}$	$216.07^{+0.13}_{-0.14}$
$T_{0,\mathrm{B}}$ [BJD]	$2458153.2^{+1.1}_{-1.1}$	$2458122.5^{+1.1}_{-1.1}$
K_{Ba} [km s^{-1}]	$13.56^{+0.10}_{-0.10}$	$11.26^{+0.17}_{-0.17}$
K_{Bb} [km s^{-1}]	$15.14^{+0.11}_{-0.10}$	$12.02^{+0.20}_{-0.19}$
$e_B \sin \omega_B$	$-0.0793^{+0.0055}_{-0.0055}$	$0.277^{+0.012}_{-0.012}$
$e_B \cos \omega_B$	$-0.0767^{+0.0051}_{-0.0052}$	$0.059^{+0.011}_{-0.011}$
e_B	$0.1104^{+0.0049}_{-0.0046}$	$0.283^{+0.012}_{-0.011}$
ω_B [deg]	$46.0^{+2.9}_{-3.0}$	$77.9^{+2.2}_{-2.3}$
γ [km s^{-1}]	$2.962^{+0.077}_{-0.065}$	$-11.409^{+0.029}_{-0.027}$
σ_{CARM} [km s^{-1}]	$0.397^{+0.041}_{-0.038}$	$0.0231^{+0.0089}_{-0.0087}$
σ_{FEROS} [km s^{-1}]	$0.76^{+0.10}_{-0.09}$	$0.13^{+0.19}_{-0.09}$
σ_{HARPS} [km s^{-1}]	$0.44^{+0.32}_{-0.22}$	$0.033^{+0.039}_{-0.023}$
σ_{UVES} [km s^{-1}]	$0.53^{+0.31}_{-0.22}$	...
Derived parameters		
$q_{AB} \equiv M_B/M_A$	$1.049^{+0.051}_{-0.040}$	$0.549^{+0.010}_{-0.010}$
$a_{AB} \sin i_{AB}$ [au]	$3.59^{+0.10}_{-0.09}$	$5.025^{+0.051}_{-0.048}$
$M_A \sin^3 i_{AB}$ [M$_\odot$]	$0.328^{+0.033}_{-0.028}$	$0.509^{+0.017}_{-0.016}$
$M_B \sin^3 i_{AB}$ [M$_\odot$]	$0.344^{+0.035}_{-0.028}$	$0.2795^{+0.0061}_{-0.0058}$
$q_B \equiv M_{Bb}/M_{Ba}$	$0.8952^{+0.0094}_{-0.0089}$	$0.937^{+0.021}_{-0.020}$
$a_B \sin i_B$ [au]	$0.3487^{+0.0018}_{-0.0018}$	$0.4436^{+0.0047}_{-0.0050}$
$M_{Ba} \sin^3 i_B$ [M$_\odot$]	$0.1511^{+0.0025}_{-0.0025}$	$0.1206^{+0.0040}_{-0.0040}$
$M_{Bb} \sin^3 i_B$ [M$_\odot$]	$0.1353^{+0.0030}_{-0.0030}$	$0.1130^{+0.0048}_{-0.0049}$
$\sin i_{AB} / \sin i_B$	$1.063^{+0.036}_{-0.031}$	$1.062^{+0.017}_{-0.015}$
Fit quality		
rms_A [km s^{-1}]	0.41	0.04
rms_{Ba} [km s^{-1}]	0.57	0.11
rms_{Bb} [km s^{-1}]	0.71	0.27

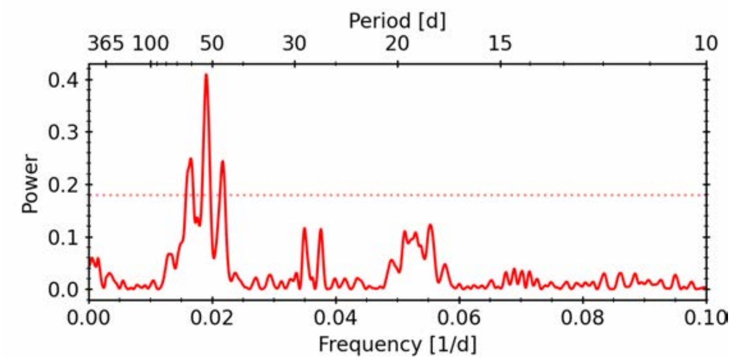

Figure 4.39: GLS periodogram of the SWASP photometry of GJ 4383. The horizontal dotted line indicates the corresponding 0.1 % FAP level.

4.5 Discussion

The multiple stars presented here add up to a total of 17 stellar systems detected among the 349 M-dwarf stars monitored with the CARMENES spectrograph. This yields a multiplicity ratio of 4.9%. This value is much lower than the M-dwarf multiplicity ratios reported by other studies of samples with significant sizes, ranging between 20 and 30% (Bergfors et al. 2010; Janson et al. 2012, 2014; Winters et al. 2019). However, this difference arises from the selection of targets for the CARMENES survey, which is aimed at the detection of exoplanets. A previous literature compilation and substantial observational effort (Alonso-Floriano et al. 2015; Cortés-Contreras et al. 2017; Jeffers et al. 2018) was done to determine the multiplicity of the stars in the CARMENES input catalogue (Caballero et al. 2013), in order to only include single stars. However, the resolution and/or the cadence of the observations was not enough to detect the multiple systems presented here.

The new binary systems can be used to update the M-dwarf multiplicity rate measured in other works. In a volume-limited sample of 1120 M dwarfs with distances below 25 pc, Winters et al. (2019) counted 265 multiple systems, from which they computed a multiplicity rate of 23.7 ± 1.3 % uncorrected for observational biases. Their sample included all the systems in this chapter except for UCAC4 355–020729, GJ 282 C, and LP 427–016, LP 395-8, and LP 790-2, and already tagged as multiple only the systems UU UMi and GJ 3916, based on the works by Heintz (1993) and Zechmeister et al. (2009), respectively, and EZ Psc and GJ 810 A based on their wide companions. Adding GJ 282 C, and LP 427-016 to the sample (UCAC4 355–020729, LP 395-8, and LP 790-2 are beyond 25 pc), and tagging as multiple the systems found in this chapter, we compute a new multiplicity rate of 24.5 ± 1.5% (275 multiple systems of 1122 stars). Similarly, Cortés-Contreras et al. (2017) computed a multiplicity ratio of 36.5 ± 2.9 % from 155 multiple systems among the 425 stars in a volume-limited sample from the CARMENES input catalogue, taking only M0-M5 stars within a maximum distance of 14 pc. Adding to their sample the 4 systems analyzed in this work that fulfill the distance and spectral type criteria we update their multiplicity ratio to 37.4 ± 3.0 %.

Figure 4.40 shows the mass ratios of the multiple systems found in this chapter as a function of their orbital period, and coloured by the pEW(Hα). Apart from the lack of systems with mass ratios lower than ~0.3, as expected from the flux ratio needed to discern the two components in the spectra with `todmor`, no clear dependence on the orbital period of the systems can be

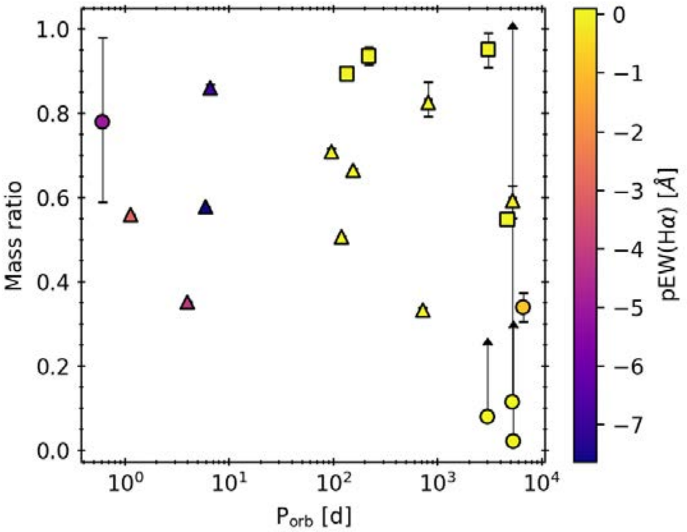

Figure 4.40: Mass ratio as a function of the orbital period of the multiple systems characterised in this, colour coded by the pEW(Hα). Circular, triangular, and squared symbols correspond to SB1, SB2, and ST3 systems, respectively. The upward arrows indicate the mass ratio limits for the systems for which only upper and lower bounds to the secondary masses could be given. We plot outer and inner orbits of the ST3 as individual binaries, with the same pEW(Hα).

observed. We do find, however, a relation between the stellar activity and the orbital period: systems with periods shorter than ~10 d have strong emission in the Hα line, whereas systems with larger periods have weak emission or even, in the earliest types, show this spectral line in absorption. This dependence on the orbital period is probably caused by the enhanced stellar activity for fast rotating M-dwarf stars (Newton et al. 2016; Suárez Mascareño et al. 2016; Astudillo-Defru et al. 2017; Jeffers et al. 2018). Tidal interactions between the components force the rotation period to synchronise with the orbital motion increasing their stellar activity. We still found systems with short orbital periods that are not synchronized, such as EZ Psc or LP 790-2. However, in this cases their high levels of stellar activity and rapid rotation may be associated to their young age, which could also explain the lack of synchronisation.

We have found a variety of stellar systems. We demonstrated that the system GJ 207.1 is probably composed of a white dwarf and an M dwarf. The short orbital period of about 14.5 hours suggests that this system may have survived a common envelope phase due to the evolution of the massive star (Nebot Gómez-Morán et al. 2011). The two components may have started off in a much wider orbit, but the engulfment of the M dwarf by the envelope of the white-dwarf progenitor caused drag forces that transported orbital angular momentum to the envelope, which was finally ejected. This process may have ended up shrinking and tidally locking the orbit to the present state (Nebot Gómez-Morán et al. 2011; Skinner et al. 2017). The number of white-dwarf plus M-dwarf close binary systems is rapidly increasing thanks to large-scale surveys such as SDSS (Rebassa-Mansergas et al. 2016) and LAMOST (Ren et al. 2018). However, these short-period post-common-envelope systems, in which the optical light is dominated by the M dwarf, are very uncommon, comprising an estimated fraction of 0.03–0.18 % of all M dwarfs (Law et al. 2012), as estimated from the detection of three such systems in a photometric survey of 45 000 M dwarfs. Only one white dwarf (in the system GJ 207.1, identified here) has been found among the ~360 stars in the CARMENES sample (Reiners et al. 2018b), a ratio larger (but compatible because of small-number statistics) than that estimated by Law et al. (2012). The larger ratio found by us could also be a by-product of the sensitivity to find white dwarfs around M stars using photometry and RVs.

Although RV surveys have detected an abundance of exoplanets, the number of close brown dwarf companions is small despite the fact that brown dwarfs should be more easily detected in comparable orbits, given the larger RV signals that they produce. Several studies estimated a stellar-brown dwarf multiplicity fraction around 1 % for a large range of primary mass and orbital separation (Halbwachs et al. 2000; Marcy & Butler 2000; McCarthy & Zuckerman 2004; Metchev & Hillenbrand 2009; Kraus et al. 2011). This is also valid for M-dwarf primaries (Dieterich et al. 2012), as suggested by the only 18 M-dwarf-brown-dwarf systems found among the 1120 M dwarfs contained in the sample of Winters et al. (2019), or by the two system candidates found in this work among the ~360 M dwarfs observed with CARMENES. Observational evidence points at a bimodal companion mass function (Grether & Lineweaver 2006) with a gap, also called the brown dwarf desert, at the intersection between the planetary and stellar-companion mass functions. The position of this minimum in the companion mass function seems to increase with the mass of the host star (Quirrenbach et al. 2019) and, therefore, objects with similar masses may have very different formation mechanisms (Armitage & Bonnell 2002; Matzner & Levin 2005). Although the masses of the brown dwarf candidates found in this work are not fully constrained, the low mass of the host stars and the highly eccentric orbits of the systems may be indicating that they probably belong to the "stellar" part of the companion mass function. If that is the case, one would expect the same metallicity as for their host stars, whereas "planet-like" objects might be metal-enhanced (Maldonado & Villaver 2017; Quirrenbach et al. 2019). GJ 912 B and GJ 3626 B, with computed minimum masses of ~60 $M_{\rm Jup}$ and ~30 $M_{\rm Jup}$, respectively, and expected angular separations between 100 mas and 300 mas, may be directly imaged with state-of-the-art imagers such as Gemini/GPI (Macintosh et al. 2014), Subaru/SCExAO (Jovanovic et al. 2015), Keck/OSIRIS-NIRC2 (Wizinowich et al. 2006; Larkin et al. 2006), or VLT/SPHERE (Beuzit et al. 2019), as estimated from simulated planet injections (Wagner et al. 2020). If the brown-dwarf nature of GJ 912 B and GJ 3626 B is confirmed with future observations, they will help to better constrain the multiplicity rate of these systems and the boundaries of the brown dwarf desert, providing additional insights into the formation mechanisms of brown dwarfs.

We unveiled the hierarchical triple nature of GJ 3916 and GJ 4383, for which we were able to detect the spectroscopic signals of all three components. Interestingly enough, the masses of the close, inner pair are nearly identical in both cases, and their combined mass is either equal to the outer component or half that value. These results could help constraining formation models. Understanding the processes leading to the formation of multiple systems is one of the fundamental challenges in astrophysics and has been a matter of debate for many years (Duchêne & Kraus 2013). One possible mechanism is the formation of these systems through the fragmentation of collapsing and rotating protostellar clouds (Boss 1988). Another possible explanation is the dynamical break-up of rapidly rotating clouds, or fission, although this mechanism does not seem to lead to the production of equal-mass binary protostars (Durisen et al. 1986), and thus is not capable of explaining the mass ratio distribution for binary systems, which shows an intrinsic excess at about unity (Lucy 2006; Simon & Obbie 2009). The formation of both democratic (all components with similar masses) and hierarchical systems could be explained by fragmentation. In the first case, the cloud fragments into three or more protostars, while in the other case the cloud first collapses into binary protostars, which then can undergo subsequent fragmentations. Most observed triples have hierarchical structures, consisting of an inner binary and a distant star (Hut & Bahcall 1983; Tokovinin et al. 2006), because democratic triples tend to be unstable and short-lived (van den Berk et al. 2007). The presence of a third body on a wide orbit around a tight binary causes an angular momentum exchange between the two orbits, which in turn produces dynamical variations, such as periodic oscillations in the eccentricity of the inner binary and in the mutual inclination through Lidov-Kozai interactions (Lidov 1962; Kozai 1962; Mazeh & Shaham 1979; Naoz 2016). Usually, the timescale of such interactions is much larger than the orbital periods and, thus, their effect in triple systems has only been detected indirectly through unusual inner eccentricity values (Kiseleva et al. 1998; Ford et al. 2000), or measured directly in very few systems (Jha et al. 2000). However, tight orbital configurations produce dynamical variations with timescales of the order of the orbital period, which lead to the disruption of the system.

In order to check the long-term stability of the triple systems found in this work, we used the Eggleton & Kiseleva (1995) criterion for the stability of triple stellar systems, which He & Petrovich (2018) found to work reasonably well for a wide range of parameters in their N-body simulations. According to this criterion, the systems are stable when the orbit separation parameter $r_{\mathrm{ap}} \equiv a_{\mathrm{AB}} a_{\mathrm{B}}^{-1}(1 - e_{\mathrm{AB}})(1 + e_{\mathrm{B}})^{-1}$ is higher than the value Y_{EK} (Eggleton & Kiseleva 1995; He & Petrovich 2018) defined as

$$Y_{\mathrm{EK}} \equiv 1 + \frac{3.7}{q_{\mathrm{AB}}^{1/3}} - \frac{2.2}{1 + q_{\mathrm{AB}}^{1/3}} + \frac{1.4}{q_{\mathrm{B}}^{1/3}} \frac{q_{\mathrm{AB}}^{1/3} - 1}{1 + q_{\mathrm{AB}}^{1/3}}. \tag{4.5}$$

For the cases of the triple systems GJ 3916 and GJ 4383, which have an orbit separation parameter r_{ap} of 5.03 and 7.89, we obtained values of Y_{EK} of 3.56 and 4.17, respectively. Therefore, both system have stable orbital configurations.

The time scale of the Lidov-Kozai interactions is also useful to assess the stability of the system. Actually, this parameter is crucial to verify if the orbit of the systems can be approximated by a Keplerian function in a hierarchical system during the time-span of all the RV measurements, as we have done in this work. This timescale τ_{LK} is defined as:

$$\tau_{\mathrm{LK}} = \alpha \frac{P_{\mathrm{AB}}^2}{P_{\mathrm{B}}} \frac{M_{\mathrm{A}} + M_{\mathrm{Ba}} + M_{\mathrm{Bb}}}{M_{\mathrm{A}}} (1 - e_{\mathrm{AB}}^2)^{3/2}, \tag{4.6}$$

where α is close to one, and weakly depends on the orbital parameters (Kinoshita & Nakai 1999; Toonen et al. 2020). Equation 4.6 yields timescales of the Lidov-Kozai oscillations for GJ 3916 and GJ 4383 of 272 years and 414 years, respectively, which, just by chance, in both cases is equivalent to 33 orbital periods of the outer binary. The time-span of the RV measurements used in the fits covered just 5.6 % and a 2.3 % of τ_{LK} for GJ 3916 and GJ 4383, respectively. This small fraction of the Lidov-Kozai cycle does not have a significant effect on the orbital fits of the RVs of these systems. This is also confirmed by the lack of systematic deviations in the residuals shown in the top panels in Figs. 4.36 and 4.38.

4.5.1 Individual masses and radii of SB2 systems

The analysis of the radial velocities of RV2 systems only yields the minimum masses of the components and their mass ratio, but an estimation of individual masses could be performed by using a recipe that we developed in Baroch et al. (2018). This method is based on the determination of the mass ratio between the components, which is easily obtained from RV curves, the magnitude of the system, and precise trigonometric distances. The absolute magnitude of the system (A_{K_s}, for instance), can be computed from the photometric data and the distance. On the other hand, the individual magnitude of each star can be computed as a function of the flux ratio between the components, α, as

$$A_{K_s,1} = A_{K_s} + 2.5\log_{10}(1+\alpha), \tag{4.7}$$

$$A_{K_s,2} = A_{K_s} + 2.5\log_{10}(1+1/\alpha). \tag{4.8}$$

Assuming now the empirical mass-luminosity relationship $f(A_{K_s})$ in Mann et al. (2019) (Eq. 1.21), it is possible to obtain an estimated value of the mass ratio q as a function of the flux ratio as

$$q = \frac{f(A_{K_s,2})}{f(A_{K_s,1})} = \frac{f[A_{K_s} + 2.5\log_{10}(1+1/\alpha)]}{f[A_{K_s} + 2.5\log_{10}(1+\alpha)]}. \tag{4.9}$$

To estimate the individual masses of the systems in this chapter, we used the systems' distance and the K_s-band magnitudes given in Table 4.1. We computed the individual masses and the corresponding mass ratio as a function of the flux ratio, and chose as the fiducial individual masses those corresponding with the flux ratio that corresponds to the mass ratio derived from the RV curves, which are listed in Table 4.7. We show in Fig. 4.41 an example of this process for the case of LP 790-2. In order to account for uncertainties of the input parameters (i.e. d, K_s, and q) we computed the standard deviation of the resulting values of 10 000 Monte Carlo realisations of the input parameter distribution. In order to account for the scatter of the residuals in the Mann et al. (2019) relationship, we added additional uncertainties to the individual masses according to the values shown in their Table 7, which are around 2.3 %, depending on the input K_s band magnitude. Additionally, since for non-eclipsing SB2 systems it is not possible to measure individual radii, we computed them by using the empirical mass-radius relation by Schweitzer et al. (2019), defined in Eq. 1.22, which is based on masses and radii of eclipsing binaries, and is valid on a mass range between 0.092 $M_\odot$ to 0.73 $M_\odot$. We list in Table 4.9 the estimated individual masses, radii, and K_s-band magnitudes of the SB2 systems analyzed in this chapter, together with the flux ratio value that using Eq. (4.9) yielded the mass ratios given in Table 4.7.

Alternatively, it is also possible to use the flux ratios derived from the spectral analysis with `todmor`, but in our case, they correspond to the flux ratio at the effective wavelengths of the VIS CARMENES channels, which have wavelengths shortward of the K_s-band used for the mass calibration. Also, the flux ratios derived with `todmor` strongly depend on the spectra used in the optimisation process, and therefore the values listed in Table 4.4 are approximated values only meant to compute the RVs of the systems.

To check the consistency of individual masses, we compared them with the minimum masses reported in Table 4.7. Figure 4.42 shows the absolute individual masses estimated for our systems, and their corresponding K_s-band absolute magnitudes computed with the mass-luminosity

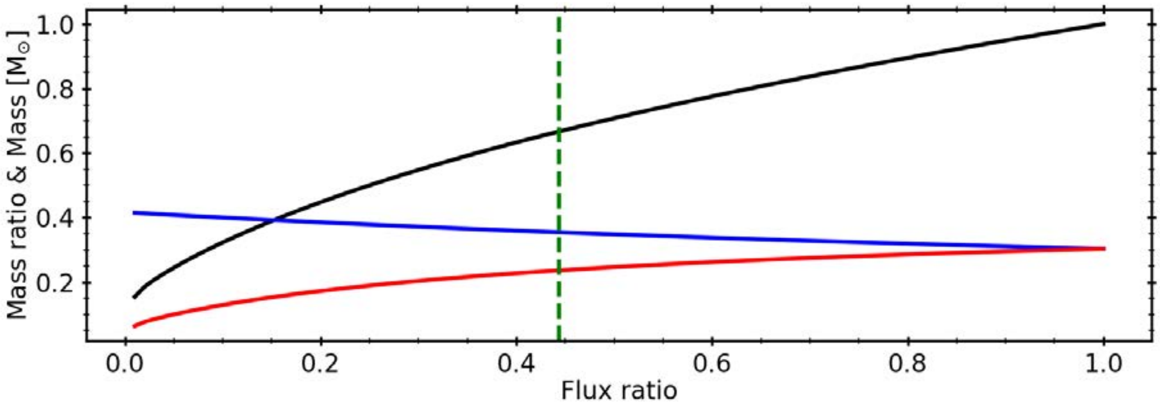

Figure 4.41: Primary (blue line) and secondary (red line) individual masses of the binary system LP 790-2 as a function of the flux ratio, computed using the empirical mass–luminosity defined in Eq. (1.21). The corresponding mass ratio, computed with Eq. (4.9) is shown as a black line, while the flux ratio at which the mass ratio equals that derived from the RV analysis, $q = 0.5784$, is indicated as a green dashed line. The adopted individual masses correspond to the values at which the green dashed line intersects the blue and red lines.

Table 4.9: Individual masses and absolute K_s-band magnitudes computed with the mass-luminosity relation by Mann et al. (2019) and individual radii computed with the empirical mass-radius relation by Schweitzer et al. (2019) of the SB2 systems analyzed in this work.

Name	M_{A} [$\mathrm{M}_\odot$]	M_{B} [$\mathrm{M}_\odot$]	R_{A} [$\mathrm{R}_\odot$]	R_{B} [$\mathrm{R}_\odot$]	$A_{K_s,\mathrm{A}}$ [mag]	$A_{K_s,\mathrm{B}}$ [mag]
EZ Psc	0.3951 ± 0.0097	0.1392 ± 0.0034	0.398 ± 0.013	0.1583 ± 0.0077	6.280 ± 0.023	8.570 ± 0.024
GJ 1029	0.1438 ± 0.0035	0.1059 ± 0.0027	0.1626 ± 0.0080	0.1271 ± 0.0076	8.495 ± 0.023	9.275 ± 0.035
Ross 59	0.569 ± 0.015	0.1866 ± 0.0047	0.560 ± 0.018	0.2027 ± 0.0086	5.106 ± 0.032	7.920 ± 0.027
UCAC4 355-020729	0.3911 ± 0.0093	0.3360 ± 0.0081	0.394 ± 0.012	0.342 ± 0.011	6.305 ± 0.020	6.666 ± 0.021
LP 790-2	0.3702 ± 0.0091	0.2141 ± 0.0051	0.374 ± 0.012	0.2285 ± 0.0089	6.440 ± 0.024	7.632 ± 0.021
GJ 3612	0.3033 ± 0.0074	0.1550 ± 0.0039	0.312 ± 0.011	0.1730 ± 0.0080	6.895 ± 0.022	8.324 ± 0.025
GJ 1182	0.1589 ± 0.0039	0.1062 ± 0.0027	0.1768 ± 0.0081	0.1274 ± 0.0074	8.268 ± 0.025	9.270 ± 0.034
UU UMi	0.2757 ± 0.0085	0.1631 ± 0.0089	0.286 ± 0.011	0.181 ± 0.011	7.102 ± 0.045	8.21 ± 0.11
LP 395-8	0.564 ± 0.015	0.3170 ± 0.0074	0.555 ± 0.017	0.325 ± 0.011	5.149 ± 0.020	6.797 ± 0.013
GJ 810 A	0.2166 ± 0.0058	0.1838 ± 0.0049	0.2307 ± 0.0092	0.2000 ± 0.0088	7.607 ± 0.033	7.953 ± 0.033

relation by Mann et al. (2019). The arrows point towards the minimum masses of each component determined from the RV analysis. Long arrows indicate systems with low inclination (i.e. small sin i), while arrows pointing to the right correspond to individual masses with values below the minimum masses, such as for UU UMi, which have $\sin i = 1.04 \pm 0.07$. Although the relatively large uncertainties of the minimum masses of UU UMi made them compatible with the estimated individual masses, this is a further indication of the almost edge on orbit as reported in Heintz (1993). Other systems such as GJ 1182 and EZ Psc have estimated inclinations close to 90 deg, with sin i values of 0.990 ± 0.009 and 0.971 ± 0.009, respectively, but no eclipses are found in their light-curves. On the contrary, the extremely small minimum masses of UCAC 355-020729 are indicative of an almost face-on orbit, obtaining a sin i of 0.0454 ± 0.0004.

Winters et al. (2021) compiled a volume-complete list of M-dwarf stars with measured masses between 0.1 and 0.3 $\mathrm{M}_\odot$ at distances $d < 15$ pc, finding a total of 512 stars, which already includes 9 stars of this work that fulfill the constraints. With the addition to this list of GJ 282 Cb

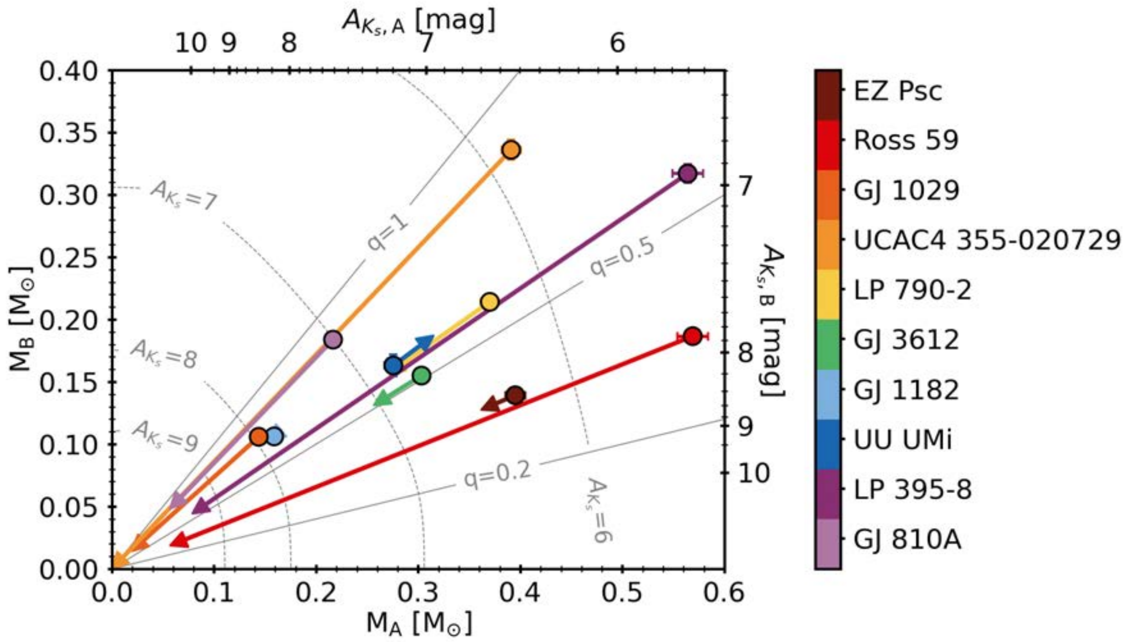

Figure 4.42: Individual masses for the primary and secondary components of the SB2 systems (circles). The absolute magnitudes on the top and right axes are computed according to the mass-luminosity relation by Mann et al. (2019). Lines of constant mass ratio are shown as grey diagonals. Dashed contours correspond to the combined magnitudes for pairs $A_{K_s,1}$ and $A_{K_s,2}$. The arrows point to the minimum masses listed in Table 4.7. Long arrows are indicative of low orbital inclinations.

and UU UMi A, the components found in this chapter represent 2 % (10 out of 514) of the M dwarfs with measured masses between 0.1 and 0.3 M$_\odot$ at distances $d < 15$ pc.

Given the orbital periods and separations of the binary systems studied here, it is worth estimating whether or not their orbits could be resolved by *Gaia*, since this would provide precise individual absolute masses independent from calibrations. Using the individual masses in Table 4.9 and the 5 Ga BHAC stellar models, we estimated individual G-band magnitudes for each component of the systems, which are listed in Table 4.10. We then computed the apparent semi-major axis of the photocenter motion in the G-band, $a_{\mathrm{app},G}$, as:

$$a_{\mathrm{app},G} = \frac{q-\alpha}{(1+q)(1+\alpha)}\frac{a}{d} \text{ arcsec}, \tag{4.10}$$

where q is the mass ratio, α the flux ratio in the G-band, a is the semi-major axis in au, and d is the distance in pc (Perryman 2018). We found values ranging from 110 μas to 50 mas; therefore, given the Gaia astrometric precision of 50 μas (Lindegren et al. 2018), the astrometric orbits of all systems could be, in principle, resolved. Furthermore, all the binary systems analysed here, except LP 395-8, show an *astrometric excess noise* (AEN, Lindegren et al. 2012) parameter above 0.25 mas, always above the median of all the *Gaia* sources (Lindegren et al. 2018). Table 4.10 also lists the renormalised unit weight error (RUWE) from *Gaia*, which is an indicator of the goodness of the fit of the astrometric observations (Gaia Collaboration et al. 2021). A RUWE $\gtrsim$ 1.4 may indicate that the source is not single, and that individual astrometric measurements are affected by the orbital motion of the system. All the systems in Table 4.10 satisfy this condition.

Table 4.10: Individual *Gaia* G-band magnitudes estimated using individual masses and the BHAC 5 Ga stellar models, and predicted motion of the semi-major axis of the photocentre in the G-band.

Name	G_1 [mag]	G_2 [mag]	$a_{\mathrm{app},G}$ [mas]	AEN [mas]	RUWE
EZ Psc	10.73	13.51	0.49	0.3	1.6
GJ 1029	12.96	14.19	3.75	2.2	7.5
Ross 59	9.94	13.31	14.03	3.0	6.1
UCAC4 355-020729	12.20	12.59	0.11	0.3	1.4
LP 790-2	11.99	13.36	0.31	0.3	1.6
GJ 3612	10.99	12.75	5.00	2.7	15.2
GJ 1182	12.87	14.41	5.28	2.9	13.2
UU UMi	11.37	12.76	50.63	3.6	9.2
LP 395-8	10.73	12.71	0.15	0.2	1.5
GJ 810 A	11.66	12.10	5.51	2.9	15.3

4.6 Summary

In this chapter we analysed 17 new M-dwarf multiple systems found in the context of the CARMENES survey of exoplanets, determining their orbital parameters using high-precision RVs collected with CARMENES and from archival data. An analysis of the spectra with `todmor` revealed the signal of both components in 10 systems, while in two systems we find the signals of three components. In the five remaining systems we only detected the signal of the brightest companion, and we obtained the minimum masses of the unseen components. In two cases, GJ 912 and GJ 3626, the minimum masses were below the stellar boundary, and therefore could be brown dwarfs. We also find a new white dwarf in a close orbit around the M dwarf GJ 207.1, which is supported by the modulations found in its TESS photometry. Adaptive optics imaging data also permitted us to measure the absolute masses of the Ursa Major moving group members GJ 282 Ca and GJ 282 Cb with uncertainties of 10 % and 3 %, respectively, making it one of the youngest systems with measured dynamical masses. We characterised the orbital architecture of two triple systems, which in both cases consist of two inner companions of similar masses, orbited by a more massive companion in a wide orbit. We tested and confirmed the stability of their orbits, with a ratio between outer and inner periods of ~22 in both cases. Finally, we estimated individual masses and radii of all SB2s, making use of mass-luminosity and mass-radius empirical relationships. We find 2 % of all the stars within 15 pc with masses between 0.1 and 0.3 $M_{\odot}$.

Publicly available photometry for these targets was also analysed. Significant periodic signals attributed to the rotation period of the brightest component are found for 14 of the systems, while for GJ 282 C we could temptatively determine the rotation period of the two components. No eclipses are found in any case.

The determination of the spectroscopic orbits and physical properties of the systems in this work will provide help to understand the galactic population as a whole. The new systems contribute to statistical studies of the stellar multiplicity and the frequency of exotic binaries. They could provide additional constraints to star formation theories, stellar evolutionary and structure models, and empirical calibrations. These constraints may become more stringent in the future thanks to measurement of absolute individual masses of the components of the systems when precise astrometric data coming from *Gaia* can be added to the analysis. Direct imaging could also provide a wealth of information for these multiple systems.

Chapter 5

Relativistic apsidal motion in binary stars

The change in the argument of periastron of eclipsing binaries, that is, the apsidal motion caused by classical and relativistic effects, can be measured from variations in the difference between the time of minimum light of the primary and secondary eclipses. Poor apsidal motion rate determinations and large uncertainties in the classical term have hampered previous attempts to determine the general relativistic term with sufficient precision to test general relativity predictions. As a product of the TESS mission, thousands of high-precision light curves from eclipsing binaries are now available. Using a selection of suitable well-studied eccentric eclipsing binary systems, we aim to determine their apsidal motion rates and place constraints on key gravitational parameters.

We compute the time of minimum light from the TESS light curves of 16 eclipsing binaries with precise absolute parameters and with an expected general relativistic contribution to the total apsidal motion rate greater than 60%. We use the changing primary and secondary eclipse timing differences over time to compute the apsidal motion rate, when possible, or the difference between the linear periods as computed from primary and secondary eclipses. For a greater time baseline we carefully combine the high-precision TESS timings with archival reliable timings.

We determine the apsidal motion rate of ten eclipsing binaries, five of which are reported for the first time. From these, we are able to measure the general relativistic apsidal motion rate of nine systems with sufficient precision to test general relativity for the first time using this method. This test explores a regime of gravitational forces and potentials that had not been probed before. We find perfect agreement with theoretical predictions, and we are able to set stringent constraints on two parameters of the parametrised post-Newtonian formalism.

In Sect. 5.2 we present the analysed sample and its general properties. In Sect. 5.3 we explain how we determine the times of eclipse, while in Sect. 5.4 we describe the methodology followed to determine the apsidal motion for each of the systems using TESS and archival timings. In Sect. 5.5 we present the determined apsidal motion rates, the theoretical prediction of their classical contributions, and compare the differences with general relativity predictions. Finally, we use our measurements to test different gravitational theories in Sect. 5.6, and provide our concluding remarks in Sect. 5.7.

Baroch, D., Giménez, A., Ribas, I., et al.
A&A, **649**, A64 (2021)

5.1 Introduction

Eclipsing binaries have demonstrated to be a basic source of fundamental information about stellar properties such as masses and radii (Andersen 1991; Torres et al. 2010). The comparison of the observed values with theoretical predictions has been used profusely to perform critical tests of stellar structure and evolution models (Pols et al. 1997; Ribas et al. 2000; Torres & Ribas 2002; Lastennet & Valls-Gabaud 2002; Feiden & Chaboyer 2012; Higl & Weiss 2017; Tkachenko et al. 2020). But eccentric eclipsing binaries offer further opportunities to gain indirect insight into the internal structure of stars through the measurement of the precession rate of the line of apsides of the orbit, that is, the apsidal motion rate ($\dot{\omega}$). Such precession motion is found to arise from two different contributions: a general relativistic ($\dot{\omega}_{\rm rel}$) term arising from general relativity (GR), and a classical or Newtonian ($\dot{\omega}_{\rm cl}$) term. These two contributions are additive, so that $\dot{\omega} = \dot{\omega}_{\rm rel} + \dot{\omega}_{\rm cl}$ (Shakura 1985). The general relativistic term of the apsidal motion rate, when only considering quadratic corrections, can be calculated with the equation given by Levi-Civita (1937), in the form presented by Giménez (1985) in degrees per orbital cycle as:

$$\dot{\omega}_{\rm rel} = 5.447 \times 10^{-4} \frac{(M_1 + M_2)^{2/3}}{(1 - e^2)\, P_{\rm a}^{2/3}} \text{ deg cycle}^{-1}, \tag{5.1}$$

where e is the orbital eccentricity, M_1 and M_2 are the component masses in solar units, and $P_{\rm a}$ is the anomalistic period in days, which measures the time between two consecutive periastron passages, and is related to the sidereal period, $P_{\rm s}$, through:

$$P_{\rm s} = P_{\rm a}\left(1 - \frac{\dot{\omega}}{360}\right), \tag{5.2}$$

where $\dot{\omega}$ is in degrees per orbital cycle. The classical contribution to the apsidal motion is produced by perturbations in the gravitational potential due to the lack of spherical symmetry in the shape of the components, which are distorted due to rotational flattening and tidal oblateness, the so-called quadrupole effect, and for the most part depends on the degree of mass concentration towards the centre (Shakura 1985). The term $\dot{\omega}_{\rm cl}$, when only considering the contributions arising from the second-order harmonic distortions of the potential, can be described by the expressions given by Sterne (1939) and Kopal (1959):

$$\dot{\omega}_{\rm cl} = 360 \times \sum_{i=1}^{2} \left(k_{2,i} c_i^{\rm rot} + k_{2,i} c_i^{\rm tid}\right) \text{ deg cycle}^{-1}, \tag{5.3}$$

where the index i refers to the stellar component and $k_{2,i}$ are the second-order internal structure constants characterising the internal mass distribution of the stars, which can be derived from theoretical models by numerically integrating the Radau differential equation (Kopal 1978; Hejlesen 1987; Schmitt et al. 2016). The parameters $c_i^{\rm rot}$ and $c_i^{\rm tid}$ are the rotational and tidal contributions to the apsidal motion, respectively, which, assuming that the stellar and orbital rotation axes are aligned, can be expressed (Kopal 1978; Shakura 1985) as:

$$c_i^{\rm rot} = \frac{r_i^5}{(1 - e^2)^2} \left(1 + \frac{M_{3-i}}{M_i}\right) \left(\frac{\Omega_i}{\Omega_m}\right)^2, \tag{5.4}$$

$$c_i^{\mathrm{tid}} = 15 r_i^5 \frac{M_{3-i}}{M_i} \frac{\left(1 + 1.5e^2 + 0.125e^4\right)}{(1-e^2)^5}, \tag{5.5}$$

where $\Omega_m = 2\pi/P_{\mathrm{s}}$ is the mean angular velocity of the orbital motion, $\Omega_i = v_{\mathrm{rot,i}}/R_i$ is the angular velocity of the rotation of each component, and $r_i = R_i/a$ are the relative component radii. In Eq. (5.3) we do not use terms with k_3 and k_4 because they usually produce negligible contributions given the uncertainties of the lower order terms (Claret & Giménez 1993; Rosu et al. 2020). As all the terms appearing in Eq. (5.1) can be obtained from observations, the GR apsidal motion rate is most often calculated analytically and subsequently subtracted from the measured rate to compare with stellar model predictions and provide constraints on interior structure (e.g. Claret & Giménez 1993; Khaliullin & Khaliullina 2007; Zasche & Wolf 2019).

Direct GR tests using measured apsidal motion rates have been hampered by the typical large relative uncertainty due to the error propagation from the dominant classical term. Eclipsing binaries suitable to test GR are those with relatively long orbital periods, where the general relativistic term makes up most of the apsidal motion contribution, that are still sufficiently short to produce an apsidal motion rate larger than the expected detection threshold (see equations 16 and 17 in Giménez 1985, and their Table 1 to see the dependence of the period limits with the eccentricity). The most famous case is that of DI Her, whose detailed initial analyses showed disagreement with GR predictions (e.g. Guinan & Maloney 1985). It was later shown (Albrecht et al. 2009) that this mismatch was actually caused by a strong spin axis misalignment of the component stars, which leads to a different classical term, with a negative contribution of the rotational term to the total apsidal motion rate. There have been some attempts to further test GR using larger samples of eclipsing binaries but these failed to reach conclusive results (e.g. De Laurentis et al. 2012). This was caused by the large relative uncertainties resulting from the subtraction of the dominant classical contributions to the total apsidal motion term. The systems selected had a small fractional contribution of the GR term. With a carefully selected sample and the use of longer time baselines and more precise eclipse timings it should be possible to perform more accurate analyses and reach conclusive tests of GR. Precise determinations and even simply the detection of apsidal motion based on eclipse timings requires in most cases a dedicated long-term monitoring, generally spanning several decades. This is particularly difficult for systems whose orbital periods are long or have very slow apsidal motion rates, which happen to be the systems with the largest relativistic contributions due to the decrease of the classical terms with the orbital period as shown by Giménez (1985).

Data from the Transiting Exoplanet Survey Satellite (TESS) mission (Ricker et al. 2015) aimed at detecting exoplanets through photometric transits provide the opportunity to obtain densely-covered light curves of eclipsing binary systems at very high precision. Stellar eclipse events are generally much deeper than exoplanet transits and therefore TESS data are of excellent quality for such studies. Largely uninterrupted monitoring of the light curves is possible from space without the disturbing effect of the day-night cycle, therefore minimising the existence of phase gaps. In addition, most eclipsing binary systems were observed by TESS at the high cadence rate of 2 minutes. Thanks to all these circumstances, accurate eclipse timings can be obtained for numerous events. Furthermore, already during its initial 2 years of mission, TESS has covered a large fraction of the sky for a duration of at least 27 days, and therefore the chances of having observed eclipse events of most well-studied eclipsing binary systems are very high. Of course, the time baseline of the typical TESS observations is rather modest, but the high-precision measurements can be combined with past timings to enlarge the covered time-span significantly.

5.2 The eclipsing binary sample

For any useful interpretation of the observed apsidal motion in eccentric eclipsing binaries, it is essential to have good knowledge of the general properties of the component stars, mainly their masses and radii. Relevant equations such as Eqs. (5.4) and (5.5) have terms with high powers (up to the fifth) of the relative radii for example, thus enhancing their potential uncertainties. For this reason, we have limited our dynamical study to cases with well-studied and precise fundamental properties. The basic source is the compilation of well-studied detached eclipsing binaries by Torres et al. (2010). This has been complemented with systems from the DEBCAT catalogue (Southworth 2015), which is permanently updated, and includes eclipsing binaries with mass and radius measurements with 2% accuracy or better, following the criterion in Andersen (1991).

From the compilations above and imposing the restriction of having TESS measurements for both primary and secondary eclipses, we selected the sample of eccentric eclipsing binaries in Table 5.1. Given our objective of testing the theoretically predicted GR contribution, as given by Eq. (5.1), with observed apsidal motion rates, we limited the sample to only systems with a literature-predicted fractional contribution greater than 60%. This threshold is high enough to

Table 5.1: Properties of 16 eclipsing binary systems with eccentric orbits, accurate absolute dimensions, and literature-predicted relativistic apsidal motion relative contribution greater than 60%.

System	P_s [d]	e	M_1 [$M_\odot$]	M_2 [$M_\odot$]	R_1 [$R_\odot$]	R_2 [$R_\odot$]	$\%\dot{\omega}_{\mathrm{Rel,Pred}}$	Ref.
KX Cnc	31.2197874(14)	0.4666(3)	1.138(3)	1.131(3)	1.064(2)	1.049(2)	99	Sow12
AL Dor	14.905353(12)	0.1950(2)	1.1018(6)	1.1028(7)	1.092(2)	1.098(2)	98	G&G
RW Lac	10.369205(2)	0.0098(10)	0.928(6)	0.870(4)	1.186(4)	0.964(4)	96	Lac05
V530 Ori	6.1107784(3)	0.0880(2)	1.004(7)	0.596(2)	0.980(13)	0.587(7)	92	Tor14
EW Ori	6.9368432(4)	0.076(2)	1.173(11)	1.123(9)	1.168(5)	1.097(5)	88	Cla10
HP Dra	10.7615(2)	0.0367(9)	1.133(5)	1.094(7)	1.371(12)	1.052(10)	89	Mil10
TZ Men	8.569000(10)	0.035(3)	2.49(3)	1.504(10)	2.02(2)	1.432(15)	86	And87
V541 Cyg	15.3378992(7)	0.4684(14)	2.335(17)	2.260(16)	1.859(12)	1.808(15)	86	Tor17
LV Her	18.435954(2)	0.6127(7)	1.193(10)	1.170(8)	1.358(12)	1.313(11)	83	Tor09
V459 Cas	8.45825381(19)	0.0244(4)	2.02(3)	1.96(3)	2.009(13)	1.965(13)	80	Lac04
RR Lyn	9.94508(6)	0.0793(9)	1.927(8)	1.507(4)	2.57(2)	1.59(3)	80	Tom06
V501 Her	8.5976870(10)	0.0956(8)	1.269(4)	1.211(3)	2.002(3)	1.511(3)	78	Lac14
KW Hya	7.750469(6)	0.094(4)	1.96(3)	1.487(13)	2.124(15)	1.44(2)	77	G&A
V501 Mon	7.0212077(10)	0.1339(6)	1.646(4)	1.459(3)	1.89(3)	1.59(3)	71	Tor15
GG Ori	6.6314936(17)	0.2218(22)	2.342(16)	2.338(17)	1.85(3)	1.83(3)	67	Tor00
EY Cep	7.971488(6)	0.4429(14)	1.523(8)	1.498(14)	1.463(10)	1.468(10)	64	Lac06

Notes. Only systems with primary and secondary eclipse coverage from the TESS mission are considered.

References. Sow12: Sowell et al. (2012); G&G: Gallenne et al. (2019) and Graczyk et al. (2019); Lac05: Lacy et al. (2005); Tor14: Torres et al. (2014); Cla10: Clausen et al. (2010); Mil10: Milone et al. (2010); And87: Andersen et al. (1987); Tor17: Torres et al. (2017); Tor09: Torres et al. (2009); Lac04: Lacy et al. (2004); Tom06: Tomkin & Fekel (2006); Lac14: Sandberg Lacy & Fekel (2014); G&A: Gallenne et al. (2019) and Andersen & Vaz (1984); Tor15: Torres et al. (2015); Tor00: Torres et al. (2000); Lac06: Lacy et al. (2006).

make sure that uncertainties due to the classical contribution do not dominate over the combined term, and small enough to allow for a meaningful sample size in order to perform statistical tests. We used the general properties, as referenced in Table 5.1, and an estimated classical contribution given by Eq. (5.3), with the assumption of rotational synchronisation at periastron and co-aligned rotational axes. Table 5.1 lists the adopted general properties of the systems such as the sidereal period, eccentricity, component masses, and radii of the 16 selected eclipsing binaries, together with the predicted GR contribution to the apsidal motion ($\%\dot{\omega}_{\mathrm{Rel,Pred}}$). It should be noted that in all tables presented throughout this chapter the values in parentheses indicate the uncertainties affecting the last digits.

Three additional eclipsing binary systems not included in Table 5.1 deserve specific attention. DI Her is known to have misaligned rotational axes (Albrecht et al. 2009). The computation of the classical term of the apsidal motion therefore requires the use of the general form of Eq. (5.3) given by Shakura (1985) and an analysis of those angles constrained but not directly observed with the Rossiter-McLaughlin effect (Claret et al. 2010), which complicates the interpretation. EP Cru has component stars with rotational velocities 5.8 times higher than synchronisation at periastron (Albrecht et al. 2013). When such rotational velocities are considered, the classical term becomes dominant and the system does not meet our limiting criterion on the fractional GR contribution to the total apsidal motion rate to be included in the present study. Finally, a detailed analysis of BF Dra revealed a trend in the primary and secondary eclipse residuals of the high-precision TESS timings. Such a trend may likely be produced by the presence of a third body orbiting the system. The unconstrained nature of the third companion makes the determined apsidal motion rate ill-suited for comparison with theoretical predictions.

5.3 Determination of times of minimum light

We used TESS data from sectors 1 to 36 to compute precise timings of the primary and secondary eclipses for all of our targets. We gathered the 2-min short-cadence simple aperture photometry (SAP) produced by the Science Process Operation Centre (SPOC, Jenkins et al. 2016) available at the Mikulski Archive for Space Telescopes[1]. In the cases of V530 Ori and V501 Mon, for which the 2-min cadence photometry was not available, we extracted the 30-min (10-min from sector 29 onward) cadence simple aperture photometry from the TESS full frame images (FFIs) using the public TESS aperture photometry tool Eleanor[2] (Feinstein et al. 2019). Table 5.2 lists the TESS sectors and cadence at which each system has been observed, the time-span between the first and last eclipse considered for each target, and their *Gaia G* magnitudes (Gaia Collaboration et al. 2016, 2018). Possible systematic deviations present in TESS data may include activity-induced modulations or other geometric effects that could bias the measurement of the time of minimum. To mitigate these effects, we employed the python package `george` (Foreman-Mackey 2015) to model the out-of-eclipse photometry using a Gaussian process correlated-noise model with a squared-exponential covariance function (see Sect. 1.3). The resulting model was used to normalise the entire light curve, including the eclipses. The length-scale hyperparameter was constrained to values above twice the duration of the eclipse to avoid adding spurious high-frequency noise inside the eclipse region.

---

[1] `https://mast.stsci.edu/portal/Mashup/Clients/Mast/Portal.html`

[2] `https://adina.feinste.in/eleanor/`

Table 5.2: TESS sectors and cadence at which the sample of studied eclipsing binary systems have been observed, the time-span between the first and last eclipse considered, and their *Gaia G* magnitudes.

System	Sector	Cad. [min]	Δt [d]	G [mag]
KX Cnc	21	2	20	7.0363(2)
AL Dor	1–6, 8–13, 27–36	2	947	7.5820(3)
RW Lac	16, 17	2	47	10.4381(3)
V530 Ori	6	30	18	9.6959(4)
EW Ori	32	2	26	9.7647(19)
HP Dra	14, 15, 26	2	344	7.8117(4)
TZ Men	12, 13, 27	2	428	6.1556(8)
V541 Cyg	14	2	22	10.3286(4)
LV Her	25, 26	2	34	10.8853(6)
V459 Cas	18, 24	2	186	10.2905(3)
RR Lyn	20	2	20	5.4696(14)
V501 Her	25, 26	2	47	10.9787(6)
KW Hya	8, 35	2	760	6.0529(7)
V501 Mon	6, 33	30, 10	756	12.1884(2)
GG Ori	6	2	16	10.2372(5)
EY Cep	19, 25	2	186	9.7154(3)

The Kwee & van Woerden (1956) method (hereafter, KvW) was adopted to determine all the times of minimum light. For consistency, we used the same orbital phase interval for all primary and secondary eclipses, and we only considered eclipses for which ingress and egress is well sampled. The median uncertainty in the obtained times of minimum are 2.5 and 12.9 seconds for the 2-min and 30-min cadence photometry, respectively. The precision of the KvW method for an equally sampled ideal eclipse is inversely proportional to the square root of the number of points used. Given that typically the number of TESS photometric points in the 2-min cadence eclipses is 15 times larger than in the 30-min cadence eclipses, we expect an error ratio between the two cadences of about $\sqrt{15}$, as approximately observed. In Fig. 5.1 we show two examples of eclipses observed with TESS using 2-min and 30-min cadence observations and we mark the time of minimum computed using the KvW method.

We computed the bisector (defined as the loci of the midpoints extending from one side to the other of the eclipses) of each eclipse to diagnose local asymmetries that could be caused by stellar activity for example. Bisector points were determined as the time average between two symmetric points of the ingress and egress branches. Cubic spline interpolation was used to define points of equal flux. From the calculated values, we defined two indicators. The bis_{odd} parameter is defined as the difference of the average bisector between 50–100% and 0–50% of the eclipse depth (i.e. $< bis_{50-100} > - < bis_{0-50} >$), while the bis_{even} parameter is computed as the difference between the average of the two intervals at the top 75–100% and the bottom 0–25%, and the average of the middle 25–75% of the eclipse depth (i.e. $< bis_{75-100}, bis_{0-25} > - < bis_{25-75} >$). These bisector parameters represent first- and second-order measures of distortions in the eclipse shapes. We used them as signposts for the potential presence of biased timing determinations, for example those due to issues with the data or effects on the stellar surface such as spots. As a result, we did not consider for further analysis those times of minimum

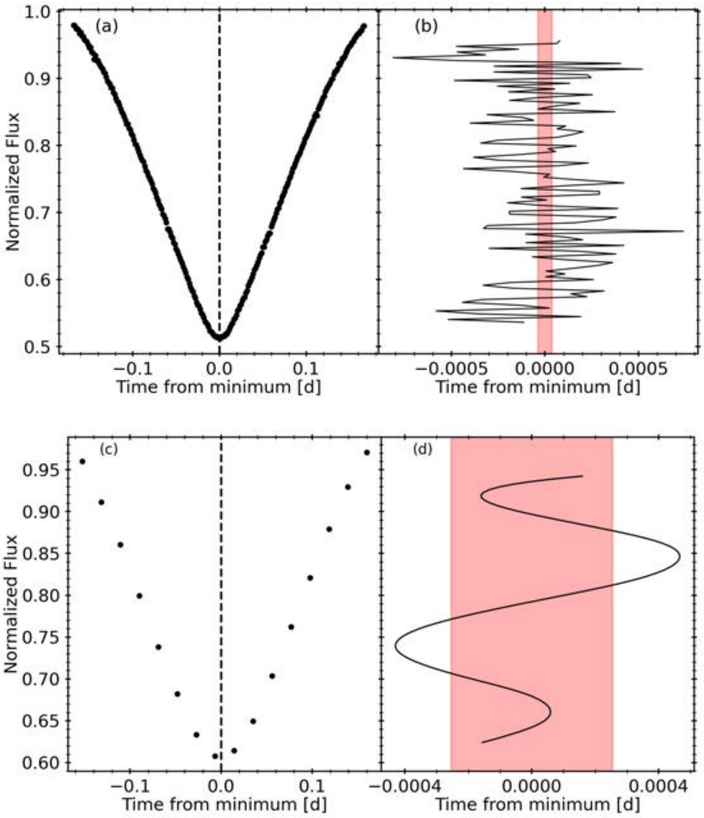

Figure 5.1: Examples of TESS data for an eclipse of V459 Cas *(a)* with 2-min cadence, and V501 Mon *(c)* with 30-min cadence. In panels *(b)* and *(d)* the black line shows the bisector corresponding to each eclipse. The computed time of minimum for each system, which is used as reference time in the plots, is marked as a black-dashed line in panels (a) and (c). Its uncertainty is illustrated in panels (b) and (d) as a read shaded area. The resulting timing uncertainty is 3.3 sec for V459 Cas and 22.0 sec for V501 Mon.

with one of these indices deviating by more than 3σ from their mean. Table A.9 provides all the measured times of minimum light, the type of eclipse (primary or secondary), and the bisector indicators bis_{odd} and bis_{even}. Also, the right panels of Fig. 5.1 shows two examples of the bisectors of two eclipses and the uncertainty in the determination of their time of minimum.

The final measurement errors in the eclipses analysed in this chapter are 1 to 11 times lower than the dispersion of the individual points used to measure the bisector. Given that the number of photometric points comprised within the eclipses ranges from 8 to 440, that the bisector points are computed from two photometric points, and that the timing error for an ideal eclipse scales with $N^{-1/2}$, we expect errors that are 2 to 15 times lower than the bisector dispersion (i.e. $\sqrt{8/2}$ and $\sqrt{440/2}$). When applied to our data, this methodology yields uncertainties that are larger than those expected for an ideal eclipse, which may be taken as an indication that the errors are not underestimated. Potential systematic deviations from an ideal eclipse that are not accounted for by the KvW method caused several works to consider the error estimates coming from this method as exceedingly optimistic (Breinhorst et al. 1973; Mikulášek et al. 2014). However, with the novel use of the bisectors as indicators for such deviations, we were able to detect the affected eclipses and discard them for further use, therefore ensuring that our measurement errors are a good representation of the true statistical precision.

5.4 Apsidal motion determinations

Several methods can be employed to estimate apsidal motion rates in eclipsing binaries, such as the changing position of the eclipses with respect to each other over time (e.g. Giménez et al. 1987; Wolf et al. 2006, 2010; Kim et al. 2018), the change in the shape of the radial velocity curve over time (e.g. Ferrero et al. 2013; Schmitt et al. 2016; Rauw et al. 2016), or the change in the shape of the light curve over time (Bakış et al. 2008; Harmanec et al. 2014; Torres et al. 2017). Here we use the equations of Giménez & Bastero (1995) defining the times of eclipse:

$$\begin{aligned} T_j =& T_0 + NP_{\rm a}\left(1 - \frac{\dot{\omega}}{360}\right) + (j-1)\frac{P_{\rm a}}{2} + \sum_{i=1}^{3}(-1)^{i-1}A_{2i}\frac{P_{\rm a}e^{2i}}{2^{2i}\pi}\sin(2i\omega) + \\ &+ \sum_{i=0}^{2}(2j-3)A_{2i+1}\frac{P_{\rm a}e^{2i+1}}{2^{2i+1}\pi}\cos(2i\omega+\omega), \end{aligned} \tag{5.6}$$

where $\dot{\omega}$ is expressed in deg cycle^{-1}, j is 1 or 2 for the primary or secondary eclipse, respectively, T_0 is the time of eclipse at epoch $N = 0$, $P_{\rm a}$ is the anomalistic period, and ω is the argument of periastron expressed in radians at time T, which depends on $\dot{\omega}$ and the argument of periastron at time T_0, ω_0, as $\omega = \omega_0 + N\dot{\omega}$. Finally, the coefficients A_i depend on the eccentricity e and the inclination of the orbit, and their full expressions are given in eqs. (16) to (21) of Giménez & Bastero (1995).

Equation (5.6) is complete up to $O(e^5)$ (Giménez & Bastero 1995), and is therefore only valid for orbital eccentricities that do not reach extremely high values, that is, below 0.7. Fitting this equation to the actual individual measurements allows the determination of the apsidal motion rate, $\dot{\omega}$, as well as the orbital eccentricity, e, the orbital period, the reference time of eclipse, T_0, and the argument of periastron at that time, ω_0. It should be noted that there are significant differences in the calculated $\dot{\omega}$ when only expressions considering low orders in e are used. The severity of the deviations is a function of the eccentricity but we use terms up to e^5 for all cases, implying relative errors well below 1%.

Strong degeneracies between e and ω_0 can limit the use of Eq. (5.6) to derive all parameters simultaneously unless a significant fraction of the apsidal motion period is covered with observational data. Attempts at five-parameter simultaneous fits using a poorly covered apsidal period may lead to biased solutions because of resulting correlations between e and ω. Potential issues are further exacerbated by the possible presence of light-time effect variations caused by an orbiting third body. To obtain non-degenerate results when the time-span of the observations is limited, the value of the eccentricity, which is directly related to the amplitude of the variations, should at least be adopted independently, for example from modelling the light and radial velocity curves. When the eccentricity is fixed, the instantaneous shape of the apsidal motion curve can be described by the tangent at ω_0, which can also be expressed in terms of the difference between the periods corresponding to primary and secondary eclipses, as described by Giménez & Bastero (1995), considering that the value of ω at the time of the eclipses does not differ from ω_0. This is just the time-derivative of the difference between the times of secondary

(T_2) and primary (T_1) eclipses:

$$\frac{d(T_2 - T_1)}{dt} = \frac{\dot{\omega} P_\mathrm{a}}{180} \left(\sum_{i=0}^{2} (-1)^i A_{2i+1} (2i + 1) \frac{e^{2i+1}}{2^{2i}} \sin[(2i + 1)\omega_0] \right), \tag{5.7}$$

with $\dot{\omega}$ expressed in deg cycle^{-1}.

In our study, we use the values of $T_2 - T_1$ from pairs of close primary and secondary minima of high-precision data. This is done to ensure maximum robustness of the apsidal motion determinations and to minimise the possible effects over the measured orbital period that might be produced by systematic errors arising from different methodologies or astrophysical variability. We favour this method over the use of the difference between periods resulting from linear fits to individual primary and secondary eclipses. This is equivalent to the right term of Eq. (5.7). Using $T_2 - T_1$ from close eclipses has several advantages, namely that these are more likely to be obtained by the same observer, that both timings correspond to the same epoch of stellar activity, and that it avoids effects from light-travel time caused by a potential third body. However, it should be noted that the presence of a third body may induce other perturbations such as the eccentric Lidov-Kozai effect (Lidov 1962; Kozai 1962; Naoz 2016) that could alter the observed apsidal motion rates. A full characterisation of the system is needed to take into account the effects of a potential third body. In the absence of such a detailed analysis, a comparison with the theoretically predicted apsidal motion rate could be affected.

The downside of our adopted approach is that the number of $T_2 - T_1$ measurements (TESS plus archival) for some of the studied systems presented below is rather low. Depending on the time baseline and the impact of effects such as stellar activity, this may lead to some unaccounted-for source of additional error. However, our entire procedure has been devised to minimise such effects (strict selection of minimum timings, bisector correction criteria, etc.) and therefore we do not expect systematic deviations to significantly affect our measurements. Also, most of the eclipsing binaries that we analyse here do not show signs of any stellar activity, either because they lack a convective envelope or because of their low rotational velocities.

The eclipsing binaries in our sample have been typically monitored between TESS and archival data for less than 1% of their apsidal motion period, of the order of thousands of years. Therefore, the observed $T_2 - T_1$ values should accurately define the tangent to the curve described by Eq. (5.7), and relying on a previously determined orbital eccentricity, Eq. (5.7) is fully applicable. The approximation of the derivative is of course sensitive to the argument of periastron and its precision decreases for values of ω_0 near 0 or 180 degrees, when the variation of $T_2 - T_1$ over time and the corresponding period differences become close to zero. We assume the eccentricity derived from the best light and radial velocity curves, with the corresponding argument of periastron, in order to obtain the apsidal motion rate. We had to restrict the analysis to systems with high-precision data, as already discussed, and we focus our analysis on the systems listed in Table 5.1, which are discussed individually below.

All obtained secondary minus primary eclipse timings, $T_2 - T_1$, for each of the available primary eclipses are given in Table 5.3 with the corresponding uncertainty computed from the propagation of errors of individual timings, given in parentheses. We also list the orbital cycle (N) computed with respect to the reference time T_0 given in the first column. For those primary eclipses without any secondary counterpart on the same orbital cycle, we computed the secondary minus primary eclipse timings as $T_2 - T_1 - dN \times P_\mathrm{s}$, where P_s is the sidereal period listed in Table 5.1 and dN is the difference in orbital cycles between the two minima. We list dN in the last column in Table 5.3.

Table 5.3: $T_2 - T_1$ computed from TESS light curves. The BJD value below each system name defines the origin epoch of the orbital cycle count (N).

Table 5.3: Continued.

System & T_0	N	$T_2 - T_1$ [d]	dN
KX Cnc 2456910.0768	63	20.077329(36)	0
AL Dor	0	6.887539(24)	0
2458368.7277	2	6.887455(27)	0
	3	6.887421(20)	−1
	4	6.887434(16)	0
	5	6.887470(19)	−1
	6	6.887408(20)	1
	7	6.887431(18)	0
	8	6.887456(17)	−1
	10	6.887478(19)	0
	12	6.887378(17)	0
	13	6.887396(18)	−1
	14	6.887361(22)	1
	15	6.887402(23)	0
	18	6.887382(22)	0
	19	6.887416(23)	0
	20	6.887391(17)	0
	21	6.887433(17)	−1
	45	6.887194(28)	2
	46	6.887195(21)	1
	47	6.887226(17)	0
	48	6.887218(19)	0
	49	6.887235(21)	0
	50	6.887211(21)	−1
	51	6.887242(30)	0
	55	6.887201(15)	0
	56	6.887201(16)	0
	57	6.887215(18)	0
	58	6.887209(22)	0
	59	6.887175(23)	−1
	60	6.887189(16)	1
	61	6.887171(17)	0
RW Lac	0	5.111455(90)	−1
2458744.8166	1	5.111474(75)	0
	2	5.11141(10)	0
	4	5.111422(82)	−1
V530 Ori	0	2.83585(35)	0
2458471.0870	2	2.83657(38)	0
	3	2.83681(53)	−1
EW Ori	1052	3.681377(0.000032)	0
2451877.1968	1053	3.681390(0.000033)	−1
	1054	3.681395(0.000027)	0
	1055	3.681455(0.000031)	0
HP Dra	0	5.568563(60)	0
2458692.9375	1	5.568771(48)	0
	2	5.568480(55)	0
	4	5.56850(19)	−1
	30	5.568262(58)	0
	31	5.568604(36)	0
TZ Men	0	4.371606(67)	0
2458633.4292	1	4.371309(52)	0
	2	4.371558(31)	0
	3	4.371976(35)	0
	5	4.371702(25)	0
	48	4.371928(53)	−1
	49	4.371867(18)	0
V541 Cyg	513	7.032672(81)	1
24550817.9760	514	7.032794(84)	0
LV Her	0	15.898401(63)	0
2458998.6220	1	15.898531(70)	0
V459 Cas	471	4.164664(60)	0
2454815.5698	472	4.164493(53)	0
	490	4.164565(70)	0
	492	4.164777(56)	0
RR Lyn	0	4.478175(71)	−1
2458851.9265	1	4.478547(46)	0
V501 Her	388	4.120736(96)	0
2455648.5943	389	4.121067(84)	0
	390	4.121030(76)	0
	392	4.12087(10)	−1
	393	4.120252(98)	0
KW Hya	0	3.549831(0.000014)	0
2458523.0016	1	3.549888(0.000016)	−1
	2	3.549827(0.000024)	−2
	95	3.550072(0.000013)	0
	97	3.550100(0.000016)	0
V501 Mon	−1	3.146778(0.000140)	0
2458477.9808	1	3.146753(0.000243)	0
	104	3.147255(0.000137)	0
	106	3.147104(0.000179)	0
GG Ori	983	2.790712(33)	0
2451952.4777	985	2.790716(35)	0
EY Cep	−2	3.140134(29)	0
2458836.4248	0	3.140225(32)	0
	19	3.139902(31)	0
	21	3.139882(35)	0

Table 5.4: Other properties used to compute the apsidal motion of the systems analysed, such as the reference time and the corresponding argument of periastron, the stellar relative radii and projected rotational velocities, and the orbital inclination of the system. References for the values are as in Table 5.1.

System	T_0 [BJD]	ω_0 [deg]	r_1	r_2	$v_1 \sin i$ [km s^{-1}]	$v_2 \sin i$ [km s^{-1}]	i [deg]
KX Cnc	2456910.0768	63.76	0.01940(4)	0.01913(4)	6.4(1.0)	6.5(1.0)	89.825(3)
AL Dor	2458368.7277	107.47	0.03291(6)	0.03311(6)	4.1(0.6)	3.9(0.7)	88.99(1)
EW Ori	2451877.1968	309.10	0.0578(2)	0.0543(2)	9.0(7)	8.8(6)	89.86(9)
V541 Cyg	2450817.9760	262.72	0.0431(2)	0.0419(3)	15(1)	15(1)	89.83(3)
V459 Cas	2454815.5698	240.32	0.0726(3)	0.0710(3)	54(2)	43(2)	89.467(7)
V501 Her	2455648.5943	250.10	0.08375(11)	0.06323(11)	14.3(1.0)	12.5(1.0)	89.11(4)
KW Hya	2453430.9533	225.29	0.0853(5)	0.0594(8)	15(2)	13(2)	87.5(3)
V501 Mon	2458477.9808	232.79	0.0838(13)	0.0707(13)	16.5(1.0)	12.4(1.0)	88.02(8)
GG Ori	2451952.4777	122.89	0.0746(10)	0.0737(10)	24(2)	23(2)	89.30(10)
EY Cep	2458836.4248	110.14	0.0603(4)	0.0606(8)	10(1)	10(1)	89.89(3)

Below we discuss the studied systems in detail and describe the methodology applied to determine their apsidal motion rates in those nine cases where such a measurement was possible. For 6 out of the 16 systems in Table 5.1, namely, RW Lac, V530 Ori, HP Dra, TZ Men, LV Her, and RR Lyn, we could not find a measurable apsidal motion rate in spite of having high-precision TESS data available, but we have nevertheless included their time of minima and $T_2 - T_1$ values in Tables A.9 and 5.3, which could be valuable for future determinations. For the systems in which we could determine an apsidal motion rate, additional values needed for their analysis, such as the relative radii or the projected rotational velocities, are listed in Table 5.4, together with the values of ω_0 and the reference time T_0.

5.4.1 KX Cnc

The general properties of this highly eccentric system ($e = 0.4666 \pm 0.0003$), such as mass, radius, eccentricity, and period, shown in Table 5.1, are the result of the combined analysis of the light and radial velocity curves carried out by Sowell et al. (2012), who reported no apsidal motion. The TESS data listed in Table 5.3 yield $T_2 - T_1 = 20.077329 \pm 0.000036$ days. This measurement can be compared with $T_2 - T_1$ values from the literature to search for the presence of apsidal motion. Sowell et al. (2012) give a phase for the secondary eclipse of 0.64325 based on the joint analysis of the light curve and the radial velocity curve, but no individual eclipse times are reported. We therefore decided to retrieve the original photometric data, b- and y-band in the Strongren system, and calculated the position of the eclipses using the same method as for the TESS measurements, yielding a value of $T_2 - T_1 = 20.08076 \pm 0.00015$ days, which is equivalent to a phase of the secondary of 0.64321. Comparing the value of $T_2 - T_1$ with the TESS results, we observe a decrease of $-(1.938 \pm 0.087) \times 10^{-5}$ days cycle^{-1}, indicating a measurable apsidal motion of $\dot{\omega} = 0.000131 \pm 0.000010$ deg cycle^{-1}, which was the value that we published in Baroch et al. (2021a).

With only two data points available, the slope measurement of the $T_2 - T_1$ values highly depends on the value of the more ancient and uncertain measurement, and its analytical error could be imprecise and underestimated. To avoid this, in this work we decided to use individual timings

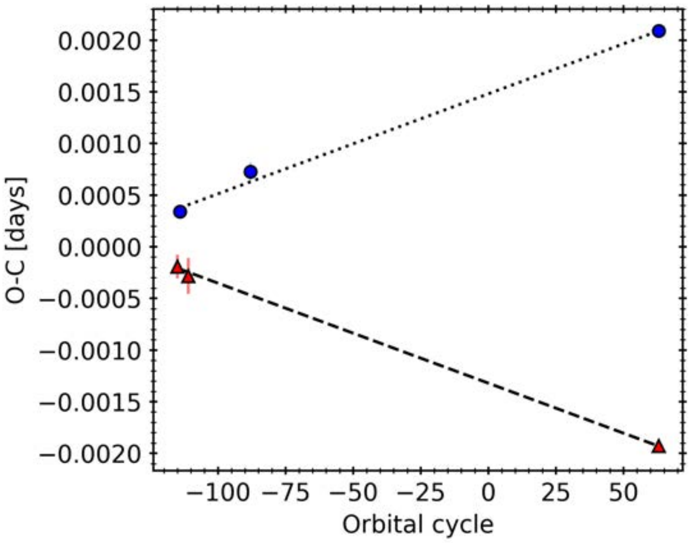

Figure 5.2: Ephemeris curve for KX Cnc as a function of the orbital cycle. The dotted and dashed lines represent fits to the primary (blue circles) and secondary (red triangles) eclipses, respectively. For a better visualisation, an arbitrary shift to the primary and secondary minima has been applied.

Table 5.5: Times of minimum light used to compute the apsidal motion rate of KX Cnc.

T_0 [d]	Type	Ref.
2453339.88285 ± 0.00022	2	Sow12
2453351.02188 ± 0.00012	1	Sow12
2453464.76215 ± 0.00034	2	Sow12
2454162.738334 ± 0.000091	1	Dav07

References. Sow12: Sowell et al. (2012); Dav07: Davies (2007).

corrected to BJD in order to identify a possible difference between the linear periods of the primary and secondary eclipses, ΔP , which corresponds to the left-hand side term in Eq. (5.7) (Giménez & Bastero 1995). For each of the three eclipses with a decent sampling in Sowell et al. (2012), we used the mean value of the recomputed eclipse timings of each of the photometric bands. In addition, we also recomputed the time of minimum light of one primary eclipse from the original photometric data by (Davies 2007). All used archival individual times are listed in Table 5.5. We obtain a difference between de periods computed from a linear fit to primary and secondary eclipses of $\Delta P = (-1.905 \pm 0.044) \times 10^{-5}$ days cycle^{-1}, which yields an apsidal motion rate of $\dot{\omega} = 0.0001287 \pm 0.0000051$ deg cycle^{-1}, fully compatible with the value published by Baroch et al. (2021a) obtained from the $T_2 - T_1$ values, but with reduced uncertainties. We show the linear fits to individual timings in Fig. 5.2.

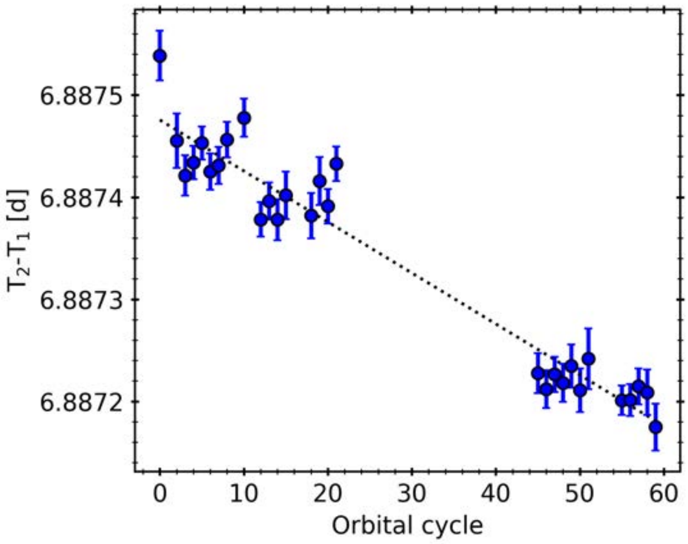

Figure 5.3: $T_2 - T_1$ as a function of the orbital cycle for AL Dor.

5.4.2 AL Dor

The general properties of the AL Dor system given in Table 5.1 are derived from the radial velocity and light curve of Graczyk et al. (2021)[3]. The authors report an apsidal motion value of 0.000130 ± 0.000005 deg cycle^{-1} based on TESS and archival eclipse timings. However, the archival minima they use are computed from the Hipparcos and ASAS phase folded light curve, which only contains $\sim$ 3 and $\sim$ 15 points in the eclipses, respectively, and contains data points from eclipses separated up to 3 000 days. We therefore do not use these archival timings in our analysis as they may be potentially biased. Fortunately, our TESS eclipse timings, shown in Table A.9, yield a good number of accurate minima values from which a slow apsidal motion can be detected without any need for archival measurements, as illustrated in Fig. 5.3, which contains 6 additional pairs with respect to our analysis published in Baroch et al. (2021a). The linear weighted fit to the $T_2 - T_1$ values listed in Table 5.3 corresponds to a slope of $-(4.96 \pm 0.22) \times 10^{-6}$ days cycle^{-1}. Using the eccentricity given by Graczyk et al. (2021), $e = 0.1950 \pm 0.0002$, the slope yields a final value of $\dot{\omega} = 0.000159 \pm 0.000007$ deg cycle^{-1}, highlighting the discrepancy between TESS and older eclipse timings mentioned above. This value is smaller but compatible with the determination we published in Baroch et al. (2021a), which used the eccentricity of $e = 0.1952 \pm 0.0002$ determined by Graczyk et al. (2019).

5.4.3 EW Ori

New TESS observations of EW Ori released after the publication of our paper, allowed us to add this system to our sample. Masses and radii for the components of EW Ori were determined by Clausen et al. (2010) using new light curves and a reanalysis of the radial velocities published by Popper et al. (1986) and Imbert (2002). They are given in Table 5.1. The authors analysed the apsidal variations by fitting the individual eclipse timings, and obtained $\dot{\omega} = 0.00042 \pm$

---

[3] This work was published just after publishing Baroch et al. (2021a). We updated this section accordingly in order to include the updated properties of AL Dor and compare our results.

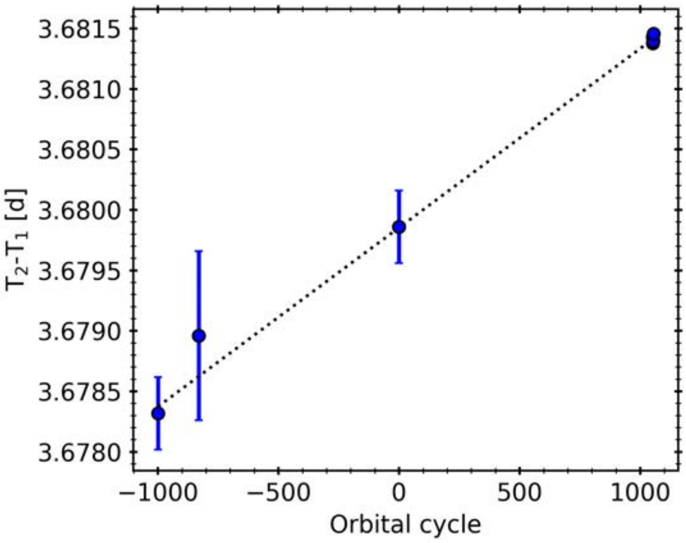

Figure 5.4: $T_2 - T_1$ as a function of the orbital cycle for EW Ori.

Table 5.6: $T_2 - T_1$ values used to compute the apsidal motion rate of EW Ori.

N	$T_2 - T_1$ [d]	Ref.
−999	3.67832 ± 0.00030	Wol97
−831	3.67896 ± 0.00070	Wol97
0	3.67986 ± 0.00030	Cla10

References. Wol97: Wolf et al. (1997); Cla10: Clausen et al. (2010).

0.00010 deg cycle^{-1}, using an eccentricity of e = 0.076 ± 0.002. Using the same eccentricity and an updated list of times of minimum light, Kim et al. (2018) obtained a value of $\dot{\omega}$ = 0.00045 ± 0.0004 deg cycle^{-1}. Leaving the eccentricity as a free parameter, Wolf et al. (2010) obtained a larger apsidal motion value, of $\dot{\omega}$ = 0.00057 ± 0.00004 deg cycle^{-1}.

To complement the TESS $T_2 - T_1$ values obtained in this work, which are listed in Table 5.3, we searched for precise archival minima timings acquired within less than ten orbital cycles. We found a total of 3 pairs in Wolf et al. (2010) from which we compute the $T_2 - T_1$ values listed in Table 5.6. From a weighted linear fit to the archival and TESS $T_2 - T_1$ values, shown in Fig. 5.4, we obtain a slope of $(1.48 \pm 0.11) \times 10^{-6}$ d cycle^{-1}. Using the eccentricity of e = 0.076 ± 0.002 derived by Clausen et al. (2010), this slope yields an apsidal motion value of 0.000327 ± 0.00026 deg cycle^{-1}, which is significantly lower than the values derived by Wolf et al. (1997) and Kim et al. (2018), and compatible with the results from Clausen et al. (2010) within uncertainties.

5.4.4 V541 Cyg

Apsidal motion in V541 Cyg was measured by Khaliullin (1985) and revised by Volkov & Khaliullin (1999). Wolf et al. (2010) used the individual times of minimum light to obtain $\dot{\omega}$ = 0.00032 ± 0.00006 deg cycle^{-1}, leaving the eccentricity as a free parameter, while Kim et al.

Table 5.7: $T_2 - T_1$ values used to compute the apsidal motion rate of V541 Cyg.

N	$T_2 - T_1$ [d]	Ref.
−387	7.0048 ± 0.0008	Vol99
−129	7.0118 ± 0.0010	DA
−82	7.0139 ± 0.0010	LG
19	7.0186 ± 0.0030	Vol99
180	7.0225 ± 0.0003	WS
395	7.0295 ± 0.0030	Hub15

References. Vol99: Volkov & Khaliullin (1999); DA: Diethelm (1992) and Agerer et al. (1994); LG: Sandberg Lacy et al. (1995) and Guinan et al. (1996); WS: Wolf et al. (2010) and Smith & Caton (2007); Hub15: Hubscher (2015) and Hubscher & Lehmann (2015).

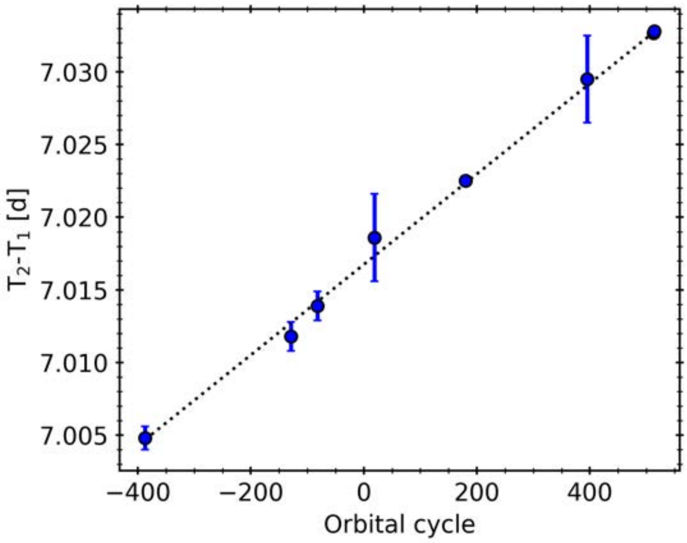

Figure 5.5: $T_2 - T_1$ as a function of the orbital cycle for V541 Cyg.

(2018) obtained $\dot{\omega} = 0.000397 \pm 0.000013$ deg cycle^{-1}, fixing the orbital eccentricity to the value of 0.479 given by Lacy (1998). Torres et al. (2017) obtained a new radial velocity curve and reanalysed the V-band light curve of Khaliullin (1985). For the apsidal motion determination, Torres et al. (2017) carried out a global analysis of all the data, photometric and spectroscopic, with variable argument of periastron. In this way, the authors determined the optimal value of the eccentricity to be $e = 0.4684 \pm 0.0014$ and an apsidal motion rate of $\dot{\omega} = 0.000360 \pm 0.000012$ deg cycle^{-1}.

For our analysis, we included in Table 5.7 the $T_2 - T_1$ values derived from Table 4 of Torres et al. (2017) which we complement with the values computed from the TESS data in Table 5.3. This was done using precise primary and secondary eclipses and the closest possible counterpart when calculating the timing differences. As mentioned by Torres et al. (2017), some values had to be excluded because of their unusually large residuals. In Fig. 5.5, the variation of $T_2 - T_1$ over time is shown and clearly indicates a well-defined increase of $(3.12 \pm 0.03) \times 10^{-5}$ days cycle^{-1}. For the value corresponding to orbital cycle 19, the authors did not report any error bar and we assumed the same uncertainty as the largest one in Table 5.7, namely 0.003 days. As a simple

Table 5.8: $T_2 - T_1$ values used to compute the apsidal motion rate of V459 Cas.

N	$T_2 - T_1$ [d]	Ref.
−349	4.1634 ± 0.0005	Lac01
−273	4.16373 ± 0.00022	Wol10
−266	4.16372 ± 0.00014	LN
−223	4.1640 ± 0.0005	WH
−216	4.1634 ± 0.0005	Lac04
0	4.1640 ± 0.0005	Wol10
28	4.1645 ± 0.0005	Wol10

References. Lac01: Lacy et al. (2001); Wol10: Wolf et al. (2010); LN: Lacy (2002) and Nelson (2003); WH: Wolf et al. (2010) and Hubscher et al. (2005); Lac04: Lacy (2004).

consistency test, we checked that the observed slope yields $T_2 - T_1 = 6.9872 \pm 0.0003$ days at the time of the photographic light curve of Karpowicz (1961), while the actual measurement given by Torres et al. (2017) in their Table 4, after a careful analysis of the original data, is 6.988 ± 0.004 days. Both values are in very good agreement in spite of the extrapolation by about 550 orbital cycles. Furthermore, the predicted position of the secondary eclipse in phase at epoch 248 is 0.45798 ± 0.00002, in excellent agreement with the light-curve solution by Torres et al. (2017) in their Table 5. Adopting $e = 0.4684 \pm 0.0014$ (Torres et al. 2017), we obtain an apsidal motion rate of $\dot{\omega} = 0.000352 \pm 0.000004\,\mathrm{deg\,cycle^{-1}}$, more precise but in good agreement with the value of $\dot{\omega} = 0.000360 \pm 0.000012\,\mathrm{deg\,cycle^{-1}}$ derived by Torres et al. (2017) using a completely different method, based on a simultaneous fit to photometric and spectroscopic data.

5.4.5 V459 Cas

Lacy et al. (2004) determined the general properties of V459 Cas and estimated the apsidal motion rate using all available minima at that time, obtaining a rather uncertain value of $\dot{\omega} = 0.0014 \pm 0.0011\,\mathrm{deg\,cycle^{-1}}$. This could not be improved by Dariush et al. (2006) because of the narrow time-span of their reliable data. Torres et al. (2010) nevertheless quote an apsidal motion rate of $0.00057 \pm 0.00006\,\mathrm{deg\,cycle^{-1}}$ as provided preliminarily to the authors by M. Wolf. This value was not confirmed later by Wolf et al. (2010), who reported $0.00071 \pm 0.00008\,\mathrm{deg\,cycle^{-1}}$, using again all available individual timings at that time.

The low eccentricity of 0.0244 ± 0.0004 (Lacy et al. 2004) of the system makes it difficult to determine the apsidal motion rate using the observed $T_2 - T_1$ values. We searched in the list provided by Wolf et al. (2010), in their Table A.1, and in Table 1 of Lacy et al. (2004) for the closest photoelectric pair of primary and secondary timings, which we list in Table 5.8. The best linear fit to these values, together with the TESS $T_2 - T_1$ measurements, is shown in Fig. 5.6, and yields a slope of $(1.30 \pm 0.19) \times 10^{-6}\,\mathrm{d\,cycle^{-1}}$, although with a large dispersion of the older timings due to the small variation in $T_2 - T_1$ in the considered time-span. Using the orbital eccentricity of Lacy et al. (2004), we obtain an apsidal motion rate of $\dot{\omega} = 0.00065 \pm 0.00010\,\mathrm{deg\,cycle^{-1}}$, which agrees with the value given by Wolf et al. (2010), although with a slightly larger uncertainty.

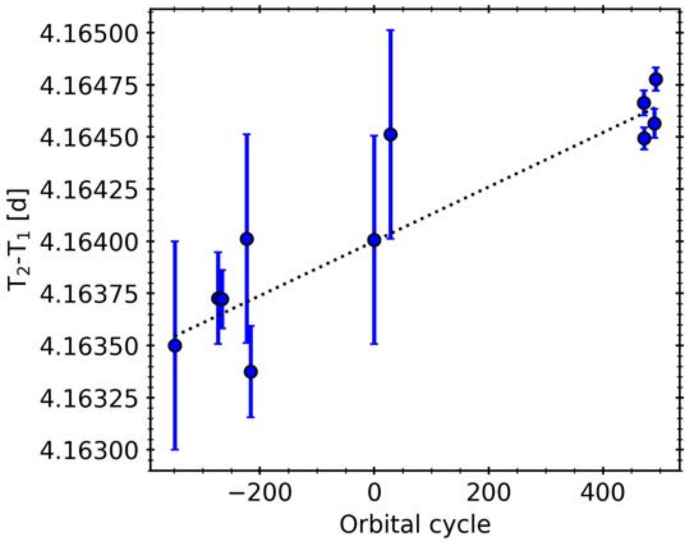

Figure 5.6: $T_2 - T_1$ as a function of the orbital cycle for V459 Cas.

5.4.6 V501 Her

The absolute parameters of V501 Her are given in Table 5.1 as derived by Sandberg Lacy & Fekel (2014) from their own light-curve and radial velocity measurements, from which no apsidal motion could be reported. The large relative radii indicate the evolved nature of the components and the difficulty in obtaining accurate times of eclipse due to their long duration. The TESS measurements given in Table 5.3 present an internal dispersion that is larger than the estimated errors of the individual measurements. The weighted mean value is $T_2 - T_1 = 4.1208 \pm 0.0004$ days, equivalent to a phase of the secondary eclipse of 0.47929 ± 0.00005 using the orbital period given by Sandberg Lacy & Fekel (2014). These authors give a secondary eclipse phase of 0.4791 ± 0.0002, implying that no significant variation is observed. From the most complete and precise light curve in Sandberg Lacy & Fekel (2014) and using the elements in their Table 4, we estimated the phase of the secondary eclipse at 0.47915 ± 0.00005, compatible with but more precise than the one given by their times of eclipse, and equivalent with a $T_2 - T_1$ of 4.1196 ± 0.0004 d. Comparing this value with that from the TESS observations, we measure a change in $T_2 - T_1$ of 0.0012 ± 0.0006 days over 354 orbital cycles, yielding a slope of $(3.4 \pm 1.7) \times 10^{-6}\,\mathrm{d\,cycle^{-1}}$. This shows the presence of apsidal motion in V501 Her but with a poorly determined rate. The corresponding apsidal motion rate is $\dot{\omega} = 0.00041 \pm 0.00020\,\mathrm{deg\,cycle^{-1}}$.

5.4.7 KW Hya

The only accurate masses and radii for this system date back to Andersen & Vaz (1984), resulting from the analysis of both light and radial velocity curves. Such results were confirmed more recently by Gallenne et al. (2019) with astrometric observations, and we adopted those values as listed in Table 5.1. Apsidal motion was not reported for KW Hya, despite the large time-span between the two orbital studies, because of the uncertainties involved in the determination of the argument of periastron.

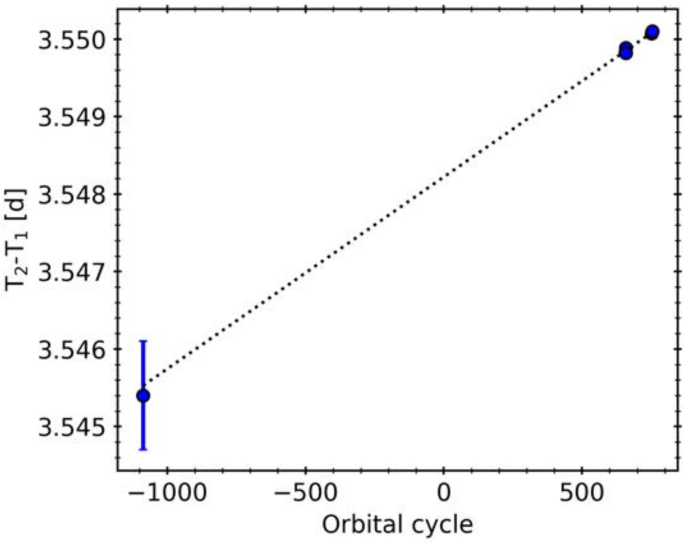

Figure 5.7: $T_2 - T_1$ as a function of the orbital cycle for KW Hya.

After the publication by Baroch et al. (2021a), new TESS measurements have been released and added to this work, expanding significantly the time span of our data. Thanks to that, the TESS $T_2 - T_1$ measurements alone show a significant slope of $(2.47 \pm 0.27) \times 10^{-6}$ days cycle^{-1}, which yields an apsidal motion rate of $\dot{\omega} = 0.000434 \pm 0.000047$ deg cycle^{-1}. We complemented these measurements with the corresponding timing difference measured by Andersen & Vaz (1984), 1740 orbital cycles before, of 3.5454 ± 0.0007 days. No other value of sufficient precision could be found in the literature. The combined measurements, shown in Fig. 5.7, yield a slope of $(2.48 \pm 0.22) \times 10^{-6}$ days cycle^{-1}. Adopting the eccentricity given by Gallenne et al. (2019), $e = 0.094 \pm 0.004$, we obtain an apsidal motion rate of $\dot{\omega} = 0.000432 \pm 0.000043$ days cycle^{-1}, fully compatible with the result obtained with the TESS data alone and with the value of 0.00045 ± 0.0007 deg cycle^{-1} published in Baroch et al. (2021a).

5.4.8 V501 Mon

A detailed analysis of the light and radial velocity curves of V501 Mon was carried out by Torres et al. (2015) and the corresponding absolute parameters are given in Table 5.1. In their study, an analysis of the available times of eclipse at that time was carried out together with the radial velocities in order to determine the orbital elements and the possible variation in the argument of periastron simultaneously. The authors obtained an estimate of the apsidal motion rate of 0.00045 ± 0.00024 deg cycle^{-1}, which we now try to improve by combining the TESS measurements given in Table 5.3 with the data used by Torres et al. (2015). The weighted mean of the TESS $T_2 - T_1$ values gives a separation between primary and secondary eclipses of 3.14676 ± 0.00020 d, which does not show a significant variation with respect to the solution by Torres et al. (2015).

We then fitted all the individual timings corrected to BJD in order to identify a possible difference between the linear periods of the primary and secondary eclipses. Using all the times of

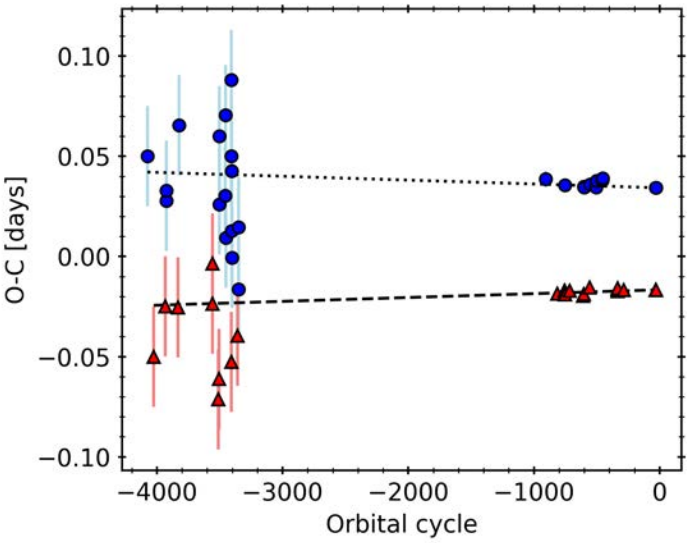

Figure 5.8: Same as Fig. 5.2 but for V501 Mon.

eclipse available in Table 1 of Torres et al. (2015) (adopting also the same scaling for the photoelectric timings) and the TESS individual eclipses, we computed the periods resulting from primary and secondary eclipses, and obtained a difference of $\Delta P = (3.79\pm0.69)\times10^{-6}$ days cycle^{-1}, which corresponds to the left-hand side term in Eq. (5.7) (Giménez & Bastero 1995). With the value of the eccentricity $e = 0.1339 \pm 0.0006$, this ΔP value yields an apsidal motion rate of $\dot{\omega} = 0.000457 \pm 0.000084$ deg cycle^{-1} , which is in excellent agreement with the value published by Torres et al. (2015) but with a reduced uncertainty. Thanks to the addition of new TESS data, the apsidal motion rate reported here improves the determination published in Baroch et al. (2021a), of 0.00046 ± 0.00011 deg cycle^{-1}. Figure 5.8 displays the linear best fit to primary and secondary individual timings. The data points on the left, showing a large dispersion, correspond to the photographic measurements in Table 1 of Torres et al. (2015), for which we assumed uncertainties of 0.025 d.

5.4.9 GG Ori

The general properties of GG Ori were determined by Torres et al. (2000), as listed in Table 5.1, together with an apsidal motion rate of $\dot{\omega} = 0.00061 \pm 0.00025$ deg cycle^{-1}. Torres et al. (2000) followed a method based on the combination of eclipse timings with radial velocities, the same used in their analysis of V501 Mon mentioned above. Later, Wolf et al. (2010) revised the analysis of the individual eclipse timings available at the time and obtained a more precise $\dot{\omega} = 0.00057 \pm 0.00006$ deg cycle^{-1}, with an orbital eccentricity of $e = 0.220 \pm 0.001$.

In order to improve the apsidal motion rate determination combining early timings with TESS, we compiled $T_2 - T_1$ measurements from the best minima given by Wolf et al. (2010) acquired within less than ten orbital cycles, but only three pairs of primary and secondary eclipses with a large dispersion met this criterion. We derived $\dot{\omega} = 0.00060 \pm 0.00003$ deg cycle^{-1}. We then performed linear fits to primary and secondary individual timings, respectively, obtaining the linear period for primary and secondary eclipses and obtained a difference of $\Delta P = -8.33 \pm 0.16 \times 10^{-6}$ days cycle^{-1} using only those eclipses with weight ten in Wolf et al. (2010).

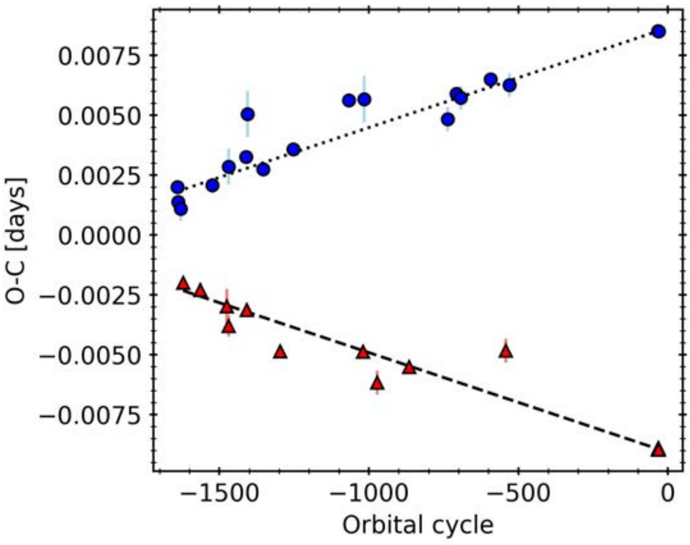

Figure 5.9: Same as Fig. 5.8 but for GG Ori.

Table 5.9: $T_2 - T_1$ values used to compute the apsidal motion rate of EY Cep.

N	$T_2 - T_1$ [d]	Ref.
−817	3.1565 ± 0.0003	Lac06
−815	3.1564 ± 0.0004	Lac06
−781	3.1557 ± 0.0005	Lac06

References. Lac06: Lacy et al. (2006).

Furthermore, using the eccentricity obtained by Torres et al. (2000), $e = 0.2218 \pm 0.0022$, we obtain an apsidal motion rate of 0.00061 ± 0.00003 deg cycle^{-1} , in good agreement with the previous determinations albeit much more precise. The ephemeris curve of the individual primary and secondary eclipse timings is shown in Fig. 5.9.

5.4.10 EY Cep

This binary system was studied by Lacy et al. (2006), who obtained the general properties given in Table 5.1. Given the short time-span of their photometric and spectroscopic observations, the authors were not able to detect any indication of apsidal motion. The new TESS data listed in Table 5.3 include two sectors and the $T_2 - T_1$ variation already indicates the presence of apsidal motion, though the modest time-span does not allow a precise rate determination. We further used the eclipses given by Lacy et al. (2006) to obtain the time differences in Table 5.9.

The graphical representation of the variations is shown in Fig. 5.10 and the linear least-squares fit yields a well-defined slope of $(-1.97 \pm 0.06) \times 10^{-5}$ days cycle^{-1}. Using the eccentricity given by Lacy et al. (2006), $e = 0.4429 \pm 0.0014$, this yields an apsidal motion rate of $\dot{\omega} = 0.000507 \pm 0.000016$ deg cycle^{-1}, which is very precise thanks to the accurate TESS data, the high orbital eccentricity, and a time coverage of more than 800 orbital cycles.

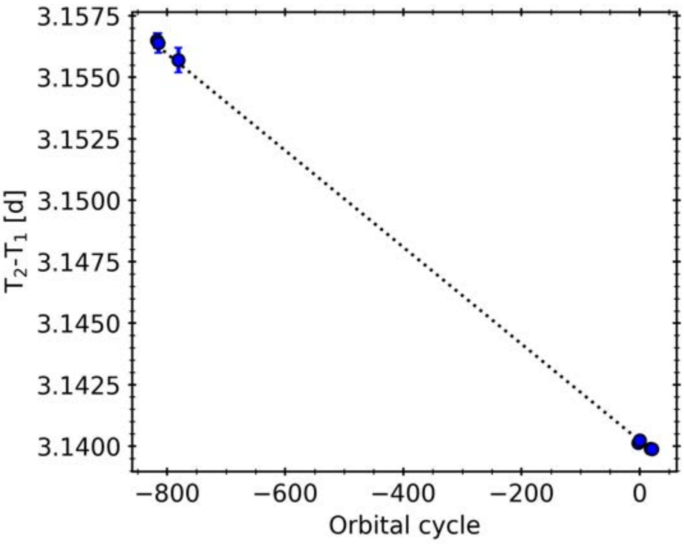

Figure 5.10: $T_2 - T_1$ as a function of the orbital cycle for EY Cep.

5.5 Comparison between theory and observations

The values of $\dot{\omega}_{\rm obs}$ obtained from the apsidal motion analysis using data from TESS and archival times of minima are listed in Table 5.10. Of the ten systems studied for which we were able to perform apsidal motion rate determinations, five are reported for the first time. The precision of the determinations varies widely but they are well above the 3σ threshold, except for the case of V501 Her, which has an apsidal motion rate determination with a significance of only 2σ. Table 5.10 provides the values of $\dot{\omega}_{\rm rel}$ and $\dot{\omega}_{\rm cl}$ for the systems with detected apsidal motion, computed using Eqs. (5.1) and (5.3). Calculating the classical term requires employing two additional parameters for each component, namely the internal structure constant, k_2, and the rotational velocity.

The values of k_2 given in Table 5.10 were specially calculated by A. Claret using theoretical models based on the Modules for Experiments in Stellar Astrophysics package (MESA; Paxton et al. 2011, 2013, 2015) and following the methodology described in the series of papers by Claret & Torres (2017, 2018, 2019). A coarse-grid search was performed over evolutionary tracks calculated for the measured masses of each component, allowing the convective core overshooting parameter (f_{ov}) and the mixing length parameter ($\alpha_{\rm MLT}$) to vary freely, with a variable metallicity (Z) common to both components. The $\log k_2$ values were determined from the best match between the grid of evolutionary tracks and the observed masses, radii, and effective temperatures. The theoretical internal structure constants, k_2, for the models fitting the observed parameters, were integrated using the Radau differential equations as given by Eqs. (1) to (3) in Claret & Giménez (2010):

$$\frac{a d\eta_j}{da} + \frac{6\rho(a)}{\bar{\rho}(a)}(\eta_j + 1) + \eta_j(\eta_j - 1) = j(j+1), \quad j = 2, 3, 4 \tag{5.8}$$

where

$$\eta_j \equiv \frac{a}{\epsilon_j}\frac{d\epsilon_j}{da}, \tag{5.9}$$

Table 5.10: $\log k_2$ values and apsidal motion rates, both observed and theoretically predicted, for the eclipsing binaries with apsidal motion measurement.

System	$\log k_{2,1}$	$\log k_{2,2}$	$\dot{\omega}_{\rm obs}$ [deg cycle^{-1}]	$\dot{\omega}$ [deg cycle^{-1}]	$\dot{\omega}_{\rm cl}$ [deg cycle^{-1}]	$\dot{\omega}_{\rm rel}$ [deg cycle^{-1}]	$\dot{\omega}_{\rm rel,mea}$ [deg cycle^{-1}]	$\frac{\dot{\omega}_{\rm rel,mea}}{\dot{\omega}_{\rm rel}}$
KX Cnc	−1.88(4)	−1.88(4)	0.000129(5)	0.0001241(3)	0.0000029(3)	0.00012127(16)	0.000126(5)	1.038(42)
AL Dor	−1.95(3)	−1.95(4)	0.000159(7)	0.0001653(4)	0.0000069(4)	0.00015837(5)	0.000152(7)	0.960(44)
EW Ori	−2.06(8)	−1.94(8)	0.00033(3)	0.000333(8)	0.000071(8)	0.0002621(10)	0.000259(3)	0.99(12)
V541 Cyg	−2.37(3)	−2.34(3)	0.000352(4)	0.0003516(22)	0.0000392(19)	0.0003124(12)	0.000313(4)	1.001(15)
V459 Cas	−2.48(3)	−2.47(3)	0.00065(10)	0.000555(13)	0.000226(13)	0.0003297(23)	0.00043(10)	1.30(31)
V501 Her	−2.13(3)	−1.96(4)	0.00041(20)	0.000521(13)	0.000281(13)	0.0002400(3)	0.00013(20)	0.5(9)
KW Hya	−2.50(3)	−2.45(10)	0.00043(4)	0.000417(8)	0.000096(8)	0.0003211(19)	0.00034(4)	1.05(14)
V501 Mon	−2.54(3)	−2.52(3)	0.00046(8)	0.000446(8)	0.000124(8)	0.0003219(3)	0.00033(8)	1.03(26)
GG Ori	−2.336(20)	−2.337(20)	0.00061(3)	0.000630(9)	0.000176(9)	0.0004541(16)	0.00043(3)	0.957(69)
EY Cep	−2.38(5)	−2.40(5)	0.000507(16)	0.000501(12)	0.000146(12)	0.0003549(14)	0.000361(20)	1.018(57)

and a is the distance from the centre of the star, ϵ_j is a measure of the deviation from sphericity, $\rho(a)$ is the density at a distance a from the centre, and $\bar{\rho}(a)$ is the mean density within a sphere of radius a. From the result of the Radau equation, the internal structure constant is defined as:

$$k_2 = \frac{3 - \eta_2(R)}{4 + 2\eta_2(R)}. \tag{5.10}$$

The other parameter used to estimate $\dot{\omega}_{\rm cl}$ is the rotational velocity. The values listed in Table 5.4 were taken from the same spectroscopic analyses in the literature from which we adopted the general properties in Table 5.1. Nevertheless, in the case of AL Dor, no rotational velocity was reported for the component stars and we used the predicted values under the assumption of pseudo-synchronisation, as described by Hut (1981).

All the parameters needed to apply Eqs. (5.1) and (5.3) are listed in Tables 5.1 and 5.4. The errors of the input parameters were propagated to obtain the uncertainty in $\dot{\omega}_{\rm cl}$ and $\dot{\omega}_{\rm rel}$. The uncertainties of the stellar rotation and k_2 dominate the error budget in the classical term, while the uncertainties in the component masses are the main source of error in the GR term. In Figure 5.11 we compare the observed apsidal motion rates with the total calculated theoretical value ($\dot{\omega} = \dot{\omega}_{\rm cl} + \dot{\omega}_{\rm rel}$), as given in Table 5.10. We excluded V501 Her from Figure 5.11 given the poor significance of the apsidal motion determination (below 2σ), although the observed value agrees with theory within the uncertainties.

The comparison of the observed apsidal motion rates with those calculated using Eqs. (5.1) and (5.3), and the parameters in Tables 5.1 and 5.4, show good agreement and no systematic deviations within their uncertainties. An equivalent approach to test GR effects was employed before by Torres et al. (2010), who also considered systems with accurate masses and radii and limited the comparison between observed and theoretical apsidal motion rates to those having a relative contribution of the GR term of at least 40%. Figure 5.11 therefore complements Fig. 11 in Torres et al. (2010), including additional systems with a relative contribution of the GR term above 60%. The values used by Giménez (1985, 2007) for the system's general properties were of insufficient precision to allow for a meaningful and unbiased test of the GR term. Claret & Giménez (1993) searched for systematic deviations in the comparison between observed and theoretical values of $\log k_2$ to falsify the predictions of the Moffat (1986) theory of gravitation. Claret (1997) and Wolf et al. (2010) studied the complementary problem, where the GR term was theoretically estimated and subtracted from the observed value. The resulting classical term

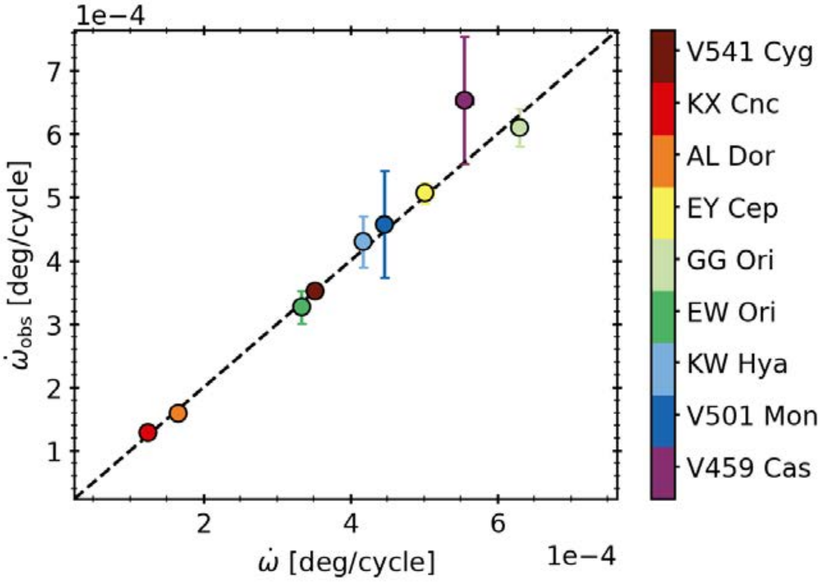

Figure 5.11: Comparison between total computed and total observed apsidal motion rates. The black dashed line indicates the 1:1 relation.

was then compared with model predictions of the k_2 parameter.

5.6 A test of gravitational theories

For a more in-depth analysis, the two apsidal motion components should be analysed separately. As explained above, we carefully selected the sample to ensure a maximum contribution of the GR term, so that, after subtraction of the (model-calculated) quadrupole Newtonian contribution, a comparison with gravitational theories could be carried out. De Laurentis et al. (2012) attempted a test of gravitational theories using a similar method but their eclipsing binary sample was not appropriate, with over half of their sample having a GR term contribution below 10%. Their results were therefore inconclusive.

Thanks to the improved precision in the apsidal motion determinations that we have attained, we can perform a comparison of the predicted theoretical relativistic apsidal motion rate with the difference between the observed values and the computed classical terms, as listed in Table 5.10. For this procedure to succeed, the uncertainty in the classical contribution needs to be well below this latter difference and therefore this limits the comparison to systems with a small non-relativistic contribution to the observed apsidal motion. In Table 5.10 we also include the measured GR rate calculated as $\dot{\omega}_{\rm rel,mea} = \dot{\omega}_{\rm obs} - \dot{\omega}_{\rm cl}$, where $\dot{\omega}_{\rm obs}$ is the observed apsidal motion from precise minima timings derived in this chapter.

Figure 5.12 shows the comparison between predicted $\dot{\omega}_{\rm rel}$, according to Eq. (5.1), and $\dot{\omega}_{\rm rel,mea}$. The measured values for all systems are compatible with the GR predictions within their errors. A more general form of Eq. (5.1), which also allows to test other possible gravitation theories in addition to GR is given by Eq. (66) in Will (2014). This uses the parametrised post-Newtonian

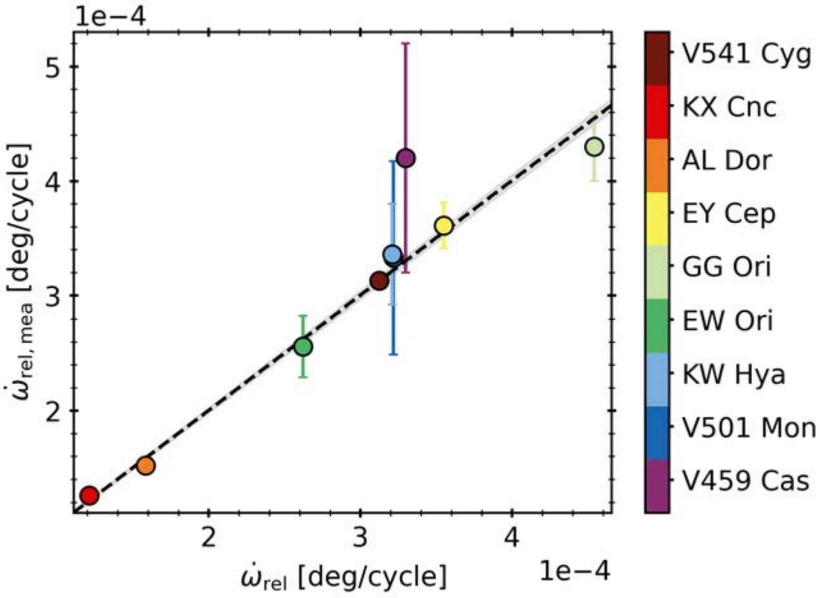

Figure 5.12: Measured GR apsidal motion as a function of the theoretically computed GR apsidal motion. The black dashed line and grey shadow area correspond to the best fit to Eq. (5.11), assuming $\alpha_i = \zeta_2 = 0$, and its 1σ uncertainty. The colour code is chosen such that redder colours correspond to systems with the smaller relative error, and therefore are dominating the fit.

(PPN) formalism, with several parameters whose values depend on the gravitation theory chosen:

$$\dot{\omega}_{\rm rel,mea} = \dot{\omega}_{\rm rel}\left(\frac{1}{3}(2+2\gamma-\beta)+\frac{1}{6}(2\alpha_1-\alpha_2+\alpha_3+2\zeta_2)\eta\right). \tag{5.11}$$

Here, $\dot{\omega}_{\rm rel}$ is the value of the apsidal motion predicted by GR, which is given by Eq. (5.1), $\eta \equiv M_1M_2/(M_1+M_2)^2$ is the dimensionless reduced mass, and γ, β, ζ_2, and α_i are the PPN parameters. In any fully conservative theory of gravity, $\alpha_i = \zeta_2 \equiv 0$, while for GR, $\gamma = \beta \equiv 1$ and $\alpha_i = \zeta_2 \equiv 0$, recovering the expression in Eq. (5.1). The PPN formalism is appropriate for weak gravitational fields and slow motions, such as the conditions in stellar eclipsing binary systems (see Will 2014, for more details).

Therefore, a test of GR can be performed by checking that the measured and theoretical GR apsidal motion rates are compatible with values of γ and β predicted by the theory, assuming a fully conservative model (i.e. $\alpha_i = \zeta_2 \equiv 0$). The black dashed line shown in Fig. 5.12 corresponds to the best fit to the measured and predicted values of the GR apsidal motion, assuming only a varying slope. This slope, as deduced from Eq. (5.11), corresponds to $A \equiv (2+2\gamma-\beta)/3$. We derive a value of $A = 1.001 \pm 0.012$, which is fully compatible with the value predicted by GR of 1. It is clear from Fig. 5.12 that the stronger constraints are set by the systems with the smaller relative uncertainties, that is, V541 Cyg, KX Cnc, and AL Dor. However, it should be noted that the fit is still compatible with GR when removing these three targets, obtaining $A = 0.996 \pm 0.037$.

From our determination of A, the validity of alternative gravitational theories in the PPN formalism can be assessed. For example, constraints can be put on the coupling constant ω_{BD} of the Brans-Dicke theory (Estabrook 1969), which takes $A = (4+3\omega_{BD})/(6+3\omega_{BD})$. Furthermore,

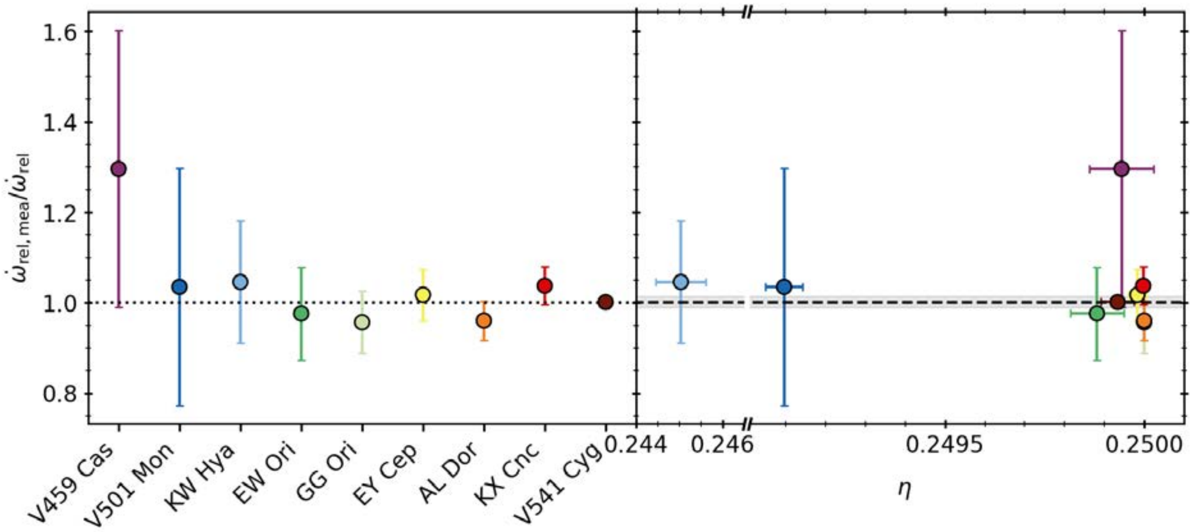

Figure 5.13: Ratio of measured and predicted GR apsidal motion rates for each system (*left*) and as a function of the dimensionless reduced mass η (*right*). The black dashed line and grey shadow area correspond to the best fit of Eq. (5.11), assuming $\gamma = \beta = 1$, and its 1-σ uncertainty. We highlight the broken x-axis and the different scales. The colour code is chosen such that redder colours correspond to systems with the smaller relative error, and therefore are dominating the fit.

our measurements can also be used to place bounds on the standard individual PPN parameters. Adopting the limit of $(\gamma - 1)$ from the Shapiro time-delay measurements using the Cassini spacecraft, of 2.3×10^{-5} (Bertotti et al. 2003), our measurement yields a constraint on β given by $(\beta - 1) = -0.003 \pm 0.036$. Equivalently, adopting the limit of $(\beta - 1)$ from the perihelion shift of Mercury, of 8×10^{-5} (Verma et al. 2014), we find a constraint to γ of $(\gamma - 1) = 0.001 \pm 0.018$.

A test of non-conservative models can be carried out by measuring the value of $B \equiv (2\alpha_1 - \alpha_2 + \alpha_3 + 2\zeta_2)/6$ in Eq. (5.11). Assuming now $\gamma = \beta = 1$, we can determine the value of B by fitting the relation $\dot{\omega}_{\rm rel,mea}/\dot{\omega}_{\rm rel} = 1 + B\eta$. Such an assumption is justified by the measurements of the perihelion shift of Mercury, which correspond to a very small value of η, and determine $A = 1$ at high significance. In the last column of Table 5.10 we list the ratio between the measured and predicted GR apsidal motion rates, and plot them for each system in the left panel in Fig. 5.13, and as a function of η in the right panel in Fig. 5.13. The black dashed line and the grey shadow region represent the best fit of B and the 1σ uncertainty. We obtain $B = 0.004 \pm 0.050$, which again is fully consistent with the predicted null value from GR. Only one system, KW Hya, has a value of η that is significantly different from the bulk of the sample at $\eta = 0.250$. This clustering of measurements at a small range in η limits the effectiveness of the sample at placing strong constraints on the slope B. For this reason, we cannot perform a fit varying simultaneously A and B from Eq. (5.11). This would be enabled by considering systems with very unequal component masses, which are difficult to discover and measure with high precision.

Our analysis provides weaker constraints to PPN parameters compared to for example those from the perihelion shift of Mercury (Verma et al. 2014), the Shapiro time-delay measured by the Cassini mission (Bertotti et al. 2003), or the spin precession of millisecond pulsars (Shao et al. 2013). Nevertheless, the results obtained from the eclipsing binaries analysed in this chapter perform a test to gravity in a yet unexplored regime of the potential-curvature diagram. Figure 5.14 reproduces this latter diagram from Baker et al. (2015) where we add the systems

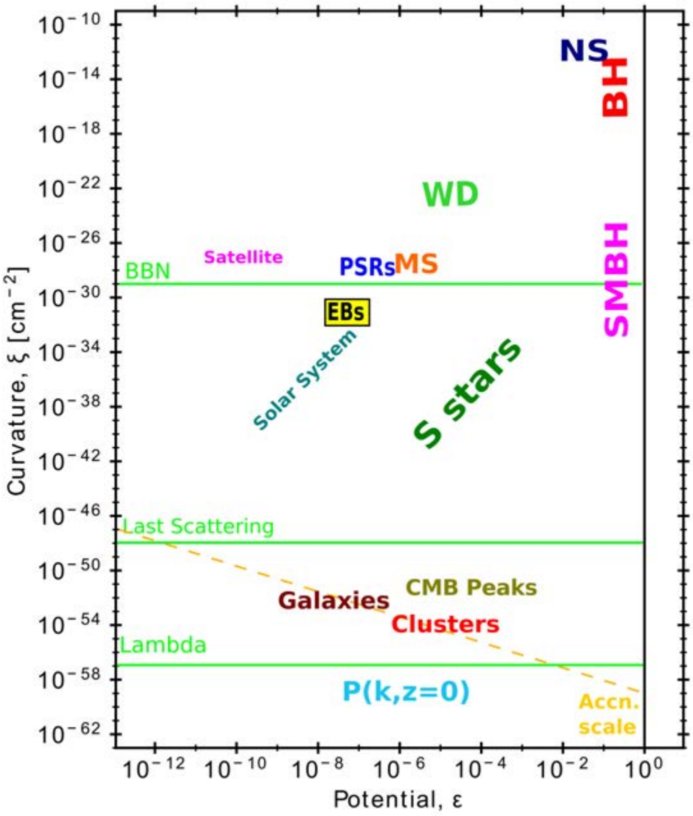

Figure 5.14: Adaptation of Fig. 1 of Baker et al. (2015) showing the parameter space for gravitational fields, including the regime probed by different astrophysical and cosmological systems. We add the regime tested by the eclipsing binaries in this chapter as a yellow square. The label abbreviations are: NS (individual neutron stars), BH (stellar mass black holes), WD (white dwarfs), PSRs (binary pulsars), MS (main sequence stars), SMBH (supermassive black holes), BBN (Big Bang nucleosynthesis). See Baker et al. (2015) for more information about the labels.

studied here. Stellar eclipsing binaries are one of the many probes of gravity in different environments, in this case covering the range between Solar System planets and binary pulsars.

Despite the addition of EW Ori and the improvement of several apsidal motion rates with respect to Baroch et al. (2021a), the lower apsidal motion rate reported for AL Dor, which is now at the limit of compatibility with the predicted value, makes the obtained constraints and GR parameters to have similar uncertainties and values than those obtained in Baroch et al. (2021a).

5.7 Summary

The continuous monitoring and the excellent precision of the TESS new times of minima allowed us to detect the apsidal motion rates for ten out of the 16 systems included in our sample. In some cases, we improved previous determinations, but for 5 of the systems (KX Cnc, AL Dor, V501 Her, KW Hya, and EY Cep) we present the first measurement of apsidal motion. Furthermore, we were able to determine apsidal motion in two systems, AL Dor and KW Hya, using data from TESS alone, which cover a very small fraction of the apsidal motion orbital cycle, thus highlighting the excellent performance of the mission for this kind of study.

A comparison between observed apsidal motion rates and theoretically predicted values yields excellent agreement. The good precision of the observed apsidal motion rates, the accurate stellar properties employed, and the relatively modest contribution from the classical term made it possible to calculate reliable estimates of the observed GR term. In some cases, when the classical contribution is especially insignificant, the GR apsidal motion could be measured with a relative precision approaching 1 per cent. This allows a thorough test of GR for the first time using this method. Our results strongly favour the predictions of GR, with no deviations observed at the level of 10^{-2}. Furthermore, we set constraints on two of the PPN parameters. These latter are not quite as stringent as those resulting from other methods (which can be three orders of magnitude more constraining; Will 2014), yet they probe a regime of gravitational forces and potentials that has not been explored before (Baker et al. 2015). Given the excellent agreement with GR, the parameter space for alternative theories continues to narrow.

The results we present are mildly model-dependent as they may be affected by deviations of the k_2 values. However, because of the small contribution of the classical term, variations of the k_2 values within their quoted uncertainties induce relative variations in $\dot{\omega}$ for the targets dominating our fits, V541 Cyg, KX Cnc, and AL Dor, lower than 1%.

With new TESS data still to come, observing new systems and increasing the data coverage of those already observed, promising systems still without a detection of apsidal motion could be added to further extend our study. In order to perform even more stringent tests of gravitation theories, an increase in the number of systems with a GR apsidal motion relative contribution larger than the threshold used in this chapter is needed. We therefore encourage spectroscopic monitoring and precise determination of absolute properties of long-period, eccentric eclipsing binaries with TESS photometric data.

Chapter 6

Conclusions and future work

Surveys dedicated to the search of exoplanets are providing a huge amount of data that can be also used to study the properties of stars. This is for instance the case of the CARMENES and TESS projects, which aim at the discovery of exoplanets by means of the radial velocity imprinted on their host star or by the detection of transits, respectively. In this thesis, we have made use of data from these surveys to gain insight into the properties of stars. In particular, CARMENES is devoted to the spectroscopic follow-up of M-dwarf stars. Although comprising most of the stars in the solar neighbourhood, the study of such kind of stars has been typically hampered due to their faintness. Nonetheless, nowadays, they represent a unique opportunity to discover and characterise rocky planets in their habitable zone. For instance, the multiplicity of M dwarfs, which provide constraints on the models of star and planet formation and evolution, is yet not as well constrained as those of solar-type stars. On the other hand, they are typically more magnetically active than more massive stars, which poses challenges to the discovery and characterisation of exoplanets. In this work, we have studied the properties of an active star (Chapter 2), analysed the properties of two exoplanet systems (Chapter 3), and announced a total of 17 new multiple systems (Chapter 4).

With respect TESS, its main goal is as well the discovery of exoplanets by the detection of transits in the photometric light curves of stars. However, the precision and high-cadence sampling of the light curves that TESS is producing can also be used to constrain the properties of stars. For instance, they can be used to put constraints on the variability of stars or to determine astroseismic masses. Besides, they became a precious source of minima timings of eclipsing binary stars, which we have used in this work to test fundamental physics theories such as General Relativity (Chapter 5).

In the following paragraphs, we provide a brief summary of the work done in each chapter and emphasise the main results.

6.1 Summary and conclusions

In the context of low-mass stars, we have made use of the CARMENES data to study the properties of the spot features caused by magnetic activity on an active M dwarf. This is described in Chapter 2. The goal was to find the best model reproducing the photometric and spectroscopic observables available. This was done using the stellar activity model code `StarSim`, a sophisticated model of a spotted rotating star that reproduces the spectroscopic and photometric variability by integrating the contribution of each surface element. The observables that we compared with the `StarSim` simulations were the photometric and spectroscopic data of the active M-dwarf star YZ CMi taken with the TJO telescope and the CARMENES spectrograph, respectively. The spectroscopic data consist of time series of RVs and of the activity indicator CRX, which is a measure of the chromatic effect of active regions on RVs as a function of wavelength.

Prior to the analysis, we revised high-cadence photometric data of YZ CMi from TESS sectors 7 and 34, which were observed with an interval of two years between them. We detected a significant decrease of the amplitude between the two sectors and also a substantial change in the shape of the modulations, a clear indication that active regions on the star evolve in both size and location. This fact highlights the importance of using observations taken in a short and similar interval of time. Therefore, we restricted our analysis to the CARMENES spectroscopic observation that were contemporaneous to the photometric data from TJO.

By performing simulations using the archival stellar properties of YZ CMi and the derived inclination of the star, we found that a single spot located close to the pole facing the observer could successfully reproduce the modulations found in the observables. The search for the best model was done by exploring a grid of spot-filling factor, contrast temperature, and convective shift, and comparing the obtained synthetic time series with the observed values by computing their likelihood statistic. Optimal parameters were computed by interpolating the grid of likelihood values with a GP and searching for the solution showing the highest $\ln L$ value. Due to the high computational cost to run each simulation, we assumed fixed stellar properties ignoring their uncertainties. For this reason, to account for the statistical uncertainties of the stellar parameters used in the simulations, we repeated the process using a set of values spanning the reported uncertainties of the effective temperature and inclination, which were found to have a larger contribution.

The best models are consistent with YZ CMi having a spot close to the pole facing the observer covering between a 9.5% and a 13.3 % of the entire stellar surface and with a temperature between 179 K to 273 K cooler than the surrounding photosphere. These results agree with the values obtained by previous authors using only light curves or from Zeeman-Doppler imaging, which yielded much broader results. The contrast temperature of the active region is also consistent with the lower temperature contrast of stars with low effective temperatures, as shown by empirical relations (Berdyugina et al. 2002; Andersen & Korhonen 2015). We also found a convective shift ranging between $+7\,\mathrm{m\,s^{-1}}$ and $+237\,\mathrm{m\,s^{-1}}$, much lower than the $-300\,\mathrm{m\,s^{-1}}$ estimated for the Sun. Although uncertain, this result represent the first physically-motivated observational evidence that a reversal of the convection effect may be happening in M dwarfs, as already suggested by Kürster et al. (2003), and is also consistent with the trend found between convective shift and effective temperatures of more massive stars (Allende Prieto et al. 2013; Meunier et al. 2017)

The method presented here represents a novel approach to estimate starspot parameters and the convective shift of active stars, and highlights the ability of a simultaneous fit to spectroscopic and photometric time series to break the degeneracy between filling factor and temperature contrast, and the importance of chromatic radial velocities in constraining the convective shift value.

Also in the context of low-mass stars and the CARMENES survey, in this thesis we contributed to the analysis of two new exoplanetary systems. More than 25 exoplanets have been discovered by the CARMENES project up to date. In Chapter 3, we studied the RV measurements from CARMENES to search for exoplanetary signals around the M-dwarf stars LSPM J2116+0234 and GJ 686. During the analysis of the data, an exoplanet around GJ 686 was announced by Affer et al. (2019) using HARPS-N data. We therefore added their RV data to our analysis to confirm that the same signal is found in the CARMENES data and to improve the orbital parameters determination.

The detection of the exoplanetary signals was done by searching for significant periodic signals in the RVs of the targets with the aid of a GLS periodogram. Additional periodic signals present in the data were found by repeating the process once the most significant signal was removed from the data. Exoplanet and stellar variability signals in the radial velocity were identified by means of the periodogram analysis of activity indicators and photometric data. We deemed periodicities found in these datasets as being produced by the stellar rotation.

Since the signal induced by rotation is also present in the RVs of both stars, we decided to model the planetary signal with the addition of an extra term modeling the rotation signal. The additional term was based on a GP with a quasi-periodic kernel as covariance function, from which we could derive relevant information of the rotation variability, such as their period and amplitude. We also used the likelihood statistic to compare the significance of different models explaining the RV signals. The preferred model in both cases was an eccentric orbit plus the stellar rotation term. The presence of the planetary signal was checked to be consistent across different wavelength ranges, in the case of LSPM J2116+0234, and across different instruments, for GJ 686.

The best model parameters for LSPM J2116+0234 yielded an exoplanet with a minimum mass of 12.8 $\mathrm{M}_\oplus$ in an eccentric orbit with a period of 14.45 d around its host star, for which we found a rotation period of 42.7 d, in agreement with the variability found in the activity indicators and photometry. For GJ 686 we confirmed the existence of the planet discovered by Affer et al. (2019), finding an exoplanet with a minimum mass of 6.50 $\mathrm{M}_\oplus$ and a period of 15.5311 d, improving considerably their uncertainties. Although the preferred model was an eccentric model, in comparison with the circular model used by Affer et al. (2019), its significance did not reach a high enough value to draw strong conclusions against the circular model. The other orbital parameters are consistent with the ones found by Affer et al. (2019), including the rotation period, which we found at 38.2 d. We used the derived properties to check that none of the exoplanets show visible transits in the available photometry. Finally, we determined that none of the planets are in the habitable zone of their respective stars, being too hot to contain liquid water, although setting some atmospheric parameters to extreme values, such as a large albedo and a low relative humidity, may result in favourable conditions to sustain liquid water. These two planets increase the rather large population of CARMENES planets between 11 d and 16 d, which was also observed in other M dwarf surveys.

But CARMENES is not only discovering planets, but also multiple systems. This is a common by-product of blind exoplanets surveys, although the previous screening of targets to exclude such kind of systems from the sample. Despite these systems can be identified with few observations and discarded from the survey, due to their utility to derive dynamical masses of stars and to understand the multiplicity fraction of the solar neighbourhood, their radial velocity curves were monitored using the CARMENES spectrograph. An important part of this thesis is devoted to their analysis, as described in Chapter 4. We presented 17 multiple systems detected among the CARMENES sample of stars, and determined their spectroscopic orbits and physical properties.

To narrow down the sample of candidates, we started by creating a subsample of those stars showing RV variations of the order of 0.5 km s^{-1}. Then, we analysed all the spectroscopic observations of the candidates with `todmor` searching for stars showing signals from more than one set of spectral lines, and extracted the RVs of all the components. For those systems not showing any sign of a stellar companion, we used the RVs produced by the CARMENES pipeline `serval` which have better precision than those computed with `todmor`. When available, we also gathered archival spectroscopic data of the stars, which expanded significantly the time span of the available measurements, a key aspect to constrain the orbital parameters of long-period systems. We included to the analysis publicly available photometry, and for one of the systems, GJ 282 C, we also found archival direct imaging data resolving the two components of the system.

We found a variety of systems, including five SB1s, ten SB2s, and two ST3s. The determination of the spectroscopic orbit parameters of SB1 and SB2 systems was done by fitting a 2-body Keplerian model to the RVs. In the case of ST3 systems, we fitted a hierarchical model of a close binary pair with a star companion at a wider separation. For the systems in which the RVs did not cover a significant portion of the orbital phase, we could only derive upper and lower limits to the orbital parameters. We also determined the minimum masses of the unseen companions of the SB1 systems, estimated the individual masses, radii and absolute magnitudes of SB2 systems using empirical relationships, and determined the rotation periods of the brightest component in 13 of the systems. The astrometric observations of GJ 282 C allowed us to fully characterize its orbit and orientation and measure the absolute dynamical masses of its components.

Among the systems discovered in this chapter, we found one of the youngest systems with measured masses (GJ 282 C), a close M-dwarf–white dwarf binary (GJ 207.1), and two brown dwarf candidates around GJ 3626 and GJ 912. The systems found in this work helps to improve our knowledge about the M-dwarf multiplicity ratio in the solar neighbourhood, which is very low for white dwarf and brown dwarfs companions. The lowest mass stars discovered in this thesis represent a 2% of all the known stars with masses between 0.1$_{\odot}$ and 0.3 M$_{\odot}$ located within 15 pc of the Sun.

With respect to multiple systems, their study could also provide precise determinations of the dynamical mass of stars, which are essential to derive empirical mass relationships that are used to estimate the mass of single stars and planet hosts. Besides, the study of eclipsing binary stars in particular can provide information about their physical properties, their interior, and even being used to prove fundamental theories. This is the case of the study described in Chapter 5.

The high precision and cadence of the space-based photometric measurements done by TESS enabled the determination of eclipse timings with a precision of a few seconds. In addition to that, TESS has covered a large fraction of the sky, obtaining light curves of most of the well-studied eclipsing binary systems. We used TESS photometric data to measure the time of minimum light of eclipsing binaries, and combined them with historical values in order to improve or compute for the first time their apsidal motion rates.

The sample of eclipsing systems was selected from the DEBCAT catalogue, requiring that systems had at least two eclipses observed by TESS, a mass and radius determination with precisions better than 2%, and with an estimated relativistic contribution to the total apsidal motion rate grater than 60%. The choice of this threshold is based in a compromise between making sure that uncertainties due to the classical contribution do not dominate over the relativistic term and having a meaningful number of systems to perform a meaningful analysis. A total of 16 systems fulfilled those requirements.

To compute the time of minimum light of the eclipses, we first normalized and removed systematic effects in the TESS light curves by modeling the out-of-eclipse phases with a GP model. We selected well sampled individual eclipses using the same orbital phase interval for all primary and secondary eclipses, and computed their time of minimum light employing the widely used Kwee & van Woerden (1956) method. We measured a total of 177 eclipse timings, after removing those eclipses with significant asymmetries. When possible, apsidal motion rates were determined from the linear change of the difference between the times of secondary and primary eclipses with time. From the 16 systems studied in this work, we could measure the apsidal motion rates for 10 of them, 5 of which were reported for the first time. For two of them, we could determine apsidal motion only using measurements from TESS. We computed the theoretical predictions of both the classical and the relativistic contribution to the apsidal motion rate, and found an excellent agreement between the predicted total apsidal motion rate and our measurements. We also computed the relativistic contribution to the observed apsidal motion rate by subtracting the predicted classical term from the observed values. Thanks to the small contribution of the classical term, in some cases we could determine the observed relativistic contribution with an accuracy of ∼1%. We compared these values to those predicted by general relativity, obtaining a good agreement for all systems. Thus, we provide a new test of general relativity and new constraints to two PPN parameters. This work represents the first test of general relativity using this method, and although the obtained constrains are much weaker than those resulting from other techniques, they probe a regime of gravitational forces and potentials that has not been tested before.

As a concluding remark, the steady increase of the interest in the exoplanet detection and characterisation of small rocky planets, which is the focus of several future missions and projects, is triggering a technical revolution aiming at the construction of more precise instruments. Even though their main driver is the exoplanet research, other astrophysical fields could also take advantage. The work done in the context of this thesis is an example of the plentiful of by-products that surveys devoted to exoplanet search allow to study. In particular, the analysis of photometric data from TESS allowed the determination of the slowest apsidal motion rates measured to date, which we used for the first time to test general relativity, while the exploitation of spectroscopic CARMENES data resulted in the determination of the surface properties of an active M dwarf, the detection of multiple stellar systems representing a considerable fraction of all known nearby low-mass stars, which included companions ranging from possible brown dwarfs to white dwarfs, and of course, the detection and confirmation of exoplanetary systems.

6.2 Future plans

In this thesis we have shown that the simultaneous fit to radial velocity, photometric and activity indices data yield the properties of stellar activity features such as spots, as well as it provides information about the convective motion of stars. This can be done using sophisticated codes such as `StarSim`. We analysed here the particular case of YZ CMi, for which data observed contemporaneously was available, but extending the analysis towards a broader range of spectral types would be very helpful for studies of stellar activity. This project would strongly benefit from an update of `StarSim` to include multiple activity indicators in order to compute optimized surface maps, from which radial velocity measurements could be predicted, positioning `StarSim` as an important player in the mitigation of stellar activity effects to improve planet detection. A parallel determination of the convective shift of all CARMENES stars may be done following the method developed by Meunier et al. (2017), which exploits the relation between the depth of spectral lines and their relative RV shift to determine the convective shift of the star.

With the approved extension of the CARMENES survey for two more years, which will keep collecting data of new targets and stars with few observations, it is possible that more interesting systems come to light, such as new binary and planetary systems or active stars, which would be ideal targets to continue the work done here.

Finally, the use of stars with a low relativistic contribution to the total apsidal motion rate in order to test theoretical models of internal structure is a natural continuation of the work done in Chapter 5. Furthermore, instead of being restricted to targets with accurate determinations of their masses and radii, we could search for systems with promising prospects as derived from TESS light curves (for example stars with a high number of observed eclipses and a estimated relativistic apsidal motion contribution larger than 90%) and then request time to perform spectroscopic observations to determine accurate physical properties by ourselves, applying the methods developed in Chapter 4. Additionally, this study would increase the number of well determined masses and radii which are essential to test stellar structure and evolutionary models.

Bibliography

Aceituno, J., Sánchez, S. F., Grupp, F., et al. 2013, A&A, 552, A31

Adams, W. S., Joy, A. H., & Humason, M. L. 1926, ApJ, 64

Adelman, S. J. 2001, Baltic Astronomy, 10, 589

Affer, L., Damasso, M., Micela, G., et al. 2019, A&A, 622, A193

Affer, L., Micela, G., Damasso, M., et al. 2016, A&A, 593, A117

Agerer, F., Busch, H., Kleikamp, W., & Moschner, W. 1994, Berliner Arbeitsgemeinschaft fuer Veraenderliche Sterne - Mitteilungen, 69, 1

Aigrain, S., Parviainen, H., & Pope, B. J. S. 2016, MNRAS, 459, 2408

Aigrain, S., Pont, F., & Zucker, S. 2012, MNRAS, 419, 3147

Aitken, R. G. 1918, The binary stars

Albrecht, S., Reffert, S., Snellen, I. A. G., & Winn, J. N. 2009, Nature, 461, 373

Albrecht, S., Setiawan, J., Torres, G., Fabrycky, D. C., & Winn, J. N. 2013, ApJ, 767, 32

Alekseev, I. Y. & Kozhevnikova, A. V. 2017, Astronomy Reports, 61, 221

Allard, F., Homeier, D., & Freytag, B. 2012, Philosophical Transactions of the Royal Society of London Series A, 370, 2765

Allende Prieto, C., Koesterke, L., Ludwig, H. G., Freytag, B., & Caffau, E. 2013, A&A, 550, A103

Alonso-Floriano, F. J., Caballero, J. A., Cortés-Contreras, M., Solano, E., & Montes, D. 2015, A&A, 583, A85

Alonso-Floriano, F. J., Sánchez-López, A., Snellen, I. A. G., et al. 2019, A&A, 621, A74

Ambikasaran, S., Foreman-Mackey, D., Greengard, L., Hogg, D. W., & O'Neil, M. 2015, IEEE Transactions on Pattern Analysis and Machine Intelligence, 38 [`arXiv:1403.6015`]

Andersen, J. 1991, A&A Rev., 3, 91

Andersen, J., Clausen, J. V., & Nordstrom, B. 1987, A&A, 175, 60

Andersen, J. & Vaz, L. P. R. 1984, A&A, 130, 102

Andersen, J. M. & Korhonen, H. 2015, MNRAS, 448, 3053

Andrews, A. D. 1966, PASP, 78, 324

Anglada-Escudé, G. & Butler, R. P. 2012, ApJS, 200, 15

Angus, R., Morton, T., Aigrain, S., Foreman-Mackey, D., & Rajpaul, V. 2018, MNRAS, 474, 2094

Ansdell, M., Gaidos, E., Mann, A. W., et al. 2015, ApJ, 798, 41

Armitage, P. J. & Bonnell, I. A. 2002, MNRAS, 330, L11

Astudillo-Defru, N., Delfosse, X., Bonfils, X., et al. 2017, A&A, 600, A13

Auvergne, M., Bodin, P., Boisnard, L., et al. 2009, A&A, 506, 411

Baker, T., Psaltis, D., & Skordis, C. 2015, ApJ, 802, 63

Bakış, V., Bakış, H., Demircan, O., & Eker, Z. 2008, MNRAS, 384, 1657

Baluev, R. V. 2009, MNRAS, 393, 969

Baluev, R. V. 2013, Astronomy and Computing, 2, 18

Bar, I., Vreeswijk, P., Gal-Yam, A., Ofek, E. O., & Nelemans, G. 2017, ApJ, 850, 34

Baraffe, I. & Chabrier, G. 2018, A&A, 619, A177

Baraffe, I., Homeier, D., Allard, F., & Chabrier, G. 2015, A&A, 577, A42

Barnard, E. E. 1913, ApJ, 38

Barnes, J. R., Jeffers, S. V., & Jones, H. R. A. 2011, MNRAS, 412, 1599

Barnes, S. A. 2003, ApJ, 586, 464

Barnes, S. A. 2007, ApJ, 669, 1167

Baroch, D., Giménez, A., Ribas, I., et al. 2021a, A&A, 649, A64

Baroch, D., Morales, J. C., Ribas, I., et al. 2021b, arXiv e-prints, arXiv:2105.14770

Baroch, D., Morales, J. C., Ribas, I., et al. 2020, A&A, 641, A69

Baroch, D., Morales, J. C., Ribas, I., et al. 2018, A&A, 619, A32

Barrado y Navascués, D., Stauffer, J. R., & Jayawardhana, R. 2004, ApJ, 614, 386

Bauer, F. F., Zechmeister, M., Kaminski, A., et al. 2020, A&A, 640, A50

Bayo, A., Rodrigo, C., Barrado Y Navascués, D., et al. 2008, A&A, 492, 277

Becerril, S., Mirabet, E., Lizon, J. L., et al. 2016, in Society of Photo-Optical Instrumentation Engineers (SPIE) Conference Series, Vol. 9912, Advances in Optical and Mechanical Technologies for Telescopes and Instrumentation II, ed. R. Navarro & J. H. Burge, 991262

Bedell, M., Hogg, D. W., Foreman-Mackey, D., Montet, B. T., & Luger, R. 2019, AJ, 158, 164

Beeck, B., Cameron, R. H., Reiners, A., & Schüssler, M. 2013a, A&A, 558, A48

Beeck, B., Cameron, R. H., Reiners, A., & Schüssler, M. 2013b, A&A, 558, A49

Beeck, B., Schüssler, M., Cameron, R. H., & Reiners, A. 2015, A&A, 581, A42

Beeck, B., Schüssler, M., & Reiners, A. 2011, in Astronomical Society of the Pacific Conference Series, Vol. 448, 16th Cambridge Workshop on Cool Stars, Stellar Systems, and the Sun, ed. C. Johns-Krull, M. K. Browning, & A. A. West, 1071

Bell, C. P. M., Mamajek, E. E., & Naylor, T. 2015, MNRAS, 454, 593

Benedict, G. F., Henry, T. J., Franz, O. G., et al. 2016, AJ, 152, 141

Benedict, G. F., Nelan, E., McArthur, B., et al. 1993, PASP, 105, 487

Bensby, T., Feltzing, S., & Lundström, I. 2003, A&A, 410, 527

Benz, W. & Mayor, M. 1981, A&A, 93, 235

Berdyugina, S. V. 2005, Living Reviews in Solar Physics, 2, 8

Berdyugina, S. V., Pelt, J., & Tuominen, I. 2002, A&A, 394, 505

Berger, T. E., Rouppe van der Voort, L., & Löfdahl, M. 2007, ApJ, 661, 1272

Bergfors, C., Brandner, W., Janson, M., et al. 2010, A&A, 520, A54

Berta, Z. K., Irwin, J., Charbonneau, D., Burke, C. J., & Falco, E. E. 2012, AJ, 144, 145

Bertotti, B., Iess, L., & Tortora, P. 2003, Nature, 425, 374

Beuzit, J. L., Vigan, A., Mouillet, D., et al. 2019, A&A, 631, A155

Biller, B. A., Close, L. M., Masciadri, E., et al. 2007, ApJS, 173, 143

Bluhm, P., Luque, R., Espinoza, N., et al. 2020, A&A, 639, A132

Bochanski, J. J., Hawley, S. L., Covey, K. R., et al. 2010, AJ, 139, 2679

Boisse, I., Bonfils, X., & Santos, N. C. 2012, A&A, 545, A109

Boisse, I., Bouchy, F., Hébrard, G., et al. 2011a, A&A, 528, A4

Boisse, I., Bouchy, F., Hébrard, G., et al. 2011b, in IAU Symposium, Vol. 273, Physics of Sun and Star Spots, ed. D. Prasad Choudhary & K. G. Strassmeier, 281–285

Boisse, I., Moutou, C., Vidal-Madjar, A., et al. 2009, A&A, 495, 959

Bondar', N. I., Gorbunov, M. A., & Shlyapnikov, A. A. 2019, Astronomical Society of the Pacific Conference Series, Vol. 518, A Search for Cyclic Activity of Red Dwarfs Using Photometric Surveys, ed. D. O. Kudryavtsev, I. I. Romanyuk, & I. A. Yakunin, 180

Bondar, N. I. & Katsova, M. M. 2018, Geomagnetism and Aeronomy, 58, 910

Bonfils, X., Lo Curto, G., Correia, A. C. M., et al. 2013, A&A, 556, A110

Bonfils, X., Mayor, M., Delfosse, X., et al. 2007, A&A, 474, 293

Borucki, W. J., Koch, D., Basri, G., et al. 2010, Science, 327, 977

Boss, A. P. 1988, Comments on Astrophysics, 12, 169

Brandt, T. D. 2018, ApJS, 239, 31

Brandt, T. D., Dupuy, T. J., Li, Y., et al. 2021, orvara: Orbits from Radial Velocity, Absolute, and/or Relative Astrometry

Breinhorst, R. A., Pfleiderer, J., Reinhardt, M., & Karimie, M. T. 1973, A&A, 22, 239

Butler, R. P., Vogt, S. S., Laughlin, G., et al. 2017, AJ, 153, 208

Caballero, J. A., Cortés-Contreras, M., Alonso-Floriano, F. J., et al. 2016a, in 19th Cambridge Workshop on Cool Stars, Stellar Systems, and the Sun (CS19), Cambridge Workshop on Cool Stars, Stellar Systems, and the Sun, 148

Caballero, J. A., Cortés-Contreras, M., López-Santiago, J., et al. 2013, in Highlights of Spanish Astrophysics VII, ed. J. C. Guirado, L. M. Lara, V. Quilis, & J. Gorgas, 645–645

Caballero, J. A., Guàrdia, J., López del Fresno, M., et al. 2016b, in Proc. SPIE, Vol. 9910, Observatory Operations: Strategies, Processes, and Systems VI, 99100E

Caballero, J. A., Martín, E. L., Zapatero Osorio, M. R., et al. 2006, A&A, 445, 143

Catalán, S., Isern, J., García-Berro, E., & Ribas, I. 2008, MNRAS, 387, 1693

Cavallini, F., Ceppatelli, G., & Righini, A. 1985, A&A, 150, 256

Cegla, H. M., Watson, C. A., Shelyag, S., Mathioudakis, M., & Moutari, S. 2019, ApJ, 879, 55

Chabrier, G. 2003, PASP, 115, 763

Chabrier, G., Baraffe, I., Allard, F., & Hauschildt, P. 2000a, ApJ, 542, 464

Chabrier, G., Brassard, P., Fontaine, G., & Saumon, D. 2000b, ApJ, 543, 216

Chabrier, G., Gallardo, J., & Baraffe, I. 2007, A&A, 472, L17

Chini, R., Hoffmeister, V. H., Nasseri, A., Stahl, O., & Zinnecker, H. 2012, MNRAS, 424, 1925

Choi, J., Dotter, A., Conroy, C., et al. 2016, ApJ, 823, 102

Christian, D. J., Craig, N., Cahill, W., Roberts, B., & Malina, R. F. 1999, AJ, 117, 2466

Chugainov, P. F. 1974, Izvestiya Ordena Trudovogo Krasnogo Znameni Krymskoj Astrofizicheskoj Observatorii, 52, 3

Cifuentes, C., Caballero, J. A., Cortés-Contreras, M., et al. 2020, A&A, 642, A115

Claret, A. 1997, A&A, 327, 11

Claret, A. & Giménez, A. 1993, A&A, 277, 487

Claret, A. & Giménez, A. 2010, A&A, 519, A57

Claret, A. & Torres, G. 2017, ApJ, 849, 18

Claret, A. & Torres, G. 2018, ApJ, 859, 100

Claret, A. & Torres, G. 2019, ApJ, 876, 134

Claret, A., Torres, G., & Wolf, M. 2010, A&A, 515, A4

Clausen, J. V., Bruntt, H., Olsen, E. H., Helt, B. E., & Claret, A. 2010, A&A, 511, A22

Cortés-Contreras, M. 2016, PhD thesis, Universidad Complutense de Madrid, Spain

Cortés-Contreras, M. 2021, in prep

Cortés-Contreras, M., Béjar, V. J. S., Caballero, J. A., et al. 2017, A&A, 597, A47

Cosentino, R., Lovis, C., Pepe, F., et al. 2012, in Society of Photo-Optical Instrumentation Engineers (SPIE) Conference Series, Vol. 8446, Ground-based and Airborne Instrumentation for Astronomy IV, ed. I. S. McLean, S. K. Ramsay, & H. Takami, 84461V

Curtis, J. L., Agüeros, M. A., Douglas, S. T., & Meibom, S. 2019a, ApJ, 879, 49

Curtis, J. L., Agüeros, M. A., Mamajek, E. E., Wright, J. T., & Cummings, J. D. 2019b, AJ, 158, 77

Cutri, R. M., Wright, E. L., Conrow, T., et al. 2013, Explanatory Supplement to the AllWISE Data Release Products, Explanatory Supplement to the AllWISE Data Release Products

Czekala, I., Mandel, K. S., Andrews, S. M., et al. 2017, ApJ, 840, 49

Dahm, S. E. 2015, ApJ, 813, 108

Damasso, M., Del Sordo, F., Anglada-Escudé, G., et al. 2020, Science Advances, 6, eaax7467

Dariush, A., Mosleh, M., & Dariush, D. 2006, Ap&SS, 305, 85

Davies, D. 2007, Peremennye Zvezdy Prilozhenie, 7, 16

Davis, A. B., Cisewski, J., Dumusque, X., Fischer, D. A., & Ford, E. B. 2017, ApJ, 846, 59

De Laurentis, M., De Rosa, R., Garufi, F., & Milano, L. 2012, MNRAS, 424, 2371

Dekker, H., D'Odorico, S., Kaufer, A., Delabre, B., & Kotzlowski, H. 2000, in Society of Photo-Optical Instrumentation Engineers (SPIE) Conference Series, Vol. 4008, Proc. SPIE, ed. M. Iye & A. F. Moorwood, 534–545

Delfosse, X., Forveille, T., Perrier, C., & Mayor, M. 1998, A&A, 331, 581

Delfosse, X., Forveille, T., Ségransan, D., et al. 2000, A&A, 364, 217

Desidera, S., Gratton, R. G., Endl, M., et al. 2004, A&A, 420, L27

Desort, M., Lagrange, A.-M., Galland, F., Udry, S., & Mayor, M. 2007, A&A, 473, 983

Díaz, R. F. 2018, in Asteroseismology and Exoplanets: Listening to the Stars and Searching for New Worlds, ed. T. L. Campante, N. C. Santos, & M. J. P. F. G. Monteiro, Vol. 49, 199

Dieterich, S. B., Henry, T. J., Golimowski, D. A., Krist, J. E., & Tanner, A. M. 2012, AJ, 144, 64

Diethelm, R. 1992, Bulletin der Bedeckungsveraenderlichen-Beobachter der Schweizerischen Astronomischen Gesellschaft, 99, 10

Díez Alonso, E., Caballero, J. A., Montes, D., et al. 2019, A&A, 621, A126

Dittmann, J. A., Irwin, J. M., Charbonneau, D., et al. 2017, ApJ, 836, 124

Donati, J. F., Semel, M., Carter, B. D., Rees, D. E., & Collier Cameron, A. 1997, MNRAS, 291, 658

Douglas, S. T., Agüeros, M. A., Covey, K. R., et al. 2016, ApJ, 822, 47

Douglas, S. T., Curtis, J. L., Agüeros, M. A., et al. 2019, ApJ, 879, 100

Drake, A. J., Djorgovski, S. G., Mahabal, A., et al. 2009, ApJ, 696, 870

Dravins, D. 1999, Astronomical Society of the Pacific Conference Series, Vol. 185, Stellar Surface Convection, Line Asymmetries, and Wavelength Shifts, ed. J. B. Hearnshaw & C. D. Scarfe, 268

Dravins, D., Lindegren, L., & Nordlund, A. 1981, A&A, 96, 345

Dreizler, S., Crossfield, I. J. M., Kossakowski, D., et al. 2020, A&A, 644, A127

Dressing, C. D. & Charbonneau, D. 2013, ApJ, 767, 95

Dressing, C. D. & Charbonneau, D. 2015, ApJ, 807, 45

Duchêne, G. & Kraus, A. 2013, ARA&A, 51, 269

Dumusque, X. 2018, A&A, 620, A47

Dumusque, X., Boisse, I., & Santos, N. C. 2014, ApJ, 796, 132

Dumusque, X., Pepe, F., Lovis, C., et al. 2012, Nature, 491, 207

Dumusque, X., Santos, N. C., Udry, S., Lovis, C., & Bonfils, X. 2011a, A&A, 527, A82

Dumusque, X., Udry, S., Lovis, C., Santos, N. C., & Monteiro, M. J. P. F. G. 2011b, A&A, 525, A140

Durisen, R. H., Gingold, R. A., Tohline, J. E., & Boss, A. P. 1986, ApJ, 305, 281

Eggleton, P. & Kiseleva, L. 1995, ApJ, 455, 640

Elvis, M., Plummer, D., Schachter, J., & Fabbiano, G. 1992, ApJS, 80, 257

Estabrook, F. B. 1969, ApJ, 158, 81

Faigler, S. & Mazeh, T. 2011, MNRAS, 415, 3921

Fang, X.-S., Zhao, G., Zhao, J.-K., & Bharat Kumar, Y. 2018, MNRAS, 476, 908

Faria, J. P., Haywood, R. D., Brewer, B. J., et al. 2016, A&A, 588, A31

Feiden, G. & Chaboyer, B. 2013, ApJ, 779, 183

Feiden, G. A. & Chaboyer, B. 2012, ApJ, 757, 42

Feiden, G. A. & Chaboyer, B. 2014, A&A, 571, A70

Feinstein, A. D., Montet, B. T., Foreman-Mackey, D., et al. 2019, PASP, 131, 094502

Ferrero, G., Gamen, R., Benvenuto, O., & Fernández-Lajús, E. 2013, MNRAS, 433, 1300

Figueira, P., Marmier, M., Bonfils, X., et al. 2010, A&A, 513, L8

Figueira, P., Santos, N. C., Pepe, F., Lovis, C., & Nardetto, N. 2013, A&A, 557, A93

Finch, C. T., Zacharias, N., Subasavage, J. P., Henry, T. J., & Riedel, A. R. 2014, AJ, 148, 119

Fleming, D. P. & VanderPlas, J. 2018, The Journal of Open Source Software, 3, 781

Ford, E. B., Kozinsky, B., & Rasio, F. A. 2000, ApJ, 535, 385

Foreman-Mackey, D. 2015, George: Gaussian Process regression

Foreman-Mackey, D., Agol, E., Angus, R., & Ambikasaran, S. 2017, AJ, 154, 220

Foreman-Mackey, D., Hogg, D. W., Lang, D., & Goodman, J. 2013, PASP, 125, 306

Fouqué, P., Moutou, C., Malo, L., et al. 2018, MNRAS, 475, 1960

Frankowski, A., Jancart, S., & Jorissen, A. 2007, A&A, 464, 377

Frieboes-Conde, H. & Herczeg, T. 1973, A&AS, 12, 1

Fuhrmann, K. 1998, A&A, 338, 161

Fuhrmeister, B. & Schmitt, J. H. M. M. 2003, A&A, 403, 247

Gaia Collaboration, Brown, A. G. A., Vallenari, A., et al. 2018, A&A, 616, A1

Gaia Collaboration, Brown, A. G. A., Vallenari, A., et al. 2021, A&A, 649, A1

Gaia Collaboration, Prusti, T., de Bruijne, J. H. J., et al. 2016, A&A, 595, A1

Gaidos, E., Mann, A. W., Kraus, A. L., & Ireland, M. 2016, MNRAS, 457, 2877

Gallenne, A., Pietrzyński, G., Graczyk, D., et al. 2019, A&A, 632, A31

Gershberg, R. E., Katsova, M. M., Lovkaya, M. N., Terebizh, A. V., & Shakhovskaya, N. I. 1999, A&AS, 139, 555

Gibson, N. P., Pont, F., & Aigrain, S. 2011, MNRAS, 411, 2199

Giclas, H. L., Burnham, R., & Thomas, N. G. 1961, Lowell Observatory Bulletin, 6, 61

Giménez, A. 1985, ApJ, 297, 405

Giménez, A. 2007, in IAU Symposium, Vol. 240, Binary Stars as Critical Tools & Tests in Contemporary Astrophysics, ed. W. I. Hartkopf, P. Harmanec, & E. F. Guinan, 290–298

Giménez, A. & Bastero, M. 1995, Ap&SS, 226, 99

Giménez, A., Kim, C.-H., & Nha, I.-S. 1987, MNRAS, 224, 543

Gizis, J. E., Reid, I. N., & Hawley, S. L. 2002, AJ, 123, 3356

Gliese, W. & Jahreiß, H. 1979, A&AS, 38, 423

González-Álvarez, E., Zapatero Osorio, M. R., Caballero, J. A., et al. 2020, A&A, 637, A93

Goodman, J. & Weare, J. 2010, Communications in Applied Mathematics and Computational Science, 5, 65

Graczyk, D., Pietrzyński, G., Gałan, C., et al. 2021, arXiv e-prints, arXiv:2103.02077

Graczyk, D., Pietrzyński, G., Gieren, W., et al. 2019, ApJ, 872, 85

Grandjean, A., Lagrange, A. M., Keppler, M., et al. 2020, A&A, 633, A44

Gray, D. F. 2005, The Observation and Analysis of Stellar Photospheres

Gray, D. F. 2009, ApJ, 697, 1032

Grether, D. & Lineweaver, C. H. 2006, ApJ, 640, 1051

Guinan, E. F., Maley, J. A., & Marshall, J. J. 1996, IBVS, 4362, 1

Guinan, E. F. & Maloney, F. P. 1985, AJ, 90, 1519

Haakonsen, C. B. & Rutledge, R. E. 2009, ApJS, 184, 138

Halbwachs, J. L., Arenou, F., Mayor, M., Udry, S., & Queloz, D. 2000, A&A, 355, 581

Hanslmeier, A., Nesis, A., & Mattig, W. 1991, A&A, 251, 307

Harmanec, P., Holmgren, D. E., Wolf, M., et al. 2014, A&A, 563, A120

Hastings, W. K. 1970, Biometrika, 57, 97

Hatzes, A. P. 2002, Astronomische Nachrichten, 323, 392

Hatzes, A. P. 2013, ApJ, 770, 133

Hawley, S. L., Gizis, J. E., & Reid, I. N. 1996, AJ, 112, 2799

Haywood, R. D., Collier Cameron, A., Queloz, D., et al. 2014, MNRAS, 443, 2517

He, M. Y. & Petrovich, C. 2018, MNRAS, 474, 20

Heintz, W. D. 1987, AJ, 94, 1077

Heintz, W. D. 1993, AJ, 105, 1188

Hejlesen, P. M. 1987, A&AS, 69, 251

Henry, T. J., Jao, W.-C., Subasavage, J. P., et al. 2006, AJ, 132, 2360

Henry, T. J., Kirkpatrick, J. D., & Simons, D. A. 1994, AJ, 108, 1437

Herbst, W. & Layden, A. C. 1987, AJ, 94, 150

Herrero, E., Ribas, I., Jordi, C., et al. 2016, A&A, 586, A131

Higl, J. & Weiss, A. 2017, A&A, 608, A62

Hilditch, R. W. 2001, An Introduction to Close Binary Stars (Cambridge University Press), 355–372

Høg, E. 2000, Tycho Star Catalogs: The 2.5 Million Brightest Stars (Murdin, P.), 2862

Høg, E., Fabricius, C., Makarov, V. V., et al. 2000, A&A, 355, L27

Hosey, A. D., Henry, T. J., Jao, W.-C., et al. 2015, AJ, 150, 6

Hotta, H. & Iijima, H. 2020, MNRAS, 494, 2523

Houdebine, E. R. & Mullan, D. J. 2015, ApJ, 801, 106

Hubscher, J. 2015, IBVS, 6152, 1

Hubscher, J. & Lehmann, P. B. 2015, IBVS, 6149, 1

Hubscher, J., Paschke, A., & Walter, F. 2005, Information Bulletin on Variable Stars, 5657, 1

Huélamo, N., Figueira, P., Bonfils, X., et al. 2008, A&A, 489, L9

Husser, T. O., Wende-von Berg, S., Dreizler, S., et al. 2013, A&A, 553, A6

Hut, P. 1981, A&A, 99, 126

Hut, P. & Bahcall, J. N. 1983, ApJ, 268, 319

Iben, Icko, J. & Livio, M. 1993, PASP, 105, 1373

Imbert, M. 2002, A&A, 387, 850

Irwin, J., Berta, Z. K., Burke, C. J., et al. 2011, ApJ, 727, 56

Irwin, J., Buchhave, L., Berta, Z. K., et al. 2010, ApJ, 718, 1353

Irwin, J., Charbonneau, D., Berta, Z. K., et al. 2009, ApJ, 701, 1436

Irwin, J. B. 1959, AJ, 64, 149

Isaacson, H. & Fischer, D. 2010, ApJ, 725, 875

Janson, M., Bergfors, C., Brandner, W., et al. 2014, ApJ, 789, 102

Janson, M., Hormuth, F., Bergfors, C., et al. 2012, ApJ, 754, 44

Jao, W.-C., Henry, T. J., Subasavage, J. P., et al. 2003, AJ, 125, 332

Jao, W.-C., Henry, T. J., Subasavage, J. P., et al. 2011, AJ, 141, 117

Jeffers, S. V., Barnes, J. R., Jones, H. R. A., et al. 2014, MNRAS, 438, 2717

Jeffers, S. V., Schöfer, P., Lamert, A., et al. 2018, A&A, 614, A76

Jenkins, J. M., Twicken, J. D., McCauliff, S., et al. 2016, in Society of Photo-Optical Instrumentation Engineers (SPIE) Conference Series, Vol. 9913, Software and Cyberinfrastructure for Astronomy IV, 99133E

Jenkins, J. S., Ramsey, L. W., Jones, H. R. A., et al. 2009, ApJ, 704, 975

Jha, S., Torres, G., Stefanik, R. P., Latham, D. W., & Mazeh, T. 2000, MNRAS, 317, 375

Jódar, E., Pérez-Garrido, A., Díaz-Sánchez, A., et al. 2013, MNRAS, 429, 859

Johnson, D. R. H. & Soderblom, D. R. 1987, AJ, 93, 864

Jones, D. E., Stenning, D. C., Ford, E. B., et al. 2017, arXiv e-prints, arXiv:1711.01318

Jovanovic, N., Martinache, F., Guyon, O., et al. 2015, PASP, 127, 890

Kallrath, J. & Milone, E. F. 2009, Eclipsing Binary Stars: Modeling and Analysis

Kaminski, A., Trifonov, T., Caballero, J. A., et al. 2018, A&A, 618, A115

Kammerer, J., Ireland, M. J., Martinache, F., & Girard, J. H. 2019, MNRAS, 486, 639

Karpowicz, M. 1961, Acta Astron., 11, 51

Kasting, J. F., Whitmire, D. P., & Reynolds, R. T. 1993, Icarus, 101, 108

Kaufer, A., Stahl, O., Tubbesing, S., et al. 1999, The Messenger, 95, 8

Kazarovets, E. V., Samus, N. N., Durlevich, O. V., et al. 1999, Information Bulletin on Variable Stars, 4659, 1

Kemmer, J., Stock, S., Kossakowski, D., et al. 2020, A&A, 642, A236

Kepler, J. 1609, Astronomia nova ..., seu physica coelestis, tradita commentariis de motibus stellae martis

Kepler, J. 1619, Ioannis Keppleri harmonices mundi libri V

Kervella, P., Arenou, F., Mignard, F., & Thévenin, F. 2019, A&A, 623, A72

Khaliullin, K. F. 1985, ApJ, 299, 668

Khaliullin, K. F. & Khaliullina, A. I. 2007, MNRAS, 382, 356

Kim, C. H., Kreiner, J. M., Zakrzewski, B., et al. 2018, ApJS, 235, 41

Kinoshita, H. & Nakai, H. 1999, Celestial Mechanics and Dynamical Astronomy, 75, 125

Kiraga, M. 2012, Acta Astron., 62, 67

Kirk, B., Conroy, K., Prša, A., et al. 2016, AJ, 151, 68

Kiseleva, L. G., Eggleton, P. P., & Mikkola, S. 1998, MNRAS, 300, 292

Koen, C., Kilkenny, D., van Wyk, F., & Marang, F. 2010, MNRAS, 403, 1949

Kopal, Z. 1959, Close binary systems (New York: John Wiley & Sons Inc.)

Kopal, Z. 1978, Dynamics of close binary systems (Springer Netherlands)

Kopparapu, R. K., Ramirez, R., Kasting, J. F., et al. 2013, ApJ, 765, 131

Kopparapu, R. K., Ramirez, R. M., SchottelKotte, J., et al. 2014, ApJ, 787, L29

Kovács, G., Zucker, S., & Mazeh, T. 2002, A&A, 391, 369

Kovaleva, D., Kaygorodov, P., Malkov, O., Debray, B., & Oblak, E. 2015, Astronomy and Computing, 11, 119

Kozai, Y. 1962, AJ, 67, 591

Kraus, A. L., Ireland, M. J., Martinache, F., & Hillenbrand, L. A. 2011, ApJ, 731, 8

Kürster, M., Endl, M., Rouesnel, F., et al. 2003, A&A, 403, 1077

Kurucz, R. L. 2017, ATLAS9: Model atmosphere program with opacity distribution functions

Kwee, K. K. & van Woerden, H. 1956, Bull. Astron. Inst. Netherlands, 12, 327

Lacy, C. H. S. 1998, AJ, 115, 801

Lacy, C. H. S. 2002, Information Bulletin on Variable Stars, 5357, 1

Lacy, C. H. S. 2004, Information Bulletin on Variable Stars, 5577, 1

Lacy, C. H. S., Claret, A., & Sabby, J. A. 2004, AJ, 128, 1340

Lacy, C. H. S., Hood, B., & Straughn, A. 2001, Information Bulletin on Variable Stars, 5067, 1

Lacy, C. H. S., Torres, G., Claret, A., & Menke, J. L. 2006, AJ, 131, 2664

Lacy, C. H. S., Torres, G., Claret, A., & Vaz, L. P. R. 2005, AJ, 130, 2838

Lafarga, M., Ribas, I., Lovis, C., et al. 2020, A&A, 636, A36

Lafarga, M., Ribas, I., Reiners, A., et al. 2021, arXiv e-prints, arXiv:2105.13467

Lalitha, S., Baroch, D., Morales, J. C., et al. 2019, A&A, 627, A116

Lamman, C., Baranec, C., Berta-Thompson, Z. K., et al. 2020, AJ, 159, 139

Lampón, M., López-Puertas, M., Lara, L. M., et al. 2020, A&A, 636, A13

Lampton, M., Lieu, R., Schmitt, J. H. M. M., et al. 1997, ApJS, 108, 545

Lanza, A. F., Bonomo, A. S., Moutou, C., et al. 2010, A&A, 520, A53

Lanza, A. F., Bonomo, A. S., & Rodonò, M. 2007, A&A, 464, 741

Larkin, J., Barczys, M., Krabbe, A., et al. 2006, in Society of Photo-Optical Instrumentation Engineers (SPIE) Conference Series, Vol. 6269, Society of Photo-Optical Instrumentation Engineers (SPIE) Conference Series, ed. I. S. McLean & M. Iye, 62691A

Lastennet, E. & Valls-Gabaud, D. 2002, A&A, 396, 551

Law, N. M., Kraus, A. L., Street, R., et al. 2012, ApJ, 757, 133

Leggett, S. K. 1992, ApJS, 82, 351

Lenzen, R., Hartung, M., Brandner, W., et al. 2003, in Society of Photo-Optical Instrumentation Engineers (SPIE) Conference Series, Vol. 4841, Proc. SPIE, ed. M. Iye & A. F. M. Moorwood, 944–952

Lépine, S. & Bongiorno, B. 2007, AJ, 133, 889

Lépine, S. & Gaidos, E. 2011, AJ, 142, 138

Lépine, S., Hilton, E. J., Mann, A. W., et al. 2013, AJ, 145, 102

Lépine, S. & Shara, M. M. 2005, AJ, 129, 1483

Levi-Civita, T. 1937, Am. J. Math., 59, 225

Lidov, M. L. 1962, Planet. Space Sci., 9, 719

Lindegren, L., Hernández, J., Bombrun, A., et al. 2018, A&A, 616, A2

Lindegren, L., Lammers, U., Hobbs, D., et al. 2012, A&A, 538, A78

Lippincott, S. L. 1952, ApJ, 115, 582

Lippincott, S. L. 1981, AJ, 86, 1401

Livingston, W., Wallace, L., Huang, Y., & Moise, E. 1999, Astronomical Society of the Pacific Conference Series, Vol. 183, High Resolution Information on Granulation from Full Disk Fe Line Asymmetry, ed. T. R. Rimmele, K. S. Balasubramaniam, & R. R. Radick, 494

Lodieu, N., Paunzen, E., & Zejda, M. 2020, Reviews in Frontiers of Modern Astrophysics, 213–243

Löhner-Böttcher, J., Schmidt, W., Schlichenmaier, R., et al. 2018, A&A, 617, A19

López-Morales, M. 2007, ApJ, 660, 732

López-Santiago, J., Micela, G., & Montes, D. 2009, A&A, 499, 129

Lowrance, P. J., Becklin, E. E., Schneider, G., et al. 2005, AJ, 130, 1845

Lucy, L. B. 2006, A&A, 457, 629

Ludwig, H. G., Caffau, E., Steffen, M., et al. 2009, Mem. Soc. Astron. Italiana, 80, 711

Luque, R., Nowak, G., Pallé, E., et al. 2018, A&A, 620, A171

Luque, R., Pallé, E., Kossakowski, D., et al. 2019, A&A, 628, A39

Luyten, W. J. 1955, Luyten's Five Tenths.

Luyten, W. J. 1979, NLTT catalogue. Volume_I. +90__to_+30_. Volume._II. +30__to_0_.

Maanen, A. V. 1945, Publications of the Astronomical Society of the Pacific, 57, 216

Macintosh, B., Graham, J. R., Ingraham, P., et al. 2014, Proceedings of the National Academy of Science, 111, 12661

Makarov, V. V. & Kaplan, G. H. 2005, AJ, 129, 2420

Maldonado, J. & Villaver, E. 2017, A&A, 602, A38

Malkov, O. Y. 2007, MNRAS, 382, 1073

Mallonn, M., Herrero, E., Juvan, I. G., et al. 2018, A&A, 614, A35

Mann, A. W., Dupuy, T., Kraus, A. L., et al. 2019, ApJ, 871, 63

Marcy, G. W. & Butler, R. P. 1998, ARA&A, 36, 57

Marcy, G. W. & Butler, R. P. 2000, PASP, 112, 137

Marigo, P., Girardi, L., Chiosi, C., & Wood, P. R. 2001, A&A, 371, 152

Matzner, C. D. & Levin, Y. 2005, ApJ, 628, 817

Mayor, M., Pepe, F., Queloz, D., et al. 2003, The Messenger, 114, 20

Mayor, M. & Queloz, D. 1995, Nature, 378, 355

Mazeh, T. 2008, in EAS Publications Series, ed. M. J. Goupil & J. P. Zahn, Vol. 29, 1–65

Mazeh, T. & Shaham, J. 1979, A&A, 77, 145

McCarthy, C. & Zuckerman, B. 2004, AJ, 127, 2871

McCully, C., Volgenau, N. H., Harbeck, D.-R., et al. 2018, in Society of Photo-Optical Instrumentation Engineers (SPIE) Conference Series, Vol. 10707, Software and Cyberinfrastructure for Astronomy V, 107070K

McQuillan, A., Aigrain, S., & Roberts, S. 2012, A&A, 539, A137

Messina, S., Guinan, E. F., Lanza, A. F., & Ambruster, C. 1999, A&A, 347, 249

Mestel, L. & Spruit, H. C. 1987, MNRAS, 226, 57

Metchev, S. A. & Hillenbrand, L. A. 2009, ApJS, 181, 62

Meunier, N., Desort, M., & Lagrange, A. M. 2010, A&A, 512, A39

Meunier, N., Mignon, L., & Lagrange, A. M. 2017, A&A, 607, A124

Mikulášek, Z., Chrastina, M., Liška, J., et al. 2014, Contributions of the Astronomical Observatory Skalnate Pleso, 43, 382

Milone, E. F., Kurpińska-Winiarska, M., & Oblak, E. 2010, AJ, 140, 129

Moffat, J. W. 1986, Canadian Journal of Physics, 64, 178

Montes, D., González-Peinado, R., Tabernero, H. M., et al. 2018, MNRAS, 479, 1332

Montes, D., López-Santiago, J., Gálvez, M. C., et al. 2001, MNRAS, 328, 45

Morales, J. C., Gallardo, J., Ribas, I., et al. 2010, ApJ, 718, 502

Morales, J. C., Mustill, A. J., Ribas, I., et al. 2019, Science, 365, 1441

Morales, J. C., Ribas, I., & Jordi, C. 2008, A&A, 478, 507

Morin, J., Donati, J. F., Petit, P., et al. 2008, MNRAS, 390, 567

Mortier, A., Bonomo, A. S., Rajpaul, V. M., et al. 2018, MNRAS, 481, 1839

Motch, C., Guillout, P., Haberl, F., et al. 1998, A&AS, 132, 341

Nagel, E., Czesla, S., Schmitt, J. H. M. M., et al. 2019, A&A, 622, A153

Naoz, S. 2016, ARA&A, 54, 441

Nebot Gómez-Morán, A., Gänsicke, B. T., Schreiber, M. R., et al. 2011, A&A, 536, A43

Nelson, R. H. 2003, Information Bulletin on Variable Stars, 5371, 1

Nesvorný, D., Kipping, D. M., Buchhave, L. A., et al. 2012, Science, 336, 1133

Newton, E. R., Irwin, J., Charbonneau, D., et al. 2016, ApJ, 821, 93

Newton, E. R., Mondrik, N., Irwin, J., Winters, J. G., & Charbonneau, D. 2018, AJ, 156, 217

Nortmann, L., Pallé, E., Salz, M., et al. 2018, Science, 362, 1388

Norton, A. J., Wheatley, P. J., West, R. G., et al. 2007, A&A, 467, 785

Nowak, G., Luque, R., Parviainen, H., et al. 2020, A&A, 642, A173

Núñez, A. & Agüeros, M. A. 2016, ApJ, 830, 44

Ondra, L. 2004, S&T, 108, 72

Oshagh, M., Santos, N. C., Figueira, P., et al. 2017, A&A, 606, A107

Osvalds, V. 1957, AJ, 62, 274

Panagi, P. M. & Mathioudakis, M. 1993, A&AS, 100, 343

Passegger, V. M., Bello-García, A., Ordieres-Meré, J., et al. 2020, A&A, 642, A22

Passegger, V. M., Reiners, A., Jeffers, S. V., et al. 2018, A&A, 615, A6

Passegger, V. M., Schweitzer, A., Shulyak, D., et al. 2019, A&A, 627, A161

Patten, B. M. & Simon, T. 1996, ApJS, 106, 489

Pavlovski, K. & Hensberge, H. 2010, in Astronomical Society of the Pacific Conference Series, Vol. 435, Binaries - Key to Comprehension of the Universe, ed. A. Prša & M. Zejda, 207

Paxton, B., Bildsten, L., Dotter, A., et al. 2011, ApJS, 192, 3

Paxton, B., Cantiello, M., Arras, P., et al. 2013, ApJS, 208, 4

Paxton, B., Marchant, P., Schwab, J., et al. 2015, ApJS, 220, 15

Pepe, F., Lovis, C., Ségransan, D., et al. 2011, A&A, 534, A58

Perger, M., Anglada-Escudé, G., Ribas, I., et al. 2021a, A&A, 645, A58

Perger, M., García-Piquer, A., Ribas, I., et al. 2017, A&A, 598, A26

Perger, M., Ribas, I., Anglada-Escudé, G., et al. 2021b, A&A, 649, L12

Perger, M., Scandariato, G., Ribas, I., et al. 2019, A&A, 624, A123

Perryman, M. 2018, The Exoplanet Handbook, 2nd edn. (Cambridge University Press)

Perryman, M., Hartman, J., Bakos, G. Á., & Lindegren, L. 2014, ApJ, 797, 14

Perryman, M. A. C., Lindegren, L., Kovalevsky, J., et al. 1997, A&A, 500, 501

Pettersen, B. R. 1980, A&A, 82, 53

Pettersen, B. R., Kern, G. A., & Evans, D. S. 1983, A&A, 123, 184

Pojmanski, G. 1997, Acta Astron., 47, 467

Pollacco, D. L., Skillen, I., Collier Cameron, A., et al. 2006, PASP, 118, 1407

Pols, O. R., Tout, C. A., Schroder, K.-P., Eggleton, P. P., & Manners, J. 1997, MNRAS, 289, 869

Popper, D. M., Lacy, C. H., Frueh, M. L., & Turner, A. E. 1986, AJ, 91, 383

Pounds, K. A., Allan, D. J., Barber, C., et al. 1993, MNRAS, 260, 77

Pourbaix, D., Tokovinin, A. A., Batten, A. H., et al. 2004, A&A, 424, 727

Poveda, A., Allen, C., Costero, R., Echevarría, J., & Hernández-Alcántara, A. 2009, ApJ, 706, 343

Queloz, D. 1995, in New Developments in Array Technology and Applications, ed. A. G. D. Philip, K. Janes, & A. R. Upgren, Vol. 167, 221

Queloz, D., Bouchy, F., Moutou, C., et al. 2009, A&A, 506, 303

Queloz, D., Henry, G. W., Sivan, J. P., et al. 2001, A&A, 379, 279

Quirrenbach, A., Amado, P. J., Caballero, J. A., et al. 2014, in Proc. SPIE, Vol. 9147, Ground-based and Airborne Instrumentation for Astronomy V, 91471F

Quirrenbach, A., Amado, P. J., Caballero, J. A., et al. 2016, in Proc. SPIE, Vol. 9908, Ground-based and Airborne Instrumentation for Astronomy VI, 990812

Quirrenbach, A., Amado, P. J., Ribas, I., et al. 2018, in Society of Photo-Optical Instrumentation Engineers (SPIE) Conference Series, Vol. 10702, Ground-based and Airborne Instrumentation for Astronomy VII, ed. C. J. Evans, L. Simard, & H. Takami, 107020W

Quirrenbach, A., CARMENES Consortium, Amado, P. J., et al. 2020, in Society of Photo-Optical Instrumentation Engineers (SPIE) Conference Series, Vol. 11447, Society of Photo-Optical Instrumentation Engineers (SPIE) Conference Series, 114473C

Quirrenbach, A., Trifonov, T., Lee, M. H., & Reffert, S. 2019, A&A, 624, A18

Raghavan, D., McAlister, H. A., Henry, T. J., et al. 2010, ApJS, 190, 1

Rajpaul, V., Aigrain, S., Osborne, M. A., Reece, S., & Roberts, S. 2015, MNRAS, 452, 2269

Rajpaul, V. M., Aigrain, S., & Buchhave, L. A. 2020, MNRAS, 492, 3960

Rasmussen, C. E. & Williams, C. K. I. 2005, Gaussian Processes for Machine Learning (Adaptive Computation and Machine Learning) (The MIT Press)

Rauw, G., Rosu, S., Noels, A., et al. 2016, A&A, 594, A33

Rebassa-Mansergas, A., Nebot Gómez-Morán, A., Schreiber, M. R., Girven, J., & Gänsicke, B. T. 2011, MNRAS, 413, 1121

Rebassa-Mansergas, A., Parsons, S. G., Dhillon, V. S., et al. 2019, Nature Astronomy, 3, 553

Rebassa-Mansergas, A., Ren, J. J., Parsons, S. G., et al. 2016, MNRAS, 458, 3808

Rebull, L. M., Stauffer, J. R., Bouvier, J., et al. 2016, AJ, 152, 113

Reffert, S. & Quirrenbach, A. 2011, A&A, 527, A140

Reid, I. N. & Gizis, J. E. 1997, AJ, 114, 1992

Reid, I. N. & Hawley, S. L. 2005, New light on dark stars : red dwarfs, low-mass stars, brown dwarfs

Reid, I. N., Hawley, S. L., & Gizis, J. E. 1995, AJ, 110, 1838

Reiners, A. & Basri, G. 2007, ApJ, 656, 1121

Reiners, A., Bean, J. L., Huber, K. F., et al. 2010, ApJ, 710, 432

Reiners, A., Joshi, N., & Goldman, B. 2012, AJ, 143, 93

Reiners, A., Ribas, I., Zechmeister, M., et al. 2018a, A&A, 609, L5

Reiners, A., Shulyak, D., Anglada-Escudé, G., et al. 2013, A&A, 552, A103

Reiners, A., Zechmeister, M., Caballero, J. A., et al. 2018b, A&A, 612, A49

Ren, J. J., Rebassa-Mansergas, A., Parsons, S. G., et al. 2018, MNRAS, 477, 4641

Ribas, I., Jordi, C., & Giménez, Á. 2000, MNRAS, 318, L55

Ribas, I., Tuomi, M., Reiners, A., et al. 2018, Nature, 563, 365

Ricker, G. R., Winn, J. N., Vanderspek, R., et al. 2015, Journal of Astronomical Telescopes, Instruments, and Systems, 1, 014003

Roberts, S., Osborne, M., Ebden, M., et al. 2012, Philosophical Transactions of the Royal Society of London Series A, 371, 20110550

Robertson, P., Endl, M., Henry, G. W., et al. 2015, ApJ, 801, 79

Robertson, P., Mahadevan, S., Endl, M., & Roy, A. 2014, Science, 345, 440

Rodríguez, E., García, J. M., Costa, V., et al. 2010, MNRAS, 408, 2149

Rodríguez-López, C. 2019, Frontiers in Astronomy and Space Sciences, 6, 76

Rodríguez Martínez, R., Lopez, L. A., Shappee, B. J., et al. 2020, ApJ, 892, 144

Rojas-Ayala, B., Covey, K. R., Muirhead, P. S., & Lloyd, J. P. 2012, ApJ, 748, 93

Rosich, A., Herrero, E., Mallonn, M., et al. 2020, A&A, 641, A82

Ross, F. E. 1939, AJ, 48, 163

Rosu, S., Noels, A., Dupret, M. A., et al. 2020, A&A, 642, A221

Rousset, G., Lacombe, F., Puget, P., et al. 2003, in Society of Photo-Optical Instrumentation Engineers (SPIE) Conference Series, Vol. 4839, Proc. SPIE, ed. P. L. Wizinowich & D. Bonaccini, 140–149

Rutten, R. G. M., Schrijver, C. J., Zwaan, C., Duncan, D. K., & Mewe, R. 1989, A&A, 219, 239

Saar, S. H. & Donahue, R. A. 1997, ApJ, 485, 319

Sandberg Lacy, C. H. & Fekel, F. C. 2014, AJ, 148, 71

Sandberg Lacy, C. H., Zakirov, M., Arzumanyants, G., et al. 1995, IBVS, 4194, 1

Santos, N. C., Mortier, A., Faria, J. P., et al. 2014, A&A, 566, A35

Sanwal, B. B. 1976, Information Bulletin on Variable Stars, 1180, 1

Schäfer, S., Guenther, E. W., Reiners, A., et al. 2018, in Society of Photo-Optical Instrumentation Engineers (SPIE) Conference Series, Vol. 10702, Ground-based and Airborne Instrumentation for Astronomy VII, ed. C. J. Evans, L. Simard, & H. Takami, 1070276

Schmitt, J. H. M. M., Schröder, K. P., Rauw, G., et al. 2016, A&A, 586, A104

Schneider, A., Melis, C., Song, I., & Zuckerman, B. 2011, ApJ, 743, 109

Schneider, A. C., Shkolnik, E. L., Allers, K. N., et al. 2019, AJ, 157, 234

Schöfer, P., Jeffers, S. V., Reiners, A., et al. 2019, A&A, 623, A44

Schönfeld, E. 1886, Eds Marcus and Weber's Verlag, 0

Schrijver, C. J. & Zwaan, C. 2000, Solar and Stellar Magnetic Activity

Schweitzer, A., Passegger, V. M., Cifuentes, C., et al. 2019, A&A, 625, A68

Serenelli, A., Weiss, A., Aerts, C., et al. 2020, arXiv e-prints, arXiv:2006.10868

Shakura, N. I. 1985, Soviet Astronomy Letters, 11, 224

Shao, L., Caballero, R. N., Kramer, M., et al. 2013, Classical and Quantum Gravity, 30, 165019

Shields, A. L., Ballard, S., & Johnson, J. A. 2016, Phys. Rep., 663, 1

Shkolnik, E., Liu, M. C., & Reid, I. N. 2009, ApJ, 699, 649

Shulyak, D., Reiners, A., Nagel, E., et al. 2019, A&A, 626, A86

Simon, K. P. & Sturm, E. 1994, A&A, 281, 286

Simon, M. & Obbie, R. C. 2009, AJ, 137, 3442

Skinner, J. N., Morgan, D. P., West, A. A., Lépine, S., & Thorstensen, J. R. 2017, AJ, 154, 118

Skrutskie, M. F., Cutri, R. M., Stiening, R., et al. 2006, AJ, 131, 1163

Smith, A. B. & Caton, D. B. 2007, IBVS, 5745, 1

Smith, J. C., Stumpe, M. C., Van Cleve, J. E., et al. 2012, PASP, 124, 1000

Soderblom, D. R. & Mayor, M. 1993, AJ, 105, 226

Soto, M. G., Anglada-Escudé, G., Dreizler, S., et al. 2021, A&A, 649, A144

Southworth, J. 2015, in Astronomical Society of the Pacific Conference Series, Vol. 496, Living Together: Planets, Host Stars and Binaries, ed. S. M. Rucinski, G. Torres, & M. Zejda, 164

Sowell, J. R., Henry, G. W., & Fekel, F. C. 2012, AJ, 143, 5

Spada, F., Demarque, P., Kim, Y. C., & Sills, A. 2013, ApJ, 776, 87

Sperauskas, J., Deveikis, V., & Tokovinin, A. 2019, A&A, 626, A31

Stauffer, J. R. & Hartmann, L. W. 1986, ApJS, 61, 531

Stauffer, J. R., Schultz, G., & Kirkpatrick, J. D. 1998, ApJ, 499, L199

Stein, R. F., Brandenburg, A., & Nordlund, A. 1992, Astronomical Society of the Pacific Conference Series, Vol. 26, Magnet Convection (Invited Review), ed. M. S. Giampapa & J. A. Bookbinder, 148

Stephenson, C. B. 1986, AJ, 92, 139

Sterne, T. E. 1939, MNRAS, 99, 662

Stock, S., Kemmer, J., Reffert, S., et al. 2020, A&A, 636, A119

Strassmeier, K. G. 2009, A&A Rev., 17, 251

Struve, O. 1952, The Observatory, 72, 199

Stumpe, M. C., Smith, J. C., Catanzarite, J. H., et al. 2014, PASP, 126, 100

Stumpe, M. C., Smith, J. C., Van Cleve, J. E., et al. 2012, PASP, 124, 985

Suárez Mascareño, A., Rebolo, R., & González Hernández, J. I. 2016, A&A, 595, A12

Suárez Mascareño, A., Rebolo, R., González Hernández, J. I., et al. 2018, A&A, 612, A89

Tabernero, H. M., Montes, D., González Hernández, J. I., & Ammler-von Eiff, M. 2017, A&A, 597, A33

Tal-Or, L., Mazeh, T., Alonso, R., et al. 2013, A&A, 553, A30

Tal-Or, L., Trifonov, T., Zucker, S., Mazeh, T., & Zechmeister, M. 2019, MNRAS, 484, L8

Tal-Or, L., Zechmeister, M., Reiners, A., et al. 2018, A&A, 614, A122

Terndrup, D. M., Stauffer, J. R., Pinsonneault, M. H., et al. 2000, AJ, 119, 1303

Title, A. M., Tarbell, T. D., & Topka, K. P. 1987, ApJ, 317, 892

Tkachenko, A., Pavlovski, K., Johnston, C., et al. 2020, A&A, 637, A60

Tody, D. 1986, in Society of Photo-Optical Instrumentation Engineers (SPIE) Conference Series, Vol. 627, Instrumentation in astronomy VI, ed. D. L. Crawford, 733

Tody, D. 1993, in Astronomical Society of the Pacific Conference Series, Vol. 52, Astronomical Data Analysis Software and Systems II, ed. R. J. Hanisch, R. J. V. Brissenden, & J. Barnes, 173

Tohline, J. E. 2002, ARA&A, 40, 349

Tokovinin, A., Thomas, S., Sterzik, M., & Udry, S. 2006, A&A, 450, 681

Tokovinin, A. A. 1990, Pisma v Astronomicheskii Zhurnal, 16, 52

Toledo-Padrón, B., Suárez Mascareño, A., González Hernández, J. I., et al. 2021, A&A, 648, A20

Tomkin, J. & Fekel, F. C. 2006, AJ, 131, 2652

Toonen, S., Portegies Zwart, S., Hamers, A. S., & Bandopadhyay, D. 2020, A&A, 640, A16

Torres, G., Andersen, J., & Giménez, A. 2010, A&A Rev., 18, 67

Torres, G., Lacy, C. H. S., Claret, A., & Sabby, J. A. 2000, AJ, 120, 3226

Torres, G., McGruder, C. D., Siverd, R. J., et al. 2017, ApJ, 836, 177

Torres, G. & Ribas, I. 2002, ApJ, 567, 1140

Torres, G., Sandberg Lacy, C. H., & Claret, A. 2009, AJ, 138, 1622

Torres, G., Sandberg Lacy, C. H., Pavlovski, K., et al. 2014, ApJ, 797, 31

Torres, G., Sandberg Lacy, C. H., Pavlovski, K., Fekel, F. C., & Muterspaugh, M. W. 2015, AJ, 150, 154

Trifonov, T., Caballero, J. A., Morales, J. C., et al. 2021, Science, 371, 1038

Trifonov, T., Kürster, M., Zechmeister, M., et al. 2018, A&A, 609, A117

Trotta, R. 2008, Contemporary Physics, 49, 71

Tuomi, M., Anglada-Escudé, G., Gerlach, E., et al. 2013, A&A, 549, A48

van den Berk, J., Portegies Zwart, S. F., & McMillan, S. L. W. 2007, MNRAS, 379, 111

van Leeuwen, F. 2007, A&A, 474, 653

Verma, A. K., Fienga, A., Laskar, J., Manche, H., & Gastineau, M. 2014, A&A, 561, A115

Vernet, J., Dekker, H., D'Odorico, S., et al. 2011, A&A, 536, A105

Voges, W., Aschenbach, B., Boller, T., et al. 1999, A&A, 349, 389

Vogt, S. S., Allen, S. L., Bigelow, B. C., et al. 1994, in Society of Photo-Optical Instrumentation Engineers (SPIE) Conference Series, Vol. 2198, Instrumentation in Astronomy VIII, ed. D. L. Crawford & E. R. Craine, 362

Vogt, S. S. & Penrod, G. D. 1983, PASP, 95, 565

Volkov, I. M. & Khaliullin, K. F. 1999, IBVS, 4680, 1

Vrijmoet, E. H., Henry, T. J., Jao, W.-C., & Dieterich, S. B. 2020, AJ, 160, 215

Wachmann, A. A. 1939, Beob. Zirk, 21, 25

Wagner, K., Apai, D., Kasper, M., et al. 2020, ApJ, 902, L6

Wang, H. & Li, J. 2017, arXiv e-prints, arXiv:1703.09930

Weis, E. W. 1991, AJ, 101, 1882

West, A. A., Hawley, S. L., Bochanski, J. J., et al. 2008, AJ, 135, 785

West, A. A., Hawley, S. L., Walkowicz, L. M., et al. 2004, AJ, 128, 426

Wilks, S. S. 1938, Annals Math. Statist., 9, 60

Will, C. M. 2014, Living Reviews in Relativity, 17, 4

Wilson, O. C. 1968, ApJ, 153, 221

Wilson, R. E. 1953, Carnegie Institute Washington D.C. Publication

Winters, J. G., Charbonneau, D., Henry, T. J., et al. 2021, AJ, 161, 63

Winters, J. G., Henry, T. J., Jao, W.-C., et al. 2019, AJ, 157, 216

Winters, J. G., Irwin, J. M., Charbonneau, D., et al. 2020, AJ, 159, 290

Wizinowich, P. L., Le Mignant, D., Bouchez, A. H., et al. 2006, PASP, 118, 297

Wolf, M., Claret, A., Kotková, L., et al. 2010, A&A, 509, A18

Wolf, M., Kučáková, H., Kolasa, M., et al. 2006, A&A, 456, 1077

Wolf, M., Sarounova, L., Kozyreva, V. S., & Pogrocheva, T. 1997, Information Bulletin on Variable Stars, 4542, 1

Wolszczan, A. & Frail, D. A. 1992, Nature, 355, 145

Woźniak, P. R., Vestrand, W. T., Akerlof, C. W., et al. 2004, AJ, 127, 2436

Wright, J. T., Marcy, G. W., Butler, R. P., & Vogt, S. S. 2004, ApJS, 152, 261

Wright, N. J., Newton, E. R., Williams, P. K. G., Drake, J. J., & Yadav, R. K. 2018, MNRAS, 479, 2351

Yan, F., Casasayas-Barris, N., Molaverdikhani, K., et al. 2019, A&A, 632, A69

Zacharias, N., Finch, C. T., Girard, T. M., et al. 2013, AJ, 145, 44

Zahn, J. P. & Bouchet, L. 1989, A&A, 223, 112

Zapatero Osorio, M. R., Béjar, V. J. S., Martín, E. L., et al. 2014, A&A, 572, A67

Zasche, P. & Wolf, M. 2019, AJ, 157, 87

Zboril, M. 2003, Astronomische Nachrichten, 324, 527

Zechmeister, M., Dreizler, S., Ribas, I., et al. 2019, A&A, 627, A49

Zechmeister, M., Kürster, M., & Endl, M. 2009, A&A, 505, 859

Zechmeister, M., Reiners, A., Amado, P. J., et al. 2018, A&A, 609, A12

Zhilyaev, B. E., Tsap, Y. T., Andreev, M. V., et al. 2011, Kinematics and Physics of Celestial Bodies, 27, 154

Zsom, A., Seager, S., de Wit, J., & Stamenković, V. 2013, ApJ, 778, 109

Zucker, S. & Mazeh, T. 1994, ApJ, 420, 806

Zucker, S., Mazeh, T., & Alexander, T. 2007, ApJ, 670, 1326

Zucker, S., Mazeh, T., Santos, N. C., Udry, S., & Mayor, M. 2003, A&A, 404, 775

Appendix A

Data tables

We provide here a list of all the planets discovered with CARMENES, their basic properties, and mass of their host stars (Table A.1), as well as the timeseries data used in Chapters 2, 3, 4, and 5. This includes the CARMENES radial velocity and chromatic index timeseries of YZ CMi (Table A.2), as well as its photometric data from the TJO telescope (Table A.3). The radial velocities of LSPM J2116+0234 and GJ 686 are provided in Tables A.4 and A.5. The different instruments used are indicated in the third column.

The radial velocity curves of the spectroscopic multiples described in Chapter 4 are provided in Tables A.6 to A.8. The instruments from which the radial velocities are computed are labeled in the third column as C (CARMENES), H (HARPS), F (FEROS), T (TRES), U (UVES), HN (HARPS-N), CO (CORAVEL), and CF (CAFE). The method used to obtain the radial velocities of SB1s is indicated in the fourth column of Table A.6 as S (`serval`) and T (`todmor`).

Finally, in Table A.9 we provide all the times of minimum light of the eclipsing binaries in Chapter 5. The type of eclipse, primary (1) or secondary (2) are labeled in the third column, while the fourth and fifth columns list the bisector indices, which measure the asymmetry of the eclipses.

Table A.1: CARMENES published exoplanet discoveries and its main properties.

Karmn	$M_\star$ [M$_\odot$]	P [d]	$M_p \sin i$ [M$_\oplus$]	Ref.
J00183+440 c	0.414 ± 0.012	7030^{+970}_{-630}	$51.8^{+5.5}_{-5.8}$	Trifonov et al. (2018)
J11417+427 c	0.357 ± 0.013	$532.6^{+4.1}_{-2.5}$	$68.1^{+4.9}_{-2.2}$	Trifonov et al. (2018)
J16167+672S b	0.58 ± 0.08	86.54 ± 0.06	25 ± 2	Reiners et al. (2018a)
J17578+046 b	0.163 ± 0.022	$232.80^{+0.38}_{-0.41}$	3.23 ± 0.44	Ribas et al. (2018)
J19169+051N b	0.45 ± 0.04	$105.90^{+0.09}_{-0.10}$	$12.2^{+1.0}_{-1.4}$	Kaminski et al. (2018)
J13229+244 b	0.27 ± 0.02	3.023 ± 0.001	8.0 ± 0.5	Luque et al. (2018)
J22137−176 b	0.178 ± 0.018	3.651 ± 0.001	7.4 ± 0.5	Luque et al. (2018)
J22252+594 b	0.406 ± 0.030	13.352 ± 0.003	$16.57^{+0.94}_{-0.95}$	Nagel et al. (2019)
J01026+623 b	0.515 ± 0.019	$13.8508^{+0.0053}_{-0.0051}$	$5.63^{+0.67}_{-0.68}$	Perger et al. (2019)
J02530+168 b	0.089 ± 0.009	4.9100 ± 0.0014	$1.05^{+0.13}_{-0.12}$	Zechmeister et al. (2019)
J02530+168 c		11.409 ± 0.009	$1.11^{+0.16}_{-0.15}$	Zechmeister et al. (2019)
J09360−216 b	0.342 ± 0.011	$3.93073^{+0.00008}_{-0.00006}$	1.84 ± 0.31	Luque et al. (2019)
J09360−216 c		$9.1247^{+0.0011}_{-0.0010}$	3.40 ± 0.46	Luque et al. (2019)
J09360−216 d		55.661 ± 0.055	6.1 ± 1.0	Luque et al. (2019)
J08413+594 b	0.123 ± 0.009	203.59 ± 0.14	$147.1^{+7.0}_{-7.3}$	Morales et al. (2019)
J08413+594 c		> 1390	> 54	Morales et al. (2019)
J09144+526 b	0.64 ± 0.07	24.45 ± 0.02	$10.3^{+1.5}_{-1.4}$	González-Álvarez et al. (2020)
J10088+692 b	0.630 ± 0.024	$3.444717^{+0.000040}_{-0.000042}$	$5.90^{+0.62}_{-0.61}$	Bluhm et al. (2020)
J03133+047 b	0.161 ± 0.010	2.29070 ± 0.00012	$3.95^{+0.42}_{-0.43}$	Bauer et al. (2020)
J10185−117 b	0.379 ± 0.016	0.768377 ± 0.000014	$2.34^{+0.24}_{-0.23}$	Nowak et al. (2020)
J10185−117 c		$12.252131^{+0.000072}_{-0.000064}$	$6.29^{+0.63}_{-0.61}$	Nowak et al. (2020)
J08023+033 b	0.360 ± 0.016	$1.1980035^{+0.0000018}_{-0.0000019}$	$1.86^{+0.30}_{-0.30}$	Kemmer et al. (2020)
J08023+033 c		15.505 ± 0.033	$7.41^{+0.91}_{-0.86}$	Kemmer et al. (2020)
J06548+332 b	0.360 ± 0.015	14.238 ± 0.002	4.00 ± 0.40	Stock et al. (2020)
J12123+544S b	0.578 ± 0.021	$13.671^{+0.011}_{-0.010}$	2.69 ± 0.25	Stock et al. (2020)
J04167−120 b	0.59 ± 0.02	4.052037 ± 0.000004	30.8 ± 1.5	Dreizler et al. (2020)
J12479+097 b	0.323 ± 0.015	$1.467119^{+0.000031}_{-0.000030}$	$2.82^{+0.11}_{-0.12}$	Trifonov et al. (2021)
J18580+059 b	0.58 ± 0.06	$2.37756^{+0.00013}_{-0.00011}$	$2.96^{+0.50}_{-0.48}$	Toledo-Padrón et al. (2021)
J02573+765 b	0.236 ± 0.012	$1.9495378^{+0.0000040}_{-0.0000041}$	2.33 ± 0.20	Soto et al. (2021)

Table A.2: Radial velocity and chromatic index timeseries from CARMENES for YZ CMi.

BJD [d]	RV [m s^{-1}]	CRX [m s^{-1} Np^{-1}]
2457655.71	163.5 ± 4.6	−179 ± 41
2457673.66	157.8 ± 2.8	−27 ± 29
2457689.73	36.6 ± 8.7	448 ± 51
2457692.72	77.2 ± 5.3	234 ± 41
2457699.65	275.4 ± 7.6	−369 ± 54
2457704.60	231.2 ± 3.9	−164 ± 32
2457735.61	310.0 ± 8.1	−411 ± 53
2457755.69	158.6 ± 3.8	−119 ± 37
2457756.56	59.9 ± 6.6	327 ± 45
2457760.50	301.9 ± 7.6	−384 ± 51
2457761.41	89.9 ± 4.1	172 ± 35
2457762.62	201.9 ± 2.8	−80 ± 26
2457763.53	284.4 ± 7.9	−412 ± 49
2457779.46	216.7 ± 3.7	−156 ± 30
2457786.49	58.7 ± 6.1	276 ± 45
2457788.48	314.0 ± 9.1	−472 ± 54
2457790.49	203.2 ± 4.1	−65 ± 41
2457798.48	134.2 ± 3.3	138 ± 26
2457800.41	49.4 ± 7.7	392 ± 45
2457815.36	193.0 ± 1.6	−27 ± 16
2457822.36	151.6 ± 2.9	−74 ± 26
2457830.42	229.2 ± 7.4	−393 ± 44
2457849.36	294.8 ± 8.6	−441 ± 56
2457852.42	274.3 ± 7.7	−380 ± 57
2457856.34	11.7 ± 8.4	416 ± 50
2457863.38	303.4 ± 8.9	−441 ± 60
2457875.36	36.7 ± 7.1	371 ± 44

Table A.3: Normalised flux of the YZ CMi TJO photometric observations.

BJD [d]	Norm. flux
2457688.643	0.9808 ± 0.0005
2457689.639	0.9827 ± 0.0005
2457692.617	1.0003 ± 0.0006
2457693.567	1.0348 ± 0.0005
2457693.651	1.0383 ± 0.0005
2457694.569	0.9655 ± 0.0007
2457694.654	0.9539 ± 0.0005
2457695.572	1.0207 ± 0.0009
2457695.573	1.0224 ± 0.0011
2457696.561	1.0122 ± 0.0006
2457696.646	0.9997 ± 0.0006
2457699.646	0.9854 ± 0.0005
2457700.567	0.9615 ± 0.0005
2457702.543	0.9833 ± 0.0005
2457708.527	0.9572 ± 0.0007
2457708.609	0.9489 ± 0.0004
2457723.526	1.0393 ± 0.0005
2457723.624	1.0371 ± 0.0005
2457724.593	0.9967 ± 0.0011
2457724.594	0.9930 ± 0.0005
2457725.570	0.9730 ± 0.0010
2457729.620	1.0390 ± 0.0012
2457730.468	0.9833 ± 0.0006
2457730.469	0.9769 ± 0.0012
2457731.467	1.0149 ± 0.0006
2457734.495	1.0202 ± 0.0007
2457734.562	1.0188 ± 0.0007
2457734.577	1.0327 ± 0.0008
2457735.456	1.0169 ± 0.0008

Table A.3: Continued.

BJD [d]	Norm. flux
2457736.536	0.9608 ± 0.0009
2457741.445	0.9859 ± 0.0005
2457741.536	0.9658 ± 0.0005
2457742.454	0.9954 ± 0.0005
2457742.540	0.9913 ± 0.0005
2457746.518	1.0185 ± 0.0005
2457746.618	1.0133 ± 0.0007
2457748.474	1.0318 ± 0.0005
2457749.447	1.0068 ± 0.0006
2457749.448	1.0096 ± 0.0013
2457750.533	0.9696 ± 0.0005
2457751.530	1.0450 ± 0.0006
2457751.531	1.0458 ± 0.0011
2457752.509	0.9830 ± 0.0006
2457752.510	0.9827 ± 0.0007
2457752.606	0.9746 ± 0.0005
2457753.471	0.9873 ± 0.0008
2457756.641	1.0318 ± 0.0005
2457758.461	0.9522 ± 0.0004
2457758.580	0.9557 ± 0.0006
2457759.423	1.0204 ± 0.0005
2457759.508	1.0228 ± 0.0005
2457759.514	1.0246 ± 0.0005
2457760.396	1.0224 ± 0.0005
2457760.433	1.0126 ± 0.0005
2457760.523	1.0015 ± 0.0009
2457761.394	0.9641 ± 0.0005
2457761.433	0.9624 ± 0.0011
2457762.382	1.0414 ± 0.0006
2457762.576	1.0411 ± 0.0005
2457763.386	0.9999 ± 0.0023
2457764.463	0.9722 ± 0.0006
2457768.459	1.0368 ± 0.0006
2457768.518	1.0264 ± 0.0006
2457768.544	1.0301 ± 0.0006
2457795.429	1.0149 ± 0.0015
2457804.485	1.0538 ± 0.0005
2457805.487	0.9620 ± 0.0005
2457807.390	1.0214 ± 0.0006
2457807.523	1.0124 ± 0.0007
2457809.450	1.0215 ± 0.0005
2457809.541	1.0282 ± 0.0006

Table A.3: Continued.

BJD [d]	Norm. flux
2457811.510	0.9641 ± 0.0012
2457813.405	0.9986 ± 0.0006
2457813.406	0.9975 ± 0.0008
2457819.468	0.9528 ± 0.0009
2457819.469	0.9525 ± 0.0007
2457821.367	1.0319 ± 0.0018
2457821.472	1.0143 ± 0.0022
2457822.389	0.9565 ± 0.0007
2457822.474	0.9583 ± 0.0010
2457827.405	0.9807 ± 0.0010
2457827.406	0.9829 ± 0.0008
2457830.419	0.9633 ± 0.0011
2457830.495	0.9717 ± 0.0006
2457831.419	1.0008 ± 0.0007
2457834.442	1.0279 ± 0.0011
2457836.439	0.9720 ± 0.0005
2457843.422	1.0434 ± 0.0010
2457857.405	1.0412 ± 0.0006

Table A.4: Radial velocities of LSPM J2116+0234 taken with the visible (VIS) and near-infrared (NIR) channels of CARMENES, respectively.

Table A.4: Continued.

BJD	RV [m s^{-1}]	Instrument
2457569.6343	−4.5 ± 3.1	VIS
2457584.6238	−5.4 ± 2.0	VIS
2457593.5656	−2.0 ± 1.5	VIS
2457608.5403	−3.0 ± 1.7	VIS
2457617.4723	9.2 ± 2.0	VIS
2457642.4415	−0.2 ± 1.5	VIS
2457647.4678	8.6 ± 2.0	VIS
2457656.4893	−2.6 ± 1.5	VIS
2457676.3731	8.2 ± 3.8	VIS
2457692.3963	−2.2 ± 1.2	VIS
2457956.5192	−9.2 ± 1.6	VIS
2457964.5477	5.7 ± 1.2	VIS
2457971.5638	−5.9 ± 1.3	VIS
2458026.3482	−8.8 ± 1.4	VIS
2458029.3943	−8.2 ± 1.5	VIS
2458032.3674	−3.0 ± 1.7	VIS
2458035.3033	−23.4 ± 1.8	VIS
2458043.4478	−17.0 ± 3.7	VIS
2458051.2827	4.2 ± 1.5	VIS
2458056.3121	−4.6 ± 1.1	VIS
2458065.3847	2.3 ± 1.2	VIS
2458244.6746	−5.3 ± 1.6	VIS
2458289.6052	−8.8 ± 1.4	VIS
2458291.5338	−4.0 ± 2.2	VIS
2458301.5964	−1.8 ± 1.3	VIS
2458303.5436	−0.8 ± 2.9	VIS
2458309.5685	9.7 ± 1.6	VIS
2458316.5615	−1.1 ± 1.3	VIS
2458322.5278	1.2 ± 1.2	VIS
2458324.5343	7.1 ± 1.4	VIS
2458326.5011	2.3 ± 1.3	VIS
2458329.5600	−3.5 ± 1.2	VIS
2458332.5189	−7.4 ± 1.2	VIS
2458334.4985	−5.5 ± 1.5	VIS
2458336.5146	−1.5 ± 1.5	VIS
2458340.4791	6.3 ± 1.4	VIS
2458342.4920	2.9 ± 1.2	VIS
2458345.4765	−1.8 ± 1.2	VIS
2458347.5294	−4.5 ± 2.3	VIS
2458348.4407	−2.6 ± 1.1	VIS
2458350.5604	0.1 ± 1.4	VIS
2458351.6293	3.0 ± 1.7	VIS
2458353.4635	9.7 ± 1.5	VIS
2458355.5027	6.8 ± 1.2	VIS
2458359.4965	−4.4 ± 1.6	VIS
2458361.4594	−8.4 ± 1.4	VIS
2458365.4361	−3.5 ± 1.8	VIS
2458381.4797	2.5 ± 1.1	VIS
2458382.4051	5.4 ± 1.2	VIS
2458383.4060	6.2 ± 1.1	VIS
2458384.3988	3.9 ± 1.2	VIS
2458385.3897	3.6 ± 1.3	VIS
2458386.3893	2.9 ± 1.2	VIS
2458387.3895	0.3 ± 1.6	VIS
2458390.3790	−3.8 ± 1.1	VIS
2458391.3786	−3.6 ± 1.1	VIS
2458392.3467	−3.6 ± 1.1	VIS
2458393.3536	−1.5 ± 1.3	VIS
2458394.4332	2.9 ± 1.8	VIS
2458395.3578	6.5 ± 1.5	VIS
2458396.3535	7.5 ± 1.3	VIS
2458398.3438	9.0 ± 1.3	VIS
2458399.3576	3.2 ± 1.4	VIS
2458405.3408	−6.7 ± 2.2	VIS
2458409.3285	−4.5 ± 1.5	VIS
2458414.4031	−14.5 ± 6.5	VIS
2458415.3673	−4.8 ± 1.6	VIS
2458417.3118	−5.2 ± 1.2	VIS
2458419.3963	−8.0 ± 3.0	VIS
2458421.4244	−3.8 ± 4.3	VIS
2458426.3922	35.1 ± 1.5	VIS
2458427.3437	5.2 ± 1.5	VIS
2458433.3611	−1.8 ± 2.7	VIS
2458434.3013	−3.9 ± 1.4	VIS
2458451.3183	−2.4 ± 1.3	VIS
2458454.3176	3.1 ± 1.7	VIS
2458455.3169	1.6 ± 1.5	VIS
2458467.2784	4.5 ± 2.8	VIS
2458468.2675	1.4 ± 2.2	VIS
2458471.2659	4.9 ± 1.5	VIS
2458477.2560	−2.9 ± 2.5	VIS
2458478.2590	−3.8 ± 1.4	VIS
2458480.2590	−1.8 ± 1.5	VIS
2458605.6666	−0.6 ± 3.5	VIS

Table A.4: Continued.

BJD	RV [m s^{-1}]	Instrument
2457569.6349	95.4 ± 36.9	NIR
2457584.6241	−11.1 ± 9.2	NIR
2457593.5649	9.4 ± 6.0	NIR
2457608.5404	−9.7 ± 5.0	NIR
2457617.4759	10.4 ± 4.2	NIR
2457642.4399	−9.5 ± 7.2	NIR
2457647.4679	−0.9 ± 7.6	NIR
2457656.4877	−1.8 ± 9.3	NIR
2457676.3762	10.2 ± 9.7	NIR
2457692.3962	0.8 ± 3.9	NIR
2457956.5198	−10.3 ± 7.9	NIR
2457964.5477	5.2 ± 9.8	NIR
2457971.5630	−0.3 ± 8.1	NIR
2458026.3464	−3.4 ± 4.7	NIR
2458029.3950	−15.8 ± 5.2	NIR
2458032.3676	−4.4 ± 5.1	NIR
2458035.3040	−5.1 ± 3.7	NIR
2458043.4453	7.6 ± 7.2	NIR
2458051.2821	9.5 ± 6.6	NIR
2458056.3121	−8.0 ± 4.4	NIR
2458065.3839	21.2 ± 9.8	NIR
2458244.6765	−13.0 ± 5.2	NIR
2458289.6053	−12.0 ± 5.2	NIR
2458291.5339	−20.6 ± 7.1	NIR
2458301.5911	27.9 ± 9.3	NIR
2458303.5429	−9.5 ± 10.9	NIR
2458309.5678	18.3 ± 6.7	NIR
2458316.5629	−3.7 ± 5.4	NIR
2458322.5286	9.9 ± 10.9	NIR
2458324.5341	5.5 ± 4.7	NIR
2458326.5007	7.0 ± 3.5	NIR
2458329.5616	−7.6 ± 3.8	NIR
2458332.5178	1.1 ± 5.3	NIR
2458334.4993	0.0 ± 5.3	NIR
2458336.5153	−3.1 ± 5.0	NIR
2458340.4783	4.6 ± 5.1	NIR
2458342.4917	6.6 ± 4.3	NIR
2458345.4762	−0.4 ± 3.9	NIR
2458347.5292	8.0 ± 6.7	NIR
2458348.4416	−6.6 ± 3.9	NIR
2458350.5608	−2.8 ± 4.6	NIR
2458351.6287	8.9 ± 5.3	NIR
2458353.4631	11.2 ± 7.3	NIR

Table A.4: Continued.

BJD	RV [m s^{-1}]	Instrument
2458365.4363	−0.8 ± 7.7	NIR
2458381.4800	0.1 ± 4.7	NIR
2458382.4054	1.0 ± 5.3	NIR
2458383.4060	1.1 ± 4.1	NIR
2458384.3986	−0.8 ± 2.9	NIR
2458385.3896	3.0 ± 4.4	NIR
2458386.3902	5.0 ± 6.1	NIR
2458387.3885	−0.3 ± 6.3	NIR
2458390.3762	−3.6 ± 4.6	NIR
2458391.3799	−13.9 ± 3.5	NIR
2458392.3469	−3.1 ± 5.1	NIR
2458393.3523	−6.5 ± 6.7	NIR
2458394.4350	−15.0 ± 10.6	NIR
2458395.3578	−5.1 ± 6.6	NIR
2458396.3537	4.9 ± 3.8	NIR
2458398.3437	10.7 ± 4.7	NIR
2458399.3569	4.6 ± 5.3	NIR
2458405.3400	−5.5 ± 5.0	NIR
2458409.3289	3.5 ± 7.3	NIR
2458414.4037	−15.8 ± 27.9	NIR
2458415.3674	12.6 ± 10.2	NIR
2458417.3090	8.0 ± 4.5	NIR
2458419.3964	7.9 ± 17.2	NIR
2458421.4242	−10.2 ± 19.2	NIR
2458426.3912	4.0 ± 5.4	NIR
2458427.3410	−3.9 ± 13.7	NIR
2458433.3581	6.0 ± 13.5	NIR
2458434.2986	5.4 ± 4.1	NIR
2458451.3182	1.0 ± 5.2	NIR
2458454.3189	−6.1 ± 8.5	NIR
2458455.3165	0.6 ± 7.6	NIR
2458467.2776	22.4 ± 14.6	NIR
2458468.2675	−4.3 ± 10.8	NIR
2458471.2664	11.6 ± 8.3	NIR
2458477.2560	−9.0 ± 14.7	NIR
2458478.2626	−7.1 ± 9.3	NIR
2458480.2586	−0.7 ± 5.6	NIR
2458605.6661	8.1 ± 29.0	NIR
2458355.5029	7.6 ± 6.1	NIR
2458359.4950	4.9 ± 5.0	NIR
2458361.4596	9.1 ± 10.8	NIR

Table A.5: Radial velocities of GJ 686 taken with HIRES, HARPS, HARPS-N, and the visible channel of the CARMENES spectrographs.

BJD	RV [$\mathrm{m\,s^{-1}}$]	Instrument
2450604.9470	−6.8 ± 1.7	HIRES
2450955.0818	4.3 ± 1.9	HIRES
2450956.9854	−3.8 ± 1.9	HIRES
2450981.8611	2.4 ± 2.0	HIRES
2451050.8022	−4.8 ± 1.9	HIRES
2451313.0310	−1.9 ± 1.7	HIRES
2451367.8307	−4.3 ± 2.2	HIRES
2451410.8169	−2.6 ± 2.0	HIRES
2451703.9460	−2.5 ± 1.9	HIRES
2452004.1131	2.4 ± 1.9	HIRES
2452097.9279	0.8 ± 2.1	HIRES
2452445.9041	9.7 ± 2.0	HIRES
2452446.8876	8.4 ± 2.2	HIRES
2452538.7482	2.0 ± 1.9	HIRES
2452777.9912	−2.9 ± 2.2	HIRES
2452803.9463	−0.0 ± 2.1	HIRES
2452849.8560	3.5 ± 2.2	HIRES
2453180.8524	1.2 ± 1.9	HIRES
2453181.8583	−3.5 ± 1.9	HIRES
2453478.9613	3.7 ± 1.6	HIRES
2453550.9287	−1.2 ± 1.9	HIRES
2453602.8651	−3.8 ± 2.0	HIRES
2453926.9486	−2.8 ± 1.8	HIRES
2453984.8251	−6.4 ± 1.7	HIRES
2454247.0275	−1.2 ± 1.5	HIRES
2454248.0407	2.7 ± 1.8	HIRES
2454249.9630	−3.9 ± 1.7	HIRES
2454251.9845	−3.6 ± 1.8	HIRES
2454255.8363	−0.1 ± 1.7	HIRES
2454255.8422	−2.1 ± 1.6	HIRES
2454277.7856	4.7 ± 1.7	HIRES
2454278.7980	0.7 ± 1.8	HIRES
2454279.7981	−5.8 ± 1.9	HIRES
2454285.8093	−3.2 ± 2.1	HIRES
2454294.9811	−1.6 ± 1.8	HIRES
2454304.9433	2.5 ± 1.9	HIRES
2454305.9445	2.8 ± 1.7	HIRES
2454306.9197	1.4 ± 1.8	HIRES
2454307.9699	2.2 ± 1.6	HIRES
2454308.9402	2.4 ± 1.9	HIRES
2454309.9321	0.6 ± 1.9	HIRES
2454310.9276	−1.3 ± 1.6	HIRES
2454311.9158	1.0 ± 1.9	HIRES
2454312.9226	0.9 ± 1.8	HIRES

Table A.5: Continued.

BJD	RV [$\mathrm{m\,s^{-1}}$]	Instrument
2454313.9200	−1.3 ± 1.7	HIRES
2454314.9628	−1.8 ± 1.8	HIRES
2454335.8435	−0.8 ± 1.7	HIRES
2454335.8636	−0.1 ± 1.7	HIRES
2454343.8038	−8.8 ± 1.7	HIRES
2454396.6967	−1.6 ± 1.8	HIRES
2454397.6978	−1.7 ± 1.8	HIRES
2454633.9259	4.2 ± 2.0	HIRES
2454666.8964	8.3 ± 1.9	HIRES
2454671.8867	−2.1 ± 1.9	HIRES
2454671.8942	−5.1 ± 1.6	HIRES
2454673.9248	−4.5 ± 1.7	HIRES
2454686.9891	5.4 ± 2.1	HIRES
2454701.9167	2.5 ± 2.0	HIRES
2454702.8773	−2.9 ± 2.0	HIRES
2454703.9516	−1.1 ± 2.8	HIRES
2454704.8849	−3.9 ± 1.8	HIRES
2454704.8924	−2.4 ± 1.8	HIRES
2454984.8828	−1.5 ± 1.9	HIRES
2455024.0372	−1.3 ± 2.0	HIRES
2455024.0446	0.3 ± 1.8	HIRES
2455025.0074	−2.2 ± 1.8	HIRES
2455025.0151	−0.2 ± 1.6	HIRES
2455042.8976	4.0 ± 2.0	HIRES
2455052.9485	8.9 ± 1.7	HIRES
2455052.9555	3.3 ± 2.0	HIRES
2455053.8513	5.0 ± 2.1	HIRES
2455053.8578	3.9 ± 1.8	HIRES
2455143.7337	10.3 ± 2.7	HIRES
2455259.0848	0.3 ± 1.9	HIRES
2455259.0972	1.1 ± 1.8	HIRES
2455260.0874	−1.9 ± 1.7	HIRES
2455372.0622	−5.2 ± 1.9	HIRES
2455408.9670	2.8 ± 1.9	HIRES
2455408.9744	5.8 ± 1.9	HIRES
2455409.9415	1.7 ± 1.7	HIRES
2455409.9490	1.2 ± 1.9	HIRES
2455462.8181	−5.5 ± 1.5	HIRES
2455637.1135	0.0 ± 1.8	HIRES
2455638.0598	−0.3 ± 1.7	HIRES
2455638.0673	1.2 ± 1.5	HIRES
2455639.1080	3.8 ± 1.5	HIRES
2455639.1154	6.3 ± 1.7	HIRES
2455664.9911	−2.4 ± 1.8	HIRES
2455664.9986	−3.2 ± 1.6	HIRES
2455670.1260	−0.6 ± 1.7	HIRES

Table A.5: Continued.

BJD	RV [m s^{-1}]	Instrument
2455670.1335	−0.6 ± 1.7	HIRES
2455720.0090	−2.0 ± 2.0	HIRES
2455720.0165	−1.7 ± 1.9	HIRES
2455749.9152	9.1 ± 2.0	HIRES
2455749.9226	10.1 ± 2.1	HIRES
2455824.7659	0.3 ± 1.8	HIRES
2455824.7733	1.7 ± 1.9	HIRES
2455879.7285	3.3 ± 1.9	HIRES
2455971.1533	6.9 ± 2.1	HIRES
2455971.1605	7.2 ± 2.1	HIRES
2456027.0881	7.2 ± 2.0	HIRES
2456116.9645	1.0 ± 2.1	HIRES
2456116.9720	−3.4 ± 2.1	HIRES
2456141.9782	3.1 ± 1.9	HIRES
2456141.9857	8.7 ± 1.9	HIRES
2456168.7913	−0.4 ± 1.9	HIRES
2456329.1408	6.7 ± 1.9	HIRES
2456329.1483	6.6 ± 1.8	HIRES
2456433.0728	3.2 ± 1.7	HIRES
2456433.0802	4.0 ± 1.8	HIRES
2456548.7875	−4.3 ± 1.6	HIRES
2456548.7949	−5.9 ± 1.6	HIRES
2456551.7804	−5.4 ± 1.7	HIRES
2456551.7876	−6.9 ± 1.6	HIRES
2453159.7492	3.62 ± 0.71	HARPS
2453574.6225	0.68 ± 0.69	HARPS
2453817.8682	−1.09 ± 0.64	HARPS
2454174.8713	−1.88 ± 0.65	HARPS
2454194.9076	2.40 ± 0.69	HARPS
2454300.6448	−2.81 ± 0.63	HARPS
2454948.8615	−1.51 ± 0.51	HARPS
2454950.8621	−2.80 ± 0.55	HARPS
2454956.8307	−0.86 ± 0.77	HARPS
2455390.6409	0.91 ± 0.79	HARPS
2455392.6327	1.92 ± 0.55	HARPS
2455407.5859	0.75 ± 0.63	HARPS
2455409.5880	2.10 ± 0.77	HARPS
2455412.5785	0.21 ± 0.84	HARPS
2455437.5293	−3.10 ± 0.59	HARPS
2455438.5335	0.00 ± 0.58	HARPS
2455446.5219	−6.48 ± 0.72	HARPS
2455450.4961	−4.5 ± 1.1	HARPS
2455450.5081	−3.65 ± 0.80	HARPS
2455458.5053	0.54 ± 0.75	HARPS
2456700.7495	3.45 ± 0.98	HARPS-N
2456702.7585	1.1 ± 1.1	HARPS-N

Table A.5: Continued.

BJD	RV [m s^{-1}]	Instrument
2457508.5930	−0.50 ± 0.72	HARPS-N
2457510.6084	−0.56 ± 0.84	HARPS-N
2457536.6013	0.89 ± 0.76	HARPS-N
2457537.5723	0.93 ± 0.58	HARPS-N
2457538.5682	−0.60 ± 0.63	HARPS-N
2457606.4629	−7.01 ± 0.81	HARPS-N
2457608.5295	−6.82 ± 0.74	HARPS-N
2457609.4813	−5.75 ± 0.88	HARPS-N
2457610.4682	−7.7 ± 1.3	HARPS-N
2457857.6418	−3.15 ± 0.80	HARPS-N
2457860.5900	0.4 ± 1.0	HARPS-N
2457881.6194	−0.66 ± 0.72	HARPS-N
2457893.6267	2.51 ± 0.48	HARPS-N
2457905.5417	−1.05 ± 0.73	HARPS-N
2457913.4278	0.57 ± 0.66	HARPS-N
2457915.4820	−0.73 ± 0.64	HARPS-N
2457928.6255	4.0 ± 1.4	HARPS-N
2457929.5786	7.2 ± 1.1	HARPS-N
2457931.6433	0.6 ± 1.6	HARPS-N
2457933.5701	−5.39 ± 0.71	HARPS-N
2457935.5527	−4.08 ± 0.63	HARPS-N
2457936.5023	−2.52 ± 0.71	HARPS-N
2457937.6160	−0.23 ± 0.68	HARPS-N
2457943.5627	1.45 ± 0.94	HARPS-N
2457944.5028	0.27 ± 0.57	HARPS-N
2457950.5135	−2.78 ± 0.86	HARPS-N
2457954.4868	5.14 ± 0.51	HARPS-N
2457956.4337	6.30 ± 0.61	HARPS-N
2457961.4873	0.79 ± 0.70	HARPS-N
2457971.4244	1.53 ± 0.62	HARPS-N
2457972.3954	3.35 ± 0.74	HARPS-N
2457973.3935	1.25 ± 0.69	HARPS-N
2457974.5443	−0.44 ± 0.94	HARPS-N
2457975.4754	−1.87 ± 0.74	HARPS-N
2457976.4298	−3.57 ± 0.67	HARPS-N
2457978.4013	−2.84 ± 0.61	HARPS-N
2457981.4653	−2.41 ± 0.55	HARPS-N
2457983.5109	−2.04 ± 0.69	HARPS-N
2457984.4986	0.08 ± 0.59	HARPS-N
2457989.4081	3.05 ± 0.73	HARPS-N
2457991.4174	10.4 ± 1.1	HARPS-N
2457992.4104	2.60 ± 0.57	HARPS-N
2457993.4198	−0.63 ± 0.93	HARPS-N
2457994.4330	1.47 ± 0.62	HARPS-N
2457995.3917	−1.06 ± 0.59	HARPS-N
2457996.4062	−5.1 ± 1.1	HARPS-N

Table A.5: Continued.

BJD	RV $[\mathrm{m\,s^{-1}}]$	Instrument
2457997.3939	-2.06 ± 0.81	HARPS-N
2457999.4129	1.53 ± 0.69	HARPS-N
2458000.3640	0.2 ± 1.0	HARPS-N
2458007.4380	1.46 ± 0.55	HARPS-N
2458010.4463	-2.78 ± 0.77	HARPS-N
2458020.3577	1.6 ± 1.6	HARPS-N
2458020.3687	-3.7 ± 2.3	HARPS-N
2458020.3795	4.2 ± 1.9	HARPS-N
2458022.3410	-1.27 ± 0.60	HARPS-N
2458024.3696	-2.12 ± 0.53	HARPS-N
2458025.3542	-1.98 ± 0.53	HARPS-N
2458027.3482	-4.02 ± 0.94	HARPS-N
2458031.4052	1.33 ± 0.59	HARPS-N
2458037.3640	1.27 ± 0.68	HARPS-N
2458044.3621	0.00 ± 0.67	HARPS-N
2458047.3108	1.94 ± 0.63	HARPS-N
2457440.7355	-4.6 ± 1.6	CARMENES
2457444.7459	0.6 ± 1.7	CARMENES
2457472.7215	-1.9 ± 1.3	CARMENES
2457490.6715	2.1 ± 2.0	CARMENES
2457493.6837	-0.5 ± 1.4	CARMENES
2457504.6632	-0.2 ± 1.3	CARMENES
2457537.6285	-0.8 ± 2.4	CARMENES
2457542.6223	-7.3 ± 1.7	CARMENES
2457550.5745	10.9 ± 3.6	CARMENES
2457553.5607	-1.3 ± 2.1	CARMENES
2457567.5029	10.5 ± 8.2	CARMENES
2457801.6782	13.3 ± 1.5	CARMENES
2457828.6905	1.1 ± 1.5	CARMENES
2457829.6992	3.8 ± 1.4	CARMENES
2457830.7226	3.7 ± 1.3	CARMENES
2457858.6792	-5.9 ± 1.5	CARMENES
2457877.6462	12.8 ± 11.1	CARMENES
2457877.6513	0.3 ± 1.3	CARMENES
2457879.6773	1.4 ± 3.0	CARMENES
2457887.5839	-6.2 ± 1.5	CARMENES
2457901.6365	-3.0 ± 1.8	CARMENES
2457907.6007	-1.3 ± 1.5	CARMENES
2457909.5146	1.1 ± 1.8	CARMENES
2457914.5686	0.6 ± 1.8	CARMENES
2457922.5677	0.0 ± 1.5	CARMENES
2457934.5419	-11.9 ± 2.4	CARMENES
2457935.4824	-5.5 ± 1.4	CARMENES
2458158.7338	6.5 ± 1.9	CARMENES
2458171.7159	4.0 ± 1.9	CARMENES
2458188.7101	1.4 ± 1.8	CARMENES

Table A.5: Continued.

BJD	RV $[\mathrm{m\,s^{-1}}]$	Instrument
2458199.7161	-0.4 ± 2.2	CARMENES
2458200.7063	2.2 ± 1.7	CARMENES
2458212.6323	-1.1 ± 1.7	CARMENES
2458213.6716	6.0 ± 1.6	CARMENES
2458237.6302	0.4 ± 2.5	CARMENES
2458238.5125	1.5 ± 2.0	CARMENES
2458245.6203	7.4 ± 2.6	CARMENES
2458261.6011	-3.3 ± 2.1	CARMENES
2458262.5657	-1.4 ± 3.4	CARMENES
2458269.5744	1.0 ± 1.7	CARMENES
2458292.5373	-3.5 ± 1.6	CARMENES
2458292.5664	-2.7 ± 1.6	CARMENES
2458293.4054	0.4 ± 1.6	CARMENES
2458294.4627	-0.8 ± 1.5	CARMENES
2458295.4348	0.4 ± 1.4	CARMENES
2458306.5580	-4.6 ± 1.8	CARMENES
2458307.3833	-2.9 ± 1.6	CARMENES
2458313.4281	4.6 ± 1.4	CARMENES
2458315.4950	3.4 ± 1.7	CARMENES
2458317.4518	6.4 ± 3.5	CARMENES
2458319.4005	0.2 ± 2.1	CARMENES
2458320.4524	3.1 ± 1.7	CARMENES
2458321.3915	1.9 ± 1.7	CARMENES
2458322.4181	1.1 ± 1.6	CARMENES
2458323.4559	2.8 ± 1.4	CARMENES
2458324.4056	2.1 ± 1.8	CARMENES
2458326.4024	4.1 ± 1.8	CARMENES
2458328.4109	4.4 ± 1.5	CARMENES
2458329.3987	5.1 ± 1.7	CARMENES
2458330.4128	4.1 ± 1.5	CARMENES
2458331.3875	2.4 ± 1.6	CARMENES
2458332.3847	2.7 ± 1.6	CARMENES
2458334.4765	0.4 ± 1.6	CARMENES
2458335.5404	-3.7 ± 1.6	CARMENES
2458336.3807	-1.4 ± 1.9	CARMENES
2458337.3720	-3.5 ± 1.8	CARMENES
2458339.4705	-2.5 ± 1.5	CARMENES
2458340.3701	-4.0 ± 1.5	CARMENES
2458342.3334	4.1 ± 1.3	CARMENES
2458342.3492	1.6 ± 1.2	CARMENES
2458343.3563	-0.3 ± 1.3	CARMENES
2458344.3802	6.1 ± 2.0	CARMENES
2458345.3552	0.2 ± 1.4	CARMENES
2458346.3949	1.0 ± 1.2	CARMENES
2458347.5135	2.5 ± 2.0	CARMENES
2458348.3681	-0.6 ± 1.0	CARMENES

Table A.5: Continued.

BJD	RV [$\mathrm{m\,s^{-1}}$]	Instrument
2458349.3399	2.2 ± 1.0	CARMENES
2458349.3622	−0.2 ± 1.3	CARMENES
2458350.4837	−2.8 ± 1.3	CARMENES
2458351.3562	−3.0 ± 1.3	CARMENES
2458352.3370	−0.1 ± 1.3	CARMENES
2458353.3404	−4.2 ± 1.6	CARMENES
2458355.3459	−1.2 ± 1.6	CARMENES
2458356.3502	0.1 ± 1.5	CARMENES
2458357.3786	−0.3 ± 1.3	CARMENES
2458360.3393	2.8 ± 1.9	CARMENES
2458361.3358	3.3 ± 1.8	CARMENES
2458362.3361	2.4 ± 1.7	CARMENES
2458366.3262	−2.2 ± 1.8	CARMENES
2458367.3357	−2.7 ± 2.4	CARMENES
2458378.3797	−2.2 ± 2.5	CARMENES
2458382.3043	−7.4 ± 2.2	CARMENES
2458385.3046	−7.3 ± 1.7	CARMENES
2458386.3668	−4.7 ± 1.5	CARMENES
2458387.3683	−5.2 ± 1.8	CARMENES
2458390.2989	0.4 ± 1.3	CARMENES
2458391.2936	0.2 ± 1.4	CARMENES
2458392.3587	−1.0 ± 1.5	CARMENES
2458393.3048	−1.6 ± 1.6	CARMENES
2458395.3148	−1.8 ± 2.2	CARMENES
2458396.2826	−2.0 ± 1.6	CARMENES
2458397.2773	−2.0 ± 1.8	CARMENES
2458409.2996	2.9 ± 1.6	CARMENES
2458414.2706	−2.6 ± 1.7	CARMENES
2458415.3223	−4.0 ± 1.8	CARMENES
2458427.2976	−1.4 ± 1.7	CARMENES
2458494.7657	0.0 ± 2.2	CARMENES
2458500.7579	1.0 ± 2.5	CARMENES

Table A.6: Radial velocity curves of SB1s described in Chapter 4.

Obs. date [BJD]	RV [$\mathrm{m\,s^{-1}}$]	Inst.	Meth.
GJ 207.1			
2453708.8474	−3700 ± 1200	F	T
2453424.6545	55250 ± 940	F	T
2454455.6240	−2810 ± 260	H	T
2457693.6299	64069 ± 12	C	S
2457985.6872	11450 ± 43	C	S
2458007.6799	29835.5 ± 9.6	C	S
2458026.6315	57691.9 ± 8.5	C	S
2458078.5036	65398 ± 15	C	S
2458094.5798	−67.0 ± 9.4	C	S
2458160.3600	−2658 ± 17	C	S
2458167.3276	65932 ± 19	C	S
2458173.2985	54835 ± 19	C	S
2458182.3093	38259 ± 16	C	S
2458187.4240	31455 ± 35	C	S
2458206.3402	−1822 ± 15	C	S
2458434.5484	24896 ± 12	C	S
2458435.7075	42661.4 ± 9.4	C	S
GJ 912			
2455046.8642	−1016.2 ± 3.2	H	S
2455053.8299	−968.7 ± 1.4	H	S
2455054.8321	−965.6 ± 1.0	H	S
2455056.8260	−931.5 ± 6.0	H	S
2455056.9116	−952.9 ± 1.9	H	S
2455057.8606	−948.9 ± 2.9	H	S
2455125.6477	−568.2 ± 1.2	H	S
2455464.6903	65.9 ± 1.0	H	S
2456235.5404	2.2 ± 1.2	H	S
2456502.9029	815 ± 447	F	T
2456612.6329	507 ± 396	F	T
2456617.7031	749 ± 362	F	T
2457593.6588	288.8 ± 2.0	C	S
2457595.6683	283.3 ± 2.0	C	S
2457604.6409	283.5 ± 2.4	C	S
2457608.6448	283.1 ± 2.1	C	S
2457625.6036	276.8 ± 2.2	C	S
2457634.5720	265.4 ± 2.4	C	S
2457644.5412	263.2 ± 2.3	C	S
2457672.5148	257.9 ± 1.7	C	S
2457753.2839	228.4 ± 2.2	C	S
2457931.6397	137.9 ± 2.2	C	S
2457951.6217	129.5 ± 2.2	C	S
2457971.5873	123.9 ± 1.8	C	S

Table A.6: Continued.

Obs. date [BJD]	RV [m s^{-1}]	Inst.	Meth.
2457997.5621	110.2 ± 1.6	C	S
2458017.4397	105.4 ± 1.9	C	S
2458065.4532	79.4 ± 1.6	C	S
2458095.3024	65.2 ± 1.5	C	S
2458134.2945	45.3 ± 1.6	C	S
2458289.6531	−30.1 ± 1.7	C	S
2458349.6060	−57.8 ± 1.1	C	S
2458416.4309	−95.7 ± 1.2	C	S
2458476.3298	−133.2 ± 1.3	C	S
2458663.6613	−242.1 ± 1.9	C	S
2458723.5831	−282.1 ± 2.1	C	S
2458783.4458	−326.4 ± 1.8	C	S
2458844.2613	−373.0 ± 3.6	C	S
2459033.6486	−528.8 ± 2.2	C	S
2459093.5803	−590.4 ± 2.1	C	S
2459153.4087	−649.2 ± 2.6	C	S
	GJ 3626		
2457472.5069	−1426.4 ± 1.7	C	S
2457534.3920	−1489.2 ± 2.6	C	S
2458078.6861	−604.4 ± 1.3	C	S
2458092.6519	−532.8 ± 1.5	C	S
2458110.6715	−442.8 ± 1.6	C	S
2458112.6498	−431.5 ± 1.3	C	S
2458161.5900	−210.8 ± 5.6	C	S
2458205.4683	−47.6 ± 1.4	C	S
2458236.5044	35.5 ± 1.8	C	S
2458270.4148	119.9 ± 1.7	C	S
2458300.3645	166.2 ± 1.5	C	S
2458413.7056	260.2 ± 1.3	C	S
2458449.7141	272.8 ± 3.6	C	S
2458480.6987	265.3 ± 1.4	C	S
2458510.6934	268.0 ± 1.6	C	S
2458540.7452	253.1 ± 1.8	C	S
2458570.5584	246.2 ± 1.8	C	S
2458600.4789	229.8 ± 1.1	C	S
2458608.5203	222.0 ± 1.5	C	S
2458615.4695	219.8 ± 1.4	C	S
2458626.4686	219.4 ± 1.4	C	S
2458633.4138	212.6 ± 2.3	C	S
2458641.4210	210.4 ± 1.6	C	S
2458649.3983	206.3 ± 1.9	C	S
2458656.3797	199.9 ± 1.2	C	S
2458663.3722	196.6 ± 2.2	C	S

Table A.6: Continued.

Obs. date [BJD]	RV [m s^{-1}]	Inst.	Meth.
2458664.3700	193.8 ± 1.4	C	S
2458804.7036	100.5 ± 2.6	C	S
2458811.7346	91.4 ± 2.8	C	S
2458831.7261	82.0 ± 2.4	C	S
2458844.7072	67.9 ± 3.1	C	S
2458851.6835	63.0 ± 1.3	C	S
2458860.6576	58.2 ± 1.7	C	S
2458878.6207	44.3 ± 2.2	C	S
2458885.6051	34.1 ± 1.6	C	S
2458893.6085	28.4 ± 1.2	C	S
2458903.5747	18.4 ± 1.4	C	S
2458911.6684	20.8 ± 4.4	C	S
2458918.5292	9.1 ± 1.9	C	S
2458978.3929	−37.3 ± 3.1	C	S
2459149.6687	−174.1 ± 2.3	C	S
2459212.7667	−231.5 ± 3.8	C	S
	LSPM 427-016		
2456353.6532	12860 ± 130	F	T
2456353.6711	12830 ± 240	F	T
2457449.5866	−202.2 ± 1.8	C	S
2457673.7141	−160.3 ± 1.7	C	S
2458059.6730	−73.3 ± 1.9	C	S
2458091.6469	−72.4 ± 1.3	C	S
2458110.4906	−66.0 ± 1.5	C	S
2458121.5078	−72.1 ± 1.4	C	S
2458135.6016	−62.1 ± 1.9	C	S
2458166.5454	−54.1 ± 1.3	C	S
2458209.4565	−47.6 ± 1.9	C	S
2458265.3527	−34.3 ± 1.7	C	S
2458405.6881	3.4 ± 6.0	C	S
2458435.7292	7.8 ± 1.7	C	S
2458468.6965	11.9 ± 1.8	C	S
2458498.6532	20.0 ± 1.4	C	S
2458528.5540	25.2 ± 1.2	C	S
2458558.4795	33.0 ± 1.5	C	S
2458589.3391	38.1 ± 1.4	C	S
2458631.3536	51.8 ± 1.6	C	S
2458769.6981	76.8 ± 2.1	C	S
2458801.7426	94.5 ± 2.3	C	S
2459151.6447	180.0 ± 1.3	C	S
2459183.7294	187.5 ± 1.4	C	S

Table A.6: Continued.

Obs. date [BJD]	RV [$\mathrm{m\,s^{-1}}$]	Inst.	Meth.
GJ 282 C			
2454040.7842	−20540 ± 210	F	T
2454040.8059	−20490 ± 200	F	T
2456294.6551	−16250 ± 190	F	T
2456982.8285	2255.3 ± 1.8	H	S
2456982.8190	2257.7 ± 1.9	H	S
2456986.8692	2238.7 ± 1.4	H	S
2456987.8191	2231.3 ± 1.7	H	S
2456987.8289	2233.0 ± 1.5	H	S
2456988.8492	2209.4 ± 1.8	H	S
2457342.8600	2016.3 ± 1.4	H	S
2457342.8709	2015.4 ± 1.7	H	S
2457344.8348	2010.5 ± 1.7	H	S
2457344.8453	2010.3 ± 1.6	H	S
2457395.5526	898.9 ± 2.7	C	S
2457401.5286	874.4 ± 1.8	C	S
2457444.4238	842.0 ± 2.0	C	S
2457466.4221	828.7 ± 2.1	C	S
2457489.3509	804.0 ± 2.6	C	S
2457493.4898	1903.3 ± 1.4	H	S
2457493.5007	1901.8 ± 1.4	H	S
2457494.5592	1885.5 ± 1.4	H	S
2457494.5699	1884.9 ± 1.4	H	S
2457699.7112	590.1 ± 3.4	C	S
2457704.6305	573.3 ± 2.1	C	S
2457712.7522	1645.8 ± 1.7	H	S
2457712.7627	1642.7 ± 1.6	H	S
2457760.5315	500.0 ± 2.4	C	S
2457769.6272	1587.7 ± 1.0	H	S
2457769.6380	1589.4 ± 1.0	H	S
2457771.7639	1596.6 ± 1.8	H	S
2457771.7745	1599.5 ± 1.6	H	S
2457788.5567	488.4 ± 2.4	C	S
2457791.4466	421.5 ± 3.7	C	S
2457793.4649	457.6 ± 2.3	C	S
2457800.4426	483.2 ± 2.9	C	S
2457821.4008	420.9 ± 1.9	C	S
2457853.3705	357.7 ± 2.0	C	S
2457857.3579	374.3 ± 2.3	C	S
2458025.7141	116.4 ± 1.9	C	S
2458029.6965	131.0 ± 2.7	C	S
2458034.6884	90.9 ± 2.3	C	S
2458040.6785	91.7 ± 2.7	C	S
2458048.6727	82.8 ± 2.0	C	S

Table A.6: Continued.

Obs. date [BJD]	RV [$\mathrm{m\,s^{-1}}$]	Inst.	Meth.
2458052.6611	66.0 ± 1.9	C	S
2458054.7226	78.1 ± 2.2	C	S
2458056.6422	66.2 ± 1.4	C	S
2458059.6546	50.3 ± 2.1	C	S
2458065.5992	48.7 ± 1.5	C	S
2458074.6706	41.2 ± 1.7	C	S
2458081.5932	6.6 ± 2.4	C	S
2458091.5506	1.7 ± 1.9	C	S
2458094.5913	−20.9 ± 1.8	C	S
2458097.7185	−5.0 ± 2.3	C	S
2458123.4250	−48.3 ± 1.8	C	S
2458140.3853	−83.3 ± 2.0	C	S
2458166.4032	−147.2 ± 2.5	C	S
2458200.3147	−167.9 ± 2.2	C	S
2458382.7032	−565.3 ± 2.5	C	S
2458451.6149	−704.8 ± 2.0	C	S
2458518.5736	−889.2 ± 2.6	C	S
2458524.5624	−900.0 ± 2.2	C	S
2458526.5304	211.3 ± 1.5	H	S
2458526.5410	212.6 ± 1.5	H	S
2458527.5310	226.9 ± 1.5	H	S
2458527.5574	224.3 ± 1.2	H	S
2458532.5496	152.2 ± 1.1	H	S
2458532.5769	152.1 ± 1.2	H	S
2458533.5557	181.4 ± 1.0	H	S
2458533.5807	180.4 ± 1.0	H	S
2458534.5343	198.3 ± 1.1	H	S
2458534.5614	198.3 ± 1.1	H	S
2458585.3259	−1027.5 ± 2.1	C	S
2458592.4805	12.6 ± 1.6	H	S
2458592.5159	11.3 ± 1.7	H	S
2458595.4924	45.6 ± 1.1	H	S
2458595.5258	44.6 ± 1.2	H	S
2458606.4830	−0.2 ± 0.9	H	S
2458606.5131	−1.2 ± 0.8	H	S
2458607.4725	7.6 ± 0.9	H	S
2458607.4982	9.5 ± 0.9	H	S
2458758.7044	−1461.6 ± 2.2	C	S
2458836.6590	−1687.4 ± 7.6	C	S
2458896.4318	−1869.8 ± 2.0	C	S
2459132.7130	−2539.1 ± 3.4	C	S

Table A.7: Radial velocity curves of SB2s described in Chapter 4.

Obs. date [BJD]	RV$_A$ [km s^{-1}]	RV$_B$ [km s^{-1}]	Inst.
EZ Psc			
2457591.6809	−19.176 ± 0.096	49.195 ± 0.691	C
2457595.6767	−20.474 ± 0.104	53.955 ± 0.814	C
2457604.6730	−18.028 ± 0.094	46.201 ± 0.563	C
2457618.5834	13.381 ± 0.112	−41.863 ± 0.680	C
2457634.5438	8.025 ± 0.108	−26.342 ± 0.737	C
2457655.5387	−28.732 ± 0.101	76.981 ± 0.643	C
2457676.4600	5.648 ± 0.096	−21.270 ± 0.638	C
2457677.5432	24.280 ± 0.107	−74.853 ± 0.793	C
2458120.2882	25.824 ± 0.097	−77.995 ± 0.586	C
2456116.9585	−17.909 ± 0.221	· · ·	F
2456497.8654	23.034 ± 0.201	−64.388 ± 1.711	F
2456497.8845	23.235 ± 0.514	−69.734 ± 3.145	F
2456616.6603	25.274 ± 0.206	−59.942 ± 1.686	F
2456616.6783	25.263 ± 0.218	· · ·	F
GJ 1029			
2457611.6660	−7.04 ± 0.11	−16.93 ± 0.37	C
2457619.6197	−7.67 ± 0.11	−16.39 ± 0.37	C
2457620.6000	−7.81 ± 0.11	−16.35 ± 0.37	C
2457625.5827	−8.50 ± 0.12	· · ·	C
2457632.6071	−9.78 ± 0.11	· · ·	C
2457636.4114	−10.40 ± 0.13	· · ·	C
2457643.6336	−12.59 ± 0.12	· · ·	C
2457786.3730	−7.11 ± 0.14	−16.59 ± 0.47	C
2457921.6445	−10.195 ± 0.095	· · ·	C
2457936.6348	−15.294 ± 0.090	−5.88 ± 0.36	C
2457951.6386	−20.208 ± 0.093	0.48 ± 0.39	C
2457966.6439	−9.73 ± 0.11	· · ·	C
2457981.6498	−6.871 ± 0.087	−17.08 ± 0.35	C
2457999.6108	−7.521 ± 0.089	−16.59 ± 0.32	C
2458020.5395	−10.743 ± 0.089	· · ·	C
2458031.5371	−15.084 ± 0.091	−6.29 ± 0.35	C
2458033.5194	−15.771 ± 0.093	−5.26 ± 0.37	C
2458040.4951	−19.121 ± 0.087	−0.72 ± 0.37	C
2458047.4815	−20.157 ± 0.085	0.48 ± 0.34	C
2458051.4670	−17.652 ± 0.084	−2.69 ± 0.36	C
2458055.4708	−14.407 ± 0.098	−6.81 ± 0.40	C
2457759.6280	−20.12 ± 0.12	0.47 ± 0.96	T
2457944.9249	−19.03 ± 0.12	0.17 ± 0.95	T
2457993.9720	−6.80 ± 0.12	−17.11 ± 0.95	T
2458002.8908	−7.73 ± 0.12	−17.12 ± 0.92	T
2458027.8068	−13.27 ± 0.11	−9.71 ± 0.87	T
2458034.8799	−16.25 ± 0.11	−3.58 ± 0.85	T
2458042.7260	−19.79 ± 0.12	0.21 ± 0.90	T
2458050.7436	−18.11 ± 0.11	−1.71 ± 0.87	T
2458055.8456	−13.81 ± 0.11	−9.02 ± 0.85	T
2458063.7882	−8.91 ± 0.11	−14.35 ± 0.89	T
2458082.6561	−6.67 ± 0.11	−18.14 ± 0.88	T
2458090.7040	−7.08 ± 0.12	−18.43 ± 0.94	T
2458107.7450	−8.91 ± 0.12	−13.70 ± 0.91	T
Ross 59			
2457400.5090	25.147 ± 0.026	34.99 ± 0.38	C
2457652.6554	28.069 ± 0.033	25.59 ± 0.24	C
2457656.6488	28.080 ± 0.031	25.52 ± 0.24	C
2457676.6899	28.228 ± 0.025	25.03 ± 0.20	C
2457689.6523	28.353 ± 0.042	24.63 ± 0.31	C
2457691.6431	28.364 ± 0.027	24.65 ± 0.18	C
2457692.6412	28.338 ± 0.027	24.48 ± 0.19	C
2457693.6380	28.348 ± 0.031	24.49 ± 0.22	C
2457701.6170	28.463 ± 0.038	24.49 ± 0.26	C
2457766.5431	29.011 ± 0.029	23.04 ± 0.19	C
2457815.3650	29.456 ± 0.024	21.91 ± 0.16	C
2457830.4307	29.585 ± 0.029	21.47 ± 0.19	C
2457851.3409	29.796 ± 0.030	21.03 ± 0.21	C
2458017.6101	25.182 ± 0.029	34.67 ± 0.20	C
2458088.6137	24.542 ± 0.030	36.61 ± 0.20	C
2458118.4846	24.983 ± 0.026	35.07 ± 0.16	C
2458149.3995	25.511 ± 0.026	33.71 ± 0.18	C
2458182.4119	26.017 ± 0.026	32.55 ± 0.32	C
2458225.3189	26.526 ± 0.028	· · ·	C
2456255.6871	28.319 ± 0.072	23.97 ± 0.62	HN
2456255.7830	28.331 ± 0.078	24.12 ± 0.65	HN
2456604.6893	24.042 ± 0.070	37.3 ± 1.1	HN
2456605.6889	24.036 ± 0.071	37.50 ± 0.82	HN
2456606.6984	24.044 ± 0.072	37.08 ± 0.95	HN
2456607.6778	24.042 ± 0.069	37.33 ± 0.98	HN
2452324.6910	24.60 ± 0.50	· · ·	CO
2455621.2820	29.50 ± 0.60	· · ·	CO
2455630.3320	29.70 ± 0.60	· · ·	CO
2455861.6050	24.90 ± 0.90	· · ·	CO
2456001.2560	23.30 ± 0.60	· · ·	CO
2456221.6400	28.30 ± 0.70	· · ·	CO
2456677.3600	26.00 ± 0.80	· · ·	CO
2456954.6010	29.40 ± 1.00	· · ·	CO
2456959.6310	30.00 ± 0.70	· · ·	CO
2458127.4620	24.58 ± 0.20	· · ·	CO
2458182.2960	25.32 ± 0.21	· · ·	CO
2458392.6430	27.91 ± 0.20	· · ·	CO
2458414.6020	27.77 ± 0.23	· · ·	CO
UCAC4 355-020729			
2457695.6848	13.294 ± 0.062	14.909 ± 0.094	C
2457759.5452	11.756 ± 0.050	16.571 ± 0.075	C
2457788.4644	15.282 ± 0.049	12.382 ± 0.077	C
2457799.4012	11.619 ± 0.041	16.650 ± 0.069	C
2457824.3610	12.993 ± 0.047	15.180 ± 0.071	C
2457832.3566	11.779 ± 0.043	16.532 ± 0.062	C
2458034.7061	12.218 ± 0.047	16.072 ± 0.077	C
2458043.7118	14.697 ± 0.045	12.940 ± 0.073	C
2458047.7093	12.394 ± 0.039	15.835 ± 0.064	C
2458051.7069	15.888 ± 0.039	11.804 ± 0.061	C
2458054.7050	11.699 ± 0.042	16.507 ± 0.069	C
2458058.6955	15.850 ± 0.047	11.804 ± 0.075	C
2458061.7292	11.578 ± 0.084	16.671 ± 0.135	C
2458064.6885	15.795 ± 0.059	11.754 ± 0.096	C
2458074.6442	11.563 ± 0.041	16.687 ± 0.062	C
2458078.6349	15.687 ± 0.040	11.895 ± 0.067	C
2458084.6432	15.848 ± 0.051	11.732 ± 0.082	C
2458123.5290	15.697 ± 0.043	11.873 ± 0.071	C
2458167.4181	12.518 ± 0.043	15.629 ± 0.069	C
2458172.3816	12.309 ± 0.051	15.911 ± 0.081	C

Table A.7: Continued.

Table A.7: Continued.

Obs. date [BJD]	RV_A [$km\,s^{-1}$]	RV_B [$km\,s^{-1}$]	Inst.
2458173.3962	11.710 ± 0.042	16.525 ± 0.072	C
2458174.3848	13.157 ± 0.053	15.019 ± 0.086	C
2458175.3863	15.206 ± 0.049	12.505 ± 0.077	C
2458182.3797	15.587 ± 0.065	12.055 ± 0.099	C
2458426.6586	15.395 ± 0.047	12.300 ± 0.073	C
2458433.6589	14.877 ± 0.046	12.815 ± 0.076	C
NLTT 23956			
2457735.7087	43.16 ± 0.13	−37.65 ± 0.33	C
2457799.5416	4.00 ± 0.14	30.03 ± 0.33	C
2457814.4799	18.32 ± 0.11	6.31 ± 0.26	C
2457821.4617	−12.86 ± 0.14	59.66 ± 0.34	C
2457830.4822	43.23 ± 0.13	−37.88 ± 0.32	C
2457832.4844	10.00 ± 0.13	19.83 ± 0.30	C
2457848.4245	45.31 ± 0.12	−41.13 ± 0.30	C
2457850.3877	5.71 ± 0.13	26.75 ± 0.31	C
2457856.3647	3.97 ± 0.13	29.94 ± 0.34	C
2457861.3722	33.38 ± 0.12	−20.49 ± 0.31	C
2457866.3890	46.14 ± 0.13	−42.66 ± 0.32	C
2458080.7339	26.84 ± 0.14	−9.11 ± 0.34	C
2458092.7091	22.64 ± 0.11	−2.54 ± 0.27	C
2458094.7477	−17.57 ± 0.11	67.41 ± 0.27	C
GJ 3612			
2457419.6610	−70.325 ± 0.081	−46.20 ± 0.35	C
2457474.4705	−54.973 ± 0.084	−76.51 ± 0.36	C
2457494.4779	−51.220 ± 0.081	−83.51 ± 0.35	C
2457672.7357	−72.172 ± 0.083	−42.30 ± 0.34	C
2457690.6364	−67.682 ± 0.079	−51.50 ± 0.32	C
2457709.5717	−56.942 ± 0.082	−71.73 ± 0.36	C
2457759.5694	...	...	C
2457761.6902	−63.837 ± 0.082	−59.70 ± 0.33	C
2457762.5343	−64.354 ± 0.085	−58.66 ± 0.36	C
2457763.6222	−64.852 ± 0.088	−57.55 ± 0.37	C
2457766.5875	−66.034 ± 0.078	−54.84 ± 0.32	C
2457787.5680	−72.133 ± 0.083	−42.38 ± 0.33	C
2457802.7532	−70.502 ± 0.080	−45.71 ± 0.34	C
2457815.7454	−64.961 ± 0.093	−57.26 ± 0.40	C
2457819.7395	...	...	C
2457823.4053	−60.041 ± 0.086	−66.10 ± 0.34	C
2457830.6792	−55.977 ± 0.077	−73.97 ± 0.35	C
2457833.3296	−54.636 ± 0.080	−77.26 ± 0.34	C
2457850.5303	−51.069 ± 0.070	−84.03 ± 0.33	C
2458088.7086	−51.038 ± 0.081	−84.13 ± 0.34	C
2458105.7093	−56.327 ± 0.077	−73.15 ± 0.34	C
GJ 1182			
2457488.5925	−2.455 ± 0.091	2.49 ± 0.36	C
2457494.5471	−3.489 ± 0.098	3.40 ± 0.35	C
2457505.5087	−5.235 ± 0.089	5.82 ± 0.35	C
2457802.6332	−3.526 ± 0.089	3.47 ± 0.34	C
2457822.6421	−6.938 ± 0.081	8.36 ± 0.32	C
2457833.6210	−9.129 ± 0.070	11.39 ± 0.30	C
2457848.5930	−11.813 ± 0.071	15.64 ± 0.32	C

Table A.7: Continued.

Obs. date [BJD]	RV_A [$km\,s^{-1}$]	RV_B [$km\,s^{-1}$]	Inst.
2457850.5784	−11.997 ± 0.070	15.95 ± 0.31	C
2457852.5734	−12.107 ± 0.071	16.13 ± 0.31	C
2457854.6329	−12.013 ± 0.071	15.96 ± 0.32	C
2457858.5516	−10.973 ± 0.075	14.18 ± 0.33	C
2457860.5355	−9.741 ± 0.075	12.28 ± 0.32	C
2457862.5431	−7.727 ± 0.073	9.46 ± 0.31	C
2457864.5170	−4.978 ± 0.090	5.53 ± 0.36	C
2457875.5984	10.891 ± 0.073	−18.50 ± 0.31	C
2457888.5064	10.429 ± 0.073	−17.88 ± 0.31	C
2457889.5389	10.194 ± 0.076	−17.46 ± 0.33	C
2457894.4574	8.925 ± 0.072	−15.76 ± 0.29	C
2457901.4802	7.202 ± 0.075	−13.16 ± 0.34	C
2457907.4334	5.847 ± 0.072	−10.37 ± 0.36	C
2457912.4396	4.752 ± 0.073	−8.28 ± 0.34	C
2457917.4318	3.794 ± 0.074	−6.74 ± 0.30	C
2457931.4500	...	...	C
2457943.4164	...	...	C
2458151.0260	−10.799 ± 0.082	14.99 ± 0.59	T
2458168.0386	−9.919 ± 0.079	13.51 ± 0.56	T
2458179.9286	7.876 ± 0.077	−13.57 ± 0.55	T
2458200.9220	9.512 ± 0.078	−14.96 ± 0.55	T
2458212.8382	6.551 ± 0.077	−10.89 ± 0.55	T
2458228.9227	3.228 ± 0.080	−6.72 ± 0.57	T
2458258.7091	−2.290 ± 0.072	1.83 ± 0.51	T
2458267.7116	−3.708 ± 0.077	5.20 ± 0.55	T
2458272.6892	−4.654 ± 0.077	5.88 ± 0.55	T
2458277.7616	−5.564 ± 0.074	7.15 ± 0.52	T
2458281.6752	−6.288 ± 0.078	7.56 ± 0.56	T
2458290.6810	−7.917 ± 0.079	10.53 ± 0.56	T
2458300.6853	−9.907 ± 0.073	13.22 ± 0.52	T
2458304.7157	−10.461 ± 0.088	15.21 ± 0.62	T
UU UMi			
2456418.4924	−41.365 ± 0.162	...	CF
2457472.6413	−38.972 ± 0.035	−45.00 ± 0.14	C
2457504.5670	−38.869 ± 0.038	−44.98 ± 0.15	C
2457529.4912	−38.934 ± 0.037	−45.14 ± 0.14	C
2457556.4629	−38.826 ± 0.041	−45.11 ± 0.16	C
2457559.5434	−38.823 ± 0.043	−45.11 ± 0.17	C
2457763.6439	−38.747 ± 0.039	−45.43 ± 0.15	C
2457800.7530	−38.655 ± 0.025	−45.48 ± 0.11	C
2457815.5392	−38.658 ± 0.030	−45.48 ± 0.13	C
2457832.5606	−38.666 ± 0.025	−45.49 ± 0.12	C
2457848.6126	−38.629 ± 0.027	−45.50 ± 0.12	C
2457867.5390	−38.647 ± 0.027	−45.52 ± 0.13	C
2457897.4662	−38.659 ± 0.031	−45.52 ± 0.14	C
2457931.5387	−38.643 ± 0.033	−45.56 ± 0.15	C
2457961.3985	−38.578 ± 0.029	−45.58 ± 0.14	C
2457993.3479	−38.642 ± 0.036	−45.62 ± 0.17	C
2458054.3032	−38.580 ± 0.029	−45.61 ± 0.12	C
2458117.7403	−38.608 ± 0.030	−45.62 ± 0.12	C
2458161.7033	−38.613 ± 0.033	−45.63 ± 0.13	C
2458200.5577	−38.631 ± 0.034	−45.61 ± 0.14	C

Table A.7: Continued.

Obs. date [BJD]	RV_A [$km\,s^{-1}$]	RV_B [$km\,s^{-1}$]	Inst.
2458263.4946	−38.646 ± 0.031	−45.57 ± 0.13	C
2458353.3698	−38.630 ± 0.033	−45.50 ± 0.15	C
2458451.7424	−38.732 ± 0.029	−45.44 ± 0.13	C
2458541.6890	−38.754 ± 0.029	−45.33 ± 0.12	C
2458631.5092	−38.860 ± 0.030	−45.12 ± 0.14	C
2458723.3696	−38.950 ± 0.029	−44.93 ± 0.14	C
2458816.7528	−39.078 ± 0.028	−44.77 ± 0.13	C
2458913.6613	−39.220 ± 0.028	−44.46 ± 0.12	C
2459003.4687	−39.440 ± 0.035	−44.26 ± 0.14	C
2459093.3467	−39.658 ± 0.029	−43.89 ± 0.14	C
2459212.7286	−39.901 ± 0.043	−43.13 ± 0.21	C
	LP 395-8		
2457545.6530	5.98 ± 0.18	−85.08 ± 0.55	C
2457566.6209	−49.37 ± 0.19	13.38 ± 0.59	C
2457573.5523	−19.62 ± 0.25	−42.03 ± 0.72	C
2457593.4966	−60.68 ± 0.19	33.67 ± 0.55	C
2457633.4363	−14.14 ± 0.29	−48.41 ± 0.86	C
2457643.4056	−50.76 ± 0.18	16.21 ± 0.54	C
2457652.3889	−57.53 ± 0.24	27.94 ± 0.75	C
2457652.4062	−55.50 ± 0.27	24.57 ± 0.85	C
2457652.4215	−53.58 ± 0.19	20.70 ± 0.57	C
2457652.4367	−51.46 ± 0.18	16.73 ± 0.54	C
2457654.3796	−48.20 ± 0.22	12.68 ± 0.62	C
2458089.2778	−61.19 ± 0.27	34.61 ± 0.86	C
2458093.2694	10.04 ± 0.11	−91.95 ± 0.36	C
2458102.2775	9.00 ± 0.17	−90.16 ± 0.52	C
	GJ 810 A		
2457642.4209	−145.502 ± 0.048	−138.232 ± 0.071	C
2457568.6143	−142.56 ± 0.10	−141.61 ± 0.16	C
2457571.5896	−142.673 ± 0.086	−141.42 ± 0.13	C
2457574.5988	−142.833 ± 0.066	−141.7 ± 0.10	C
2457586.5633	−143.195 ± 0.048	−140.745 ± 0.076	C
2457604.5331	−143.923 ± 0.053	−140.027 ± 0.078	C
2457608.5009	−144.129 ± 0.046	−139.919 ± 0.069	C
2457626.5156	−144.782 ± 0.059	−138.976 ± 0.083	C
2457630.4562	−144.973 ± 0.053	−138.825 ± 0.085	C
2457652.3733	−145.840 ± 0.073	−137.74 ± 0.11	C
2457655.4534	−145.997 ± 0.055	−137.626 ± 0.080	C
2457673.3313	−146.714 ± 0.045	−136.813 ± 0.067	C
2457677.3211	−146.820 ± 0.044	−136.648 ± 0.066	C
2457704.2706	−147.757 ± 0.043	−135.566 ± 0.060	C
2457911.6195	−139.039 ± 0.043	−145.692 ± 0.062	C
2457928.5978	−138.493 ± 0.044	−146.466 ± 0.070	C
2457943.5924	−138.078 ± 0.047	−146.920 ± 0.075	C
2457958.5804	−137.831 ± 0.043	−147.274 ± 0.066	C
2457975.5164	−137.634 ± 0.047	−147.513 ± 0.069	C
2457990.4604	−137.536 ± 0.049	−147.605 ± 0.072	C
2458020.3798	−137.614 ± 0.045	−147.544 ± 0.065	C
2458048.3226	−137.823 ± 0.041	−147.241 ± 0.064	C
2458074.2575	−138.172 ± 0.039	−146.782 ± 0.061	C
2458089.2567	−138.446 ± 0.059	−146.499 ± 0.086	C
2458093.2450	−138.556 ± 0.037	−146.421 ± 0.060	C
2458260.6585	−143.276 ± 0.047	−140.785 ± 0.069	C
2458320.6599	−145.644 ± 0.055	−138.031 ± 0.076	C
2458384.3730	−147.883 ± 0.045	−135.358 ± 0.068	C
2458451.2468	−147.743 ± 0.043	−135.541 ± 0.065	C

Table A.8: Radial velocity curves of ST3s described in Chapter 4.

Obs. date [BJD]	RV_A [$km\,s^{-1}$]	RV_{Ba} [$km\,s^{-1}$]	RV_{Bb} [$km\,s^{-1}$]	Inst.
		GJ 3916		
2453099.8240	4.073(95)	−10.21(41)	12.11(33)	U
2453112.6457	4.25(12)	···	···	U
2453453.7944	8.291(97)	···	···	U
2453480.6825	8.879(97)	−18.55(41)	···	U
2453488.6672	8.736(92)	−18.63(36)	···	U
2453505.8286	8.31(10)	−8.90(37)	2.58(25)	U
2454167.8224	3.18(95)	−5.0(3.3)	11.50(1.84)	F
2454569.6487	−1.675(99)	···	14.34(30)	F
2454570.8108	−2.037(86)	···	12.84(27)	H
2454580.8485	−1.24(10)	···	···	F
2454583.8633	−2.029(84)	11.57(25)	3.25(26)	H
2454628.5259	−2.43(72)	16.9(2.5)	···	F
2454639.7481	−1.83(70)	13.2(2.5)	···	F
2454661.5681	−2.248(79)	···	14.54(29)	H
2454939.7950	−2.616(82)	−9.26(21)	20.77(26)	F
2454943.8549	−2.544(96)	−9.67(26)	22.06(30)	F
2454951.8029	−2.623(91)	−9.71(24)	22.11(30)	F
2454984.6058	−0.876(82)	13.04(31)	···	F
2454993.7310	−1.771(80)	17.20(32)	···	F
2455003.5563	−2.36(14)	20.80(48)	···	F
2455053.5303	−0.846(87)	···	9.75(35)	F
2455066.4967	−1.995(93)	···	17.59(28)	F
2455075.4993	−2.10(70)	···	20.9(2.4)	F
2455338.7519	−0.91(10)	−8.80(25)	19.37(28)	F
2455397.5650	−0.798(88)	18.45(29)	−7.40(17)	F
2455407.5645	−1.127(86)	19.65(32)	−7.97(20)	F
2455430.5447	−0.392(81)	14.24(33)	···	F
2455434.5660	−0.20(75)	12.5(2.3)	···	F
2455438.4973	0.14(64)	···	···	F
2455615.8289	0.77(10)	−11.16(34)	19.57(26)	F
2456352.8951	6.87(75)	···	−10.2(2.4)	F
2456500.6423	7.59(91)	···	−6.0(2.1)	F
2457476.6461	−1.098(78)	−8.69(22)	22.32(24)	C
2457493.6138	−1.448(34)	−1.22(29)	14.76(22)	C
2457504.5889	−1.511(43)	6.67(25)	7.70(18)	C
2457540.4868	−2.167(41)	21.32(27)	−4.59(37)	C
2457910.4391	−1.398(60)	14.35(29)	1.48(48)	C
2457916.5426	−1.794(47)	17.79(34)	−1.61(36)	C
2457949.3780	−1.865(42)	18.61(32)	−1.99(34)	C
2457977.3697	−1.537(36)	3.81(34)	11.21(26)	C
2458166.6713	−1.126(35)	6.91(55)	7.00(42)	C
2458177.7400	−0.872(62)	14.23(33)	−0.63(36)	C
2458186.7186	−1.501(40)	18.85(27)	−2.95(38)	C
2458200.6650	−1.417(41)	20.75(22)	−5.71(23)	C
2458207.6529	−1.469(41)	19.72(23)	−4.83(29)	C
2458225.6859	−0.626(49)	13.26(28)	0.26(36)	C
2458237.5692	−0.749(65)	6.68(35)	6.63(27)	C
2458244.5965	−0.544(38)	1.02(55)	10.43(27)	C
2458249.6074	−0.835(33)	−0.65(33)	13.27(24)	C
2458261.4581	−0.905(37)	−7.11(25)	19.01(23)	C
2458269.5321	−0.803(35)	−9.38(25)	21.28(22)	C
2458275.5228	−0.789(56)	−9.26(30)	21.09(26)	C
2458283.5380	−0.813(46)	−6.85(28)	18.48(24)	C
2458289.5200	−0.921(38)	−1.68(47)	14.87(26)	C
2458297.4920	−0.390(42)	4.63(26)	8.82(18)	C
2458575.7001	0.331(53)	12.69(25)	−0.46(32)	C
2458587.6266	0.657(37)	18.01(22)	−6.07(21)	C
2458597.6156	0.725(62)	19.26(29)	−7.15(25)	C

Table A.8: Continued.

Obs. date [BJD]	RV_A [$\mathrm{km\,s^{-1}}$]	RV_{Ba} [$\mathrm{km\,s^{-1}}$]	RV_{Bb} [$\mathrm{km\,s^{-1}}$]	Inst.
2458603.5602	0.753(38)	18.55(24)	−6.79(22)	C
2458609.5737	0.732(42)	17.15(23)	−5.63(21)	C
2458615.5395	0.446(38)	15.19(25)	−4.18(26)	C
2458626.5359	0.830(46)	10.28(31)	0.60(31)	C
2458636.4799	1.381(35)	5.70(16)	5.74(14)	C
2458643.4509	0.894(35)	0.64(35)	9.36(26)	C
2458656.4064	0.993(39)	−7.21(25)	15.64(22)	C
2458662.3779	1.102(43)	−9.81(26)	17.89(25)	C
2458679.3749	1.157(39)	−9.89(25)	17.94(22)	C
2458690.3681	1.000(38)	−2.14(43)	11.34(28)	C
2458696.3722	1.774(60)	−0.16(31)	7.22(30)	C
2458708.3595	0.956(40)	12.13(30)	−0.72(44)	C
GJ 4383				
2455046.8563	−12.63(11)	···	···	H
2455053.8419	−12.608(96)	···	···	H
2455054.8560	−12.622(87)	···	···	H
2455056.8369	−12.58(12)	···	···	H
2455056.8994	−12.58(11)	···	···	H
2455124.6171	−12.257(83)	···	···	H
2455537.5585	−10.154(87)	···	···	H
2455541.5532	−10.067(85)	···	···	H
2455550.5263	−9.997(94)	···	···	H
2456496.8926	−7.47(28)	···	···	F
2456496.9060	−7.49(22)	···	···	F
2456614.6481	−7.54(22)	···	···	F
2456614.6626	−7.58(22)	···	···	F
2457587.6611	−10.559(38)	···	···	C
2457604.6500	−10.629(30)	···	···	C
2457622.6367	−10.730(29)	···	−18.93(53)	C
2457623.5259	−10.57(31)	···	···	C
2457623.5458	−10.717(33)	−6.08(75)	−19.17(50)	C
2457654.5045	−10.941(31)	−0.46(48)	−24.88(53)	C
2457672.4896	−10.984(29)	−1.26(40)	−23.64(45)	C
2457695.3885	−11.147(33)	···	···	C
2457786.2850	−11.615(43)	···	···	C
2457916.6483	−12.511(25)	···	−6.01(58)	C
2457942.6396	−12.612(27)	−19.57(42)	2.28(50)	C
2457999.5659	−12.937(24)	···	−4.17(43)	C
2458051.4269	−13.287(28)	−2.49(37)	···	C
2458092.3378	−13.540(20)	4.25(31)	−20.19(35)	C
2458122.2522	−13.636(21)	−4.21(36)	···	C
2458283.6381	−14.622(29)	3.26(43)	···	C
2458343.6430	−14.896(22)	−5.05(26)	···	C
2458410.5819	−15.148(33)	···	3.99(54)	C
2458471.3527	−15.450(22)	−1.05(34)	−7.37(43)	C
2458656.6395	−15.975(24)	−5.82(41)	−0.80(57)	C
2458718.5956	−15.981(23)	6.44(36)	···	C
2458784.4240	−16.111(25)	−7.59(38)	1.80(42)	C
2458844.3742	−16.019(27)	−10.53(55)	5.52(47)	C
2459074.6456	−15.606(23)	−9.04(31)	1.97(37)	C
2459138.4984	−15.398(26)	2.64(35)	···	C
2459214.3691	−15.135(25)	−8.49(38)	−0.45(47)	C

Notes. The number between parentheses indicate the uncertainty of the last digits.

Table A.9: Computed *TESS* times of minimum light and bisector indicators of the systems in Table 5.1.

System	T_0 [BJD]	Type	bis_{odd} [s]	bis_{even} [s]
KX Cnc	2458876.936865 ± 0.000007	1	-0.1	-1.4
	2458897.014194 ± 0.000035	2	29.4	24.3
AL Dor	2458330.899178 ± 0.000015	2	-0.6	1.1
	2458345.804510 ± 0.000017	2	-5.4	0.1
	2458360.709872 ± 0.000014	2	-2.6	-4.5
	2458368.727679 ± 0.000011	1	0.3	3.3
	2458375.615218 ± 0.000022	2	10.4	-4.9
	2458390.520581 ± 0.000012	2	9.7	-6.9
	2458398.538454 ± 0.000021	1	-0.1	-2.8
	2458405.425910 ± 0.000016	2	-0.3	-0.3
	2458413.443841 ± 0.000012	1	1.2	7.7
	2458428.349174 ± 0.000010	1	-1.8	2.2
	2458435.236608 ± 0.000013	2	13.5	-2.2
	2458443.254508 ± 0.000009	1	2.6	1.9
	2458458.159905 ± 0.000010	1	-0.3	-3.6
	2458473.065252 ± 0.000011	1	-1.1	-4.4
	2458479.952683 ± 0.000015	2	9.6	12.7
	2458487.970580 ± 0.000009	1	2.1	6.1
	2458517.781254 ± 0.000011	1	5.8	-3.6
	2458524.668732 ± 0.000015	2	12.7	-5.1
	2458547.592004 ± 0.000010	1	-6.8	-3.2
	2458554.479382 ± 0.000014	2	3.8	-3.7
	2458562.497339 ± 0.000012	1	4.7	0.2
	2458577.402706 ± 0.000009	1	3.3	-1.7
	2458592.308035 ± 0.000015	1	-6.3	3.6
	2458599.195437 ± 0.000018	2	1.8	-13.7
	2458607.213415 ± 0.000013	1	-1.8	-1.0
	2458622.118801 ± 0.000011	1	-7.1	0.7
	2458637.024117 ± 0.000014	1	11.2	-3.8
	2458643.911499 ± 0.000017	2	2.0	-10.8
	2458651.929448 ± 0.000010	1	0.4	2.8
	2458658.816864 ± 0.000021	2	-5.4	15.9
	2458666.834837 ± 0.000011	1	6.5	-5.1
	2458673.722229 ± 0.000013	2	2.2	-2.7
	2458681.740149 ± 0.000011	1	2.4	0.7
	2459039.468685 ± 0.000013	1	8.6	4.6
	2459046.355977 ± 0.000016	2	-5.8	-20.9
	2459054.374054 ± 0.000011	1	1.7	3.0
	2459069.279392 ± 0.000009	1	-6.5	-2.5

Table A.9: Continued.

System	T_0 [BJD]	Type	bis_{odd} [s]	bis_{even} [s]
	2459076.166619 ± 0.000015	2	-4.6	8.0
	2459084.184755 ± 0.000010	1	-8.2	2.9
	2459091.071973 ± 0.000016	2	-12.7	3.0
	2459099.090104 ± 0.000011	1	-0.4	4.0
	2459105.977338 ± 0.000018	2	3.5	3.8
	2459113.995480 ± 0.000011	1	3.5	-0.7
	2459120.882721 ± 0.000021	2	-13.5	24.2
	2459128.900816 ± 0.000020	1	-12.6	0.8
	2459135.788058 ± 0.000022	2	2.8	2.9
	2459150.693449 ± 0.000026	2	-2.1	-9.9
	2459165.598792 ± 0.000016	2	-3.3	7.2
	2459180.504092 ± 0.000013	2	-3.2	5.7
	2459188.522240 ± 0.000008	1	-1.3	-2.8
	2459195.409441 ± 0.000012	2	11.2	14.7
	2459203.427605 ± 0.000008	1	0.9	-0.2
	2459210.314806 ± 0.000013	2	6.9	2.2
	2459218.332924 ± 0.000009	1	-0.9	2.3
	2459225.220139 ± 0.000015	2	-0.9	-4.0
	2459233.238303 ± 0.000009	1	2.2	4.7
	2459240.125512 ± 0.000020	2	5.5	-10.8
	2459248.143691 ± 0.000011	1	8.9	5.5
	2459263.048993 ± 0.000007	1	-2.6	1.9
	2459277.954364 ± 0.000009	1	1.3	-0.7
	2459284.841535 ± 0.000014	2	-2.3	-6.4
RW Lac	2458739.558831 ± 0.000069	2	-6.1	-10.6
	2458744.816580 ± 0.000058	1	-0.5	-0.9
	2458755.185769 ± 0.000055	1	3.7	-1.6
	2458760.297243 ± 0.000050	2	6.5	-15.4
	2458765.554954 ± 0.000075	1	10.5	-2.8
	2458770.666367 ± 0.000066	2	9.0	-4.2
	2458781.035546 ± 0.000061	2	-1.8	3.1
	2458786.293329 ± 0.000055	1	9.7	-22.6
V530 Ori	2458473.922862 ± 0.000215	2	25.6	4.7
	2458480.033789 ± 0.000481	2	-37.6	17.6
	2458483.308375 ± 0.000215	1	-18.6	-8.1
	2458486.144969 ± 0.000250	2	44.4	-13.2
	2459204.380285 ± 0.000016	1	-1.5	-0.3
	2459207.216815 ± 0.000120	2	-13.2	-13.6
	2459210.491025 ± 0.000020	1	-10.3	1.9
	2459213.327678 ± 0.000113	2	-34.3	27.0
	2459216.601766 ± 0.000028	1	-2.9	-8.7
	2459219.438215 ± 0.000149	2	9.1	20.6
	2459222.712589 ± 0.000020	1	-0.4	-0.9
	2459225.548865 ± 0.000146	2	33.8	-3.2

Table A.9: Continued.

System	T_0 [BJD]	Type	bis_{odd} [s]	bis_{even} [s]
EW Ori	2459175.361678 ± 0.000017	1	3.7	5.8
	2459179.043055 ± 0.000027	2	-12.9	-14.1
	2459182.298508 ± 0.000019	1	2.6	3.5
	2459189.235445 ± 0.000014	1	3.4	-2.1
	2459192.916840 ± 0.000023	2	-4.8	-8.0
	2459196.172271 ± 0.000018	1	-2.1	-3.7
	2459199.853725 ± 0.000025	2	-10.1	-9.9
HP Dra	2458687.744593 ± 0.000061	2	4.2	-2.7
	2458692.937554 ± 0.000038	1	-0.7	-11.4
	2458698.506117 ± 0.000046	2	-4.0	-11.0
	2458703.698977 ± 0.000031	1	3.1	-1.0
	2458709.267748 ± 0.000036	2	-4.0	-5.0
	2458714.460702 ± 0.000036	1	-9.8	-2.5
	2458720.029182 ± 0.000042	2	-10.9	-24.0
	2458725.222114 ± 0.000057	1	-25.4	-13.9
	2458730.790673 ± 0.000025	2	0.6	-5.0
	2458735.983699 ± 0.000020	1	-0.4	3.2
	2459010.590854 ± 0.000031	2	-1.7	-7.0
	2459015.783859 ± 0.000038	1	-0.4	-8.2
	2459021.352122 ± 0.000044	2	-11.3	16.5
	2459026.545402 ± 0.000027	1	7.4	1.0
	2459032.114006 ± 0.000024	2	5.3	0.0
TZ Men	2458629.231962 ± 0.000051	2	-40.9	8.3
	2458633.429286 ± 0.000014	1	9.1	-2.5
	2458637.800892 ± 0.000066	2	-19.0	9.3
	2458641.998406 ± 0.000011	1	-8.7	0.0
	2458646.369715 ± 0.000051	2	39.1	-2.4
	2458650.567458 ± 0.000008	1	4.3	-0.5
	2458654.939016 ± 0.000030	2	-0.6	-16.5
	2458659.136412 ± 0.000013	1	-12.8	3.2
	2458663.508388 ± 0.000032	2	4.8	-6.9
	2458672.077195 ± 0.000038	2	27.1	2.2
	2458676.274576 ± 0.000009	1	-5.5	-0.6
	2458680.646278 ± 0.000024	2	-10.2	7.6
	2459040.546846 ± 0.000051	2	-45.9	21.5
	2459044.743918 ± 0.000006	1	-1.2	-0.3
	2459053.312816 ± 0.000008	1	4.5	-4.3
	2459057.684683 ± 0.000016	2	-8.7	2.6
V541 Cyg	2458686.305678 ± 0.000065	1	23.1	-7.0
	2458701.643429 ± 0.000067	1	15.6	-10.1
	2458708.676227 ± 0.000049	2	-19.5	18.8
LV Her	2458998.622068 ± 0.000042	1	2.6	3.8
	2459014.520470 ± 0.000047	2	13.9	-7.5
	2459017.058105 ± 0.000050	1	-24.1	-7.7
	2459032.956636 ± 0.000049	2	-13.5	-4.0

Table A.9: Continued.

System	T_0 [BJD]	Type	bis_{odd} [s]	bis_{even} [s]
V459 Cas	2458795.116894 ± 0.000030	2	-1.9	-9.0
	2458799.410466 ± 0.000036	1	-6.3	7.4
	2458803.575131 ± 0.000048	2	-14.3	11.1
	2458807.868807 ± 0.000043	1	-18.0	14.9
	2458812.033300 ± 0.000031	2	6.8	-4.7
	2458960.117373 ± 0.000035	1	-6.2	-6.7
	2458964.281938 ± 0.000061	2	13.6	26.4
	2458972.740318 ± 0.000041	2	-5.5	5.7
	2458977.033806 ± 0.000040	1	6.7	-5.0
	2458981.198583 ± 0.000038	2	8.1	-6.6
RR Lyn	2458846.459621 ± 0.000026	2	-22.2	2.6
	2458851.926525 ± 0.000028	1	5.4	30.4
	2458861.871504 ± 0.000032	1	-6.2	-35.7
	2458866.350051 ± 0.000032	2	-30.8	-5.9
V501 Her	2458984.501296 ± 0.000077	1	-11.1	-39.7
	2458988.622032 ± 0.000058	2	5.0	-14.8
	2458993.098781 ± 0.000062	1	3.4	3.3
	2458997.219848 ± 0.000057	2	9.8	-14.3
	2459001.696416 ± 0.000057	1	20.5	-7.0
	2459005.817446 ± 0.000050	2	3.6	4.9
	2459014.415024 ± 0.000084	2	-10.6	2.0
	2459018.891839 ± 0.000060	1	21.1	-8.4
	2459027.489911 ± 0.000072	1	46.0	-13.3
	2459031.610163 ± 0.000067	2	23.6	9.1
KW Hya	2458518.800943 ± 0.000019	2	16.3	3.3
	2458523.001593 ± 0.000008	1	-2.3	0.5
	2458526.551424 ± 0.000012	2	3.9	-1.1
	2458530.752004 ± 0.000009	1	6.6	1.9
	2458538.502533 ± 0.000017	1	4.0	0.2
	2459259.295667 ± 0.000007	1	-4.1	2.0
	2459262.845739 ± 0.000011	2	-0.8	7.8
	2459274.796586 ± 0.000008	1	2.3	5.7
	2459278.346687 ± 0.000014	2	12.5	8.0
V501 Mon	2458470.959595 ± 0.000122	1	10.6	1.2
	2458474.106373 ± 0.000069	2	-6.8	5.1
	2458481.127529 ± 0.000109	2	26.2	-12.8
	2458485.001952 ± 0.000224	1	-7.6	-14.9
	2458488.148705 ± 0.000094	2	-26.6	16.0
	2459204.311745 ± 0.000105	2	1.0	-9.6
	2459208.185948 ± 0.000084	1	-51.6	7.3
	2459211.333204 ± 0.000108	2	-32.7	33.5
	2459218.354372 ± 0.000107	2	37.1	-21.0
	2459222.228435 ± 0.000124	1	-62.0	23.3
	2459225.375540 ± 0.000129	2	-35.0	-27.4

Table A.9: Continued.

System	T_0 [BJD]	Type	bis_{odd} [s]	bis_{even} [s]
GG Ori	2458471.237183 ± 0.000020	1	1.6	-0.2
	2458474.027894 ± 0.000026	2	1.7	8.9
	2458480.659446 ± 0.000032	2	-4.5	-0.1
	2458484.500153 ± 0.000021	1	3.1	-1.5
	2458487.290868 ± 0.000028	2	-1.3	3.1
EY Cep	2458820.424811 ± 0.000016	1	-4.7	0.8
	2458823.564945 ± 0.000024	2	6.1	-2.9
	2458831.536413 ± 0.000028	2	-13.6	1.0
	2458836.367713 ± 0.000015	1	2.5	0.9
	2458839.507938 ± 0.000028	2	9.9	-1.2
	2458987.825909 ± 0.000019	1	-0.7	2.9
	2458990.965811 ± 0.000025	2	4.9	-6.1
	2458998.937048 ± 0.000037	2	-7.6	-6.6
	2459003.768839 ± 0.000017	1	-3.4	1.9
	2459006.908721 ± 0.000030	2	-12.4	-4.0

Appendix B

Additional figures

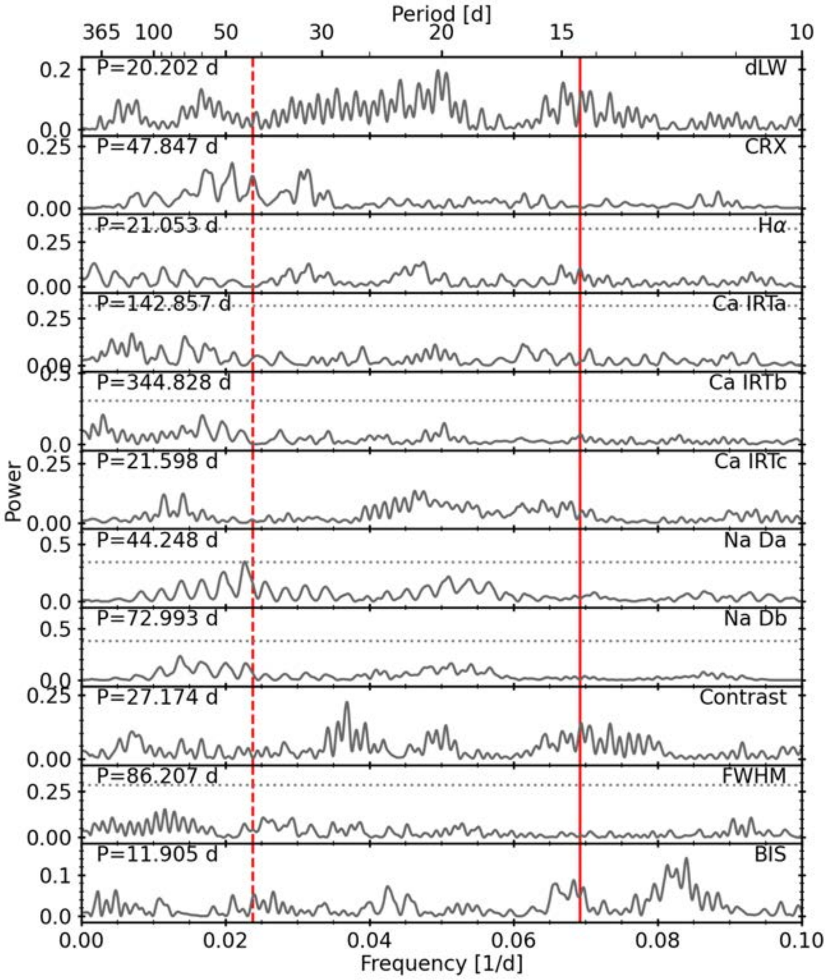

Figure B.1: Periodograms of the residuals after subtracting the highest significant signal of the activity indicators of LSPM J2116+0234. The vertical solid line indicates the period of the suggested planet, while the vertical red dotted line marks the period attributed to the rotation period. The periods reported in each panel refer to the highest peak. The horizontal line represents the bootstrapped 0.1% FAP level.

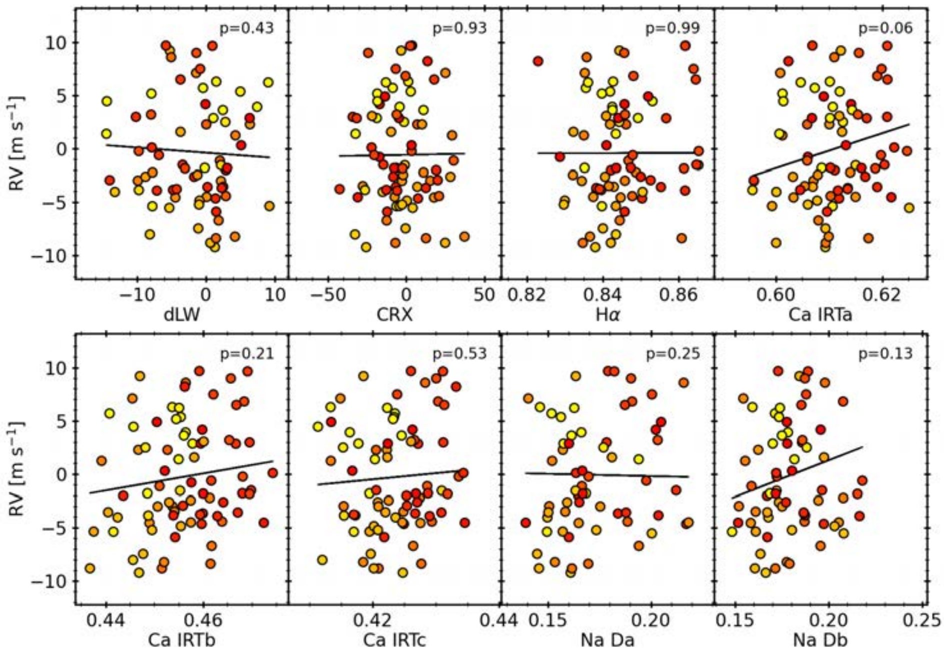

Figure B.2: Correlation plots between the activity indices and radial velocities of LSPM J2116+0234. Colour code represents the phase with the estimated rotation period of 42.7 d. The p-value of a linear fit is shown.

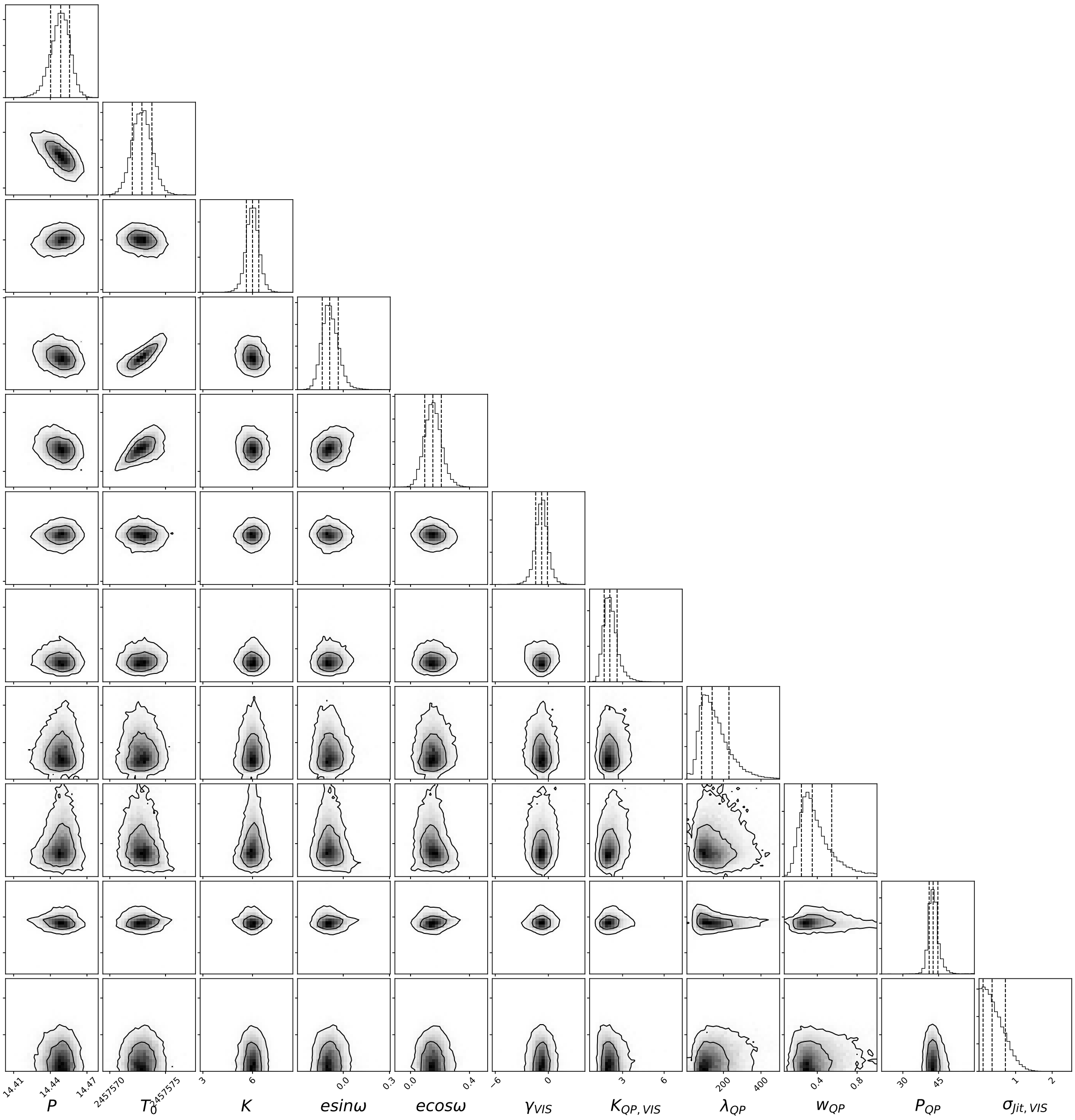

Figure B.3: Posterior distributions from the MCMC analysis on LSPM J2116+0234 b. Plotted are the planetary parameters, instrumental offset ($\gamma_{\rm VIS}$), GP hyper-parameters ($K_{\rm QP}$, $\lambda_{\rm QP}$, $w_{\rm QP}$, $P_{\rm QP}$) and additional jitter term ($\sigma_{\rm Jit,VIS}$). The vertical dashed lines indicate the mean and 1σ uncertainties of the fitted parameters.

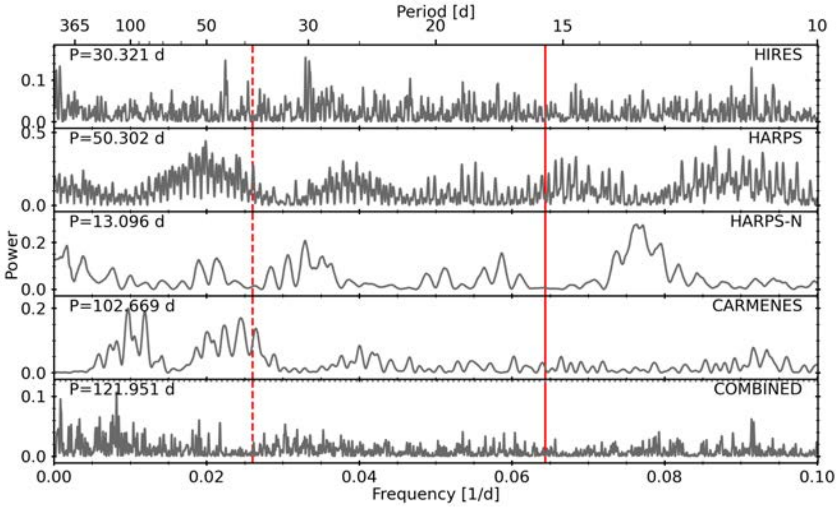

Figure B.4: GLS periodograms of GJ 686 RV data after the first two significant signals are removed. The first four panels represent the HIRES, HARPS, HARPS-N, and CARMENES data, respectively, and the bottom panel shows the periodogram of the combined dataset. The periods reported in each panel refer to the highest peak. Horizontal dotted lines represent the bootstrapped FAP level of 0.1%. The vertical solid and dashed red lines indicate the period of the proposed planet and estimated stellar rotation period at 15.53 and ~38 d, respectively.

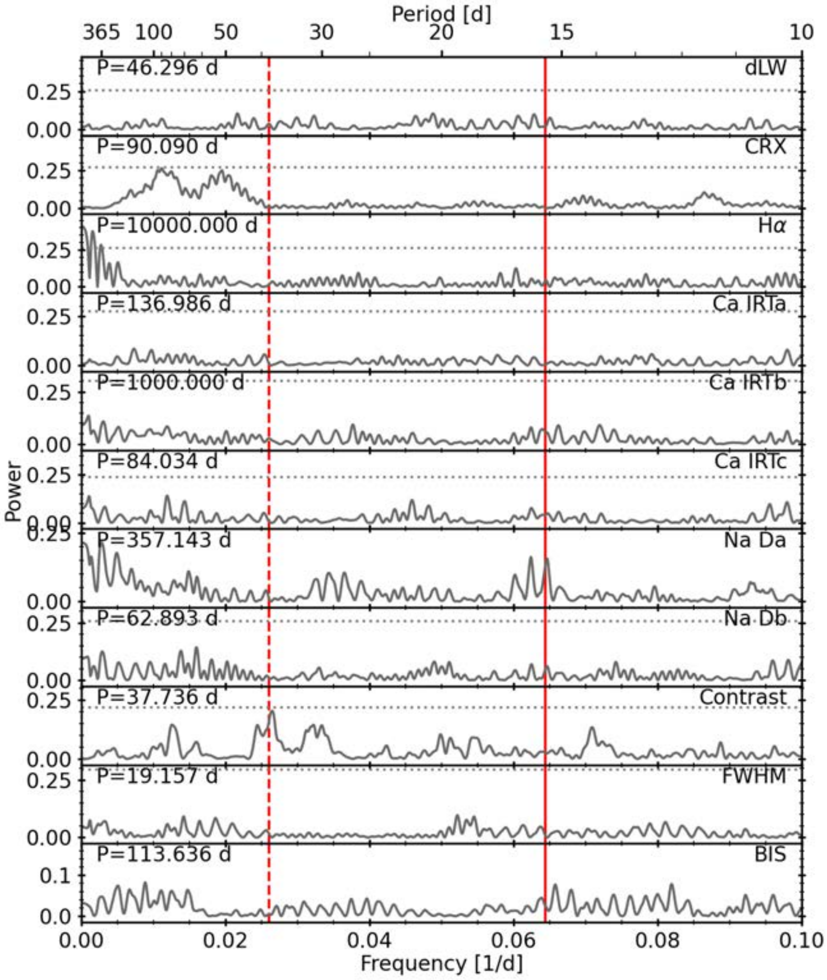

Figure B.5: Periodograms of the residuals after subtracting the highest significant signal of the activity indicators of GJ 686. The vertical solid line indicates the period of the suggested planet, while the vertical red dotted line marks the period attributed to the rotation period. The periods reported in each panel refer to the highest peak. The horizontal dotted line represents the bootstrapped 0.1% FAP level.

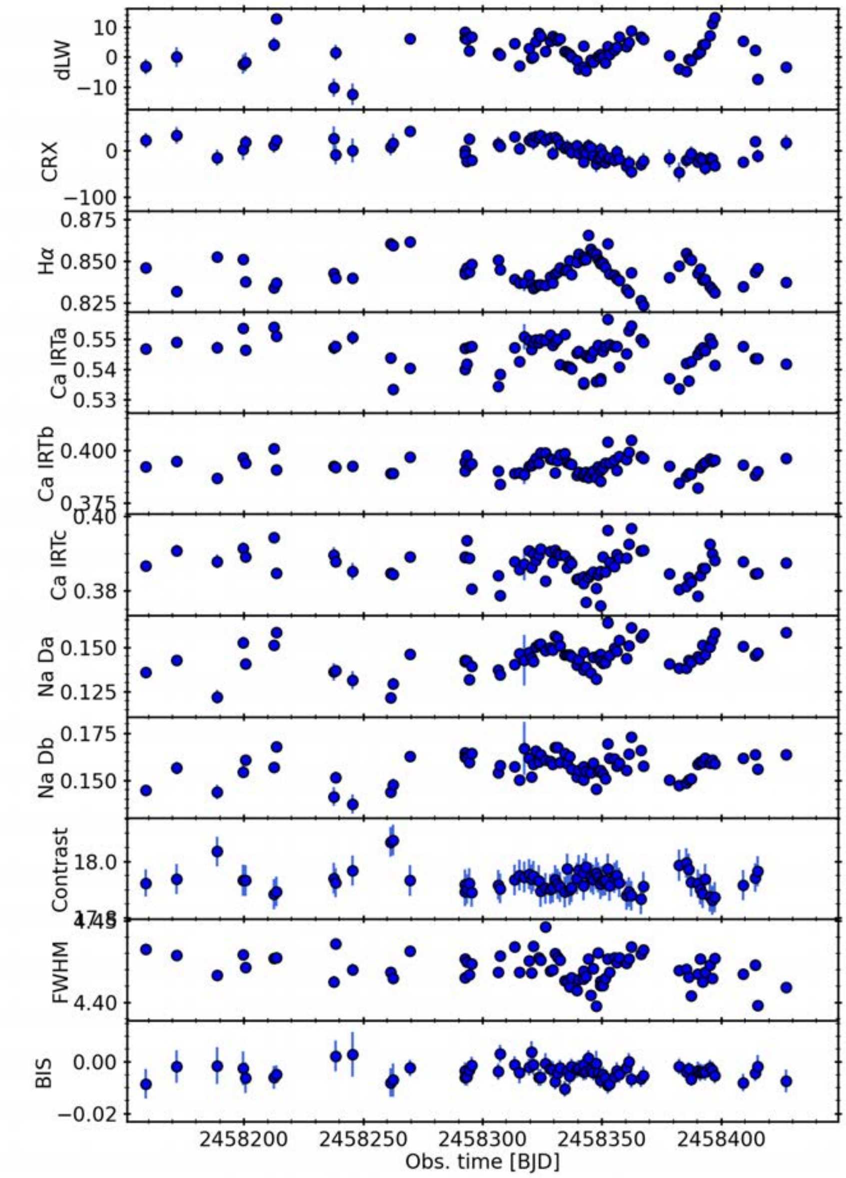

Figure B.6: Time series of the CARMENES activity indicators for the last year of observations of GJ 686, where the rotation modulation is evident in several of the indicators.

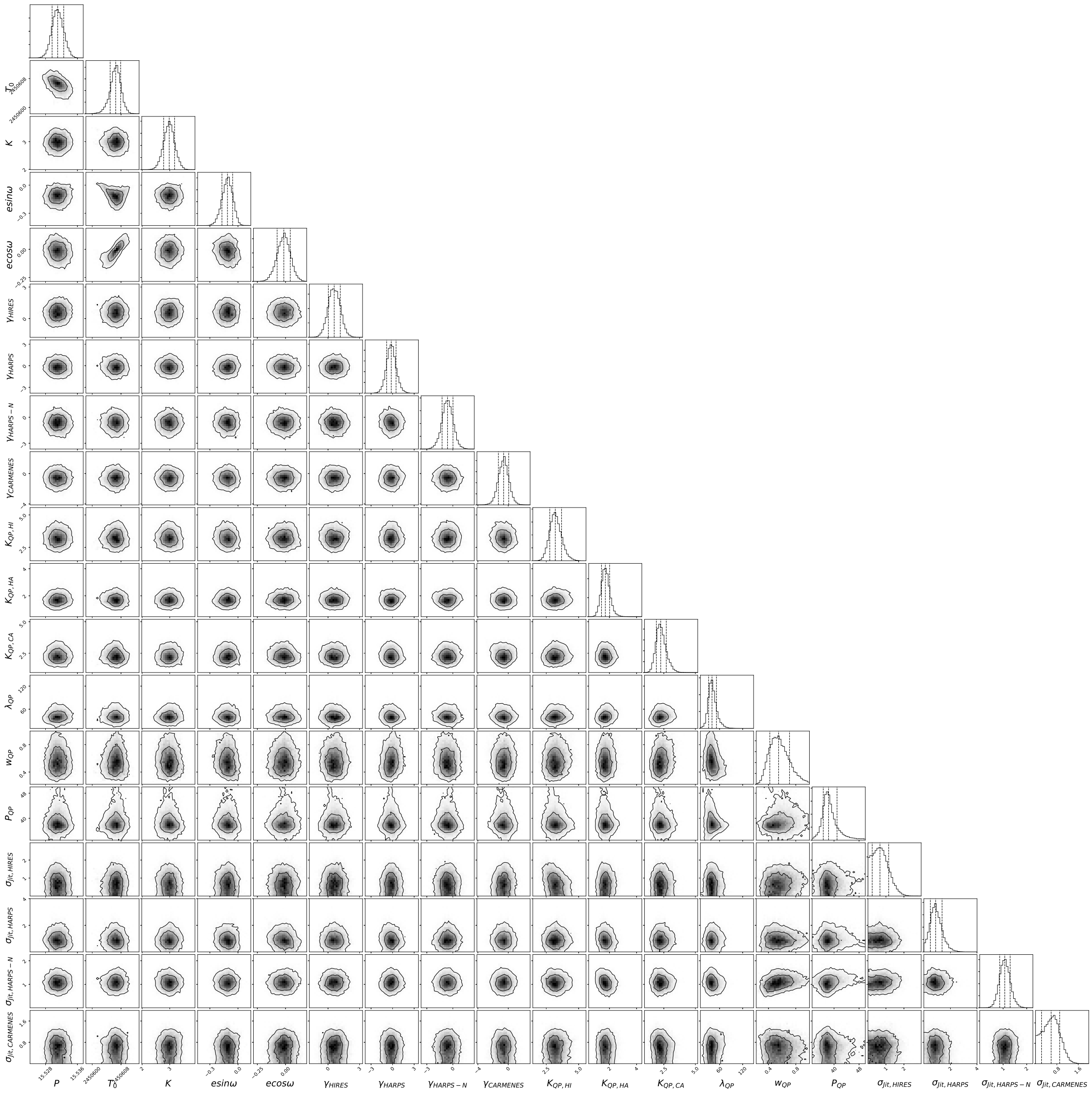

Figure B.7: Posterior distributions from the MCMC analysis on GJ 686 b. Plotted are the planetary parameters, instrumental offsets (γ_{HIRES}, γ_{HARPS}, $\gamma_{\mathrm{HARPS-N}}$, $\gamma_{\mathrm{CARMENES}}$), GP hyper-parameters ($K_{\mathrm{QP}}$, λ_{QP}, w_{QP}, P_{QP}) and additional data jitters ($\sigma_{\mathrm{Jit,HIRES}}$, $\sigma_{\mathrm{Jit,HARPS}}$, $\sigma_{\mathrm{Jit,HARPS-N}}$, $\sigma_{\mathrm{Jit,CARMENES}}$). The vertical dashed lines indicate the mean and 1σ uncertainties of the fitted parameters.

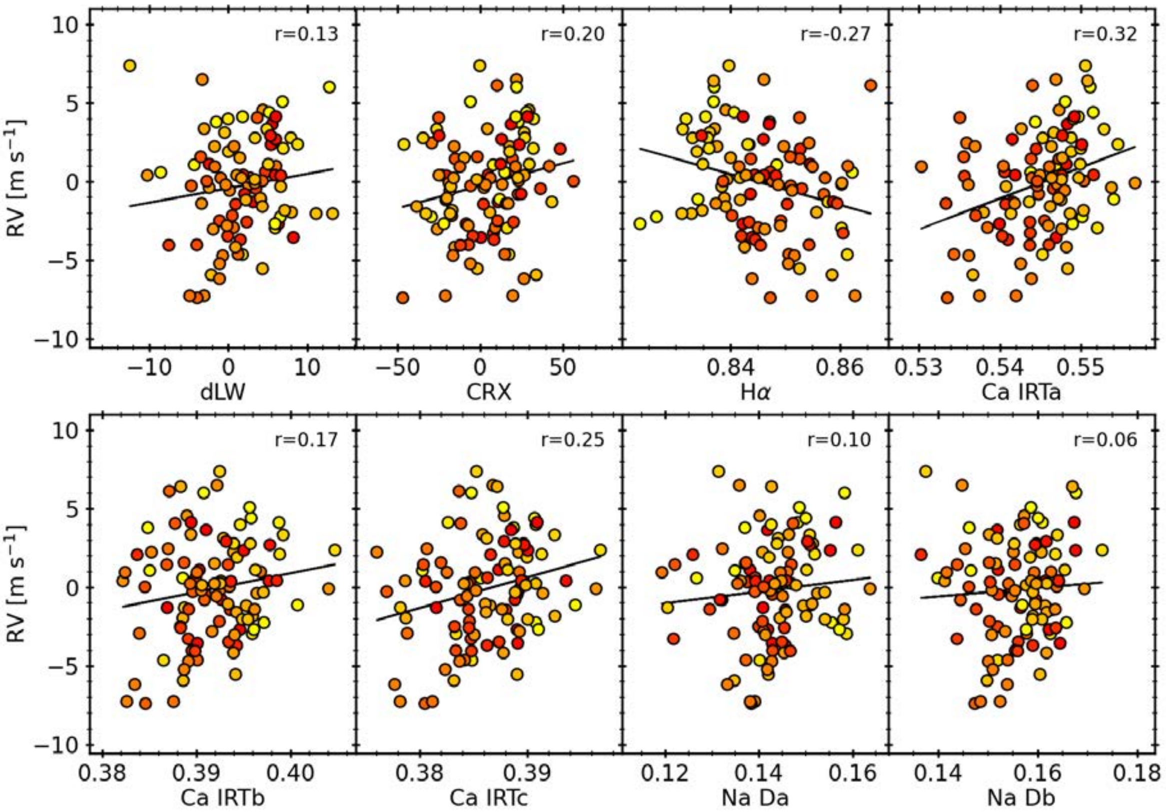

Figure B.8: Correlation plots between the activity indices and radial velocities of GJ 686. Colour code represents the phase with the estimated rotation period of 38.2 d. The p-value of a linear fit is shown.